

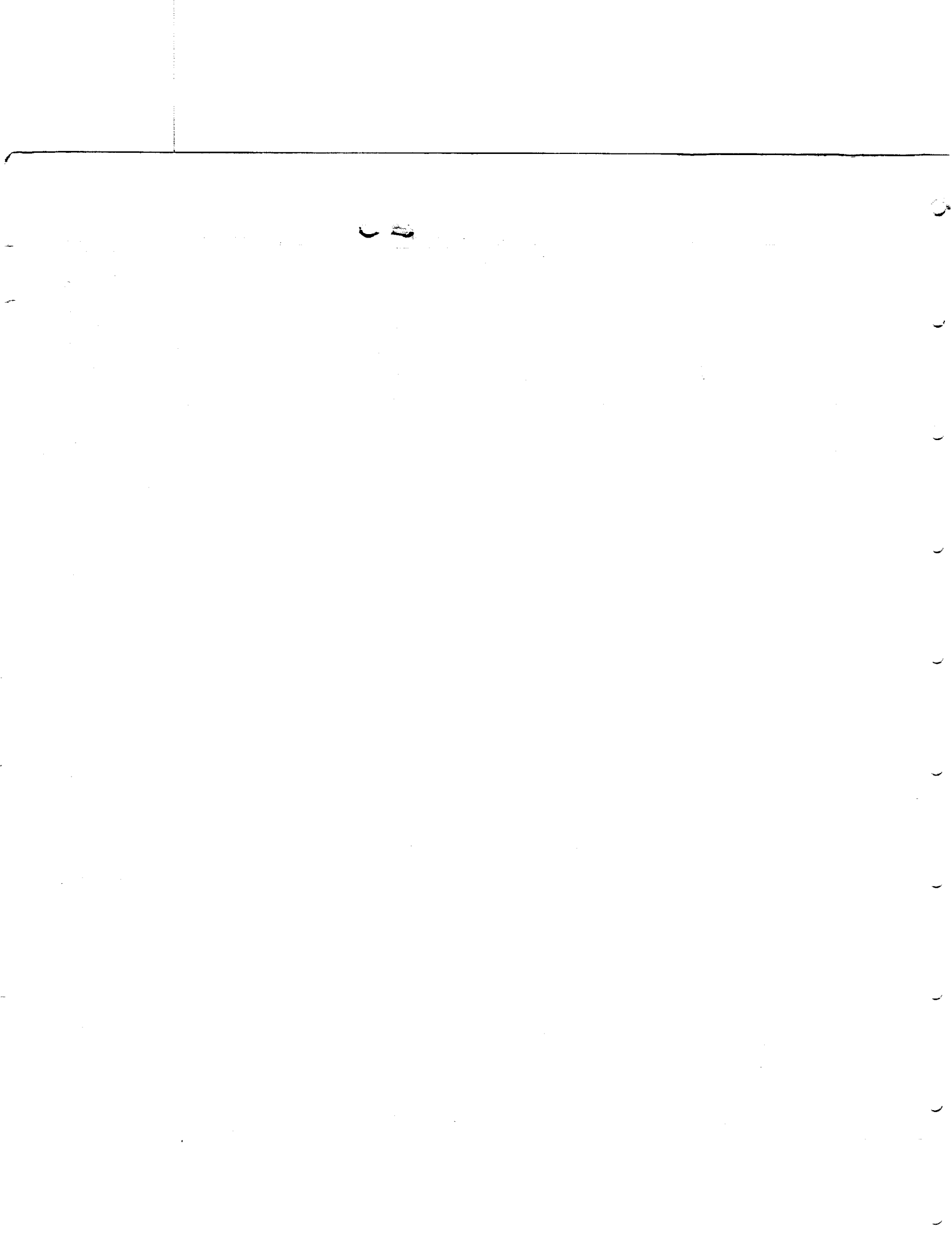
NASW-4435

Apollo

Lightcraft Project



NASA/USRA Advanced Design Program
5th Annual Summer Conference



Apollo

Lightcraft Project

Prepared For:

The NASA/USRA Advanced Design Program
5th Annual Summer Conference
Marshall Space Flight Center
Huntsville, Alabama
June 12-16, 1989

INSTRUCTOR

Professor Leik N. Myrabo
Dept. of Mechanical Engineering, Aeronautical Engineering, and Mechanics
Rensselaer Polytechnic Institute, 4004 JEC
Troy, NY 12180-3590
Phone: (518) 276-6545

Editor-in-Chief

Mark A. Antonison
(Teaching Assistant)

Editorial Staff and Major Contributors

Mark A. Antonison, Sammy G. Chen, Casimer DeCusatis,
Karl P. Kusche, Marco A. Minucci, Jeffrey P. Moder,
Ciro Morales, Caroline V. Nelson, Jacques C. Richard,
Shawn D. Sarbacker

Cover Art Credit

Ronald K. Levan, Instructional Media Services, R.P.I.

Design Class Participants

Transatmospheric Vehicle Design — Fall 1988

Burnett, John R.	Kusche, Karl P., Jr.	Sarbacker, Shawn D.
Hulscher, Mark E.	Nelson, Caroline V.	Sheets, Wayne H.
Hurst, Victor W.	Pavlovic, Erin K.	Sontrop, Ted F.
Knochen, Marybeth	Post, Peter R.	Spyropoulos, Harry M.

ACKNOWLEDGEMENT

The participants would like to acknowledge additional support from NASA-Lewis Research Center and the SDIO Laser Propulsion Program.

Model Construction

Mark A. Antonison

Contents

LIST OF FIGURES	v
LIST OF TABLES	vii
ABSTRACT	1
1 EXECUTIVE SUMMARY	3
1.1 Introduction	3
• 1.2 Initial LTD Design Concept	4
1.3 Ground Based Laser Launch Facility	5
1.4 The LTD Combined-Cycle Engine Concept	7
1.5 Focus of the LTD Design Project	8
1.5.1 Aerodynamics and Propulsion	8
1.5.2 Trajectory Analysis	9
1.5.3 Structural Design	9
1.5.4 Structural Dynamic Analysis	10
1.5.5 Propellant Management Systems Design	11
1.5.6 Optics for Propulsion	13
1.5.7 Optics for Sensor Satellite Mission	14
1.5.8 Lightsat Systems Design	14
1.6 Future Directions	15
2 VEHICLE CONFIGURATION AND STRUCTURAL DESIGN	19
2.1 Introduction	19
2.2 The Structural Design Process	19
2.3 LTD Vehicle Configuration	20
2.4 LTD Forebody	23
2.5 LTD Shroud/Impulse structure	28
2.6 LTD Afterbody	31
2.7 Primary Internal Support Structure	34
2.8 LTD Mass Requirements	36

3	PROPELLANT MANAGEMENT	41
3.1	Introduction	41
3.2	Propellant Management Criteria	41
3.3	System Description and Layout	42
3.4	Cryogenic Fluid Options	44
3.5	Cryogenic Storage and Handling Considerations	45
3.6	Propellant Tank Pressurization System Requirements	48
3.7	Pressure Vessel Design	48
3.8	Thermal Insulation Requirements	50
3.9	Conclusions	51
4	INJECTOR DESIGN: THE LASER HEATED ROCKET MODE	57
4.1	Introduction	57
4.2	Underlying Technologies	58
4.3	The Injector Array	59
4.4	Injector Element Design	59
4.5	Injector Orifice Design	60
4.6	Injector Manifold Design	62
4.7	Film Cooling for the Shroud Surface	63
4.8	Transpiration Cooling of Leading Edges	65
4.9	Pulsed Flow Control	65
4.10	Injector Design Alternatives for the LTD	67
4.11	Conclusions	72
5	FINITE ELEMENT MODELING AND ANALYSIS	75
5.1	Introduction	75
5.2	Finite Element Modeling/Analysis Package	75
5.3	Advantages/Disadvantages of the 3-D Model	77
5.4	Results	79
5.4.1	Volumes and Masses	79
5.4.2	Global Analysis	80
5.4.3	Local Modes	80
5.4.4	Overview of Results	82
5.5	Frequency Information and LTD Operation	84
5.6	Mode Shapes	86
5.7	Conclusions of Dynamic Analysis	86
5.8	Static Analysis	89
5.9	Static Analysis Model	89
5.10	Results of Static Analysis	89
5.11	Conclusions of Static Analysis	92

6	OPTICAL SYSTEM FOR SENSING MISSION	93
6.1	Introduction	93
6.2	Characteristics of the primary mirror	94
6.3	Sensors for the LTD retina	100
6.4	Conclusions	103
7	OPTICAL SYSTEM FOR LASER PROPULSION	105
7.1	Introduction	105
7.2	Design and manufacture of the LTD primary mirror	106
7.3	Power beam system analysis	110
7.4	Effects of pointing error	112
7.5	Conclusions	114
8	MODELING OF LASER-GENERATED IMPULSE	117
8.1	Introduction	117
8.2	Initial State of an LSD Wave	117
8.3	Application of the Method of Characteristics	122
8.4	Sedov's Solution of the Equations	125
8.5	Calculating the Impulse with Sedov's Scaling Laws	132
9	THE LTD ENGINE PERFORMANCE ANALYSIS	143
9.1	Analysis of LTD Inlet Flow Aerodynamics	143
9.1.1	Investigative Procedure	143
9.1.2	Alternate Subsonic Inlet Model	153
9.2	LTD Performance Projections	155
10	LASER-HEATED ROCKET MODE	165
10.1	Plug Nozzle Rocket Engines	166
10.2	Injector Head Design	170
11	EARTH-TO-ORBIT TRAJECTORY SIMULATION	177
11.1	Vehicle and Environmental Models	178
11.1.1	Aerodynamics	178
11.1.2	Engine	178
11.1.3	Steering	183
11.2	Simulation Parameters	186
11.3	Trajectory Sequence	186
11.4	Results	189
11.4.1	Case I	189
11.4.2	Cases II, III and IV	192
11.5	Summary	194

12 LIGHTSAT SYSTEMS DESIGN	197
12.1 Lightsat Background	197
12.2 Orbital Positioning	198
12.2.1 Attitude Determination	199
12.2.2 Orbital Position Determination	200
12.2.3 Attitude and Orbital Control	200
12.3 Communications and Sensing	203
12.3.1 Orbital Parameters	203
12.3.2 Communication Frequencies	205
12.3.3 Antenna Options	207
12.4 On Board Computer	207
12.5 Power Systems	209
12.5.1 Shadow Factor	210
12.5.2 Solar Array	210
12.5.3 Battery	211
12.6 Conclusion	212
13 FUTURE DIRECTIONS	215
13.1 Computer Modeling Efforts	215
13.2 Wind Tunnel Experiments	216
13.3 Laser Impulse Experiment	216
13.4 Systems-Integration Issues	217
A RESULTS OF COMPUTER GENERATED RAY TRACES	221
B SENSITIVITY ANALYSIS: LTD ENGINE PARAMETERS	225

List of Figures

1.1	Ground-based FEL laser launch facility.	5
1.2	Lightcraft Technology Demonstrator (1.4 meter diameter).	7
1.3	The LTD Shroud and support Strut.	10
1.4	Finite element models of Shroud and Strut.	11
1.5	Cutaway view of LTD showing storage tanks for LN ₂ and Helium.	12
1.6	Proposed LTD Injector design	13
1.7	LTD satellite functional hardware is located in the forward payload section of the vehicle.	15
1.8	LTD wind tunnel model Laser Impulse Experiment Test Section	16
1.9	LTD Laser Impulse Experiment Test Section (side view).	17
2.1	The Lightcraft Technology Demonstrator: top view, and side (cross sectional) view	21
2.2	The LTD engine/vehicle external geometry	22
2.3	Forebody flaps open and close to deploy inlet shutter and retina	23
2.4	Side (cross sectional) view of forebody	24
2.5	Super-Zip Linear Ordnance separating device	25
2.6	Side (cross-sectional) view of proposed forebody aeroshell.	26
2.7	Bow shock wave and forebody contour at inlet design Mach number	27
2.8	T-tail shroud support strut assembly (24)	28
2.9	Typical platelet flow metering and distribution schematic	30
2.10	Metal pipes integrated into a carbon-carbon structure provide active cooling (from Ref. 19).	31
2.11	Proposed technique for "outside-in" fabrication of regeneratively cooled primary optic (not to scale).	33
2.12	LTD internal support frame	35
3.1	Schematic of Propellant Management System	43
3.2	A Supercritical Cryogenic Gas Storage System (Ref. 4).	44
3.3	Helium pressurization system using heaters in storage vessel.	46
3.4	Pressure-enthalpy diagram of supercritical storage (Ref. 4).	46
3.5	Single wall composite fiber cryogenic storage tank.	49

3.6	Positive expulsion tank; successive positions during diaphragm reversal (Ref. 8).	50
3.7	Schematic of single wall cryogenic gas storage tank for heat transfer analysis.	51
3.8	Analytical model of pressurized propellant tank (Ref. 15).	53
3.9	Logic diagrams of pressurization and expulsion process (Ref. 15). . .	54
4.1	Side view of like-impinging doublet injector element.	59
4.2	Mass flux contour for doublet injector element (Ref. 1).	60
4.3	Bottom view of LTD showing location of injector array.	61
4.4	Element orientation options for LTD injector array (Ref. 1).	61
4.5	Unconventional orifice shapes improve mixing performance.	62
4.6	Two-way valves control propellant flow to each T-tail strut assembly.	63
4.7	Typical platelet flow metering and distribution schematic for a T-tail strut assembly.	64
4.8	Injector face and manifold design details (Ref. 1).	64
4.9	Proposed models for active cooling.	66
4.10	Side (cross sectional) view of Shroud/Injector assembly, Design No. 1.	68
4.11	Shroud/Injector assembly, Design No. 2.	70
4.12	Blast wave pressure versus radius from blast wave center.	71
4.13	Shroud/Injector assembly, Design No. 3.	71
4.14	Shroud/Injector assembly, Design No. 4.	72
5.1	Finite element model of the Shroud and its support structure.	76
5.2	T-tail Shroud/Strut assembly including carbon-carbon lower half ("entire" section).	77
5.3	T-tail Shroud/Strut assembly less carbon-carbon ring lower half ("cut-off" section).	78
5.4	Strut mounting detail.	78
5.5	Various mode shapes for the entire LTD shroud (deformations are exaggerated).	81
5.6	Normalized Displacement versus Frequency.	85
5.7	Various mode shapes for the T-tail Strut Assembly (deformations are exaggerated).	87
5.8	Static Stress Analysis of Strut Assembly.	90
5.9	Stress contours for a loaded shroud strut assembly.	91
6.1	Deployment mechanism for LTD retina.	94
6.2	The geometric comatic image formed by an off-axis object point (Ref.3).	97
6.3	Sample meridonal error plots (Ref. 4).	99

6.4	Meridional error plot for right side of the LTD primary mirror at 0.1° angle of incidence.	99
6.5	Alternative primary optic contours and focal lengths.	101
6.6	Effect of a cosmic ray on Reticon CCD.	103
7.1	Cross sectional view of LTD primary optic in the y-z plane.	107
7.2	Multi-layer dielectric coating for high reflectivity.	108
7.3	Proposed models for mirror face cooling channels.	109
7.4	Graphic map of laser uplink propagation parameters (Ref. 3).	111
8.1	The control volume used by Raizer in modeling an LSD wave.	118
8.2	Raizer's shock adiabat for a laser radiation absorption wave (Ref. 2).	119
8.3	Peak LSD wavefront velocity vs. flight Mach number and altitude.	120
8.4	CJ pressure vs. flight Mach number and altitude.	121
8.5	CJ temperature vs. flight Mach number and altitude.	121
8.6	Shock tube gas dynamics.	124
8.7	Peak surface pressure, before cylindrical blast wave decay.	125
8.8	A real chemical detonation (Ref. 7).	126
8.9	Dynamics of a propagating Laser Supported Detonation.	127
8.10	Surface Pressure vs. time using Sedov's equations ($\Phi_{LSD} = 500 \text{ MW/cm}^2$, $r_{LSD} = 0.5 \text{ cm}$, $M_\infty = 0.1$, 0 km , with P_{LSD} at t_{2D}).	131
8.11	Surface Pressure vs. radius using Sedov's equations ($\Phi_{LSD} = 500 \text{ MW/cm}^2$, $r_{LSD} = 0.5 \text{ cm}$ at t_{2D} , $M_\infty = 0.1$, 0 km , with P_{LSD} at t_{2D}).	132
8.12	Wavefront temperature vs. time using Sedov's equations ($\Phi_{LSD} = 500 \text{ MW/cm}^2$, $r_{LSD} = 0.5 \text{ cm}$ at t_{2D} , $M_\infty = 0.1$, 0 km , with T_{LSD} at t_{2D}).	133
8.13	Blast wave radius vs. time using Sedov's equations ($\Phi_{LSD} = 500 \text{ MW/cm}^2$, $r_{LSD} = 0.5 \text{ cm}$ at t_{2D} , $M_\infty = 0.1$, 0 km).	134
8.14	Top view of the line source showing the semi-cylindrical control volume.	134
8.15	End view of the control volume drawn around the thrust surface.	135
8.16	Cross sectional view of LTD ERH thruster surface	138
8.17	The delay time, t_{2D} , after which the blast wave assumes a semi-cylindrical shape ($\Phi_{LSD} = 500 \text{ MW/cm}^2$, $r_{LSD} = 0.5 \text{ cm}$)	139
8.18	Blast wave radius after complete expansion to ambient pressure ($\Phi_{LSD} = 500 \text{ MW/cm}^2$, $r_{LSD} = 0.5 \text{ cm}$)	140
8.19	The time required for blast wave expansion to ambient pressure ($\Phi_{LSD} = 500 \text{ MW/cm}^2$, $r_{LSD} = 0.5 \text{ cm}$)	141
8.20	Gross impulse produced by the laser-generated blast wave for one complete engine cycle (with units of $N - sec$), for various vehicle flight conditions ($\Phi_{LSD} = 500 \text{ MW/cm}^2$, $r_{LSD} = 0.5 \text{ cm}$)	142
9.1	LTD forebody flow parameters.	145

9.2	LTD inlet Mach number schedule for subsonic flight speeds.	145
9.3	LTD forebody/inlet Mach number schedule assumed for supersonic flight speeds. 30° and 51° cones (semi-vertex angle) model the forebody geometry.	146
9.4	Stagnation pressure recovery schedule for the LTD inlet	147
9.5	Inlet static pressure vs. Mach number and altitude.	147
9.6	Inlet static temperature vs. Mach number and altitude.	148
9.7	Refresh time vs. flight Mach number.	149
9.8	Ram drag coefficient for the LTD ERH thruster.	150
9.9	LTD inlet ram drag vs. Mach number and altitude.	150
9.10	LTD inlet mass flow rate vs. Mach number and altitude.	151
9.11	Ratio of inlet gap to maximum "capture" mass flow rate, vs. flight Mach number.	152
9.12	Blast wave pressure at the inlet outer lip (i.e., $r = 10.8$ cm), in bars, vs. flight Mach number and altitude, with $\Phi_{LSD} = 500$ MW/cm ² using Raizer and Sedov's equations.	152
9.13	Model of subsonic flow over a cone.	153
9.14	Alternate forebody/inlet Mach number schedule; 30° and 51° cones model the forebody.	155
9.15	Net coupling coefficient vs. Mach number and altitude, for the baseline case (inlet gap = 3 cm, $\Phi_{LSD} = 500$ MW/cm ² , $r_{LSD} = 0.5$ cm, and $M_{refresh} = 1.0$ when $M_{\infty} \geq 0.6$).	156
9.16	Laser pulse time vs. Mach number and altitude, for the baseline case.	157
9.17	Time-averaged power vs. Mach number and altitude, for the baseline case.	157
9.18	Net time-averaged thrust vs. Mach number and altitude, for the baseline case.	158
9.19	Pulse Repetition Frequency vs. Mach number and altitude, for the baseline case.	158
9.20	Pulse energy vs. Mach number and altitude, for the baseline case.	159
9.21	Gross time-averaged thrust vs. Mach number and altitude, for the baseline case.	160
9.22	Gross coupling coefficient vs. Mach number and altitude, for the baseline case.	160
9.23	$t_{refresh}/t_{expansion}$ vs. Mach number and altitude, for the baseline case.	161
10.1	Cutaway View of LTD Aerospace Vehicle	166
10.2	Primary Optic contours vs. Focal Locations.	167
10.3	16 Klb H ₂ O ₂ Plug Nozzle Development Thrust Chamber in Test Cell (After Graham and Bergman, Ref. 1)	168

LIST OF FIGURES

10.4	Detail of 16 Klb H_2O_2 Plug Nozzle Configuration (from Ref. 1)	169
10.5	Isentropic Plug Nozzle, External Expansion (from Ref. 1)	170
10.6	Outline of 50% Internal Expansion Plug Nozzle (from Ref. 1)	171
10.7	Cooled Engine Prior to Wire Wrapping and Thrust Mount Installation (from Ref. 1)	172
10.8	50 Klb Plug Nozzle Configuration (Dimensions in Inches)(from Ref. 1)	172
10.9	Cooled Segment (from Ref. 1)	173
10.10	Cone Segment Assembly (from Ref. 1)	173
10.11	Quarter Sector of 33.33% <i>C</i> Primary Optic (from Ref. 1)	174
10.12	Injector Model III (from Ref. 1)	175
11.1	Ground-Based Laser Launch	179
11.2	Theoretical and experimental drag coefficients of various <i>conical heads</i> at transonic and supersonic Mach numbers (from Ref. 2).	180
11.3	Classification of "engine" and "airframe" components, for the purpose of determining vehicle drag profile.	181
11.4	Drag coefficients of wedges, <i>cones</i> and similar shapes as a function of their half-vertex angle (from Ref. 2).	182
11.5	"Case I" Launch Trajectory (No Relay Satellite)	184
11.6	Boost Reference Angle vs. Time for Case I	185
11.7	Chemical "Kick" Rocket Option (for orbit circularization)	185
11.8	Use of Laser Relay Satellite for Orbit Circularization (Cases II, II and IV)	187
11.9	LTD Pitch Angle vs. Time (for Cases II, III, IV)	188
11.10	Thrust vs. Time (Case I)	190
11.11	Altitude vs. Time (Case I)	190
11.12	Altitude vs. Downrange Distance (Case I)	190
11.13	Flight Mach Number vs. Time (Case I)	191
11.14	Acceleration vs. Time (Case I)	191
11.15	Velocity vs. Altitude (Case I)	191
11.16	Power vs. Time (Case I)	191
11.17	Coupling Coefficients vs. Time (Case I)	192
11.18	Thrust vs. Time (Cases II, III, &IV)	192
11.19	Altitude vs. Time (Cases II, III, &IV)	192
11.20	Altitude vs. Downrange Distance (Cases II, III, &IV)	193
11.21	Flight Mach Number vs. Time (Cases II, III, &IV)	193
11.22	Acceleration vs. Time (Cases II, III, &IV)	193
11.23	Velocity vs. Altitude (Cases II, III, &IV)	193
11.24	Power vs. Time (Cases II, III, &IV)	194
11.25	Coupling Coefficients vs. Time (Cases II, III, &IV)	194

12.1 Tracking and Data Relay Satellite System	201
12.2 Locations and Geodetic Coordinates of STDN Stations.	202
12.3 TDRSS Geometric Zone of Exclusion	203
12.4 Satellite-Earth Angles	204
12.5 Antenna Gain Pattern (see Ref. 8)	207
12.6 LTD will deploy an antenna for communications during satellite mode.	209
12.7 Solar cell array exposed during LTD satellite mode.	210
A.1 RMS blur vs. angle of incidence.	222
A.2 Geometry for ray trace analysis, indicating the focus of parallel incident light rays.	222
A.3 Ray traces for oblique angles of incidence.	224
B.1 Net coupling coefficient vs. Mach number and altitude using $M_{refresh} = 0.75$ for $M_\infty \geq 0.6$ (the only change from baseline case).	226
B.2 Net coupling coefficient vs. Mach number and altitude, using $M_{refresh} = 0.5$ for $M_\infty \geq 0.6$ (the only change from baseline case).	227
B.3 Net coupling coefficient vs. Mach number and altitude, using $M_{refresh} = 0.25$ for $M_\infty \geq 0.6$ (the only change from baseline case).	227
B.4 Net coupling coefficient vs. Mach number and altitude, with the inlet gap reduced by 1 cm (the only change from baseline case).	228
B.5 Net coupling coefficient vs. Mach number and altitude, with the inlet gap increased by 1 cm (the only change from baseline case).	228
B.6 Net coupling coefficient vs. Mach number and altitude, with r_{LSD} changed to 0.1 cm at t_p (the only change from the baseline case).	229
B.7 Net coupling coefficient vs. Mach number and altitude, with r_{LSD} changed to 0.25 cm at t_p (the only change from the baseline case).	229
B.8 Net coupling coefficient vs. Mach number and altitude, with r_{LSD} changed to 0.75 cm at t_p (the only change from the baseline case).	230
B.9 Net coupling coefficient vs. Mach number and altitude, with r_{LSD} changed to 1 cm at t_p (the only change from the baseline case).	230
B.10 Net coupling coefficient vs. Mach number and altitude, with $r_{LSD} = 0.1$ cm and $\Phi_{LSD} = 3 \times 10^9$ W/cm ² at t_p	231
B.11 Net coupling coefficient vs. Mach number and altitude, with $r_{LSD} = 0.25$ cm and $\Phi_{LSD} = 3 \times 10^9$ W/cm ² at t_p	231
B.12 Net coupling coefficient vs. Mach number and altitude, with $r_{LSD} = 0.5$ cm and $\Phi_{LSD} = 3 \times 10^9$ W/cm ² at t_p	232
B.13 Net coupling coefficient vs. Mach number and altitude, with $r_{LSD} = 1$ cm and $\Phi_{LSD} = 3 \times 10^9$ W/cm ² at t_p	232
B.14 Net time-averaged thrust vs. Mach number and altitude, with $r_{LSD} = 0.25$ cm and $\Phi = 3 \times 10^9$ W/cm ² at t_p	233

B.15 Pulse Repetition Frequency vs. Mach number and altitude, with $r_{LSD} = 0.25$ cm and $\Phi_{LSD} = 3 \times 10^9$ W/cm ² at t_p .	233
B.16 Pulse energy vs. Mach number and altitude, with $r_{LSD} = 0.25$ cm and $\Phi_{LSD} = 3 \times 10^9$ W/cm ² at t_p .	234
B.17 Laser pulse time vs. Mach number and altitude, with $r_{LSD} = 0.25$ cm and $\Phi_{LSD} = 3 \times 10^9$ W/cm ² at t_p .	234
B.18 Time-averaged power vs. Mach number and altitude, with $r_{LSD} = 0.25$ cm and $\Phi_{LSD} = 3 \times 10^9$ W/cm ² at t_p .	235
B.19 Net coupling coefficient vs. Mach number and altitude, with $r_{LSD} = 0.1$ cm and $\Phi_{LSD} = 10^{10}$ W/cm ² at t_p .	235
B.20 Net coupling coefficient vs. Mach number and altitude, with $r_{LSD} = 0.2$ cm and $\Phi_{LSD} = 10^{10}$ W/cm ² at t_p .	236
B.21 Net coupling coefficient vs. Mach number and altitude, with $r_{LSD} = 0.5$ cm and $\Phi_{LSD} = 10^{10}$ W/cm ² at t_p .	236
B.22 Net coupling coefficient vs. Mach number and altitude, with $r_{LSD} = 1$ cm and $\Phi_{LSD} = 10^{10}$ W/cm ² at t_p .	237
B.23 Laser pulse time vs. Mach number and altitude, with $r_{LSD} = 0.2$ cm and $\Phi_{LSD} = 10^{10}$ W/cm ² at t_p .	237
B.24 Time-averaged power vs. Mach number and altitude, with $r_{LSD} = 0.2$ cm and $\Phi_{LSD} = 10^{10}$ W/cm ² at t_p .	238
B.25 Net time-averaged thrust vs. Mach number and altitude, with $r_{LSD} = 0.2$ cm and $\Phi_{LSD} = 10^{10}$ W/cm ² at t_p .	238
B.26 Pulse Repetition Frequency vs. Mach number and altitude, with $r_{LSD} = 0.2$ cm and $\Phi_{LSD} = 10^{10}$ W/cm ² at t_p .	239
B.27 Pulse energy vs. Mach number and altitude, with $r_{LSD} = 0.2$ cm and $\Phi_{LSD} = 10^{10}$ W/cm ² at t_p .	239

List of Tables

2.1	LTD Vehicle Mass Breakdown.	37
3.1	Physical properties of Nitrogen and Helium	45
3.2	Physical Properties of External Foam Insulation	52
5.1	Volumes and Masses for Shroud Structure.	80
5.2	Modal Data for the Shroud Global Analysis.	82
5.3	Modal Data for LTD Single Strut Section	83
5.4	Mode Shapes and Description	88
6.1	Resolution limits for LTD mirror at various wavelengths (all angles in radians, all distances in meters).	96
6.2	Spot size due to aberrations in coma at oblique incidence (wavelength = 1 micron; diffraction limit = 4.88×10^{-6} radians).	98
6.3	Aberration spot size for various primary optic contours at incident angle = 0.5° (diffraction limit at 1 micron length = 4.88×10^{-6} radians).	101
8.1	Sedov's Scaling Laws	130
12.1	Electromagnetic Frequency Spectrum	206
12.2	Satellite Frequency Spectrum	206
12.3	Typical Antenna Gain Patterns (see Ref. 8)	208
12.4	Power Requirements for Solar Array	211
A.1	Perpendicular distance from ray intercepts to focal point at oblique incidence, and RMS blur (all values in cm)	223
A.2	Perpendicular distances and RMS blur for intermediate angles.	223

•

Abstract

The ultimate goal for this NASA/USRA-sponsored "Apollo Lightcraft Project" is to develop a revolutionary manned launch vehicle technology which can potentially reduce payload transport costs by a factor of 1000 below the Space Shuttle Orbiter. The Rensselaer design team proposes to utilize advanced, highly energetic, beamed-energy sources (laser, microwave) and innovative combined-cycle (airbreathing/rocket) engines to accomplish this goal.

The research effort focuses on the concept of a 100 MW-class, laser-boosted Lightcraft Technology Demonstrator (LTD) drone. The preliminary conceptual design of this 1.4 meter diameter microspacecraft involved an analytical performance analysis of the transatmospheric engine in its two modes of operation (including an assessment of propellant and tankage requirements), and a detailed design of internal structure and external aeroshell configuration. The central theme of this advanced propulsion research was to pick a known excellent working fluid (i.e., air or LN_2), and then to design a combined-cycle engine concept around it. Also, a structural vibration analysis was performed on the annular shroud pulsejet engine. Finally, the sensor satellite mission was examined to identify the requisite subsystem hardware: e.g., electrical power supply, optics and sensors, communications and attitude control systems.

This is the third year of RPI's participation in the NASA/USRA University Advanced Design Program for Aeronautics.

Chapter 1

EXECUTIVE SUMMARY

For this year's effort, the detailed description and performance analysis of an unmanned 1.4 m Lightcraft Technology Demonstrator (LTD) drone is presented. The novel launch system employs a 100 MW-class ground-based laser to transmit power directly to an advanced combined-cycle engine that propels the 120 kg LTD to orbit — with a mass ratio of two. The single-stage-to-orbit (SSTO) LTD machine then becomes an autonomous sensor satellite that can deliver precise, high quality information typical of today's large orbital platforms.

The dominant motivation behind this study is to provide an example of how laser propulsion and its low launch costs can induce a comparable order-of-magnitude reduction in sensor satellite packaging costs. The issue is simply one of production technology for future, survivable SSTO aerospace vehicles that intimately share both laser propulsion engine and satellite functional hardware. A mass production cost goal of $\$10^3/\text{kg}$ for the LTD vehicle is probably realizable.

1.1 Introduction

In order for laser propulsion to enable a significant reduction in the cost of certain critical space systems, both launch and payload costs must be reduced by an order of magnitude or two. Canavan [1] was first to bring this fact to light, noting that a reduction in either category alone would have much less economic impact. This conclusion emerged from recent in-depth examinations of the economics for laser propulsion deployment of sensors, interceptors, and decoys [1,2]. Furthermore, Canavan affirms that the minimum effective system must be able to launch 60-100 kg payloads. After evaluating cost projections, he concludes that a system designed for payloads smaller than this could increase costs significantly, reducing laser propulsion's margin with respect to conventional chemical rocket alternatives [1].

Apparently, the true costs of building and launching today's large satellite platforms are not widely known, as discussed in a recent *Aerospace America* article [3]. For

example, sensor hardware can cost upwards of \$200,000/kg (10^5 /lb); and to boost that sensor into geostationary orbit (GEO) typically requires \$10,000/kg (\$4,500/lb) of payload. Flying the Shuttle Orbiter to a 250 km low Earth orbit (LEO) may cost \$6,600/kg (\$3000/lb), but the actual price is really almost twice that amount because the shuttle itself is *not* amortized against the payload [4]. The projected launch cost goal for the Advanced Launch System (ALS) is roughly \$660/kg (\$300/lb) to LEO. Hence, for laser propulsion to play a significant role in boosting future critical space systems, launch costs must fall to \$66/kg (\$30/lb), or at least below \$100/kg.

Canavan has raised the fascinating issue of whether and how laser propulsion and its low launch costs could induce a substantial reduction in satellite package costs [1]. In the opinion of the authors, such reductions could be facilitated by an exceptionally close integration of the laser-propulsive engine and satellite functional hardware. Pushed to the extreme, almost every vehicle component could be designed to serve multiple functions, in both transatmospheric and orbital flight modes.

Clearly, the final configuration of any laser-boosted machine will be strongly driven, if not entirely dominated by the mission it must perform, be it interceptor, decoy or sensor. A near infinite number of successful configurations could be alleged to exist, but it is most instructive to select a *specific mission*, and then to explore a single configuration from the initial design concept, through the preliminary engineering design process.

1.2 Initial LTD Design Concept

The advanced aerospace vehicle considered here is exemplary of a class of sensor machines that can be derived largely from an intimate integration of propulsion and sensor systems. The proposed design exploits the inherent advantages of advanced beamed-energy sources (i.e., high power lasers) and innovative combined-cycle (air-breathing/rocket) engines to accomplish this goal. The authors believe that this unique approach could possibly enable a reduction in both launch and sensor package costs by two orders of magnitude below present levels. However, as pointed out by Canavan [1], the numbers of these sensor satellites may not be great enough to justify the expense of the entire laser launch facility for this application alone. Nevertheless, the laser launch facility is likely to be built for a completely different defense-related purpose, and amortized over a great number of users and dissimilar mission applications anyway.

1.3. GROUND BASED LASER LAUNCH FACILITY

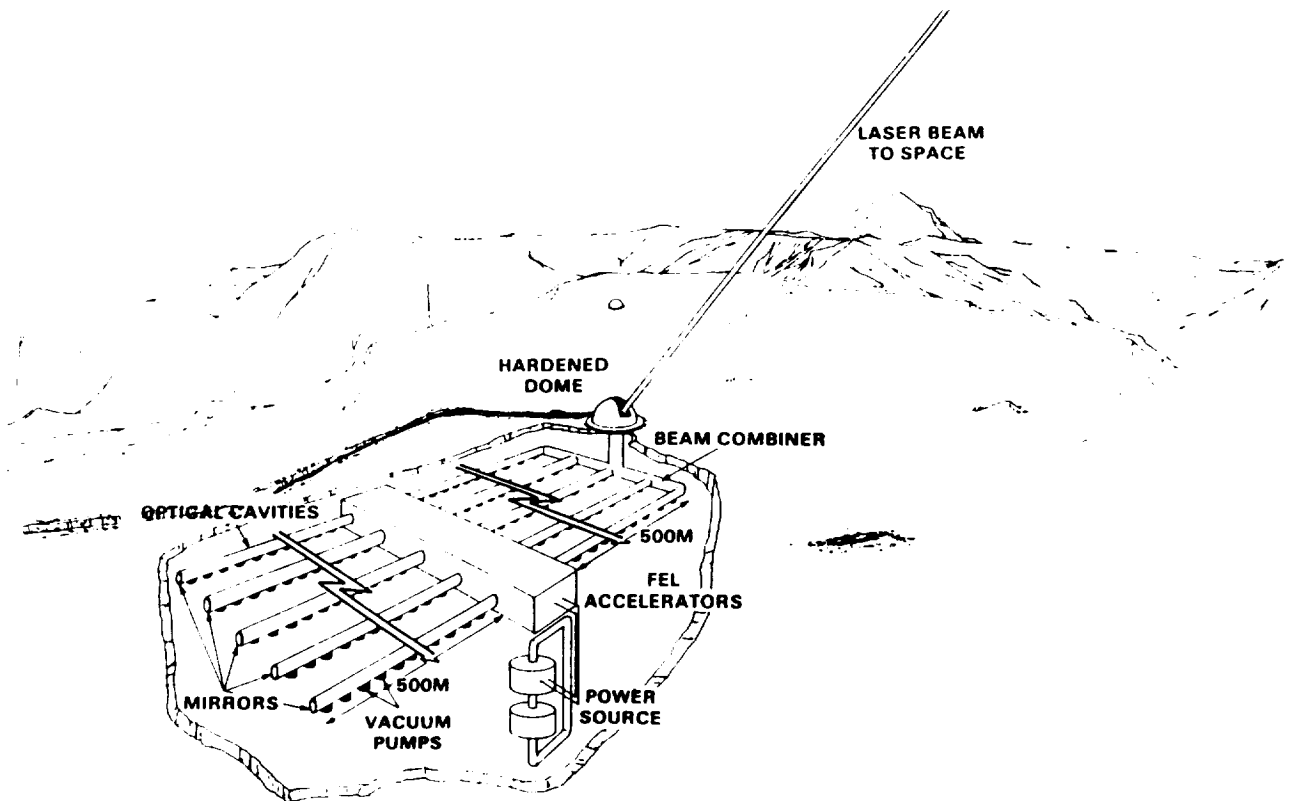


Figure 1.1: Ground-based FEL laser launch facility.

1.3 Ground Based Laser Launch Facility

Portrayed in Figure 1.1 is a 100 MW-class ground-based laser (GBL) that could be built with free-electron laser technology in the next 5 years, by assembling numerous (e.g., 5) smaller units into an array. Redundant units could be built into the system so that inoperative modules could be dropped out, with no loss in system utility during a boost. As shown in Figure 1.1, a beam combiner could then be invoked to link all the output beams together.

All the units could be fired *simultaneously* to give the lowest pulse repetition frequency (PRF) of perhaps several hundred Hertz at the highest pulse energy (E_p); at the other extreme, each unit could be triggered *sequentially* to yield the lowest E_p 's and PRF's up to 10 kHz. Near-term pulsed laser propulsion engines can be designed

around whatever laser pulse durations are available (e.g., from 40 to 400 nsec.).

Configured in this manner, the GBL facility can be programmed to deliver a complicated pulse train sequence of PRF's, E_p 's and t_p 's with the utmost of ease. This pulse train can be calculated to exactly match what a laser propulsion engine will need along a given launch trajectory — i.e., normally a direct function of flight Mach number and altitude. The goal is to produce an efficient thruster without introducing too much flight hardware, which has added so much to the cost of chemical rockets, as Kantrowitz [4] has observed.

The essential point of this advanced launch scheme is to place as much of the laser power transmission system complexity as possible *on the ground* (where there is no weight penalty) so that it can be serviced easily. With this approach, laser powered thrusters can be reduced to their simplest, and most reliable configuration.

The "straw man" GBL facility suggested here is set at the 250 MW level (peak) which is adequate to launch a 120 kg (dry mass), 1.4 meter diameter Lightcraft Technology Demonstrator (LTD) to low Earth orbit. The range of laser pulse energies required by its combined-cycle (airbreathing/rocket) engine is $40 \text{ KJ} < E_p < 70 \text{ KJ}$; PRF varies from 200 Hz to 10 kHz, and t_p varies from 0.3 to 0.4 μsec — depending on the exact trajectory (i.e., Mach number vs. altitude) flown to orbit. With these parameters, the peak flux across the 1.0 m diameter LTD primary optic will fall in the range of 13.0 to 30.0 MW/cm².

Kantrowitz [5] notes that the important costs for a GBL installation, are for capital and operating expenses (which might add another 20% of the capital cost per year). Refer to Ref. 5 for an in-depth accounting of the economics for a GBL launch facility. The Free Electron Laser (FEL) is the favored future GBL system due to its promise of high electric-to-laser conversion efficiency and reliability.

Kantrowitz [5] has noted that to make laser propulsion a serious contender for space transportation to low Earth orbit (LEO), it is necessary to develop propellants that can achieve high thruster efficiency at low incident laser flux levels. It is also apparent that atmospheric transmission problems must be considered, especially in the immediate vicinity of the vehicle where the beam must propagate unhampered through the thruster's rapidly expanding, and potentially absorbing exhaust.

Adaptive transmitter optics can be invoked to successfully bring the power beam up through the atmosphere. The 10 m diameter beam-director mirror would allow a 10 μm beam to be focused on a one meter diameter vehicle base, out to a range of about 800 km. This performance is, of course, close to the diffraction limit. With even shorter wavelengths (e.g., 1 μm), the transmitter diameter could be reduced to 4 m (and below).

1.4. THE LTD COMBINED-CYCLE ENGINE CONCEPT

7



Figure 1.2: Lightcraft Technology Demonstrator (1.4 meter diameter).

1.4 The LTD Combined-Cycle Engine Concept

The Lightcraft Technology Demonstrator (LTD) is a single-stage-to-orbit transatmospheric vehicle utilizing both airbreathing and rocket propulsion modes. The LTD will transition into the rocket mode at about Mach 5 and 30 km altitude.

The LTD advanced microspacecraft is in several respects literally a "flying engine." The forebody aeroshell acts as an external compression surface: e.g., the airbreathing engine inlet. The afterbody has a dual function: it is the primary receptive optic (parabolic mirror) for the laser beam which provides power to the engine, and it is also an external expansion surface (plug nozzle) during the rocket engine mode. It is the opinion of the authors that focusing mirrors mounted on the laser-propelled vehicle are the most expedient way to permit both low flux levels in the atmospheric transmission link and elevated flux levels within the thruster (which are required for high propulsive efficiency). The reference "point design" for the LTD is configured around a 1.0 meter diameter parabolic receiving mirror, as shown in Figure 1.2.

The primary thrust structure is the annular shroud. The shroud serves as both inlet and impulsive thrust surface during the airbreathing engine mode; at this time, the LTD centerbody is treated as the "vehicle airframe" component. In the rocket mode, the annular inlet is closed; the afterbody and shroud combine to form the rocket thrust chamber. The three primary structures: forebody, shroud, and afterbody, are

interconnected by an internal support frame to which all internal subsystems are attached.

1.5 Focus of the LTD Design Project

This year's efforts have been to develop a conceptual design for a small, 1.4 meter diameter Lightcraft Technology Demonstrator around components derived from current liquid propellant chemical rocket engines, advanced composite structures, and high power laser mirrors. Specific areas that were addressed by the design team included aerodynamics, propulsion, structures, propellant management, heat transfer, optics for sensor and propulsion missions, lightsat/microsat subsystems, mechanical subsystems, detailed LTD mockup construction, and finally, the definition of future experimental test facilities (for next year's effort).

1.5.1 Aerodynamics and Propulsion

In the area of aerodynamics and propulsion, an analytical computer model of the airbreathing pulsejet cycle was first developed, providing a data base of engine performance characteristics. A vehicle aerodynamic drag model was then assembled. Next, an optimal trajectory analysis was then performed using a computer code called SORT (Simulation and Optimization of Rocket Trajectories), which had previously been modified for lightcraft engines and aerodynamics.

The focus of the propulsion analysis was to model the laser-heated blast wave and impulse-generation process using an axi-symmetric representation, that excludes radiation and convection. For the most part, air within the laser-generated blast wave was modeled as an ideal gas, throughout the expansion process. The engine inlet air state (i.e., pressure, temperature, density, etc.) prior to laser-heating, was a direct function of flight Mach number and altitude; hence, graphical results are presented versus these flight variables. The equations developed by Raizer [6,7] to describe the initial state of the laser-induced blast waves, were used in modeling the "line-source," impulse-generation process.

The simple LTD inlet flow model predicted the state of the inlet air (pressure, temperature, velocity, etc.) which refreshes the lower annular shroud impulse surface. This aerodynamic model was needed not only for the refresh air state, but also for defining external drag characteristics of the entire vehicle. In the latter, it is important to distinguish between the drag produced by engine-related vs. airframe-related components, so as not to over penalize Lightcraft performance.

1.5.2 Trajectory Analysis

The trajectory analysis of any launch vehicle becomes a critical step in the overall system integration process. Many important engine/vehicle related characteristics must come together for the final product: *performance*. Launch vehicle performance is typically measured by payload capability, which for the LTD is the entire dry mass and ullage gas, totaling 124 kilograms. The LTD must attain low Earth orbit with the available propellant, while minimizing total laser energy consumed along the launch trajectory.

The trajectory was evaluated using a computer tool called SORT which was written by McDonnell Douglas Astronautics Co. for NASA, to design space shuttle trajectories [8]. The code is sufficiently general such that it can analyze any trajectory and model all important environmental parameters that affect vehicle dynamics. Engine performance, vehicle aerodynamics, guidance algorithms, and mass histories interact with atmosphere and gravity models.

The capability of the SORT program is quite extensive in its use of these sophisticated vehicle and environmental models. The program can iterate on trajectory parameters to optimize performance, achieve a desired criteria, or constrain the solution to avoid some specified limit.

Even with all of the generality built into SORT certain modifications were required for the LTD. The most significant software modification involved the unique energy source, a laser. A new vehicle steering option was also encoded so that the LTD could always point at the ground-based laser station (or laser relay satellite). After these modifications were included, SORT was able to model Lightcraft performance to a high degree of accuracy.

1.5.3 Structural Design

Once the overall LTD vehicle structural configuration was defined, more detailed analysis of primary and secondary structure subcomponents was carried out. Consideration was given to using state-of-the-art materials technology and mass production techniques for low unit cost (e.g., \$10⁵/vehicle). A close integration of laser-propulsive engine and satellite functional hardware was necessary. Much emphasis was placed on the annular shroud structure — the primary impulsive thrust surface (see Fig. 1.3). A finite element computer code called CAEDSTM (Computer Aided Engineering Design System) was used to conduct both static and dynamic structural analyses; stress and modal behavior of the LTD shroud structure were extracted. This work will continue in the future as the LTD structural model becomes more elaborate.

Driving issues in the LTD structural design process were the component mass allowances, and propulsion system requirements; aerothermal loads were also considered in a generic sense, to identify the current operating limits. Specific transatmospheric



Figure 1.3: The LTD Shroud and support Strut.

flight paths must be analyzed in future studies to assess their suitability for alternative engine and structures technology.

The LTD structure must meet the combined challenge of providing a lightweight, efficient airframe that can survive severe engine and aerodynamic heating: i.e., a “thermo-structural” viewpoint. Clearly, any successful thermo-structural concept must meet existing materials and manufacturing limitations.

The LTD primary structure is a large fraction of the vehicle’s inert weight; yet, this comprises a small structural weight fraction. Applied loads must be predicted to an accuracy that will allow knowledgeable reductions in margins of safety, to eliminate every ounce of non-optimum structure. A large experimental data base of aerothermal loads must now be assembled, for future detailed finite element structural and heat transfer analyses.

1.5.4 Structural Dynamic Analysis

Finite element modeling techniques were used to evaluate the annular shroud and support strut design proposed for the LTD (see Fig. 1.4). Both static and dynamic structural analyses were implemented to extract the stress and modal behavior. Pulsed airbreathing or rocket engines must avoid the natural frequencies of the vehicle structure, or catastrophic failure of the system will result. The present analysis concluded

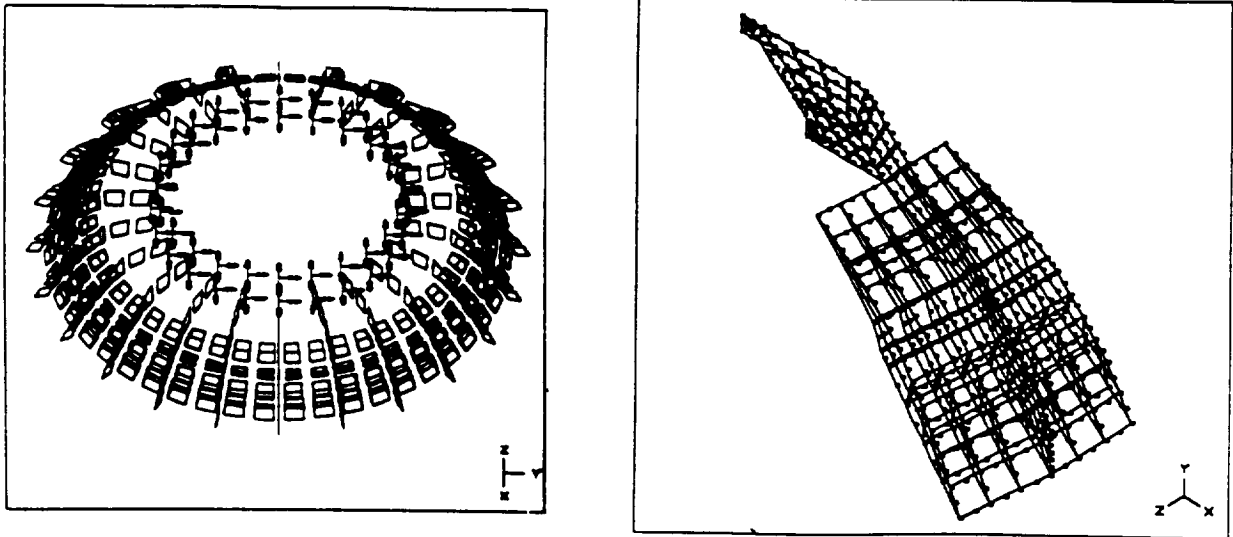


Figure 1.4: Finite element models of Shroud and Strut.

that the LTD shroud and support structure is able to withstand stresses of induced oscillations at the current engine design PRF's of 1 to 10 kHz. Even though resonant frequencies may be produced in flight, extremely small amplitudes (of displacement) will not cause damaging stress levels. The LTD structure seems to resonate at frequencies in the 10 to 100 Hz range.

The static stress analysis examined the integrity of the shroud/strut section, and revealed areas that needed further refinement. The shroud itself was found to be excessively strong and can easily sustain the applied loads; thus some material can be removed from the shroud interior to permit further weight reduction. Also, the proposed strut mounting design provides sufficient strength for attaching the struts securely to the internal LTD support frame.

1.5.5 Propellant Management Systems Design

The LTD combined-cycle, laser-propulsion system employs onboard cryogenic fluids for reaction propellant, sacrificial coolant and feed system pressurant. Liquid nitrogen has been chosen as the propellant for several reasons. Although liquid hydrogen would be the most desirable propellant because of its low molecular weight (and higher rocket specific impulse), only 14 kg would fit into the LTD's 28 in. diameter storage tank; in contrast, 140 kg of LN_2 would occupy the same volume (see Fig. 1.5). Heated to

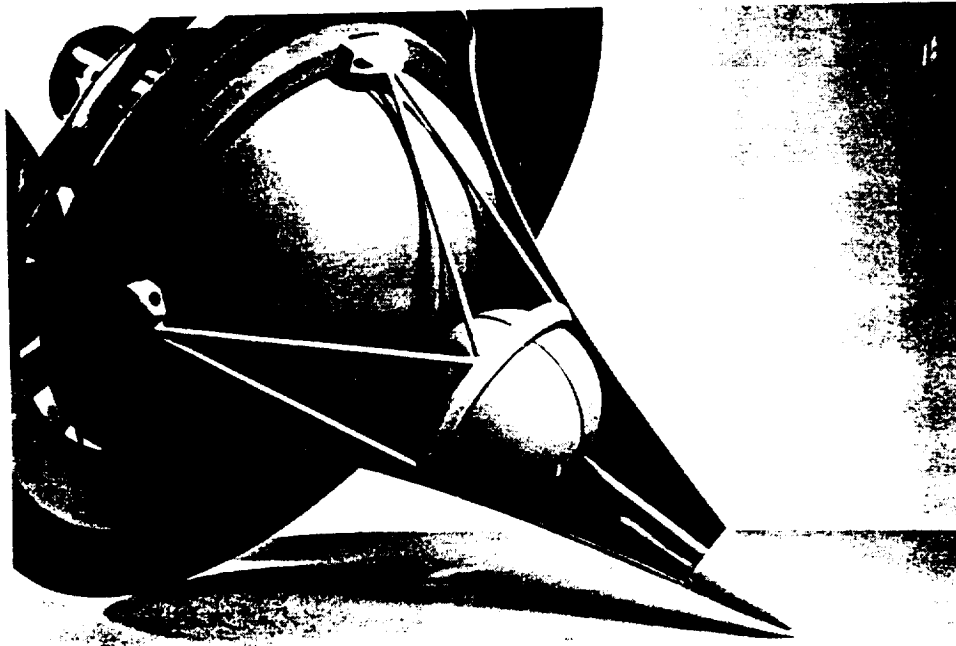


Figure 1.5: Cutaway view of LTD showing storage tanks for LN₂ and Helium.

high temperature and pressure, nitrogen can produce specific impulses in the range of 725 to 1025 seconds — depending on whether the exhaust gases are dissociated or not. (LN₂ is also favored because it is an inert and exceptionally clean coolant, a consideration which is especially important for high power laser optics.)

Several candidate injector designs have been identified for the rocket engine mode (see Fig. 1.6). The injector orifices are designed to act as “acoustic-valves,” to automatically deliver propellant into the rocket engine thrust chamber. Precise control of injector orifice pressure is necessary for optimum propellant utilization during flight.

High pressure, super-critical helium was chosen for the pressurant because of its superiority as an inert agent with a very low boiling point. The LTD pressurant system is modeled after one flown on the Apollo Lunar Module descent rockets. Storing the helium at near liquid temperatures enables maximum pressurant density.

The computer-controlled propellant management system must: 1) deliver the proper mass flow rate of liquid nitrogen coolant to critical actively-cooled engine components during the airbreathing propulsive mode; and 2) provide uniform propellant mass flow during the rocket mode. Sensors distributed over the vehicle’s outer skin and engine will monitor surface temperatures. The mass flow rate of LN₂ coolant will be adjusted to compensate for variations in laser power absorbed by the primary mirror during the airbreathing mode. Laser power input is constant during the rocket mode.

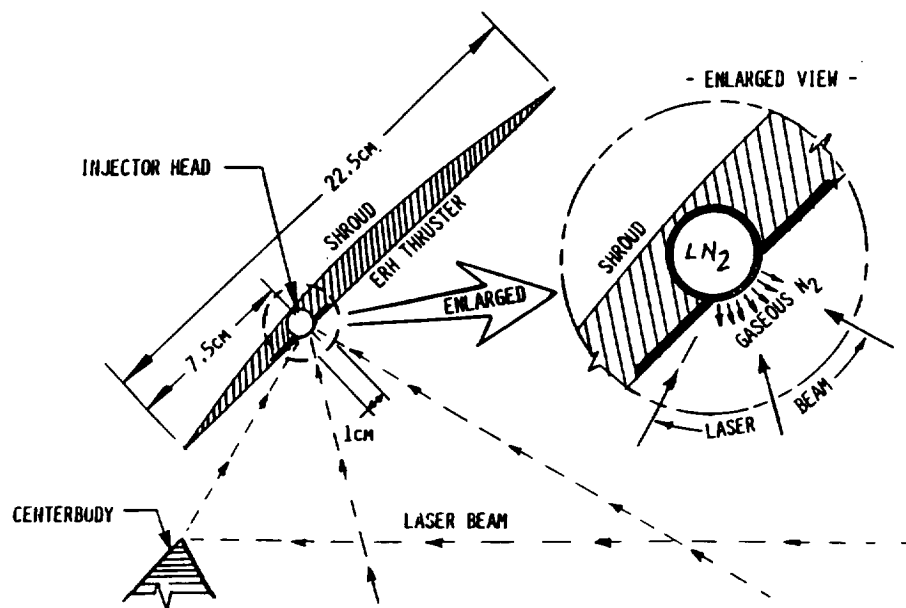


Figure 1.6: Proposed LTD Injector design

The heat transfer analysis has focused upon active cooling of the LTD's engine hot structures: i.e., mirror, shroud and shroud support struts. Regenerative cooling will be employed by the primary mirror/plug nozzle and hot thruster impulse surfaces. The leading edges of the shroud support struts and the shroud will utilize transpiration cooling, and platelet technology. The shroud thruster surface and propellant injector array will be film cooled. A thermal protection system (TPS) such as used on the Space Shuttle Orbiter will cover the vehicle forebody.

1.5.6 Optics for Propulsion

The design and fabrication of the LTD primary receptive mirror has been investigated. Although some of the physics behind propagating the high energy laser beam through the heated exhaust plume is not fully understood, the concept is shown to be within reach of current technology. The primary optic could be manufactured using existing diamond-turning lathe facilities. Development of multi-layer high reflectivity coatings and microchannel cooling systems are the main technical problems encountered. The mirror must exhibit high figure quality and minimal surface roughness throughout the launch trajectory. Calculations of beam divergence indicate that a 4 m diameter adaptive ground-based transmitter is entirely sufficient for a 1.0 micron wavelength. The effects of pointing error were evaluated using a computer ray trace routine; errors

of 0.5 degrees or less shift the focus asymmetrically on either side of the annular engine, but the effect is self-correcting and the LTD is therefore stable in this respect. At incident angles up to 1 degree, the power loss and spot size increase but do not cause a critical loss of thrust for near, intermediate, or far field beam profiles. An adaptive pointing error correction system is proposed, using retroreflectors to sample the power beam edges (at 24 azimuthal locations) and feed data back to the ground power source via laser ranging.

1.5.7 Optics for Sensor Satellite Mission

The use of the LTD as a sensor satellite has been explored. The primary mirror could serve a dual purpose on each mission; however, since the mirror is designed primarily for propulsion applications, its performance in other respects is limited. A ray trace analysis of the primary optic indicates that it has superior light gathering ability, but the angular field of view is limited to only about 0.5 degrees. Coma is the dominant aberration over the entire field of view; a small amount of astigmatism is present for larger angles of incidence, while other aberrations are essentially negligible. Several candidate sensors, including CCD and CID technology, are commercially available and meet the requirements of the LTD retina.

A special mechanical subsystem was developed to deploy this advanced segmented photo-optic sensor (the "ring retina"), into the focal region of the primary mirror; in this manner, the propulsive optics are transformed into a powerful one meter diameter telescope. Functional hardware necessary for the LTD to perform satellite functions is located in the forward (nose) payload section of the vehicle.

1.5.8 Lightsat Systems Design

Once in orbit, the LTD will function as a light-weight sensor satellite, complete with all the requisite on-board electronics, communications, and attitude control systems (see Fig. 1.7). The LTD senses its attitude with a sun sensor and a Earth horizon sensor. To change attitude, it uses a combination of cold gas jets and/or magnetic torque bars. It will be equipped with an erectable light-weight antenna for communicating with launch command, accessing the TRDSS (and STDN) network, and relaying data gathered from LTD sensors. An on board computer will manage satellite electrical, mechanical and attitude control systems, coolant flow rates, and solar array actuators. The solar array is mounted onto the inner forebody surface, which opens into four "petals" to collect solar energy for recharging on-board nickel-hydrogen batteries. The batteries are used primarily when the satellite traverses the Earth's shadow. This combination of satellite components is chosen for minimal cost and weight, so that the LTD can fulfill its primary objective of a self-launched lightsat.

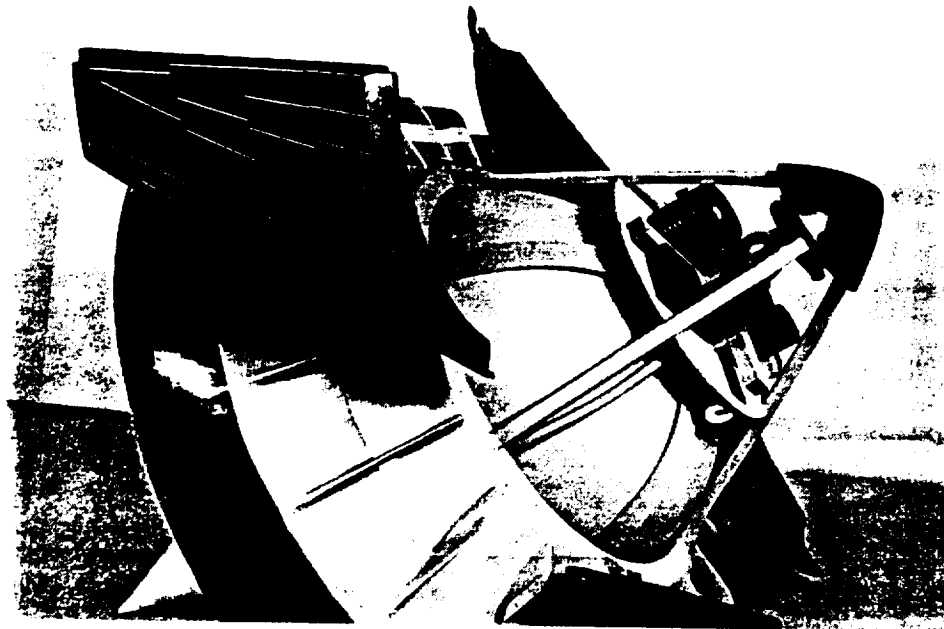


Figure 1.7: LTD satellite functional hardware is located in the forward payload section of the vehicle.

1.6 Future Directions

In the upcoming year, efforts will be focused on the LTD's propulsion system and vehicle aerodynamics rather than on its mission as a sensor satellite. A 3-D computational fluid dynamic (CFD) model of the LTD's external inlet will be assembled, and run for a variety of different shapes and flight speeds. From these computer simulations, the boundary layer thickness, external surface pressure distribution, and transition point (from laminar to turbulent flow) can be determined. A Naval Research Laboratory (NRL) 2-D blast wave code may also be employed to model the impulsive thrust generated by laser-induced blast waves. In addition, a computer analysis of the radiation/convection heat transfer to the LTD will be conducted to find the engine/vehicle thermal profile. All of this will enable the choice of appropriate spacecraft materials (specifically tailored to withstand the hypersonic transatmospheric environment), and also to design active thermal cooling systems for the primary optic and engine hot-sections. Finally, a more detailed vibrational analysis will be performed that includes not only the shroud/strut assembly, but also the spacecraft internal support structure.

Several experiments will be performed to validate theoretical vehicle and engine performance simulations (see Fig. 1.8). Hot and cold flow wind tunnel tests are planned,

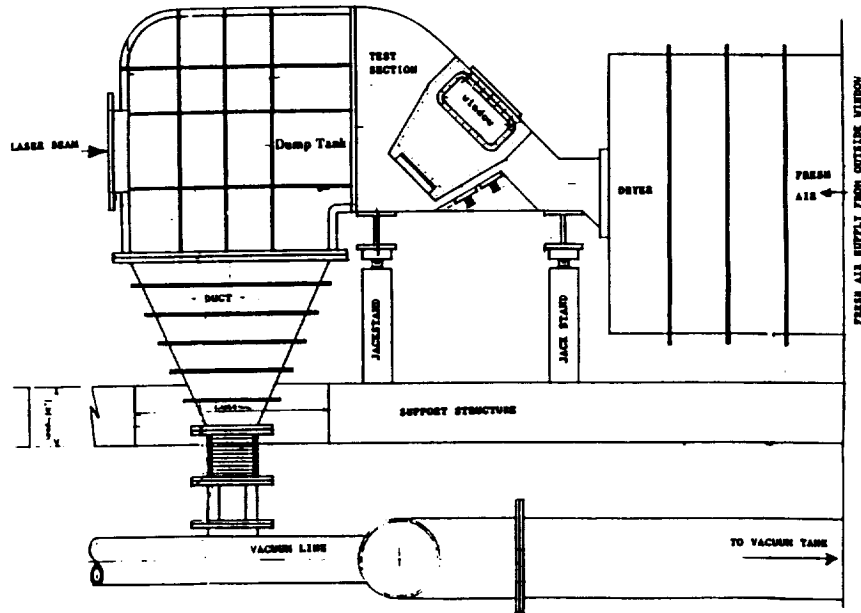


Figure 1.8: LTD wind tunnel Laser Impulse Experiment Test Section

with two different scale models, 5.5 in. diameter and 1.25 in. diameter. The air speeds will be varied from subsonic to hypersonic. Schlieren photographs and pressure data will be taken. Laser impulse experiments will also be performed with an exact 1/15th segment of the annular engine (see Fig. 1.9), in both static and dynamic wind conditions. These high power laser experiments will yield engine impulse and heat transfer data to prove technical feasibility of the propulsion concept.

Finally, additional systems-integration questions that were not addressed in this final report may be explored: e.g., LTD range safety issues, manufacturing cost analyses, and high power laser attenuation by the engine exhaust plume.

ORIGINAL PAGE IS
OF POOR QUALITY

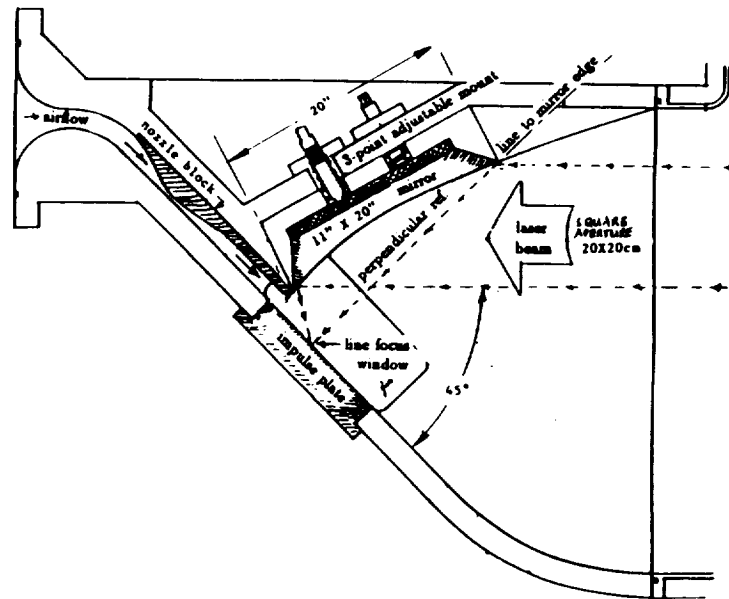


Figure 1.9: LTD Laser Impulse Experiment Test Section (side view).

REFERENCES

- [1] Canavan, G.H., "Laser Propulsion of Sensors and Interceptors," LA-UR-87-3208, Los Alamos National Laboratory, Los Alamos, NM, 1987.
- [2] Canavan, G.H., "Decoy Development with Laser Propulsion," LA-UR-88-1246, Los Alamos National Laboratory, Los Alamos, NM, April 1988.
- [3] Fuhs, A.E. and Mosier, M.R., "A Niche for Lightweight Satellites," *Aerospace America*, April 1988, pp. 14-26 and 36.
- [4] Mozey, R., "The Cost of Lifting Weapons to Space," Center for International Security and Arms Control, Stanford University, Stanford, CA, Oct. 1986.
- [5] "Proceedings of the First SDIO/DARPA Workshop on Laser Propulsion," J.T. Kare, Technical Editor, Lawrence Livermore National Laboratory, CONF-860778, Livermore, CA, July 7-18, 1986.
- [6] Raizer, Yu P., "Heating of a Gas by a Powerful Light Pulse," *Soviet Physics, JETP*, Vol. 21, No. 5, Nov. 1965.
- [7] Raizer, Yu P., *Laser Induced Discharge Phenomena*, Consultants Bureau (Div. of Plenum Publishing), New York, 1977.

- [8] Berning, M., "Version IV User's Guide for the Simulation and Optimization of Rocket Trajectories Program," McDonnell Douglas Astronautics Co., Houston, TX, Transmittal Memo No. 1.2-TM-FM86028-53, December 1985.

Chapter 2

VEHICLE CONFIGURATION AND STRUCTURAL DESIGN

2.1 Introduction

The purpose of this chapter is twofold: first, to present an overview of the LTD structural design influences from the perspective of the aerothermal flight environment; and second, to describe the overall LTD vehicle configuration and structural design. It is important to note that the vehicle preliminary conceptual design documented in this report is a bold first step in resolving conflicting design requirements and integrating complex vehicle systems.

There are two stages in the conceptual design process. First is the creation of a preliminary concept, in which the functions and desired features that comprise a successful design are identified. Alternative concepts that also meet these requirements should be explored. In the second stage the most promising concept is selected for further analysis. The structural design of the LTD has emerged from the conceptual design phase and is now undergoing more detailed analysis.

Driving issues in the LTD structural design process are the component mass allowances, and propulsion system requirements; aerothermal loads have been considered in a generic sense, to identify the current operating limits. Specific transatmospheric flight paths must be analyzed in future studies to assess their suitability for LTD engine and structures technology.

2.2 The Structural Design Process

The LTD structure must meet the combined challenge of providing a lightweight, efficient airframe that can survive severe engine and aerodynamic heating: i.e., a "thermo-structural" viewpoint [1]. Clearly, any successful thermo-structural concept must meet existing materials and manufacturing limitations. Initial selection of ma-

materials which may be considered for application to the LTD requires that the range of operating temperatures and the accumulated time at maximum operating temperature be known.

The LTD primary structure is a large fraction of the of vehicle's inert weight; yet this comprises a small structural weight fraction. Applied loads must be predicted to an accuracy that will allow knowledgable reductions in margins of safety, to eliminate every ounce of non-optimum structure. A large experimental data base of aerothermal loads must now be assembled, for future detailed finite element structural and heat transfer analyses.

A transatmospheric vehicle must withstand aerothermal, aerothermoelastic, acoustic, inertial, and engine thrust loads. Aerothermal loads are high because a single-stage-to-orbit vehicle with airbreathing propulsion follows a high dynamic pressure trajectory to achieve the necessary propulsion efficiency [2]. Added to this thermal load is the severe radiation environment imposed on the power-beam receptive optics, essential to laser-propulsive engines.

A compilation of the structures and materials technology needs for the LTD are represented below:

1. Propulsion/Thrust Structures: for which rigorous advancements are required.
2. Hot Structures: to handle high operating temperatures without degradation of strength or structural integrity.
3. Cryogenic Tankage: requiring simple and lightweight insulated structures able to handle cryogenic temperatures and supercritical fluids.
4. Thermal Protection Systems (TPS) : Utilizing a diverse range of materials including ceramics, carbon-carbon and refractory metals.
5. Dimensionally Stable Materials: which are essential for rigid optical platforms (carbon fiber composite structures are ideal candidates).
6. Active Control Surfaces: that will enable the propulsion system to transition smoothly between engine modes during flight.
7. Thermal Control Coatings: to reduce the severe heating loads experienced by hypersonic vehicles and laser-receptive optics.

2.3 LTD Vehicle Configuration

The Lightcraft Technology Demonstrator (LTD) is a single-stage-to-orbit transatmospheric vehicle utilizing both airbreathing and rocket propulsion modes (see Fig. 2.1).

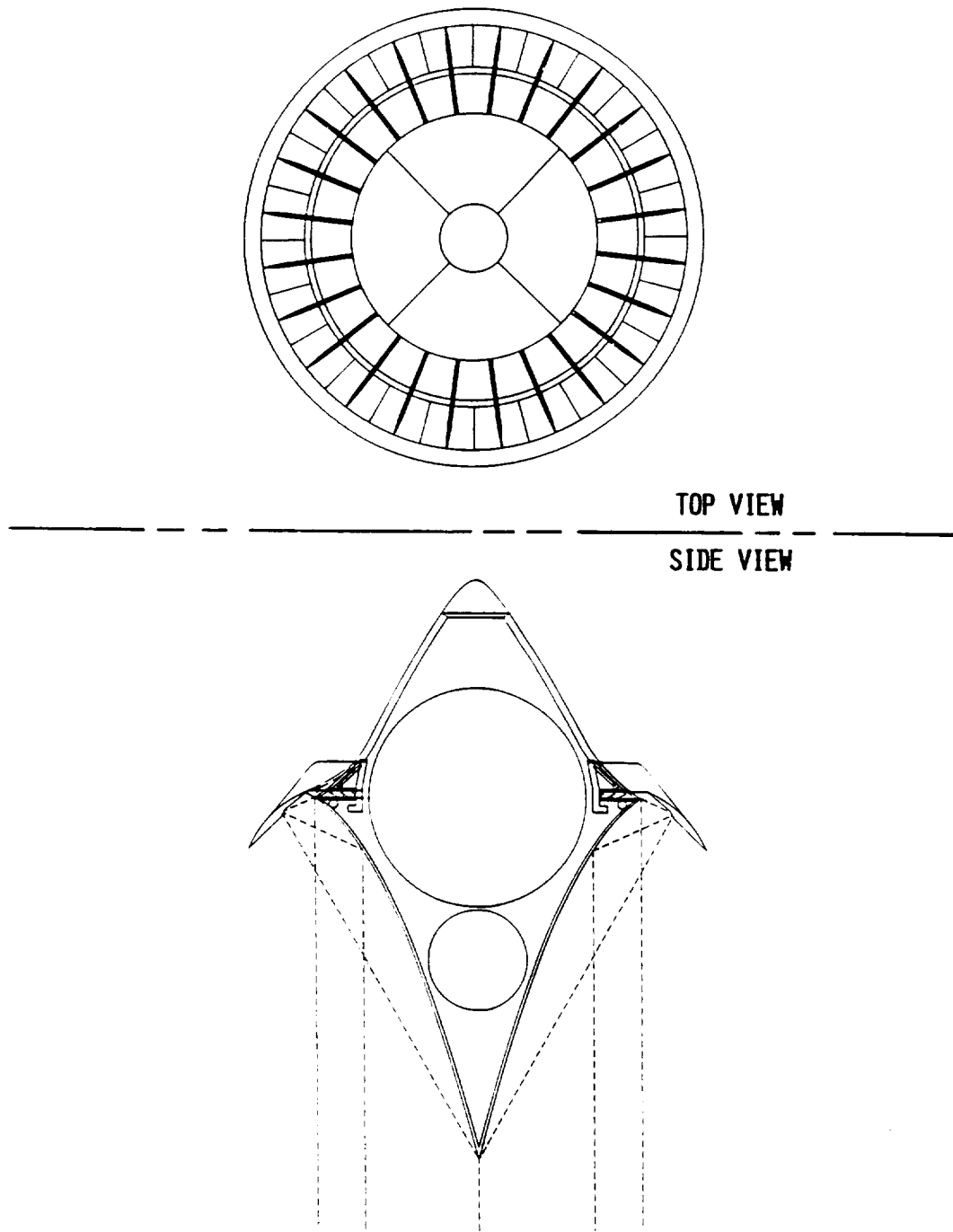


Figure 2.1: The Lightcraft Technology Demonstrator: top view, and side (cross sectional) view

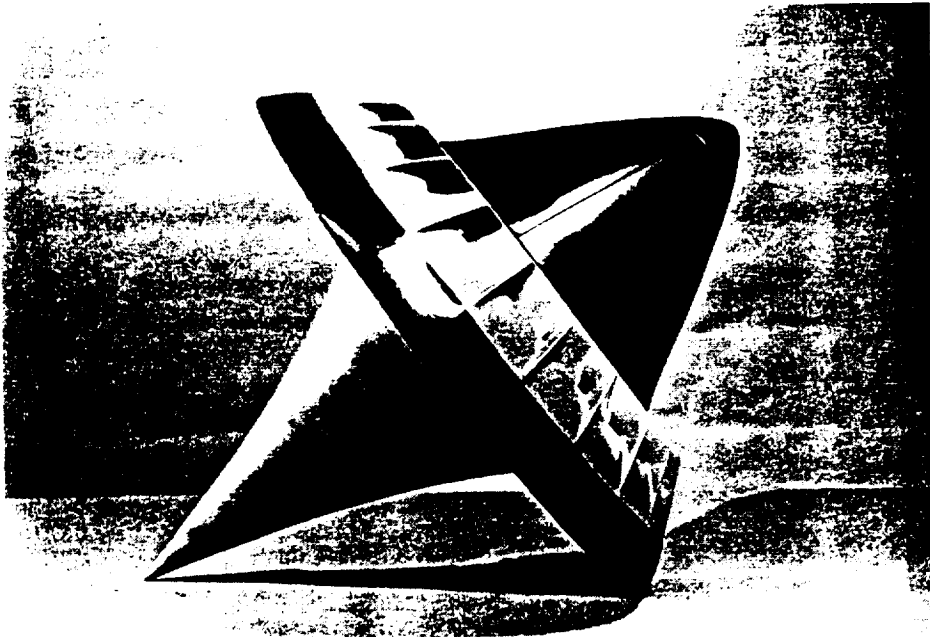


Figure 2.2: The LTD engine/vehicle external geometry

The LTD, an unmanned launch vehicle, 1.4 meters in diameter and 1.77 meters in length, will transition into a remote sensor satellite upon reaching orbit. The motivation behind this vehicle concept is to provide an example of how laser propulsion and its low launch costs can induce a comparable order-of-magnitude reduction in satellite packaging costs. The LTD will serve as a test bed for near term demonstration of laser propulsion technology. In its role as a 'lightsat', the LTD provides a low cost alternative for remote sensor satellite missions. This is accomplished by an exceptionally close integration of the laser propulsion engine and satellite functional hardware.

The LTD advanced microspacecraft is in several respects literally a "flying engine" (see Fig. 2.2). The forebody aeroshell acts as an external compression surface for the airbreathing engine inlet. The afterbody has a dual function: it is the primary receptive optic (parabolic mirror) for the laser beam which provides power to the engine, and it is also an external expansion surface (plug nozzle) during the rocket engine mode. The primary thrust structure is the annular shroud. The shroud serves as both inlet and impulsive thrust surface during the airbreathing engine mode. In the rocket mode, the annular inlet is closed; the afterbody and shroud combine to form the rocket thrust chamber. The three primary structures: forebody, shroud and afterbody, are interconnected by an internal support frame to which all internal subsystems are attached.

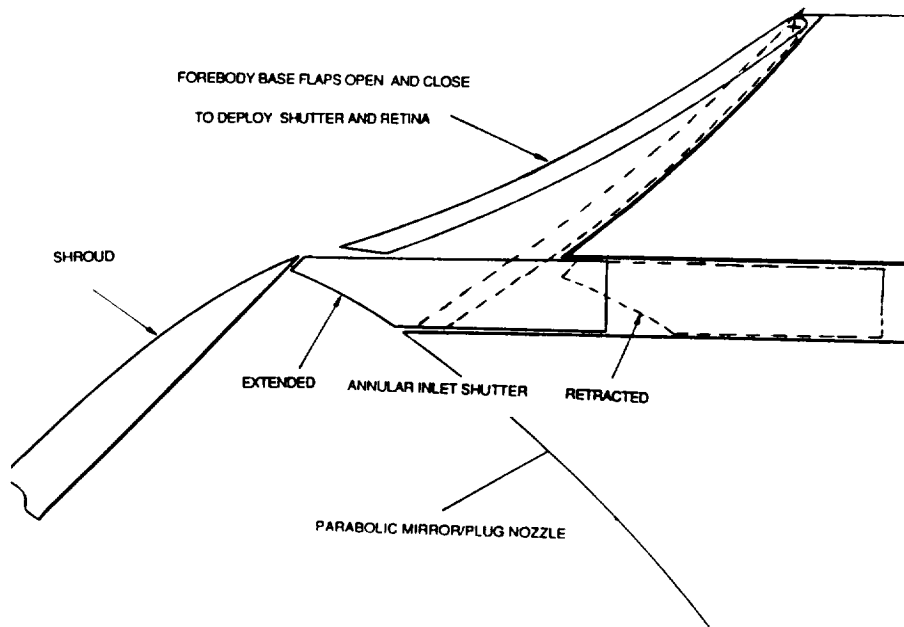


Figure 2.3: Forebody flaps open and close to deploy inlet shutter and retina

2.4 LTD Forebody

As mentioned above, the LTD forebody acts as an external compression surface. In addition, the forebody encloses the payload compartment, which is dedicated to satellite and launch control system electronics. The forebody is assembled from three separate sections. The advanced carbon-carbon (ACC) nosecap is designed to withstand the highest thermal loads (at the stagnation point) experienced during hypersonic flight. The forebody mid-section consists of four hinged petals. Once in orbit the petals open and reveal photovoltaic arrays which are mounted to the inner petal surfaces. Finally, the base section is comprised of twenty-four "flaps" (ACC material) that are hinged at the forward edges (see Fig 2.3). During a flight to orbit, they are opened twice: first, when the annular air inlet shutters are closed, and later after orbit is achieved (to permit deployment of the ring retina sensors). The entire forebody is hermetically sealed to prevent infiltration from the environment during the transatmospheric flight.

The forebody nosecap will not require active cooling. Advanced carbon-carbon composite structures have been flight tested on the Space Shuttle Orbiter and have proven ideal for the high temperature transatmospheric environment. Carbon-carbon composites utilize carbon fibers in a carbon matrix. The nosecap is a shell structure provided with thermal barriers to minimize heat transfer into the payload compart-

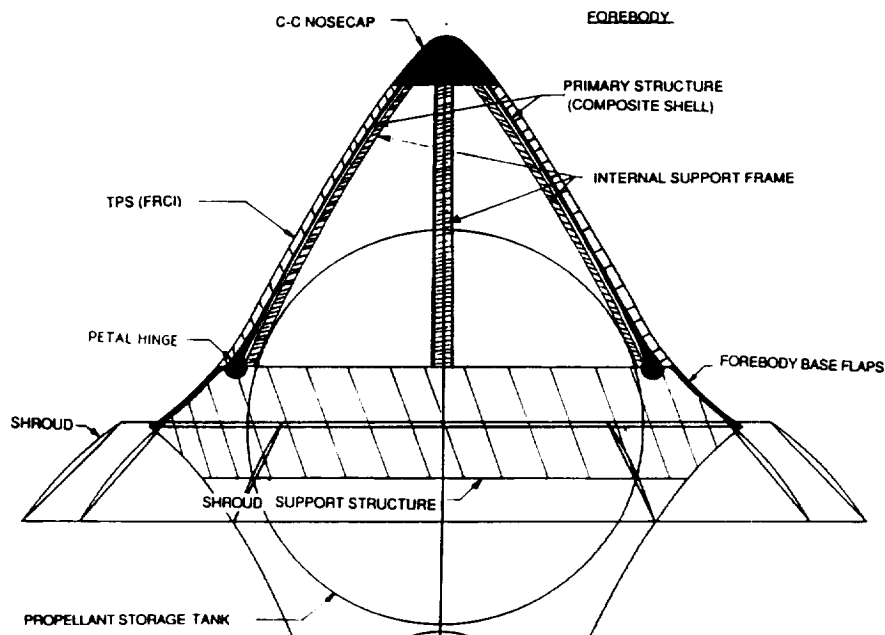


Figure 2.4: Side (cross sectional) view of forebody

ment. The ACC parts must be protected from oxidation by a high temperature oxidation-stable coating such as silicon carbide. On the shuttle orbiter leading edges ACC materials have performed well at elevated temperatures of 2500° F [3].

The forebody mid-section forms a composite shell structure (see Fig. 2.4) and has a truss-reinforced primary sub-structure made of polyimide graphite (PG) laminates. The structural temperature limit of PG laminates is superior to graphite/epoxy, and they enable a forty percent weight savings over aluminum [4]. The forebody shell structure will be covered by a thermal protection system (TPS), consisting of tiles made from boron rich fibrous refractory composite insulation (FRCI) [5]. FRCI is a re-radiative thermal protection system; the tiles dissipate most of the heat load before it can reach the vehicle primary structure. This is accomplished by a reaction cured glass coating (RCG) only twelve mils thick; it forms the forebody aerodynamic skin and re-radiates 90% of the incident heat energy back to the environment. These tiles require a flexible attachment system based on strain isolation pads, and carefully designed gaps at tile interfaces. The reduced heat pulse will not reach the primary structure until after the LTD achieves orbit. The photovoltaic array is attached to inner petal surfaces, and is thermally protected by radiation heat shields which prevent overheating from the residual heat pulse (see Fig. 2.5).

In order to provide a rigid forebody shell during flight, the mid-section petals are firmly secured by a 'Super-Zip' separation system (see Fig. 2.6), used for many

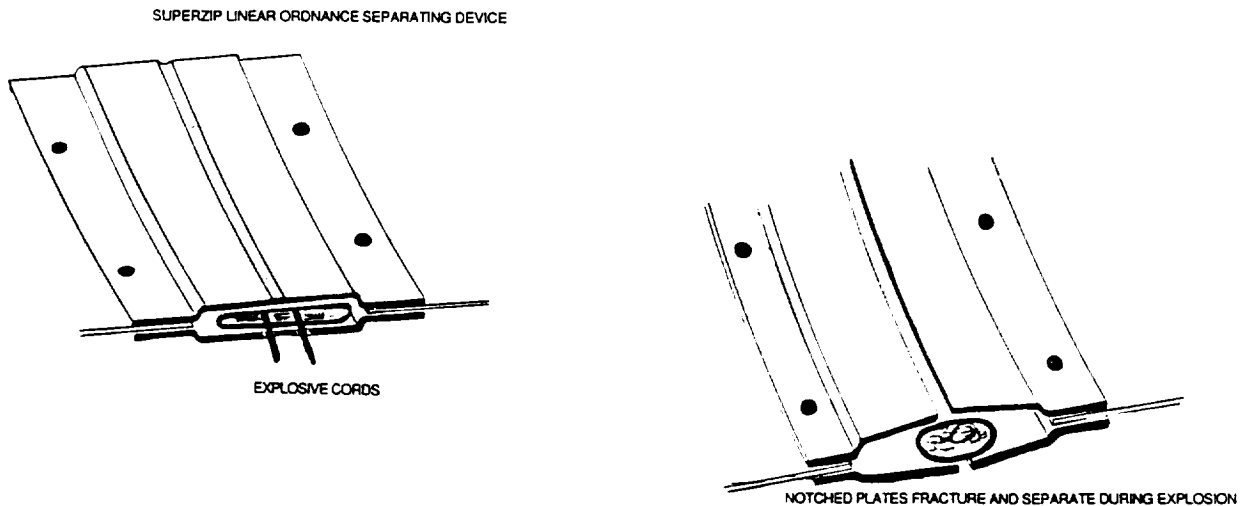


Figure 2.5: Super-Zip Linear Ordnance separating device

years in the space program [6]. Petal interfaces are temporarily fastened together by notched plates. Within the notched plate joint is a tube containing linear ordnance (an exploding cord) embedded in silicon rubber matrix. When the pyrotechnic cord is detonated, the resulting explosion fractures the notched plates, and a clean separation is produced in milliseconds. The mechanical interface must be designed to attenuate vibration from the explosion.

The aerodynamic contour of the LTD forebody can be described as a doubly-curved ogive with blunted nose. The initial design contour for the forebody was a thirty degree half-angle cone atop a forty-five degree half-angle conical frustrum. The ogive shape (see Fig. 2.7) was chosen after a preliminary bow shock wave analysis (using NACA 1135) indicated that the shock would be swallowed by the annular engine inlet before the transition from airbreathing to rocket mode (inlet design Mach number, $M = 5$).

The forebody aerodynamics are intimately related to the vehicle propulsion system. At supersonic flight speeds, the vehicle bow shock wave pre-compresses the free stream air for the airbreathing engine cycle; hence, the inlet is formed between the forebody and the shroud leading edge. The ideal geometry for this inlet would have the bow wave attach to the inlet lip at the design mach number; all the air compressed by the bow wave would thereby be ingested into the engine at Mach 5 [7].

The pressure and density flow fields around the annular inlet station provide insight into the uniformity and magnitude of the external compression process. Total pressure recovery, process efficiency, and kinetic efficiency provide measures of inlet

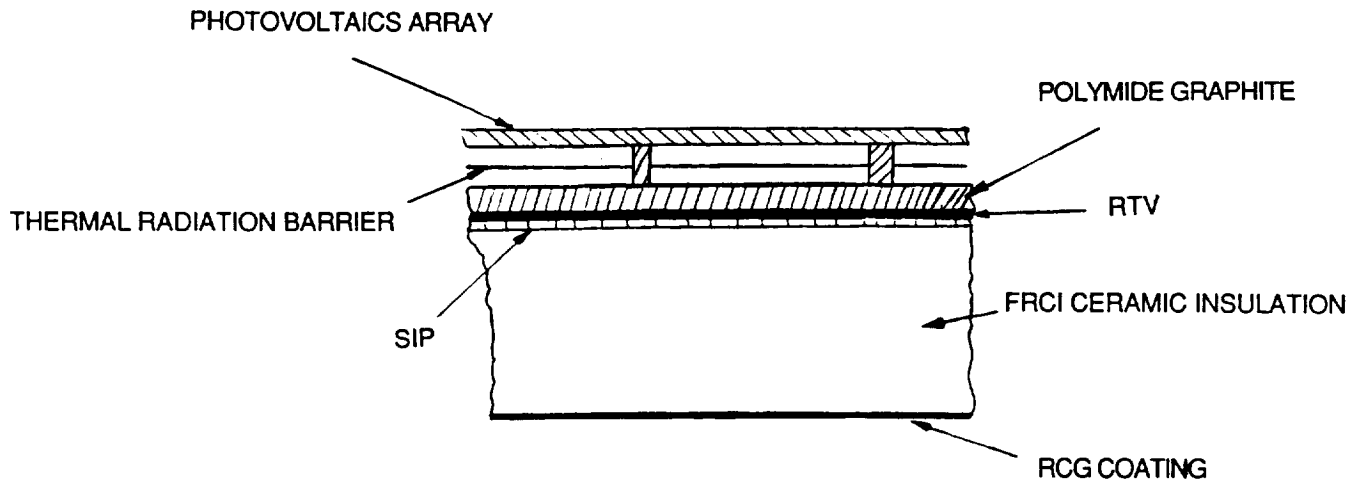


Figure 2.6: Side (cross-sectional) view of proposed forebody aeroshell.

performance. Optimal design of an inlet requires sophisticated 3-D computational fluid dynamic (CFD) codes, as well as wind tunnel experiments to validate analytical results [8].

The forebody shape was selected to minimize vehicle pressure drag characteristics. The resulting contour can be described as n -power body:

$$(y/b) = (x/a)^n \quad (2.1)$$

where $n = 2/3$, and the resulting shape is an approximation of the minimum pressure drag body for a given fineness ratio (i.e., length/diameter) [9]. This blunted, minimum pressure contour should also delay attachment of the bow wave to the inlet lip until the design Mach number is reached.

Obviously, several criteria could be used for optimizing the aerodynamic contour of the LTD forebody; pressure drag, total pressure recovery, heat transfer, etc. It is clear that a single optimum shape necessitates compromise between several conflicting measures of aerodynamic efficiency [10].

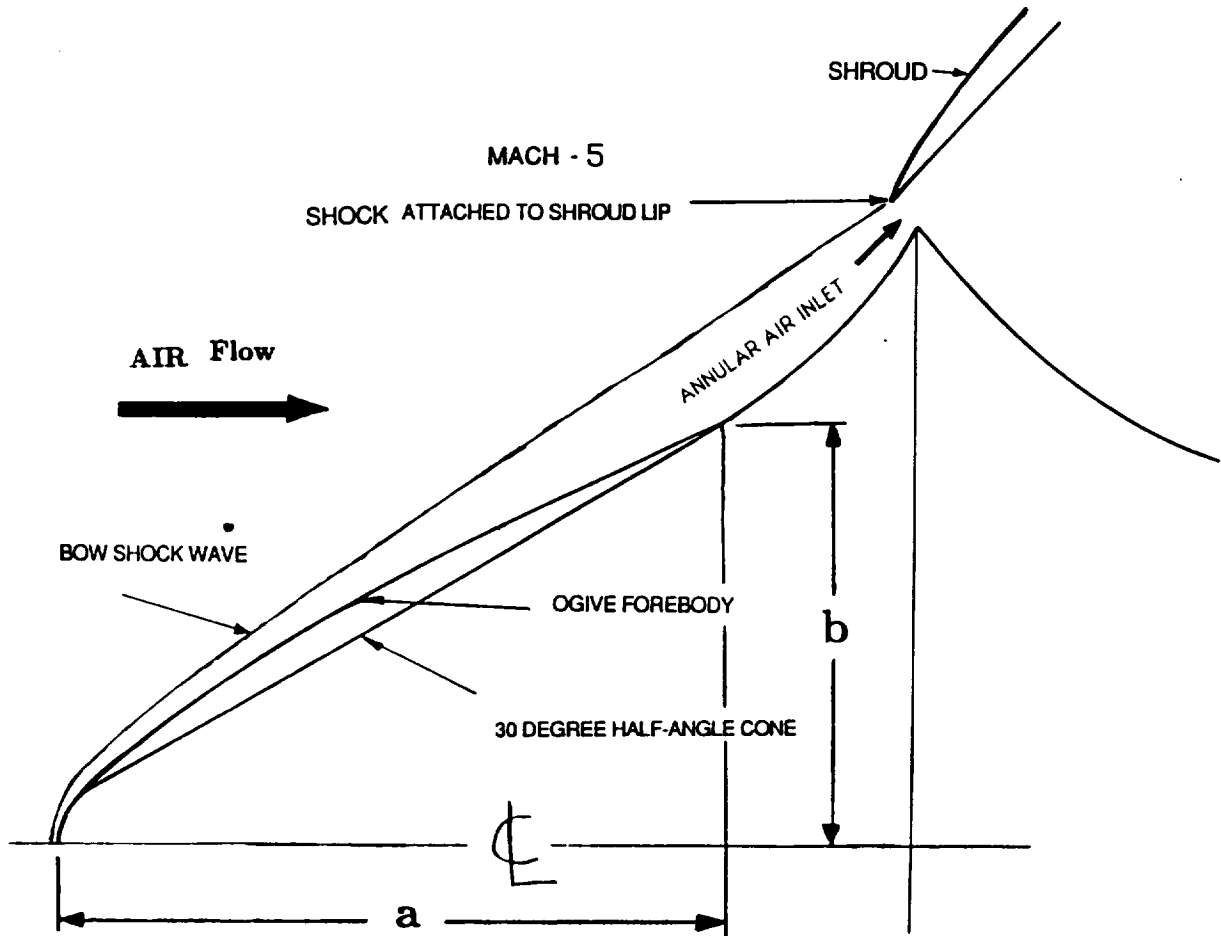


Figure 2.7: Bow shock wave and forebody contour at inlet design Mach number

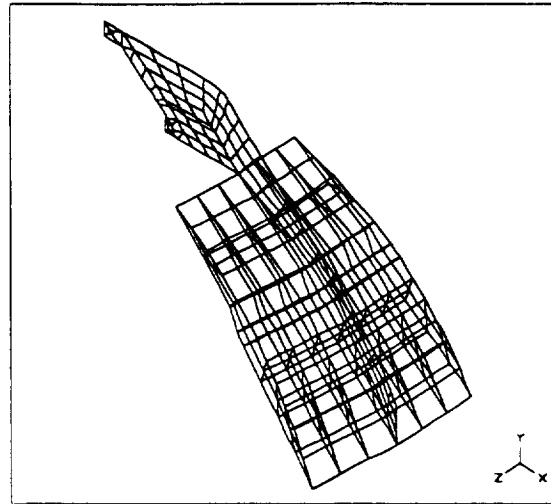


Figure 2.8: T-tail shroud support strut assembly (24)

2.5 LTD Shroud/Impulse structure

As mentioned earlier the shroud also serves as primary structure for delivering impulse to the LTD. In the airbreathing mode the ERH thruster itself is extremely simple, consisting only of an impulse surface (inner, or lower shroud surface) which can withstand high temperatures and pressures. To generate thrust, a laser-induced plasma is first ignited over the thruster surface. This high pressure (600 atm) plasma bubble then expands as it is convected down stream across the lower shroud surface. The shroud structure will be the most abused part of the vehicle during powered flight, and must be exceedingly strong.

The shroud structure is comprised of two major subassemblies: 1) the leading edge section is assembled from twenty-four nickel alloy “T-tail” support struts that also form the forward half of the shroud (see Fig. 2.8); and, 2) a single continuous ACC composite ring section forms the aft half (or trailing edge) of the shroud. The nickel T-tail assemblies require active cooling at the leading edges (transpiration) and thruster surfaces (film), in order to withstand the harsh aerothermal and laser propulsive environments. The rear half of the shroud is an ACC hot structure (passively cooled), to which the T-tails are firmly attached.

Actively-cooled structures must be used when radiation equilibrium temperatures, which are dependent on vehicle configuration and flight trajectory, exceed usual material limits. (e.g., about 2000° F for nickel-based alloys). The proposed shroud cooling system includes transpiration techniques and platelet technology [11]. Each

T-tail support strut would be manufactured by stacking numerous thin metal plates, into which intricate flow passages are chemically etched (see Fig. 2.9). The etch patterns combine to form complex flow paths and super-fine filters (for the sacrificial coolant) that determine the appropriate coolant flow rates to all hot areas of the structure. Once stacked the plates are diffusion bonded (at high temperatures and pressures) together, providing a high degree of structural integrity and strength [16]. This construction technique has been successfully demonstrated in experimental rocket engine programs [12], and in scramjet fuel-spray struts developed for the X-30 National Aerospace Plane (at Aerojet Techsystems).

As indicated above, the material favored for the rear half of the LTD shroud is the ACC structure which has also been used in the solid rocket booster cases for the Space Shuttle Orbiter. Two critical design issues for candidate materials are: thermal shock experienced at extremely high operating temperatures without the benefit of active cooling; and cyclic fatigue resulting from repetitively pulsed engine operation.

The maximum heat-flux capability of a carbon-carbon structure is currently limited by the temperature capability (about 2800° F) of its oxidation protection coating. If necessary, it will be possible to actively cool the shroud's carbon fiber structure by incorporating heat pipe technology into the carbon-carbon structure. A new design concept developed at NASA Langley Research Center [19], which NASA intends to patent, combines high temperature heat pipe and carbon-carbon technologies to extend both the thermo-structural capabilities and the maximum heat-flux capability of leading edge structures of hypersonic vehicles. The new design uses refractory-metal heat pipes embedded within a carbon-carbon structure (see Fig. 2.10). The walls of the heat pipes are thin and contain the working fluid (lithium or sodium) of the heat pipe. The primary application considered for such a structure is removal of high local heat from a leading edge surface, for transport to cooler surfaces, where it can be removed by radiation and/or active cooling.

The shroud structure is the most massive component in the LTD vehicle. This hollow, stressed-skin structure is comprised of an outer, load carrying shell which is reinforced by internal vertical ribbing. A common example of this technology is actively-cooled jet engine turbine blades [13]. A critical design issue is the thermal expansion evidenced by such components under typical load conditions. The interfaces between each hot component must accommodate both radial and circumferential expansions. Since the LTD lower shroud surface must coincide with the laser beam focus, radial shroud motion (i.e., expansion) would result in the loss of focusing precision, and degradation of thruster performance. The shroud support struts must therefore be attached to the control support frame in such a manner that compensates for all thermal expansions, especially in the radial and circumferential directions. Differential thermal expansions will also occur at the interfaces between the nickel alloy "T-tail" and the carbon fiber composite rear shroud ring, possibly producing

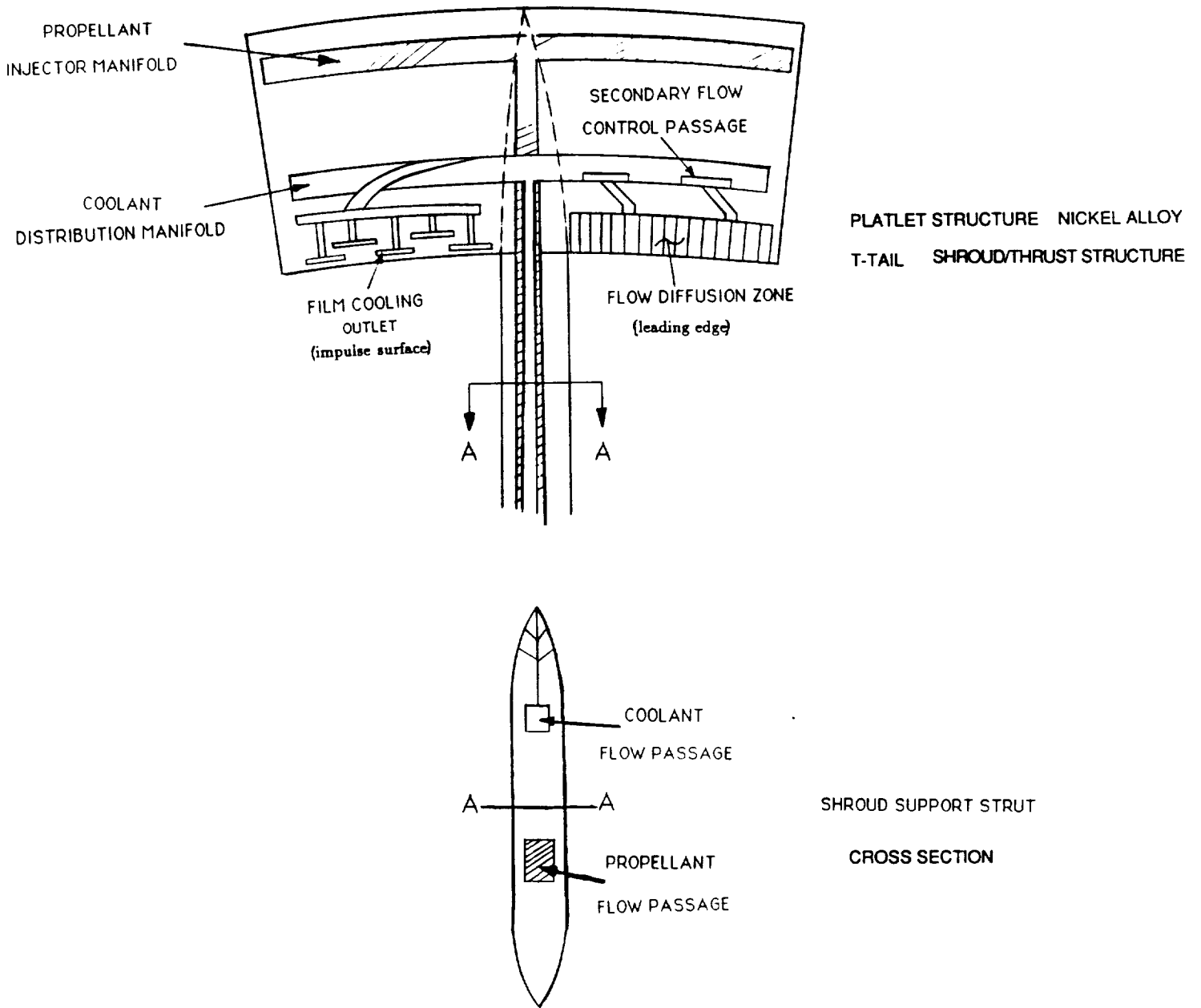


Figure 2.9: Typical platelet flow metering and distribution schematic

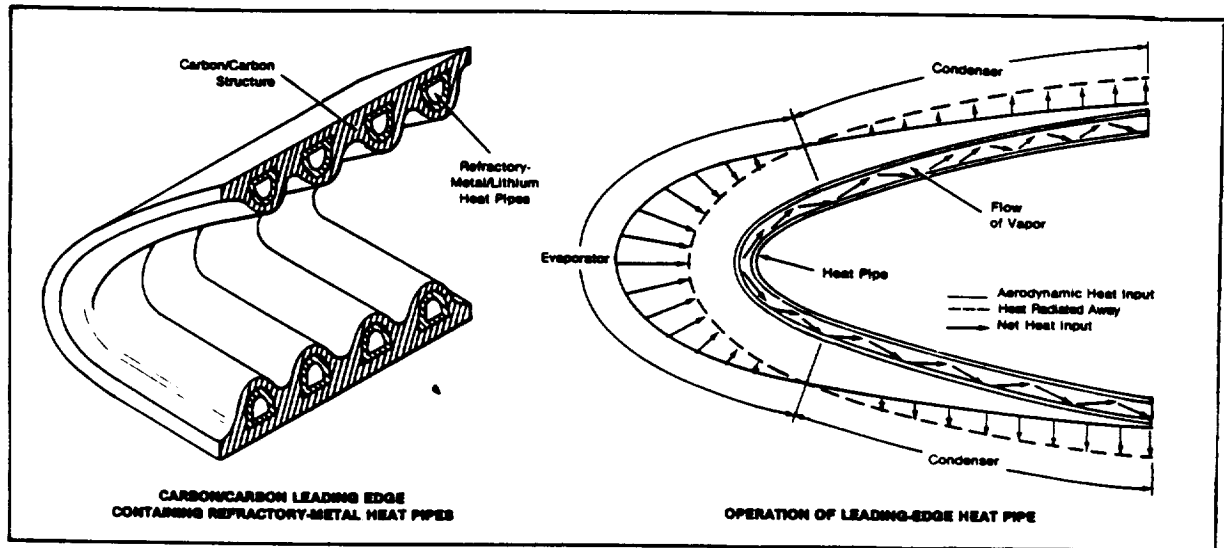


Figure 2.10: Metal pipes integrated into a carbon-carbon structure provide active cooling (from Ref. 19).

high shear stresses at the contact surfaces. These interfaces may require innovative joining techniques and fastener technology.

2.6 LTD Afterbody

The Afterbody of the LTD performs two functions: 1) It is the primary receptive optic (parabolic mirror) for capture and reflective focusing of the incoming laser power beam; and 2) it acts as an external expansion surface (plug nozzle) for the laser-heated rocket engine mode. The receptive mirror function is the driving issue in the geometry and structural design of the afterbody; the mirror must be dimensionally stable over the entire LTD operating range in order to maintain its precise focusing ability. High energy laser mirror technology will be pushed to the limit, with reflectivities approaching the theoretical maximum values (e.g., > 99.9%) attainable by multi-layer film coating technology. Active cooling is essential in order to keep temperature gradients in the mirror substrate structure within limits; thermally-induced stresses produced by even moderate temperature gradients would seriously degrade the mirror focusing ability and therefore thruster performance. Internal mirror stresses resulting from high coolant operating pressures must be considered. The mirror surface must

also survive the pulsed thermal shock during engine operation, and will require a durable outer coating (e.g., vapor deposited diamond) that can maintain a superior surface quality.

The afterbody structural design calls for a carbon composite inner shell sandwich to provide the necessary strength and dimensional stability. Since carbon-carbon is a composite material, its mechanical and thermophysical properties can be tailored to specific requirements by selection of the type of the weave, and the type and condition of the fibers. The optimum choice of properties of the composite will result in a minimum-mass design that satisfies peak-temperature and thermal stress constraints [19].

This composite shell will be bonded to the outer metallic mirror substrate; polished aluminum, copper or nickel are likely candidates. The parabolic mirror could be mass-produced at a reasonable price using an electro-forming process (see Fig 2.11). A highly-polished metal mandrel would first be cut using a high precision diamond-turning lathe; the female mold would then be constructed by electro-depositing metal upon this mandrel. Once reinforced, this female mold could generate thousands of identical, light weight parabolic mirrors. A second electro-forming and machining process could possibly be used to add the coolant channels on the mirror inner surface. As indicated above the afterbody mirror substrate will require active cooling for two reasons: 1) in its role as a plug nozzle there will be convective and radiative heat transfer from the laser-heated exhaust gases; 2) also, as the primary receptive optic, even 0.1 percent absorption of the incident laser energy will result in enormous absorbed heat loads that will ruin the mirror figure quality. The obvious solution is to provide active cooling, using onboard cryogenic fluids to flow through channels formed into the metallic mirror substrate structure.

Careful attention must be applied to the design of these afterbody cooling channels. The coolant inlet manifold is positioned at the aft end of the mirror. After flowing through mirror cooling channels, the LN_2 enters the outlet manifold at the top of the mirror, which delivers the propellant to the shroud support strut "T-tails". The radius ratio between mirror outlet to inlet is 8:1. This could result in an unacceptable pressure drop if the coolant channels are not properly engineered. Coolant channel passages could vary in depth from bottom to top in order to maintain constant cross-sectional flow area; also individual channels may split in two at each doubling of the afterbody radius. Thinner walls and more, smaller, channels will enhance cooling and chamber life [11].

The outer surface of the afterbody mirror structure must survive a harsh operating environment without degradation of reflectivity or loss of figure contour [17]. Mirror surface defects produced during powered flight could create localized regions of seriously lowered reflectivity. The resultant increase in absorbed laser flux could create localized hot spots and a mirror 'burn-through' [18]. Mission failure would be

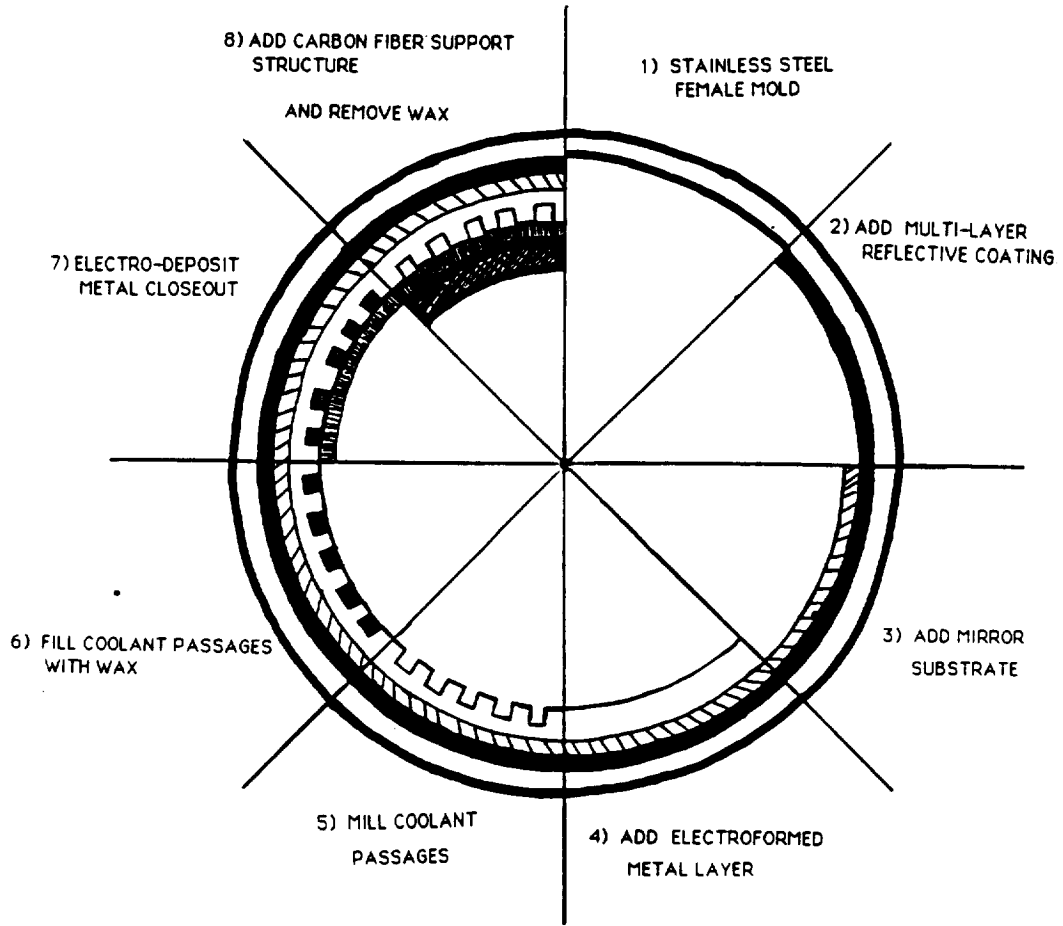


Figure 2.11: Proposed technique for “outside-in” fabrication of regeneratively cooled primary optic (not to scale).

inevitable.

A diamond film outer coating on the receptive optic surface could provide the required exterior hardness, and enable the mirror to withstand abrasion from particles impacting at extreme velocities. Recent research has produced new diamond film manufacturing techniques, now available at a reasonable cost [14]. It uses chemical vapor deposition (CVD) techniques, a process normally applied in making semiconductor films. This technique has the potential to make continuous films with controlled material properties. Diamond film coatings are strong, stiff, hard, and slippery; they can transmit light from the far infrared through ultraviolet, and are five times more thermally conductive than copper. Diamond films can also stand up to high power cycling without cracking.

2.7 Primary Internal Support Structure

The LTD primary internal support structure (i.e., the backbone) interconnects the three primary sub-structures: the forebody, shroud and afterbody (see Fig. 2.12). The “backbone” is an annular internal support ring with a U-channel cross-section, viewed sideways. Conceived as a molded construction graphite/epoxy structure, this main support ring must perform a multitude of functions. Internal trusses that support the electronics payload and propellant storage tanks will attach to the ring. Also, the shroud support struts will be bolted into the ring, and transmit thrust loads from the shroud pulsejet engine to the rest of the vehicle. The main support ring may therefore include active or passive damping mechanisms to attenuate engine vibrations. The upper surface of the ring provides receptacles for attaching the forebody shell by means of hinges and a “Super-Zip” separation system. Recesses must also be provided for storage of the “ring-retina” sensors during powered flight. The bottom portion of the primary structure will enclose the annular inlet shutters. The structural ring must exhibit near-zero deflection in flight, to prevent binding of the shutters when they are deployed and retracted. The afterbody will bolt onto the lower main support ring surface.

Detailed mechanical design of the LTD internal support structure will require finite element modeling to accurately evaluate structural performance. Similar carbon fiber structural components have been successfully demonstrated in the optical bench for the High Resolution Spectrograph Experiment used on the Hubble Space Telescope, and wing spars for advanced fighter aircraft [15].

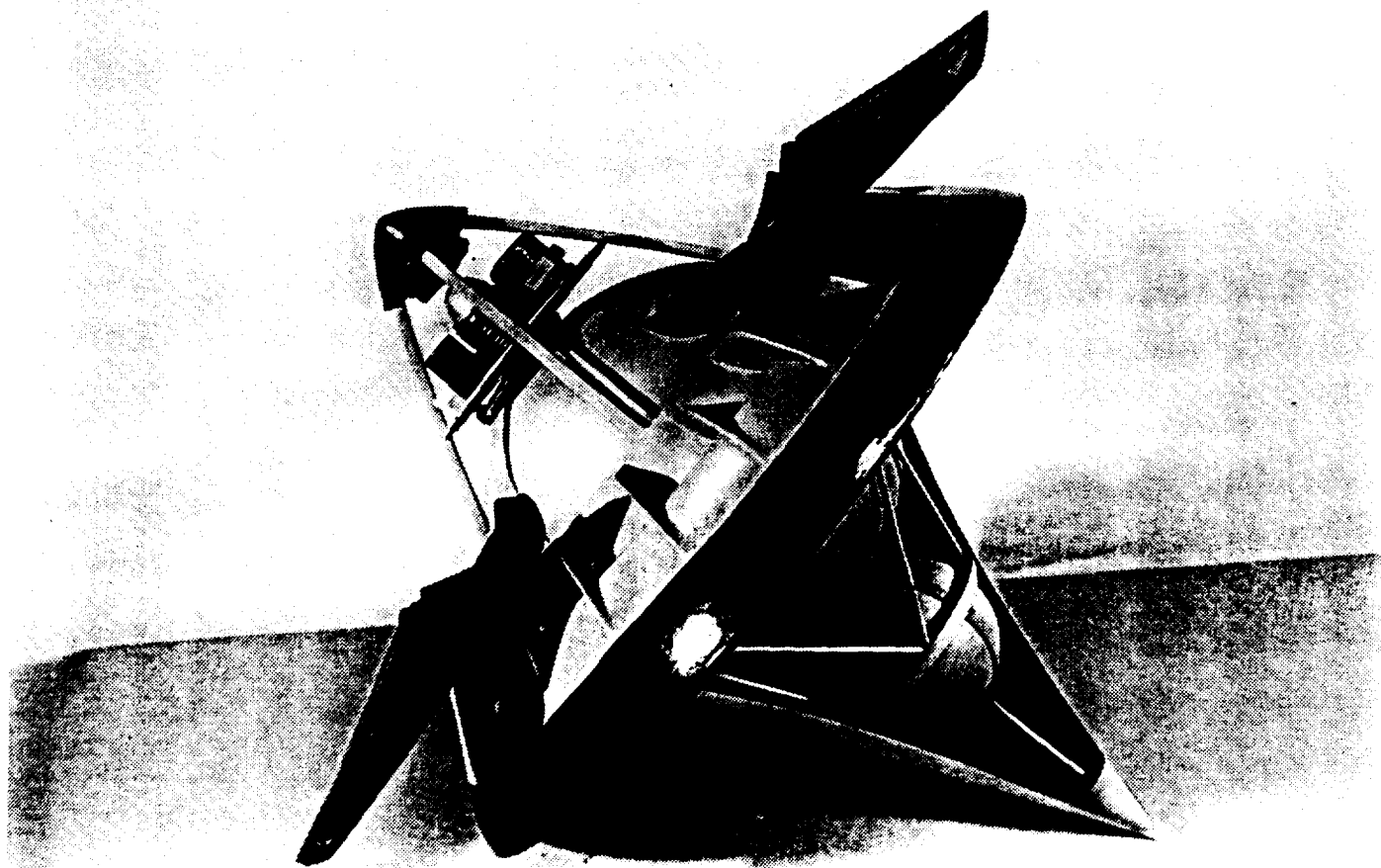


Figure 2.12: LTD internal support frame

2.8 LTD Mass Requirements

The LTD has a dry mass of 120 kg, and is filled (just prior to launch) with 140 kg of liquid nitrogen and 2 kg of supercritical helium gas. One tenth of the liquid nitrogen (14 kg) is allocated for use as sacrificial coolant during the airbreathing engine cycle to cool the laser mirror and engine hot section. Of the remaining nitrogen, several kilograms will be trapped in the propellant feed system at engine burnout. The result is a mass fraction of two for the vehicle which appears to be a reasonable goal. Table 2.1 lists the vehicle mass breakdown by component.

Table 2.1: LTD Vehicle Mass Breakdown.

<i>Section</i>	<i>Mass(kg)</i>
FOREBODY	
<i>C-C Nosecap</i>	1.0
<i>Primary Structure</i>	4.0
<i>TPS(FRCI)</i>	3.5
<i>Internal Support Frame</i>	10.0
AFTERBODY	
<i>Parabolic Mirror (Faceplate)</i>	12.0
<i>Mirror Support Structure</i>	8.0
<i>Manifolds</i>	2.0
THRUST STRUCTURE	
<i>Shroud</i>	15.0
<i>Strut Support Structure (24)</i>	15.0
<i>Air Inlet Shutters</i>	5.0
PROPELLANT MANAGEMENT SYSTEM	
<i>LN2 Tank</i>	8.0
<i>He Tank</i>	2.5
<i>Insulation</i>	1.0
<i>Feed Lines/Regulators</i>	5.5
SATELLITE SYSTEMS	
<i>Mechanical Actuators</i>	3.0
<i>Electrical</i>	5.0
<i>Electronics</i>	5.0
<i>Attitude Control</i>	2.5
GROWTH CONTINGENCY (10%)	12.0
	VEHICLE TOTAL DRY MASS 120.0

REFERENCES

- [1] Kelly, H.N., Rummer, D.R. and Jackson, L.R., "Research in Structures and Materials for Future Space Transportation — An Overview," *Journal of Spacecraft and Rockets*, Volume 20, January-February 1983, pp. 85-96.
- [2] Jackson, L. Robert, et. al., "Hypersonic Structures and Materials — A Progress Report," *Aerospace America*, Volume 25, October 1987, pp. 24-30.
- [3] Venneri, S.L., et. al., "Future Directions in Materials and Structures for Space Applications," *AIAA Systems Technology Conference*, 1986, AIAA Paper 86-1185.
- [4] Eaton, D.C.G. and Slachmuylder, E.J., "The Use of Advanced Materials in Space Structure Applications," *IAF International Astronautical Conference*, 1987, IAF Paper 87-305.
- [5] Pitts, W.C. and Murbach, M.S., "Heatshield Design for Transatmospheric Vehicles," *AIAA/ASME Joint Thermophysics and Heat Transfer Conference*, June 1986, AIAA Paper 86-1258.
- [6] "SuperZip Separation Systems," Lockheed Missiles and Space Company, Sunnyvale, Ca, 1986.
- [7] Johnston, Patrick J. et. al., "Fitting Aerodynamics and Propulsion into the Puzzle," *Aerospace America*, Volume 25, September 1987, pp. 32-37.
- [8] Waltrup, P.J., Billig, F.S., and Stockbridge, R.D., "A Procedure for Optimizing the Design of Scramjet Engines," *Journal of Spacecraft and Rockets*, Volume 16, Number 3, May-June 1979, pp. 163-171.
- [9] Truitt, Robert Wesley, *Hypersonic Aerodynamics*, Ronald Press, N.Y., 1959.
- [10] Miele, Angelo, "On the Theory of Optimum Aerodynamic Shapes," Thirteenth AFOSR Science Seminar, *Vistas in Science*, University of New Mexico, 1968.
- [11] Schoenman, Leonard, "High Pressure Propulsion Advanced Concepts for Cooling," *IAF 36th International Congress*, 1985, IAF Paper 85-191.
- [12] LaBotz, R.J. and Vallor, H., "Performance of a Transpiration-Regenerative Cooled Rocket Thrust Chamber," *NASA CR-159742*, September 1979.
- [13] "The Aircraft Gas Turbine Engine and its Operation," *United Technologies Corporation*, 1988.

- [14] Brown, Alan S., "Diamonds Shine Brightly in Aerospace Future," Volume 25, November 1982, pp.12-15,37.
- [15] "Carbon Fiber Composite Materials," Hercules Aerospace Company, 1988.
- [16] Ghosk, A.K., and Hamilton, C.H., "Superplastic Forming and Diffusion Bonding of Titanium Alloys," Rockwell International Science Center, Thousand Oaks, USA, January, 1986.
- [17] Porteus, J.O. and Seitel, Steven C., "Absolute Onset of Optical Surface Damage using Distributed Defect Ensembles," U.S. Naval Weapons Center, Physics Division, China Lake, CA , March , 1984.
- [18] Draggoo, Vaughn G., et al., " Optical Coating Measurement for High Power Laser Systems," Lawrence Livermore National Laboratory, SPIE O-E/LASE '86 Technical Symposium, Los Angeles, CA, January 1986.
- [19] Camarda, Charles J. and Ransone, Philip O., "Carbon-Carbon Panels Cooled by Heat Pipes," NASA Langley Research Center, NASA Tech Briefs, July, 1989.

Chapter 3

PROPELLANT MANAGEMENT

3.1 Introduction

The LTD propulsion system requires onboard reaction propellant after transitioning to the rocket mode at Mach 5 and 100 kft altitude, when the atmosphere is too thin for airbreathing engines to produce thrust. The annular inlet is closed, and the mass flow rate of propellant is increased. After being expelled by an injector array into the annular laser beam focus, the propellant is super heated (by the beam) into an incandescent gas. With the inlet closed off, the LTD afterbody and shroud act together to form a rocket engine absorption chamber and nozzle. The heated, high pressure exhaust gases expand against the LTD afterbody which functions as a high expansion ratio nozzle for efficient thrust production. The rocket engine mode continues until all usable onboard propellant has been depleted; the final portion (i.e., ullage gas) evaporates and is used by the cold gas jets for satellite attitude control maneuvers.

3.2 Propellant Management Criteria

A suitable propellant feed system is needed to transfer propellant from on-board storage tanks to the laser-heated rocket thrust chamber, at specific fluid flow rates and pressures. The feed system design depends upon the mission parameters, vehicle size, and mass ratio. Due to the small propellant tank volume, a pressurized tank system (using stored gas for pressurant) has been chosen for its simplicity, reliability and minimum weight penalty [1]. A schematic of the propellant management system is shown in Fig. 3.1.

The following criteria are essential to the design of the LTD pressure-fed propellant system [1].

1. Maximum operating pressures and "burst" pressures (i.e., factor-of-safety) of the propellant and pressurant tanks.
2. Propellant mass and volume as a function of operating temperature and pressure.
3. Tank mass and internal volumes for liquid propellant and gas pressurant.
4. Ullage as a fraction of the total tank volume.
5. Remaining propellant and pressurant mass at engine cutoff available for satellite attitude control.
6. Design of auxillary valves, pressure regulators, etc. for the complete plumbing system.

3.3 System Description and Layout

The LTD propellant management system consists of a 28 in. diameter pressure vessel for liquid nitrogen (LN_2) propellant, and a 12 in. diameter vessel (with internal heating system) for the gaseous helium (He) pressurant. A start/shutoff valve, over-pressure vent valve, and pressure regulator are required for each tank, along with temperature, pressure and flow rate sensors. During normal operation, the LTD has a non-vented fluid storage system; however, safety vent valves are essential to prevent catastrophic failure from over-pressurization (see Fig. 3.2).

The computer-controlled propellant management system must: 1) deliver the proper mass flow rate of liquid nitrogen coolant to critical actively-cooled engine components during the airbreathing propulsive mode; and 2) provide uniform propellant mass flow during the rocket mode. Sensors distributed over the vehicle's outer skin and engine will monitor surface temperatures. The mass flow rate of nitrogen coolant will be adjusted to compensate for variations in laser power absorbed by the primary mirror during the airbreathing mode. Laser power input is constant during the rocket mode.

Propellant will flow from the bottom to top of the mirror (while providing regenerative cooling), and then enter the nickel "T-tail" strut structure. The auxiliary flow passages (i.e., for the airbreathing mode) to the strut shroud cooling system will be separate from the main rocket propellant feed lines. Coolant flow rates must be monitored carefully to avoid excessive and wasteful use of LN_2 . Propellant flow

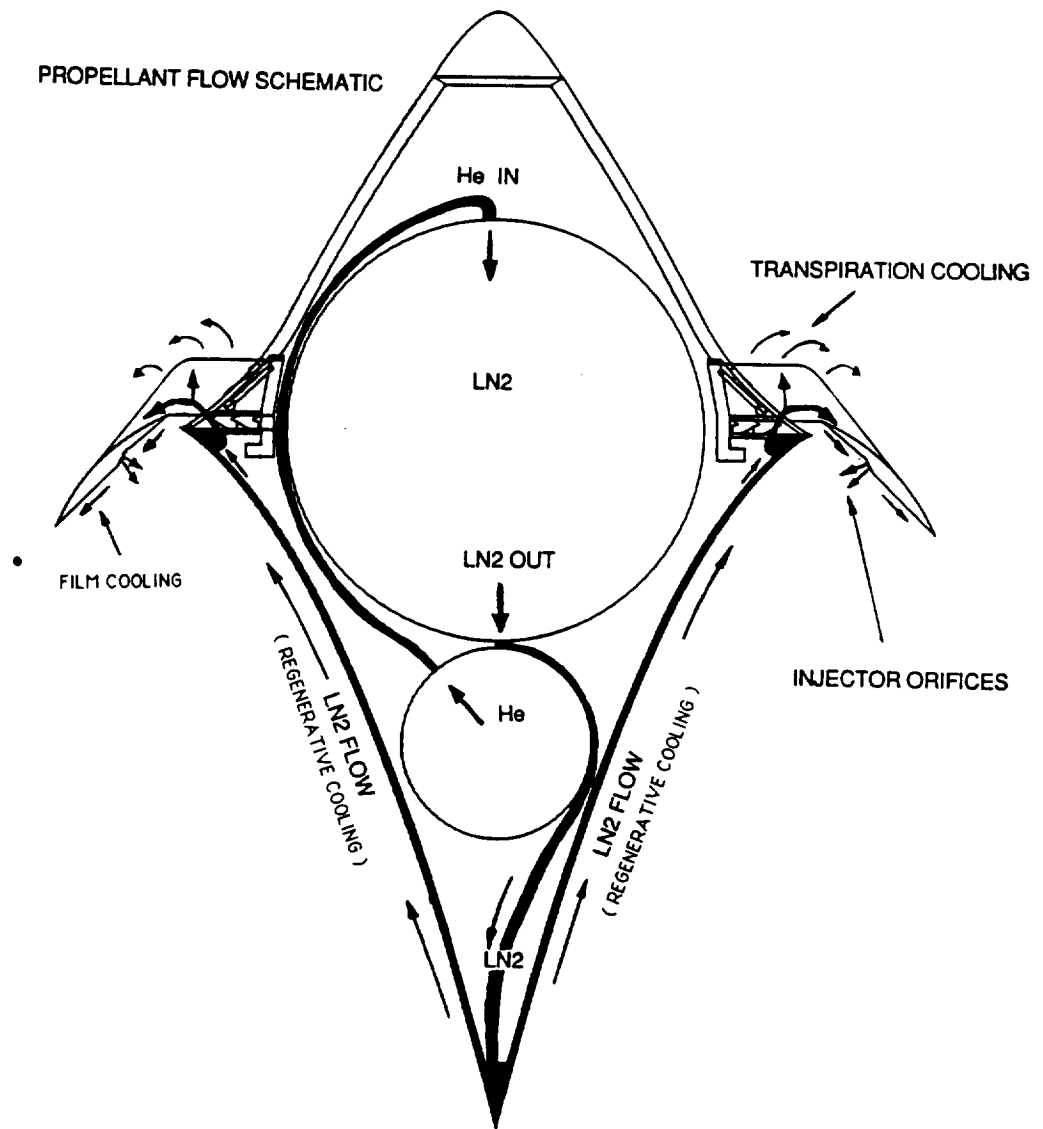


Figure 3.1: Schematic of Propellant Management System

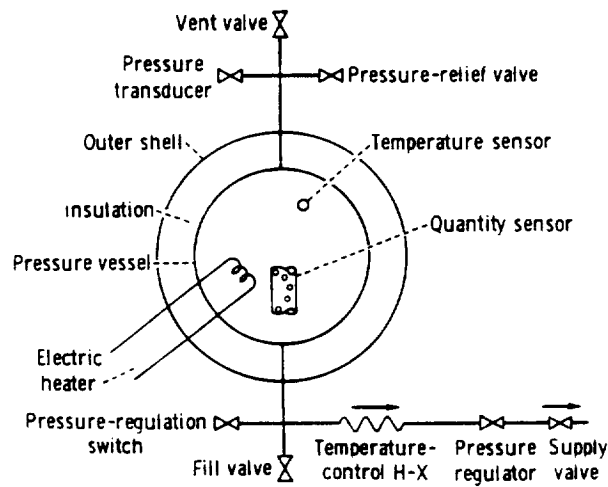


Figure 3.2: A Supercritical Cryogenic Gas Storage System (Ref. 4).

passages terminate at the shroud engine injector array. The injector orifices are designed to act as “acoustic valves”, automatically controlling the injection sequence of propellant into the rocket engine thrust chamber. Precise control of injector orifice pressure is necessary for optimum propellant utilization during flight.

3.4 Cryogenic Fluid Options

The LTD combined-cycle, laser propulsion system employs onboard cryogenic fluids for reaction propellant, sacrificial coolant and feed system pressurant. Liquid nitrogen has been chosen as the propellant for several reasons. Although liquid hydrogen (LH_2) would be the most desirable propellant because of its low molecular weight (and higher rocket specific impulse), only 14 kg of LH_2 would fit in the LTD’s 28 in. diameter tank; in contrast, 140 kg of LN_2 would occupy the same volume. Heated to high temperature and pressure, nitrogen can produce specific impulses in the range of 725 to 1025 seconds — depending whether the exhaust gases are dissociated or not. (LN_2 is also favored because it is an inert and exceptionally clean coolant, a consideration which is especially important for high power laser optics [2]).

High pressure, super-critical helium was chosen for the pressurant because of its superiority as an inert agent with a very low boiling point. The helium tank will contain a heat exchanger system (see Fig. 3.3). The LTD pressurant system is modeled after the Apollo Lunar module descent rockets. This pressurant system operated at near liquid helium temperatures (5.2 K), thereby enabling the maximum pressurant density [3].

PHYSICAL PROPERTY	N ₂	He
MOLAR MASS	28.0134 g/mol	4.0026 g/mol
CRITICAL TEMPERATURE	126.20 K	5.2 K
CRITICAL PRESSURE	3.400 MPa (493.1 psi)	0.227 MPa (32.99 psi)
CRITICAL MOLAR DENSITY	0.01121 mol/cm ³	0.0174 mol/cm ³

Table 3.1: Physical properties of Nitrogen and Helium

3.5 Cryogenic Storage and Handling Considerations

Cryogenic fluids for the LTD will necessitate launch site storage and handling of extremely cold gases in their supercritical state. Table 3.1 lists several physical properties of nitrogen and helium. Such cryogenic fluids are known to be compressible, a desirable characteristic for achieving maximum fluid mass within fixed storage tank volume constraints. Strictly speaking, cryogenic fluids are normally stored (at the launch site) as compressed liquids, rather than in a supercritical state. However, cryogenic fluids behave as a high density gas in either regime. "Supercritical" storage simply means that the fluid pressure is elevated beyond the "critical" pressure, and that it remains a single phase for the duration of the mission [4]. A pressure-enthalpy diagram (from ref. 4) for supercritical storage of cryogenic fluids is displayed in Figure 3.4.

The charging process for a typical supercritical system normally begins with a purge and vacuum pumping of the tank and all its lines. In Figure 3.4 state "1" represents the "fill" condition, after which heat is added to increase the pressure

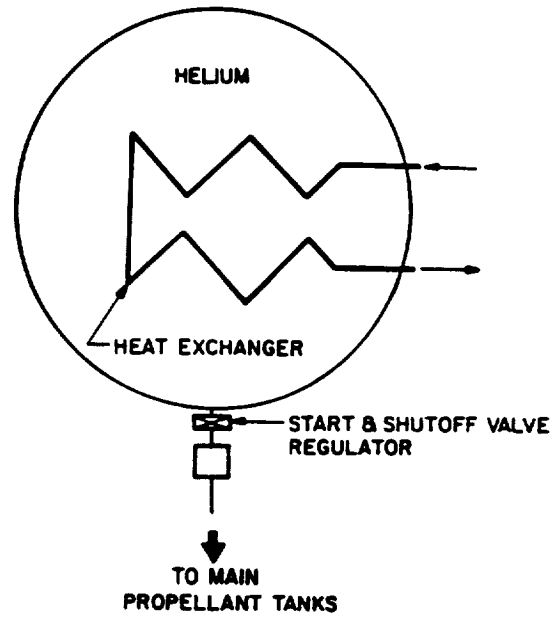


Figure 3.3: Helium pressurization system using heaters in storage vessel.

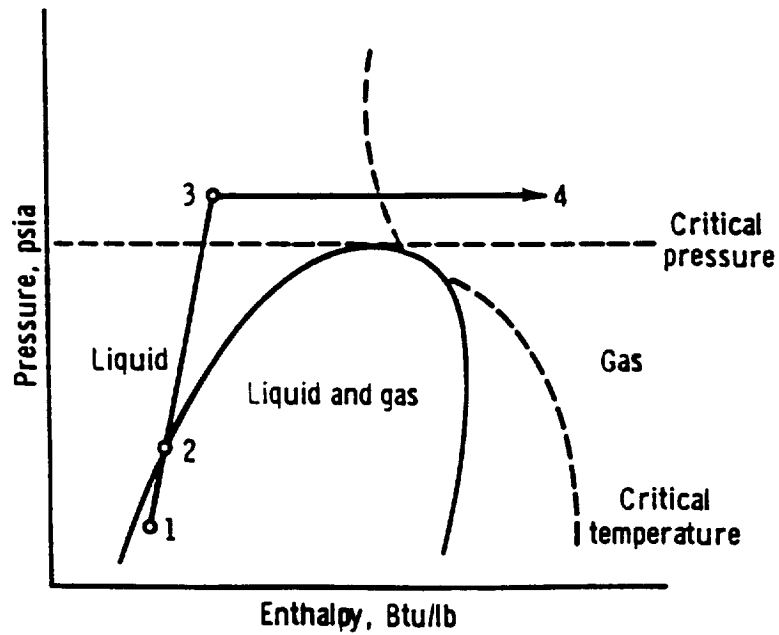


Figure 3.4: Pressure-enthalpy diagram of supercritical storage (Ref. 4).

while maintaining a constant density (at a constant volume). In moving from state "1" to "2," the liquid expands and the ullage gas condenses until the entire volume is filled with liquid. From state "2" to "3" thermal energy is added until the fluid rises above critical pressure. For a nonvented system, the heat that is required to pressurize the vessel is given by:

$$Q = M_f H_i - M_f P_f V_f + M_i P_i V_i \quad (3.1)$$

where

Q	=	heat energy	{KJ}
M	=	stored Mass	{Kg}
H	=	specific enthalpy	{KJ/Kg}
P	=	pressure	{KPa}
V	=	specific volume	{m ³ /Kg}
f	=	final fluid state	
i	=	initial fluid state	

During withdrawal of fluid, constant supercritical operation is maintained from state "3" to "4" by additional heat input to the stored liquid. The supercritical state insures that the stored mass remains a single phase, and fluid expulsion is assured because of the high operating pressure. The thermal energy input required to maintain pressure in a supercritical system is given by:

$$Q = -D(dH/dD)_p \quad (3.2)$$

where D is density (Kg/m³) and p is constant pressure. The solution of Eqn. 3.2 yields the heat energy per Kg of fluid withdrawn, for maintaining constant pressure as a function of density. The total required heat input is delivered to the internal tank by the internal heater and from environmental, electrical, and any other heat sources associated with on-board LTD systems. Individual LTD launch trajectories will require a specific fluid flow rate schedule; the vessel heat exchanger and heat-input rates must be carefully designed (and controlled) to avoid excessive pressurization and the need for venting.

The helium gas expansion process will be polytropic. The following correlation can be used to obtain the final gas temperature (in the storage tank), as a function of pressure:

$$T_f/T_i = (P_f/P_i)^{n-1/n} \quad (3.3)$$

$$\text{with } n = (C - C_p)/(C - C_v)$$

where C is the specific heat (which will vary during system operation) and C_p and C_v are the specific heat at constant pressure and volume, respectively. The exponent n can be estimated analytically and verified experimentally [5].

3.6 Propellant Tank Pressurization System Requirements

Determination of the pressurant gas weight for a cryogenic propellant is complex and defies exact analytical treatment because of the interdependent transient phenomena of heat and mass transfer that occur simultaneously in a propellant tank. Mathematical models describing the internal thermodynamics of tank pressurization have been developed by various investigators [13]. Although the most accurate method of predicting pressurant requirements is to use a computer program that has been verified by experiment, initial design studies require fast, reasonably accurate analytical methods.

The total mass of pressurant gas required is a function of the ullage mean temperature at cutoff, derived with the gas equation of state:

$$W_{TOTAL} = \frac{PV M_w}{\alpha R T_m} \quad (3.4)$$

where

W_{TOTAL}	= total pressurant weight
P	= ullage pressure
V	= propellant tank volume
α	= gas compressibility factor
R	= universal gas constant
M_w	= pressurant molecular weight
T_m	= mean ullage temperature

Therefore the total pressurant mass required may be calculated if the ullage mean temperature at cutoff can be determined. Dimensional analysis provides a relation for T_m as a function of twelve system design variables, seven physical properties, the mechanical equivalent of heat, and the gravitational constant [14]. For the design of the LTD pressurization system, vehicle parameters such as tank volume, engine flow rate, tank material, etc., determined by mission profile, are fixed input values. However, there are various controllable parameters in the LTD pressurization system that can be used to optimize the system without affecting basic vehicle characteristics [14].

3.7 Pressure Vessel Design

The LN_2 and He pressure vessels will utilize filament-wound, prestressed composite fiber (and metal liner) construction (see Fig. 3.5). This construction technique consists of a pretensioned fiber that is wound over a stretch-formed metal liner that acts

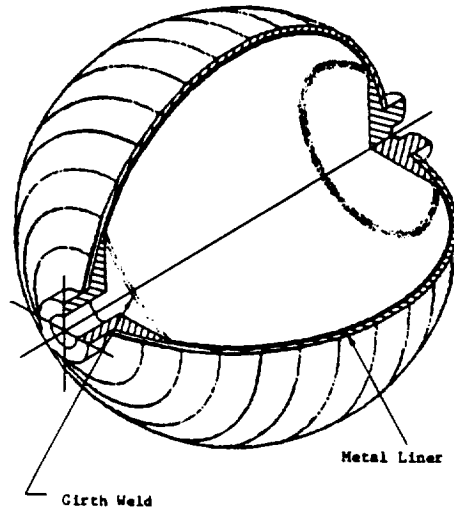


Figure 3.5: Single wall composite fiber cryogenic storage tank.

as a vapor barrier. Proper choice of prestress and operating stress states enables ultra-lightweight, high pressure storage vessels. The metal liner is prestressed with compressive load to increase its strain limit to the point of rupture; this permits both the metal liner and fiber wrap to achieve their ultimate strength capabilities simultaneously at rupture [7]. Candidate fibers include Kelvar-49 for the nitrogen tank, and graphite for the helium tank.

The LN₂ tank design is simple: helium pressurant flows in from the top, expelling LN₂ out the bottom. Several problems may arise:

- solubility of pressurant into propellant.
- evaporation of propellant at interface into ullage gas.
- propellant sloshing during flight.

One well proven solution to all these problems is the “positive-expulsion” tank, which contains an integrally welded stainless steel ring-reinforced diaphragm (see Fig. 3.6). This tank design inherently provides compatibility for a wide range of fluids, excellent center of gravity control (during the expulsion mode), and high resistance to dynamic loads [8]. Application to the LTD may require alternative designs for fluid flow lines.

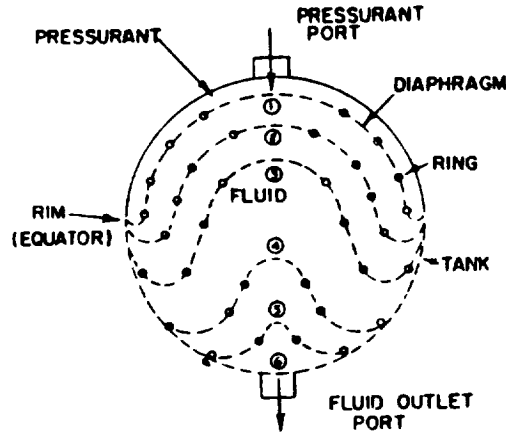


Figure 3.6: Positive expulsion tank; successive positions during diaphragm reversal (Ref. 8).

3.8 Thermal Insulation Requirements

External thermal insulation is an essential requirement for the cryogenic storage tanks. Cryogenic insulation minimizes propellant boiloff and prevents liquefaction of air and the condensation of water vapor/ice onto the outer tank wall (cryopumping) [9]. The LTD mission includes four phases for which effective cryogenic insulation is necessary:

- ground hold period
- compressed air cannon launch
- laser boost phase
- orbital phase

Two candidate materials have been evaluated for external insulation: rigid closed cell polyvinyl chloride foam (PVC), and polymethacrylimide foam (Rohacell 110WF). Table 3.2 lists typical material properties. The PVC foam has a lower density, but higher thermal conductivity. Insulative performance of the two options is similar when equal weight layers are compared. Both foams are widely used on LOX and LN₂ storage tanks and can be expected to perform well in the LTD [10].

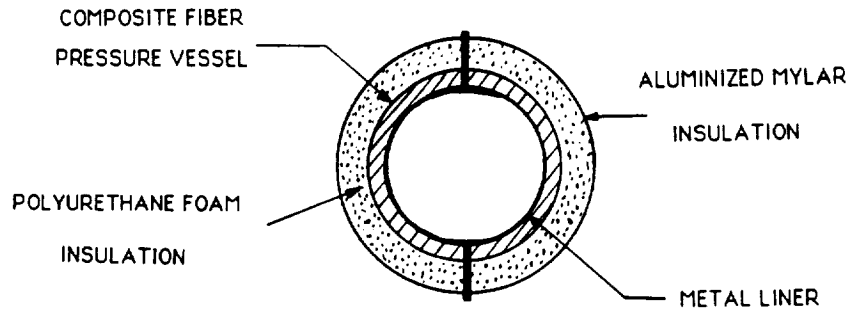


Figure 3.7: Schematic of single wall cryogenic gas storage tank for heat transfer analysis.

In addition to foam insulation, thermal radiation barriers can also reduce heat leaks from the forebody and afterbody exteriors. Aluminized mylar layers applied to the exterior of the foam insulation will function as both vapor barrier and thermal radiation barrier. Figure 3.7 illustrates an insulated single wall cryogenic storage tank schematic for future heat transfer analyses, that may focus on, amongst other issues, the optimization of the propellant tank heat leak factor, Q/A .

The tank support design also has a great influence on the tank's heat leak factor because conduction heat transfer through the truss and tank straps is inevitable. Each storage tank is attached to a truss support structure by two belts that wrap completely around the tank and act as a cradle. This proven method for tank support evenly distributes flight dynamic loads onto the tank surface. Fluid lines are routed over the outer surface of the tank supports to reduce conduction heat transfer.

3.9 Conclusions

The physical processes which take place during the expulsion of a liquid propellant from a storage tank by a gas are numerous and difficult to analyze. Applicable data for the LTD system is limited. Thus the basis for an analytical approach is uncertain.

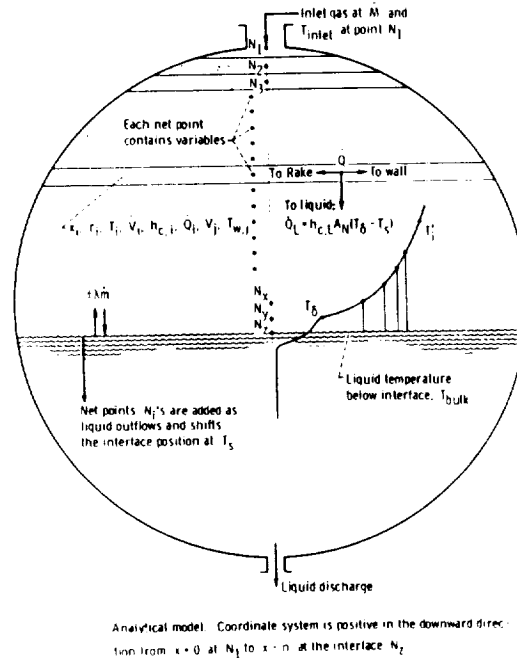


Figure 3.8: Analytical model of pressurized propellant tank (Ref. 15).

As a result, the initial design calculations for the propellant management system must be considered approximate. Fluid properties will undergo wide variations from initial to final states, and cannot be assumed constant. A more detailed analytical model of the physical process is required.

A logical next step in the propellant management system design is the application of numerical methods for the pressurization and expulsion processes (see Ref. 15). Figure 3.8 illustrates an analytical model of a propellant tank internal volume, and algorithms for pressurization and expulsion processes are shown in Figure 3.9.

These algorithms may be implemented in two computer programs: first, to predict helium pressurant gas requirements for the pressurization (ramp) phase of bringing the propellant tank up to its operating pressure; then, second, to predict system characteristics during expulsion of the LN_2 propellant at a uniform pressure. This method of analysis will involve a numerical solution of the temperature and velocity functions for the tank ullage at a discrete set of points in time and space [15].

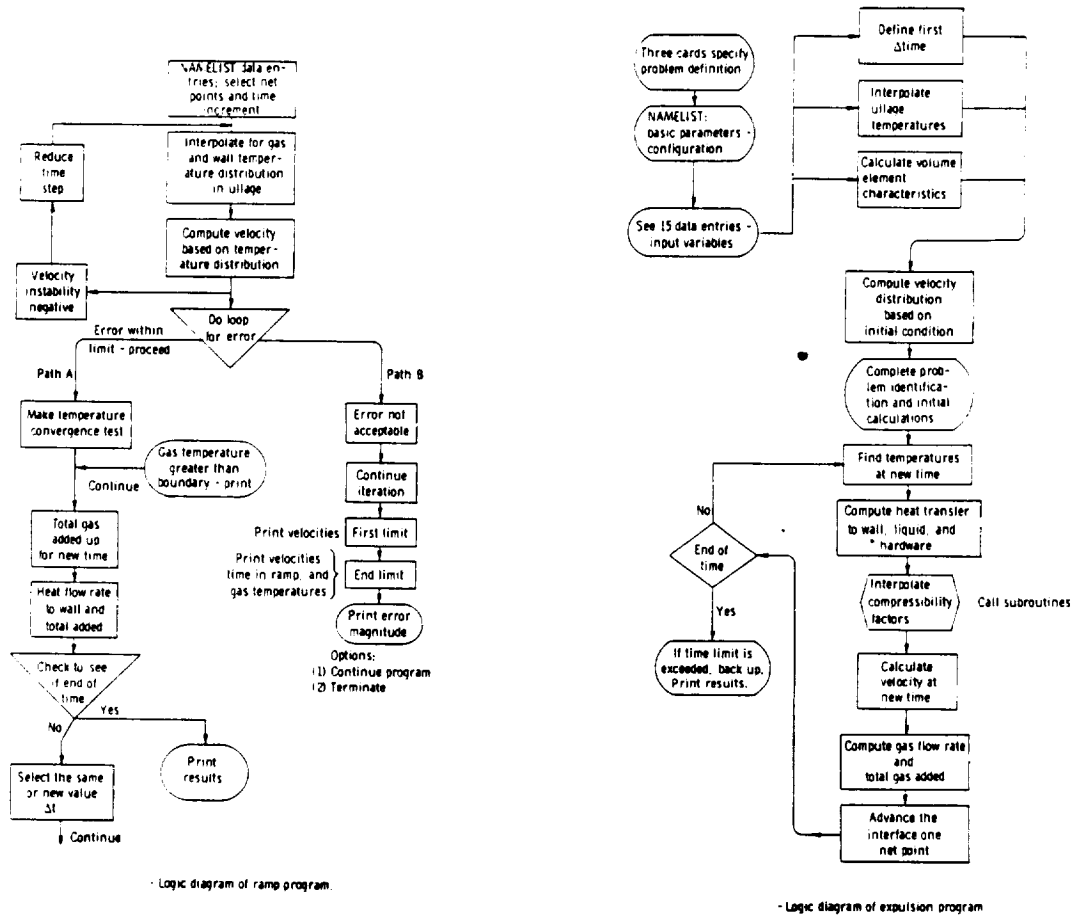


Figure 3.9: Logic diagrams of pressurization and expulsion process (Ref. 15).

PVC FOAM INSULATION

MASS DENSITY	50 kg/m ³
THERMAL EXPANSION COEFFICIENT	36 X 10 ⁻⁶ mm/mm-K
TEMPERATURE LIMIT	120°C
THERMAL CONDUCTIVITY :	
	W/m-K
20 K	0.2 X 10 ⁻²
72 K	1.2 X 10 ⁻²
300 K	3.5 X 10 ⁻²

Table 3.2: Physical Properties of External Foam Insulation

REFERENCES

- [1] Huzel, Dieter K. and Huang, David H., *Design of Liquid Propellant Rocket Engines*, NASA SP-125, 1971.
- [2] Richard, J.C. et al., "Transatmospheric Laser Propulsion of a 100MW-Class Lightcraft Technology Demonstrator," AIAA Paper 88-2970, 1988.
- [3] *Pressurization Systems for Liquid Rocket Engines*, NASA SP-8112, 1976.
- [4] Davis, Michael L. and Allgeier, Robert K., "The Development of Cryogenic Storage Systems for Space Flight," NASA SP-247, 1970.
- [5] Van Wylen, Gordon J. and Sonntag, Richard E., *Fundamentals of Classical Thermodynamics*, John Wiley and Sons, New York, 1985.
- [6] Ring, Elliot, editor, *Rocket Propellant and Pressurization Systems*, Prentice Hall, Englewood Cliffs, N.J., 1964.
- [7] Gleich, D., "Design Considerations and Structural Performance of Prestressed Composite Pressure Vessels," AIAA Paper 82-1230, 1982.

- [8] Gleich, D., "High Performance Positive Expulsion Tankage and Pressure Vessel Constructions," ASME Paper 78-WA / AERO-19, 1978.
- [9] Glaser, Peter A., et al., *Thermal Insulation Systems : A Survey*, NASA SP-5027, 1967.
- [10] McAuliffe, Patrick S., et al., "Development of a Reusable, Flight-Weight Cryogenic Foam Insulation System," AIAA Paper 1189-CP, 1986.
- [11] *International Thermodynamics Tables of the Fluid State: Helium - 4*, International Union of Pure and Applied Chemistry, Pergamon Press, New York, 1975.
- [12] *International Thermodynamics Tables of the Fluid State: Nitrogen*, International Union of Pure and Applied Chemistry, Pergamon Press, New York, 1977.
- [13] Nein, M.E., and Thompson, J.F., "Experimental and Analytical Studies of Cryogenic Propellant Tank Pressurant Requirements," NASA Technical Note, NASA TN D-3177, February, 1977.
- [14] Thompson, J.F., and Nein, M.E., "Prediction of Propellant Tank Pressurization Requirements by Dimensional Analysis," NASA Technical Note, NASA TN D-3451, June 1966.
- [15] Masters, Philip A., "Computer Programs for Pressurization (RAMP) and Pressurized Expulsion from a cryogenic Liquid Propellant Tank," NASA Technical Note, NASA TN D-7504, July, 1974.

Chapter 4

INJECTOR DESIGN: THE LASER HEATED ROCKET MODE

4.1 Introduction

The purpose of this chapter is to describe the basic components of four candidate LTD propellant injector arrays, with an emphasis on the fundamental injector design methodology. Essential features of the four proposed injector arrays are outlined; each configuration has particular advantages and disadvantages. An experimental testing program is needed to generate performance data and evolve the final injector configuration.

The function of the injector is to feed a controlled flow of propellant to the LTD thrust chamber during the repetitively-pulsed rocket propulsion mode. Liquid nitrogen propellant is supplied to a linear array of injector elements by a series of flow passages routed through the nickel shroud/strut "T-tail" structure. Streams of supercritical nitrogen rapidly vaporize as they expand out of numerous small orifices in the shroud lower surface, and arrive as a uniform flowfield at the laser beam focus. At the beginning of the laser pulse, laser-induced breakdown is triggered, whereupon the resulting plasma strongly absorbs the beam, creating a laser-supported detonation wave. The wave propagates through the N_2 gas and heats it to a very high temperature and pressure. After the laser pulse is terminated, the high pressure gas then expands against the shroud and afterbody mirror surface. Thrust is generated by converting the input laser thermal energy into exhaust kinetic energy. The parabolic afterbody mirror acts as a large area ratio "plug" nozzle to maximize the efficiency of this process, in part by giving the nitrogen gas sufficient time to cool between laser pulses. The nozzle is large enough that the exhaust gases can re-combine and again become transparent (i.e., to the next incoming laser pulse), and still exert force against the plug nozzle surface.

4.2 Underlying Technologies

The objective of a propellant injector is to enable high rocket engine performance and stable operation, without adversely affecting either the injector or thrust surface durability. In a conventional chemical rocket engine, injector design specifications must encompass the entire flow system geometry, including the injector element pattern or "array," individual orifice geometry, and flow distribution system upstream of the orifice (i.e., manifold) [1]. The LTD injector design attempts to exploit the large data base of knowledge accumulated by rocket designers; however, several underlying technologies specific to pulsed laser propulsion must be considered. An operational injector design for the LTD will require research in the following areas:

1. Propellant Technology: For a given propellant, the physical/chemical processes that occur during injection, kinetics of stream breakup and mixing, vaporization and heat transfer must be clearly understood. The goal for the LTD is to optimize laser energy absorption by the propellant; chemical combustion processes are not relevant.
2. Pulsed Flow Control: A repetitively-pulsed engine will require high frequency acoustic valving technology. This implies a strong coupling between propellant injection flow dynamics and the impulsive thrust generation environment. In conventional liquid rockets, similar "coupling" effects can lead to low frequency combustion instability (chugging), and are strenuously avoided [2]. A successful rocket design must eliminate all such dangerous instabilities.
3. Structures Concepts: The shroud structure contains the injector array and manifolds. Since the shroud is essentially a thin annular airfoil, its narrow cross section imposes certain volumetric restrictions on the injector/manifold design. Advanced manufacturing techniques such as platelet technology and diffusion bonding [3,4] offer promising solutions to the LTD's structural design constraints.
4. Laser Optics: Injected propellant mass flux must be delivered with high precision to the primary mirror focal region. The injector array can simultaneously serve as a secondary optic to provide further focusing of the incident laser radiation. Alignment of the secondary optics can, of course, influence laser energy absorption into the propellant.

The LTD injector designer must combine conventional liquid chemical rocket technology with unconventional laser propulsion requirements, to produce practical solutions that exploit the unique repetitively-pulsed engine operating environment.

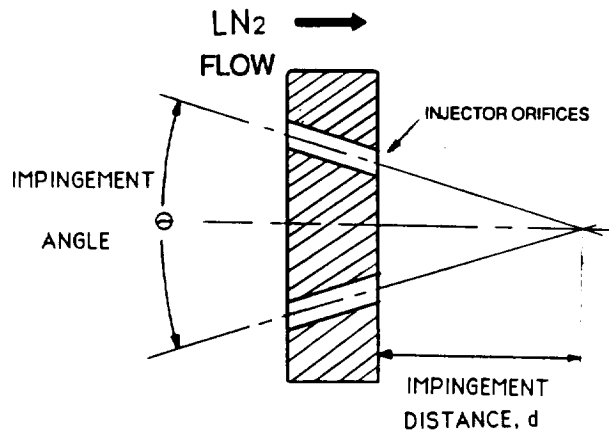


Figure 4.1: Side view of like-impinging doublet injector element.

4.3 The Injector Array

For optimum gas-phase absorption of incident laser energy, it is necessary to first atomize the propellant; the great increase in liquid surface area accelerates vaporization. Atomization involves the breakup of liquid jets and/or sheets into droplets. By directing two or more streams of propellant to impinge upon each other, droplet and gas bubble formation occurs (see Fig. 4.1). For the LTD, the atomized propellant vaporizes very quickly upon exiting the injector array; the LN_2 will be heated above critical temperature and flash into a gaseous phase as the pressure drops below critical.

4.4 Injector Element Design

To design the injector element pattern, one must select the injection element (i.e., doublet-impinging, triplet-impinging, etc.), and element distribution (i.e., the complete annular injector array) across the lower shroud surface. Since the LTD is a 'monopropellant' rocket system, the injector elements are termed 'like-impinging'. The choice of injector element type is influenced by the desired mass flux contours. Figure 4.2 shows typical mass flux contours for a like-impinging doublet element [1].

These injector elements should be distributed across the lower LTD shroud surface so as to insure the delivery of a uniform propellant mass flux at the laser optic focal region, a narrow (1 cm wide) circular strip above the lower shroud surface (Fig. 4.3).

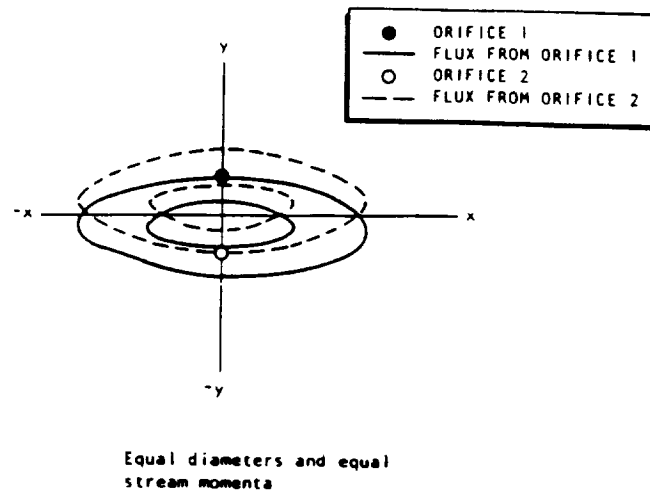


Figure 4.2: Mass flux contour for doublet injector element (Ref. 1).

Therefore it makes sense to place a single-file row of elements (i.e., strip injector) at some position near the primary mirror focus. Element orientation can be either 'in-line' edge touching, or 'parallel-overlapping' opposed doublet (see Fig. 4.4). The position of one element with respect to the others should provide for maximum inter-element mixing and uniform mass distribution [1].

4.5 Injector Orifice Design

Options in the design of injector element orifices include the geometric shape, orifice dimensions and the impingement angle between opposing jets of injected propellant (see Fig. 4.1). The impingement angle determines the position where stream mixup and droplet formation occurs above the injector surface. The most common impingement angle is 60° . At impingement angles greater than 60° , propellant backsplash onto the injector face increases surface heat flux, resulting in injector face burnout [5].

The diameter of the orifice directly affects mixing and atomization levels produced by an injector element. Smaller orifices have higher performance than larger orifices, because the smaller droplet size results in increased vaporization rates. Impingement distance is another factor influenced by orifice diameter. A performance parameter often used is the ratio of free stream length, L_{st} , divided by orifice diameter, D_{or} . Values of L_{st}/D_{or} from 5 to 7 are good. Larger values tend to produce misimpingement of streams, because instabilities within a free jet are able to cause directional

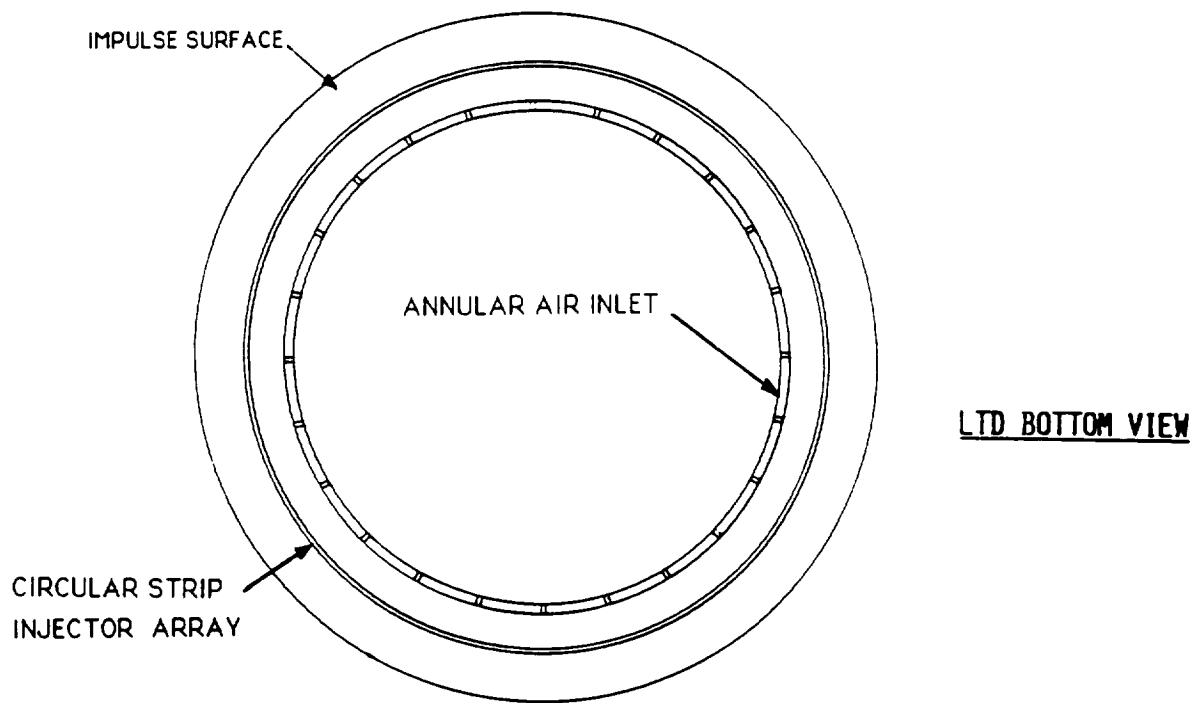


Figure 4.3: Bottom view of LTD showing location of injector array.

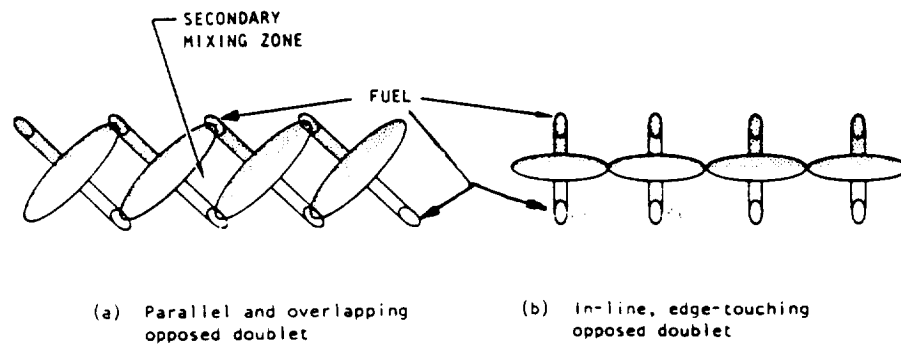


Figure 4.4: Element orientation options for LTD injector array (Ref. 1).

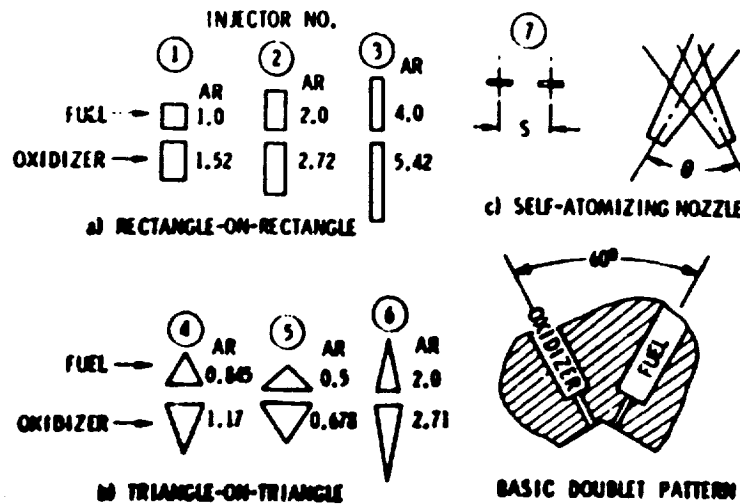


Figure 4.5: Unconventional orifice shapes improve mixing performance.

wandering [1].

Flashing injection is another process which may find application in the LTD rocket engine. In this process the propellant is expanded through an injector orifice until the supersaturated state is reached, whereupon a portion of the fluid flashes into vapor [11]. This is a well-known method for improving atomization properties, i.e., reducing droplet sizes and spray penetration, and increasing the rate of spray spread. Several methods have been used to promote flashing injection, depending on the nature of the injected liquid. Further evaluation of this concept for use in the LTD engine is necessary.

The circular orifice shape has historically been the standard for most injector designs because passageways were drilled. With the advent of platelet technology (see chapter two), rectangular orifice shapes are now possible (Fig. 4.5). Experiments with rectangular passages have shown a measurable increase in mixing performance over the circular geometry [6].

4.6 Injector Manifold Design

In the LTD, LN_2 propellant flows upward through the primary mirror coolant passages to the annular manifold at the top. From here the LN_2 enters the T-tail support struts by means of a two-way valve. As mentioned earlier, the twenty four T-tail support struts combine to form the forward half of the shroud structure. Each T-tail strut has its own two-way valve, which initially is set for the airbreathing mode, then later

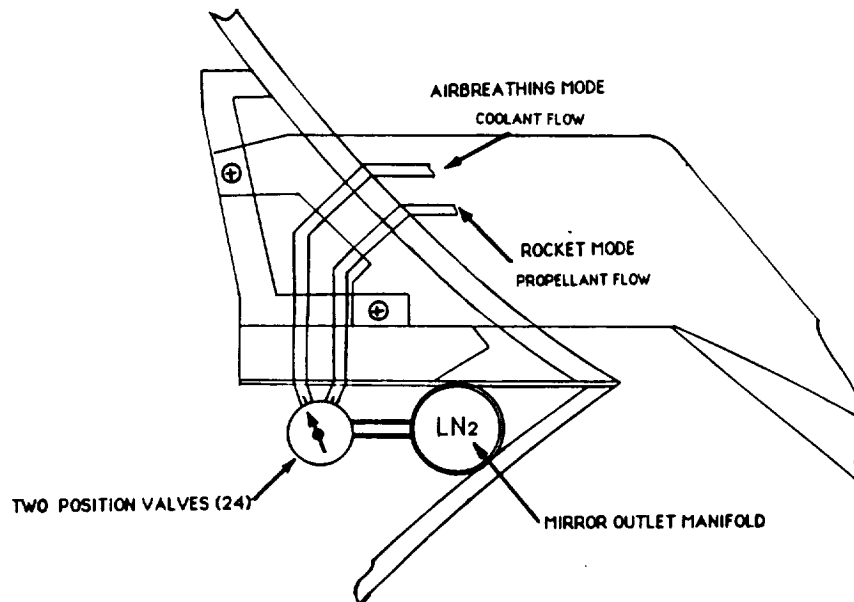


Figure 4.6: Two-way valves control propellant flow to each T-tail strut assembly.

switches to the rocket mode position. In the airbreathing mode, it will feed LN₂ to the T-tail leading edges and shroud impulse surface for transpiration cooling and film cooling, respectively. At the start of the rocket mode, it then switches the flow to the rocket injector array. The twenty four two-way valves must be 100% reliable during operation (see Fig. 4.6).

Within each T-tail strut, LN₂ propellant must be uniformly distributed to the individual injector orifices by way of a mini-manifold (see Fig. 4.7). This injector manifold is sized to deliver a specific propellant flow rate through a minimum cross sectional flow area while incurring a small pressure loss. The total pressure losses suffered by the flow from the propellant tank to the orifice exit must be minimized; otherwise substantial weight penalties will result for the pressurized propellant tank. Within each T-tail strut manifold system, a central 'downcomer' will feed propellant to a distribution ring (Fig. 4.8), which contains ports designed to reduce static pressure variations in the flow region immediately behind the injector face [1]. Finally, prior to entering each injector, the flow is put through an ultra-fine mesh filter (also constructed with platelet technology).

4.7 Film Cooling for the Shroud Surface

The lower surface of the shroud fulfills three functions: impulsive thrust surface, injector face, and (optional) secondary optic surface. The surface will be subjected

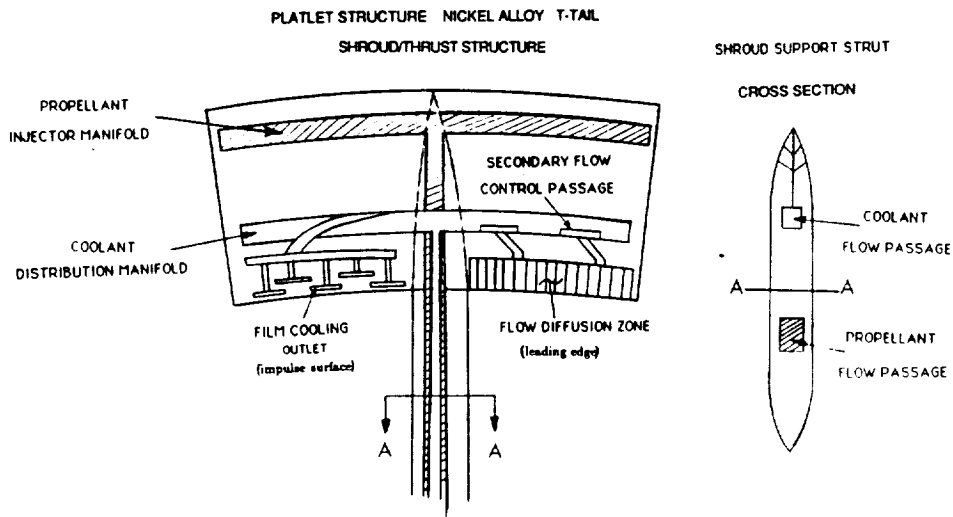


Figure 4.7: Typical platelet flow metering and distribution schematic for a T-tail strut assembly.

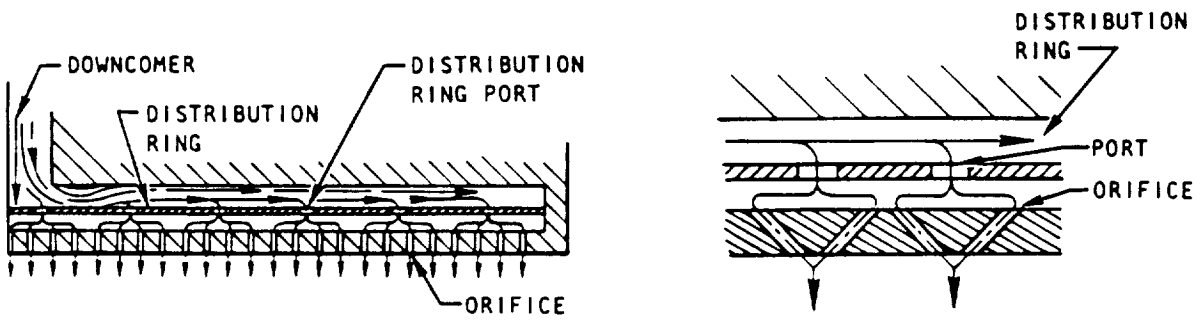


Figure 4.8: Injector face and manifold design details (Ref. 1).

to direct ablation and erosion by the pulsed laser beam and resultant high temperature/pressure blast waves (i.e., exhaust gases). The surface will also sustain large pulsed mechanical loads and severe thermally-induced mechanical stresses. Temperatures within the laser induced blast waves can reach 10,000 K. Reduction of adverse thermal effects is readily accomplished by regenerative and film cooling methods [7].

Auxiliary film cooling for the lower shroud surface is accomplished by injecting a portion of the propellant to flow along the external surface and act as a buffer region against the high temperature exhaust gases (Fig. 4.9). These film injection sites will be placed near the shroud leading edge; they are completely independent of the main injector array. The film coolant layer thus absorbs and carries away a portion of the radiant energy transmitted to the shroud walls. Injected as a supercritical liquid, the film rapidly flashes to a gas state. The gas film temperature will rise largely as a result of convective heat transfer with the shroud wall. A thermal balance will be attained between the radiant heat input rate and coolant temperature rise. Once this equilibrium condition is reached, no further heat transfer occurs, and the shroud is maintained within structural-temperature limits [5]. The shroud and injector array material temperatures will be substantially lower than those in the laser-induced blast wave.

Temperatures on the lower shroud surface will increase in the downstream direction, as a function of the flow distance from the film injection site. The forward half of the shroud ("T-tail" strut assembly) will be metallic and have a lower temperature limit; the aft half of the shroud will be carbon-carbon composite, with a very high limit.

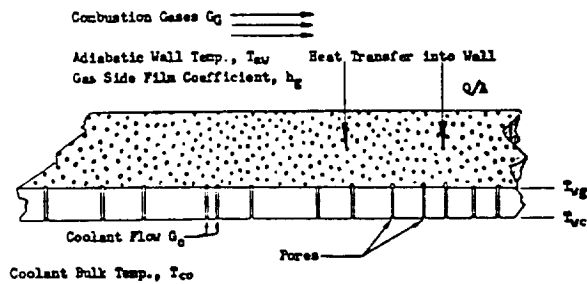
4.8 Transpiration Cooling of Leading Edges

Again using platelet technology, transpiration cooling ports are formed into the shroud/strut leading edges, as shown in Figure 4.7. This sacrificial coolant counteracts aerodynamic heating at the air inlet stagnation regions during hypersonic flight speeds. Incidentally, transpiration cooling is also planned for the scramjet fuel spray bars on the X-30 NASP.

4.9 Pulsed Flow Control

To achieve efficient LN_2 mass utilization high frequency valving of the propellant is required [8]. These valves must operate at frequencies of 1000 Hz or greater, with closing and opening times of 10^{-4} sec. Specially engineered propellant orifice arrays are known to interact with the pulsed rocket engine chamber environment in a self-regulating manner. In this "acoustic-valving" process, pressure fluctuations at the

Transpiration cooling model.



Film-cooling model.

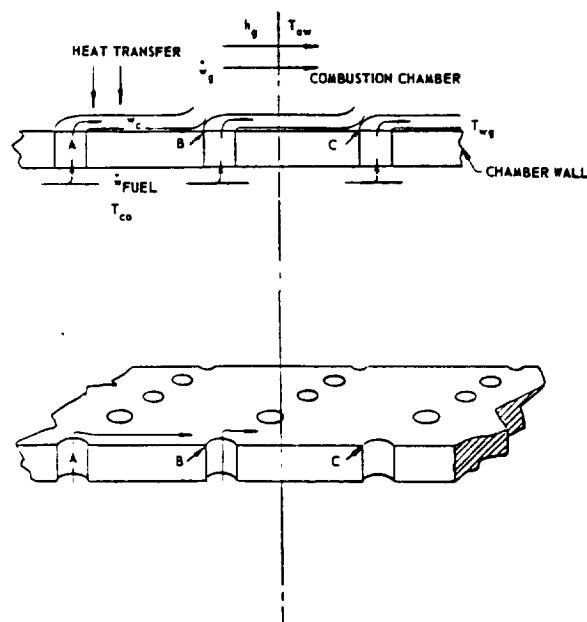


Figure 4.9: Proposed models for active cooling.

injector orifice exits serve to start and stop the propellant flow, thereby metering the desired propellant mass [9,10].

The propulsion sequence for a repetitively-pulsed laser powered thruster is comprised of four steps:

1. Cold propellant is injected into the laser beam focus.
2. Laser pulse electrical breakdown in the propellant ignites a Laser Supported Detonation wave (LSD wave) which produces high temperature plasma and throws off a strong blast wave.
3. Shocked exhaust gas expands (generating thrust) and shuts off propellant flow, because of the high over-pressures (up to 600 atm).
4. Blast wave pressure decays to a low level at the orifice exit while the exhaust flow expands across the large plug nozzle; the propellant flow then resumes in preparation for arrival of the next laser pulse.

The sequence then repeats. Propellant consumption is controlled by the peak injector mass flow rate, blast wave characteristics and laser pulse repetition rate.

An important parameter in the design of self-regulating valves is the propellant jet velocity, as it emerges from each orifice. This jet velocity is determined by orifice geometry and injector operating pressure. Sufficient propellant mass must leave the injector face to arrive at the laser focal region in the short time between blast wave decay and the arrival of the next laser pulse. This time interval during which propellant will flow is governed by the blast wave decay time, 'setback' distance between the injector face and the the primary mirror focus, and the laser pulse repetition frequency. The decay of blast wave pressure to sea level pressure can be as fast as 10^{-4} seconds.

Several questions arise as to the degree of propellant flow stability and uniformity that will result from acoustic-valving. Unstable oscillations of propellant flow (and resultant thrust), could cause destructive vibrations in the LTD shroud structure. Another design issue is exactly what critical pressure differential will stop the flow of injected propellant, without causing flow reversal inside the injector. Clearly, analytical models must be developed to predict pulsed flow control dynamics, and experiments are needed to validate how each design parameter affects overall engine performance.

4.10 Injector Design Alternatives for the LTD

As mentioned earlier, the LTD rocket engine needs an injector array to supply liquid propellant into the thrust chamber; four different injector schemes were identified. The rocket engine's initial impulse surface (i.e, the lower surface of the shroud) was

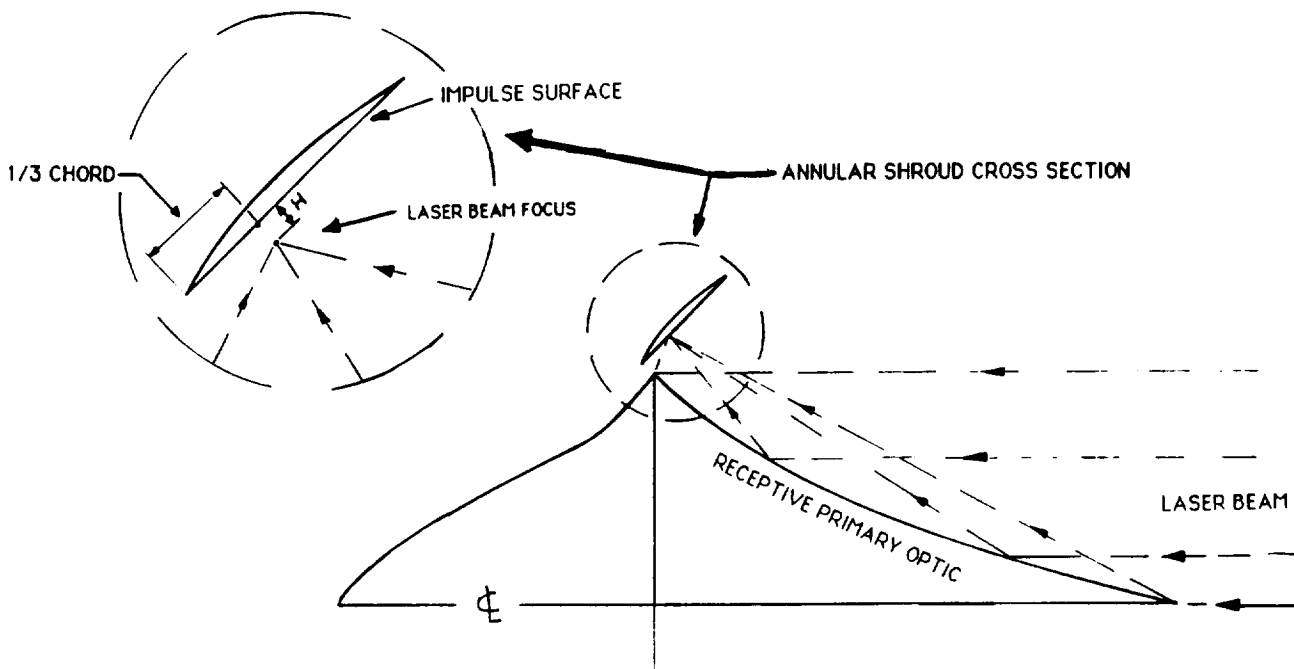


Figure 4.10: Side (cross sectional) view of Shroud/Injector assembly, Design No. 1.

recognized as the proper place for a circular-strip injector array. The analytical propulsion system model dictated the position of the injector array at the 1/3 chord point, measured aft from the shroud leading edge. The first design variable to be revealed in this injector scheme was the height, H , of the laser beam focus above the shroud's impulse surface (see Fig. 4.10).

Design No. 1 consists of a 'flat-plate' impulse surface tilted at 45° to the vehicle centerline, with the P.O. annular focus positioned at the 1/3 chord point and lying exactly on the lower shroud surface ($H = 0$). This initial configuration contained no provision for injectors or active cooling of the hot structures. The central motivation for this early design was to illustrate the interdependence between primary optic and shroud geometry.

A Super Ignitor Array (SIA) concept successfully tested at LLNL (ref. 10) provided insight for injector design No. 2 (see Fig. 4.11). This design integrates an injector array into a honeycomb-patterned, one centimeter wide annular secondary optic (S.O.), whose function is to provide final focusing of the incident laser energy to intensities high enough to initiate air breakdown and plasma formation. The face of this super ignitor array will experience extremely high pressures and temperatures during operation. There exists the possibility that unwanted plasma formation may occur along the many sharp edges of the dimpled surface. The structural cooling requirements may tax the limits of the LTD propellant management system. The

geometry of the P.O. and laser beam structure may also distribute the incident laser energy in an unsymmetric manner across the surface of the SIA, thereby complicating cooling requirements. Generally, the injector array and secondary optics are pointed directly into the focused laser beam.

Design No. 3 completely separates functions performed by the secondary optics and the injector array (see Fig. 4.12), by physically removing the injector orifices to a distance 'd', away from the laser focus (i.e., site of the cylindrical blast wave center). Note that the 1 cm wide, flat plate S.O. is inclined at an angle of 20° to the shroud impulse surface and that the sharply focused laser beam reflects off the S.O. to focus roughly 1/2 cm above this surface. The orifice exit pressure will be elevated above propellant critical pressure to insure that a single phase supercritical fluid flows throughout the LN₂ feed system. For a given injector pressure, the value for 'd' may be obtained from Sedov's scaling law which relates the blast wave pressure versus radius:

$$P = \left(\frac{r_{ref}}{r} \right)^2 P_{ref} \quad (4.1)$$

A plot of equation 4.1 is given in Figure 4.13. The results are based on the following conditions, which represent typical operating values during the rocket mode:

altitude	=	30 km
speed	=	Mach 5
r_{ref}	=	0.5 cm
P_{ref}	=	500 atm

By moving the injector array away from the region of high blast wave pressures, injector orifice pressures effective for pulsed flow control can be lowered to levels conventionally used in pressurized propellant tank systems. By varying the distance 'd', the optimum acoustic-valving effect can be obtained. The annular S.O. is aligned to an angle of 25° with the vehicle centerline; a ray trace from the .707 m beam diameter (on the P.O.) is normal to this S.O. surface (see Fig. 4.14). Assuming a 'top-hat' beam intensity distribution exactly aligned with the vehicle central axis, laser energy will be uniformly focused upon this S.O. surface. Design No. 3 still faces the potential pitfall of high radiation heat transfer to the S.O. surface.

Design No. 4 removes the final focusing function of the secondary optic until after the beam has passed through the focus (see Fig. 4.15). The final P.O. focus lies in the plane of the lower shroud surface, as in design No. 1. Hence, the S.O. serves only to reflect that portion of the laser radiation, which passes completely through the line-breakdown region unabsorbed, back into the P.O. focus. Radiation heat transfer to the S.O. should be significantly reduced from the other designs.

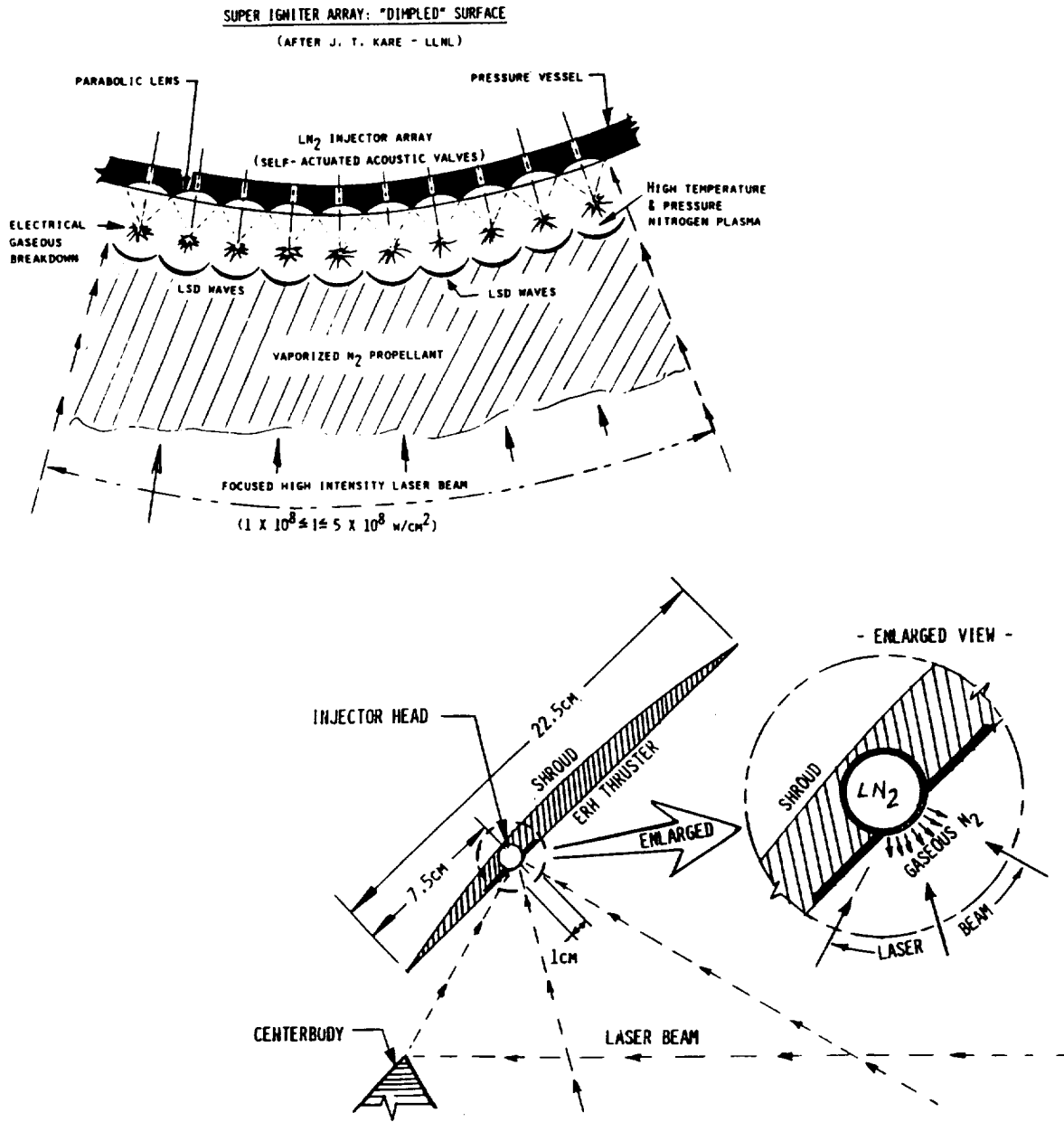


Figure 4.11: Shroud/Injector assembly, Design No. 2.

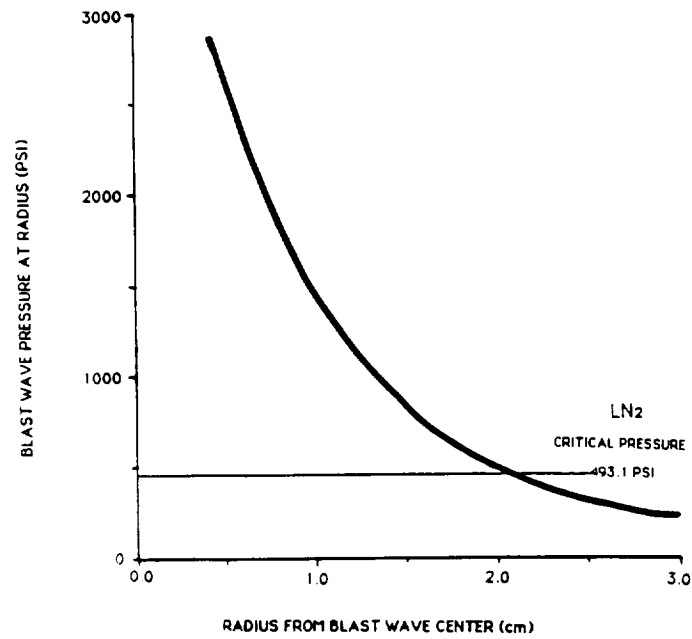


Figure 4.12: Blast wave pressure versus radius from blast wave center.

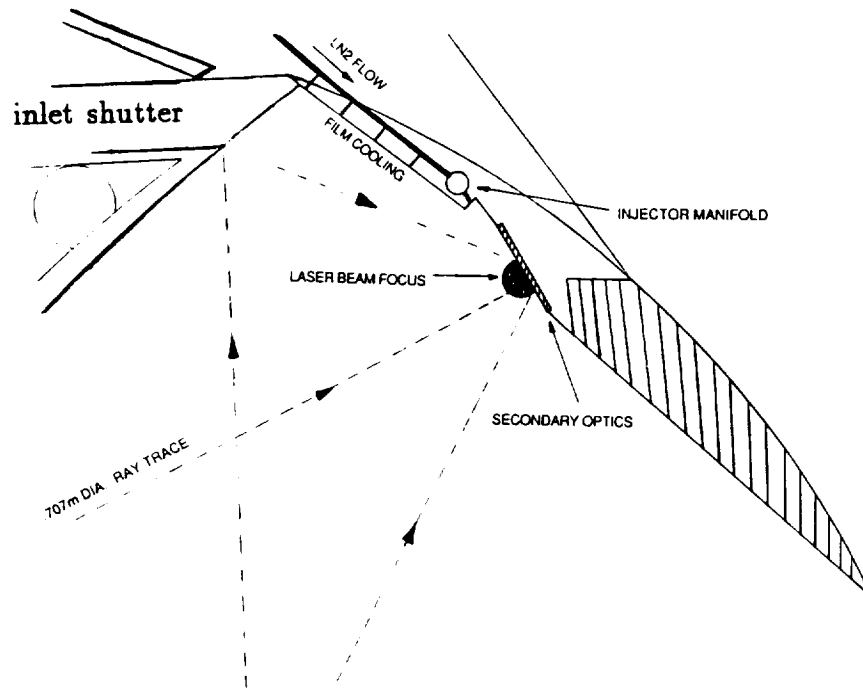


Figure 4.13: Shroud/Injector assembly, Design No. 3.

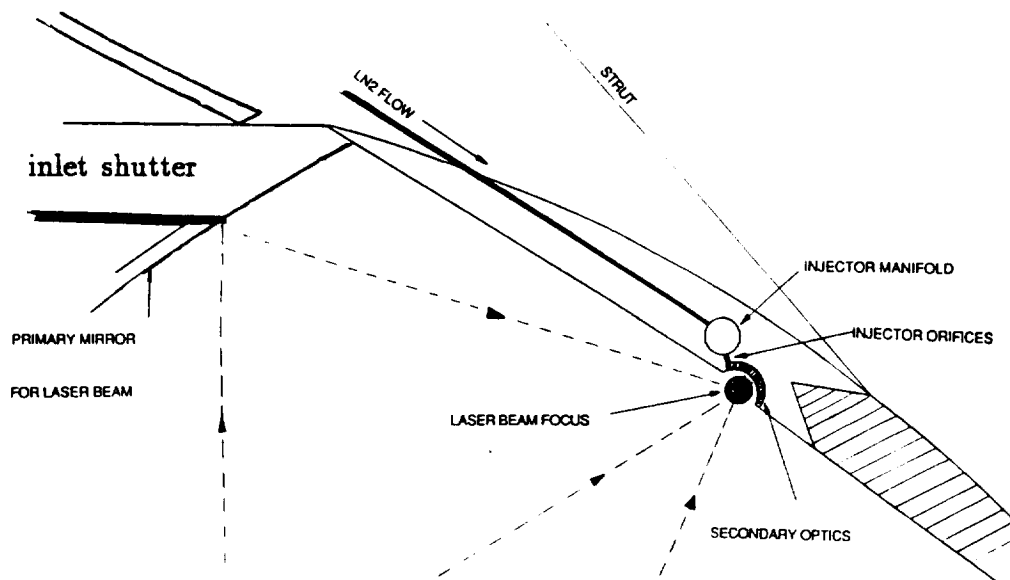


Figure 4.14: Shroud/Injector assembly, Design No. 4.

4.11 Conclusions

An examination of injector design fundamentals as they relate to laser propulsion has enabled identification of critical technology issues facing the LTD shroud/injector assembly. The next step is to develop a detailed analytical injector model that integrates propellant system design parameters with the vehicle configuration and laser-propulsive physics.

An important issue that must be examined in this modeling effort is the integrated LN_2 propellant mass per laser pulse as it relates to engine PRF, thrust duration, and total propellant consumed in the rocket mode; the latter must match the laser-heated rocket specific impulse projections. A detailed analysis of the LN_2 mass flow rate versus blast wave pressure over time is needed. Another critical issue is the injected stream impingement site: should it be coincident with the laser beam focus, or perhaps at some shorter distance, to insure that a wide-angle, vaporized spray arrives at the focus.

Satisfactory performance for the shroud/injector assembly requires a high degree of reliability, propellant flow stability, and compatibility with the pulsed laser-heating dynamics. Although analytical performance projections will aid in the development process, a rigorous experimental verification program is mandatory. Finally, with the advent of advanced fabrication techniques (i.e., platelet structures and diffusion

bonding), and high temperature materials, unconventional injector designs for laser propulsion engines might be manufactured with relative ease.

REFERENCES

1. *Liquid Rocket Engine Injectors*, NASA SP-8089, March, 1979.
2. *Liquid Propellant Rocket Combustion Instability*, NASA SP-194, 1972.
3. Kahl, R.C. and LaBotz, R.J., "Platelet Injectors for Space Shuttle Orbit Maneuvering Engine," AIAA Paper 74-1108, October 1974.
4. Knight, R.M. and Gurnitz, R.N., "Advanced Solid-State Diffusion Bonded Injectors," AIAA Paper 70-639, June 1970.
5. Huzel, D.K. and Huang, D.H., *Design of Liquid Propellant Rocket Engines*, NASA SP-125, 1971.
6. McHale, R.M., et al., "Injector Design using Noncircular Orifice Geometry," *Journal of Spacecraft and Rockets*, Vol. 8, April 1971, p. 408-410.
7. Brunner, M.J., "Active Cooling Heat Protection," *Journal of Spacecraft and Rockets*, Vol. 6, June 1969, p.661-666.
8. Rosen, D.I, Pirri, A.N., Weiss, R.F., and Kemp, N.H., "Repetitively Pulsed Laser Propulsion: Needed Research," *Physical Sciences, Inc.*, Woburn Mass., 1982.
9. Simons, G.A. and Pirri, A.N., "The Fluid Mechanics of Pulsed Laser Propulsion," *AIAA Journal*, Vol. 15, June 1977, p.835-842.
10. Kare, J.T., "Dimpled Surface for Laser Coupling to Air," *SDIO Laser Propulsion Workshop*, Lawrence Livermore National Laboratory, October 1988.
11. Solomon, A.S.P., et al., "Atomization and Combustion Properties of Flashing Injectors," AIAA Paper 82-0300, AIAA 20th Aerospace Sciences Meeting, January, 1982.

Chapter 5

FINITE ELEMENT MODELING AND ANALYSIS

5.1 Introduction

Finite Element Analysis techniques were used to evaluate the annular shroud and support strut design proposed for the Lightcraft Technology Demonstrator. Both static and dynamic analysis were implemented to extract the stress and modal behavior. Pulsed airbreathing or rocket engines must avoid the natural frequencies of the vehicle structure, or catastrophic failure of the system will result.

During previous research efforts, analysis of a similar annular shroud (i.e., for the Apollo Lightcraft) has been accomplished using a highly simplified analytical approach to determining shroud natural frequencies. Although beneficial in determining 'ballpark' concepts of shroud dynamics, the previous analysis simply does not provide sufficient useful information.

However, by utilizing available computer based 3-D Finite Element Analysis tools, a much more accurate natural frequency analysis was obtained. In addition to its much greater accuracy, the Finite Element Modeling output facility allows for the animated viewing of mode shapes, as well as providing numerical values for solutions. This allows the designer to evaluate which components are dominating the model characteristics, and to redesign accordingly.

5.2 Finite Element Modeling/Analysis Package

The Finite Element Modeling (FEM) and Finite Element Analysis (FEA) package is a design and analysis tool that has recently become practical for use by the engineer/designer. It is a computer software package that allows static and dynamic (i.e. stress and vibrational) analysis of structures, as affected by operating conditions, including physical and thermal loads, boundary constraints, geometry, and material

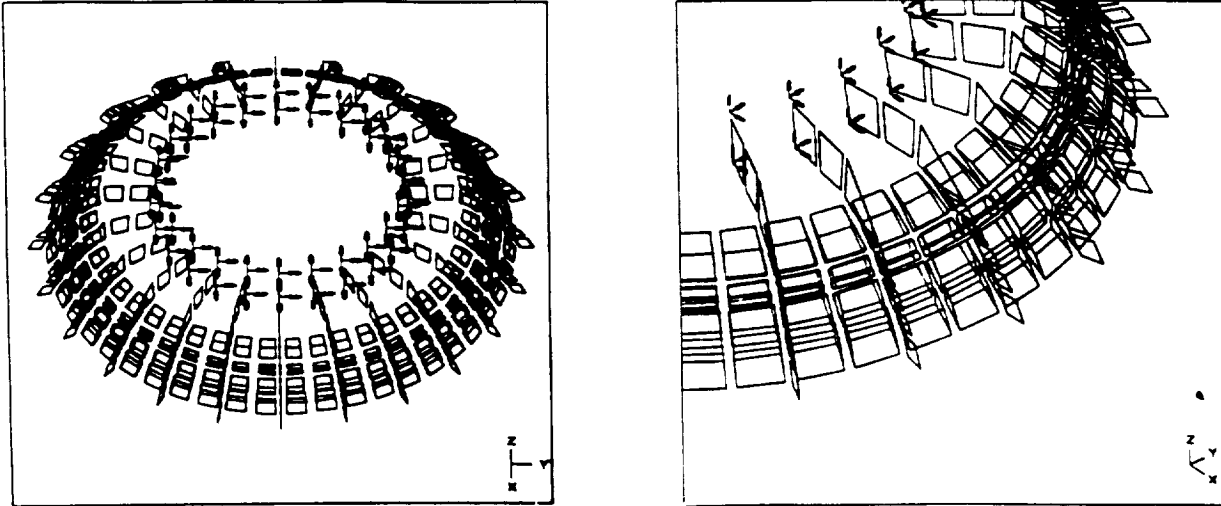


Figure 5.1: Finite element model of the Shroud and its support structure.

properties. Specific structures can be analyzed for stresses, deflections, and natural frequencies of vibration. This package is a powerful tool for analysis of existing designs, as well as testing of conceptual designs: it can reveal problem areas without necessitating creation of physical models or prototypes.

The FEM package implemented for the LTD shroud mechanical analysis was the IBM Computer Assisted Engineering Design System (CAEDSTM), presently running on Rensselaer Polytechnic Institute's IBM 4341 computing facility.

It was determined that a full three-dimensional Finite Element Model of the shroud and its 24 support struts would be the most accurate and efficient finite element model for this analysis (see Fig. 5.1). The shroud was modeled by solid linear brick elements; thin shell elements of varying thickness were used to model the tapered struts.

Due to computer limitations, it was necessary to use an interactive analysis process, starting with the global modes for the shroud and strut system. Then, to extract more detailed information about the modal behavior of the struts themselves, a single section (1/24th of the shroud structure) was examined. This allowed a much more dense finite element mesh with higher-order parabolics to be applied to the strut structure, thus yielding a more accurate and complete analysis of strut behavior.

Two different analyses were performed on the "single" sections. One included the entire section of the shroud and its associated strut (see Fig. 5.2). This second

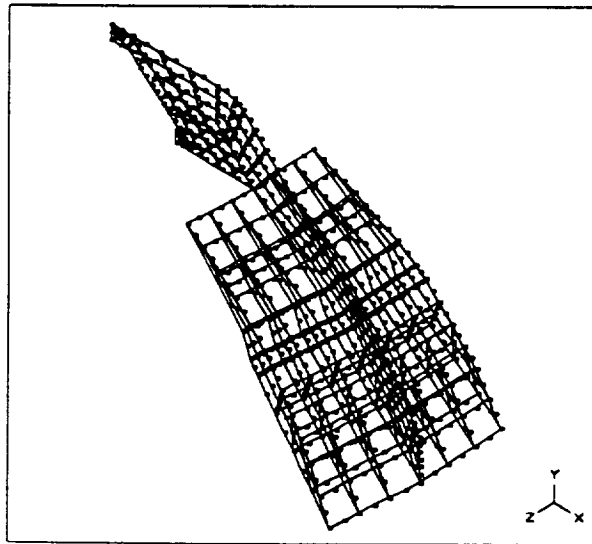


Figure 5.2: T-tail Shroud/Strut assembly including carbon-carbon lower half ("entire" section).

analysis removed the trailing edge of the shroud, which would be made of carbon-carbon composites (see Fig. 5.3). The reasons for considering the second case is that the strut and leading edge of the shroud structure will be manufactured as 24 individual sections; however, the carbon-carbon trailing edge will be a continuous ring. Thus, the leading edge of the shroud and its associated strut sections can be considered a single structure. It is important to note that the smallest single structure will exhibit the highest modal frequencies; hence, it could become the critical case at comparatively high engine frequencies.

The finite element models of the struts and shroud leading edge were given the properties of Nickel-200; the trailing edge was assigned the properties of carbon-carbon composite material. These material properties include density, Elastic modulus, and Poisson's ratio. The struts are considered fixed at their internal vehicle mounts (i.e., the inside edge for the global analysis; see Fig. 5.4), and at the mounting holes for the strut section analysis.

5.3 Advantages/Disadvantages of the 3-D Model

The three dimensional FEM has many advantages, and several disadvantages. The most significant disadvantages are:

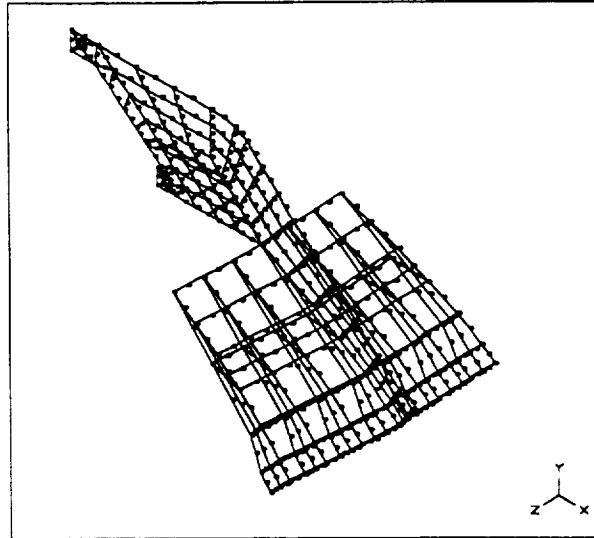


Figure 5.3: T-tail Shroud/Strut assembly less carbon-carbon ring lower half (“cutoff” section).

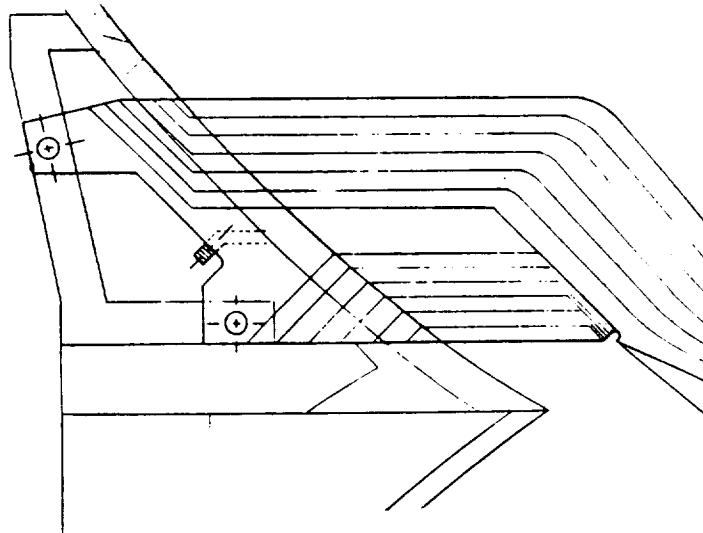


Figure 5.4: Strut mounting detail.

1. Time consuming - the 3-D modeling process takes an extreme amount of time to implement. For example, the finite element analysis of the Space Shuttle's main fuel pump took twelve man-years to complete.
2. Computer Costs - much numerical computation is needed to reduce the three dimensional stress matrices. CPU time required for the shroud analysis was 37 minutes. This translates to a cost around \$70.00; it is not uncommon to see several thousand dollar runs for complex 3-D models.

while the most significant advantages are:

1. Very accurate — the 3-D analysis allows for up to six degrees of freedom for each structure node; 2-D models allow for only three degrees. Therefore the actual behavior of the structure at the node points is much more closely represented.
2. Excellent Analysis Output Capabilities — the 3-D CAEDSTM System model has high powered output capabilities, including graphic and numerical displays of deflections, stress concentration, and mode shapes. This permits the engineer or designer to more fully understand the true behavior of the structure.
3. Modifiable — once the 3-D model has been created, it can be modified to study the effects of design changes. It is possible to change material properties, structure geometry, and operating conditions such as external loading and accelerations. This gives the designer great freedom to test different theories or ideas without having to build a new model each time.

From the above it should be clear that the advantages of the 3-D model far outweigh the disadvantages; it was the correct choice for the LTD shroud stress and vibrational analysis.

5.4 Results

5.4.1 Volumes and Masses

The detailed section modeling also enabled a very accurate measure of volumes and masses for the various LTD structural components. The initial dynamic analysis assumed completely solid elements and thus had component masses which were considerably higher than the design limits (see Table 5.1). However, the static analysis of the strut-shroud section (discussed subsequently) revealed very low stresses in the shroud structure, as compared with the strut. Consequently, the shroud will utilize a semi-hollow structure which will permit the design mass limits to be reached.

COMPONENT	VOLUME (cm ³)	SOLID MASS (kg)	DESIGN LIMIT (kg)
STRUTS	1,964	15.8	16.0
LEADING EDGE	6,074	48.9	10.0
TRAILING EDGE	7,877	14.3	7.0

Table 5.1: Volumes and Masses for Shroud Structure.

5.4.2 Global Analysis

The global analysis involved the implementation of a 3-D linear solid finite element model for the entire shroud-strut structure; from this, the first 10 natural modes of global vibration were extracted. Results included both numeric data for the modal frequencies and graphic depictions of the various mode shapes.

The numerical results are presented in Table 5.4. Note that the frequencies for modes 2, 3, 4 and 5, as well as 6 and 7, (respectively) are identical. This phenomenon is principally due to the orthogonal, or coupled modes. Note in Table 5.4 that the structural component (shroud or support) is the primary oscillator for a given mode. Figure 5.5 presents plots of the various mode shapes (deformations are exaggerated). Only the lower numbered mode is included for each coupled mode, since the orthogonal mode is identical in shape to its counterpart.

5.4.3 Local Modes

The first fifteen natural vibration modes were extracted for both the “entire” section and “cutoff” section finite element models. The natural frequencies of the “cutoff” section structure are considered the critical frequencies to be compared against engine pulse repetition frequency (PRF); the “entire” section model was considered primarily

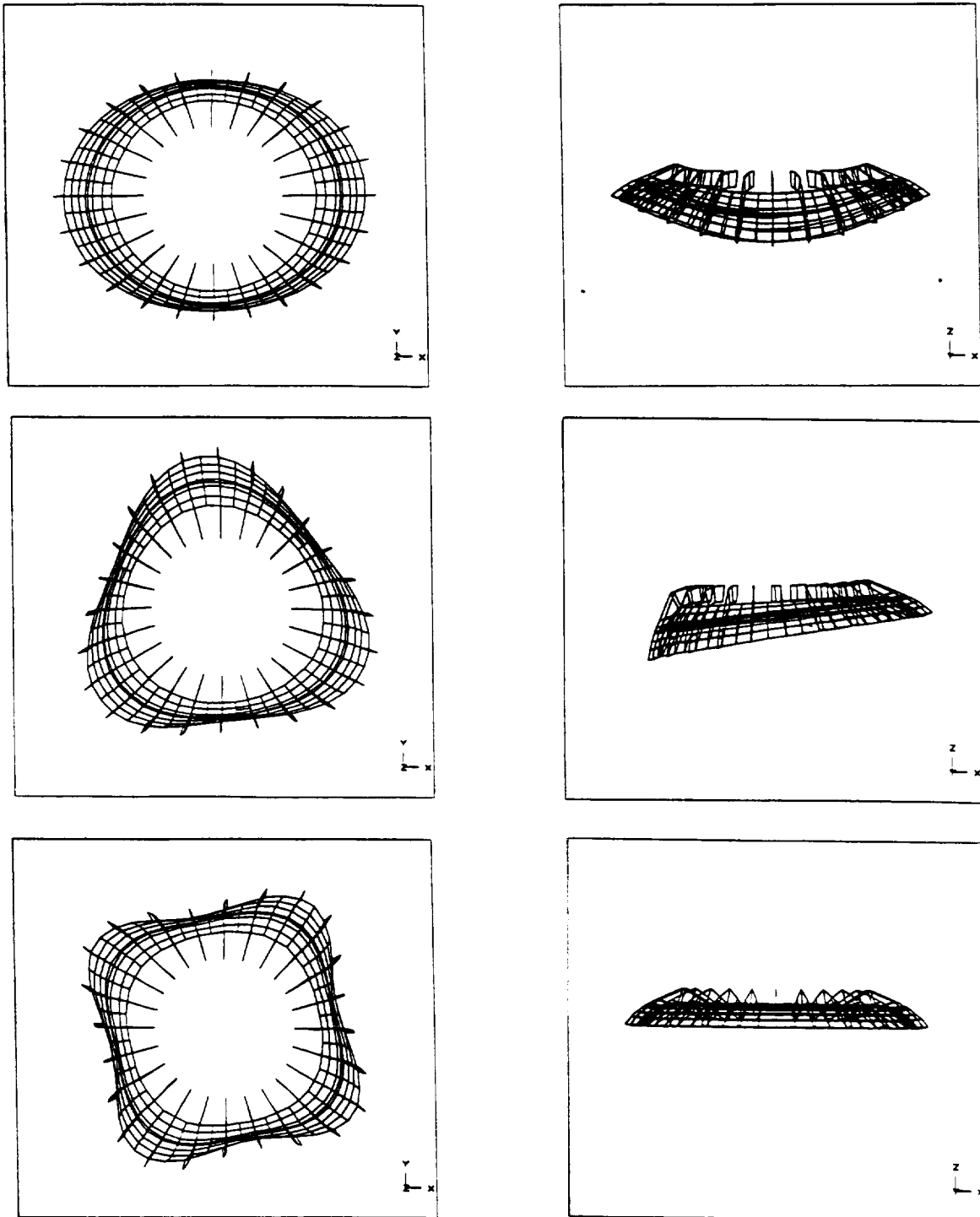


Figure 5.5: Various mode shapes for the entire LTD shroud (deformations are exaggerated).

MODE No.	COMPONENT	FREQUENCY (Hz)
1	STRUT	3.0
2 - 3	STRUT	14.8
4 - 5	SHROUD	15.1
6 - 7	SHROUD	20.7
8	STRUT	34.0
9 - 10	SHROUD	34.5

Table 5.2: Modal Data for the Shroud Global Analysis.

to obtain its qualitative behavior.

The modal frequency change from the entire section model to the cutoff version was found to be insignificant; i.e., by less than a factor of 1.5. The resulting frequencies of the first 15 modes of vibration are presented in Table 5.3.

Again, the component column refers to the structural element which is found to demonstrate the most pronounced oscillatory behavior for the given mode shape. The “solid” model and “hollow” model results in Table 5.5 refer to the solidity options for the shroud leading and trailing edges. To approximate the hollow shroud option, the densities of the shroud elements were just reduced to bring their masses within design limits (i.e., the design goal in Table 5.1).

5.4.4 Overview of Results

The first measure of accuracy for an analysis is whether the output makes intuitive sense. For the shroud vibrational analysis, both the numerical and graphical data appear reasonable, and relatively predictable. When evaluating finite element analysis, the primary concern is the graphical output. A major source of error in finite element analysis is improper geometry definition, which is easily identified by observing the graphic output. No such improper geometry was found to exist in the shroud FEA; thus the data is considered accurate.

MODE No.	COMPONENT	SOLID MODEL FREQUENCY (Hz)	HOLLOW MODEL FREQUENCY (HZ)
1	ST	2.5	5.1
2	ST	4.2	8.1
3	ST	21.6	40.8
4	ST	37.9	59.6
5	ST	103.3	121.4
6	SH	104.5	186.2
7	SH	168.5	197.2
8	ST	188.3	309.3
9	SH	229.8	312.8
10	ST	296.4	414.9
11	SH	341.1	454.8
12	ST	393.7	527.9
13	SH	475.3	580.2
14	ST	522.5	586.1
15	ST	540.4	703.3

ST = STRUT SH = SHROUD

Table 5.3: Modal Data for LTD Single Strut Section

5.5 Frequency Information and LTD Operation

The major concern which necessitated the shroud modal analysis was the interaction of the LTD's pulsejet engine "source frequency" with the response of the shroud and inner support structure. The shroud and support struts comprise the main engine/vehicle structure; thus structural resonant frequencies must be avoided. If the input frequency of engine pulses correspond with destructive resonant modes of the structure, catastrophic failure would be probable.

The cause of failure in structures undergoing resonant vibrations is due to the inherent stress associated with unusually large displacements of the oscillating structure. Induced stress has a linear relationship with displacement. As the mode number increases, so do the frequencies needed to excite them. However, the maximum displacement of a given particle of mass is inversely proportional to the input frequencies, as follows:

For a mass-spring system:

$$\text{Excitation Force } F = F_{max} \cos(\omega t)$$

$$\text{Displacement } x = (F_{max}/G) \sin(\omega t)$$

$$\text{Max. Displ. } X = (F_{max}/G)$$

where

$$G = \sqrt{(m\omega)^2 + (b\omega)^2}$$

$$m = \text{mass}$$

$$b = \text{Damping Coefficient}$$

Assuming unit coefficients (i.e., $m^2 + b^2 = 1$, $F_{max} = 1$):

$$\begin{aligned} X &= 1/w & X &= \text{Normalized Max. Displacement} \\ &= 1/2f & w &= \text{Ang. Frequency of Excitation} \\ & & f &= \text{Frequency of Excitation (Hz)} \end{aligned}$$

Figure 5.6 clearly indicates the inverse relationship between displacement of a particle in an oscillating body and input frequency. Although the derivation of this relation is for a mass-spring system, the basic behavior may be generalized to all structures. This generally holds true because any structure can be approximated by an infinite number of mass-spring systems.

Although large displacement responses may be obtained from lower harmonics at low frequency excitation, the response quickly diminishes with increasing frequency. Even at 50 Hz, the normalized response has fallen to only 2% that of a 1 Hz excitation

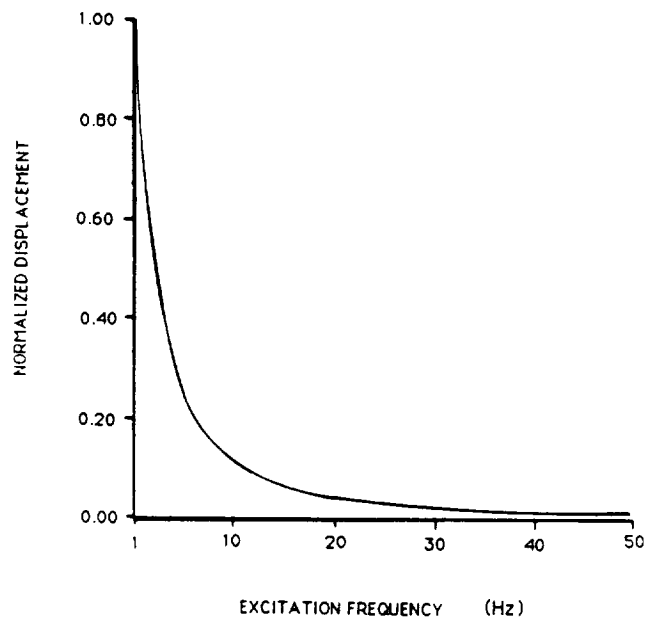


Figure 5.6: Normalized Displacement versus Frequency.

as shown in Figure 5.6. Clearly, at an input frequency of 10,000 Hz, the normalized response will be nominal for the high mode numbers obtained. Therefore, it may be concluded that the LTD shroud and support strut structure is able to withstand stresses of induced oscillations at the current engine design PRFs of 1 to 10 kHz. Even though resonant frequencies may be produced in flight, extremely small amplitudes (of displacement) will not cause damaging stress levels.

For next year's research effort, it has been proposed to lightweight the entire craft, including the shroud and strut assembly in order for the LTD to fly on $10\times$ less laser power. With such a lightened lightcraft engine, PRF's would be lowered significantly, perhaps to the range of 100 Hz to 1 kHz. As observed in the lightened shroud analysis (Table 5.5), modal frequencies increase with decreasing shroud mass. This could put destructive modes in the range of engine PRF, an effect that will need further attention and analysis.

The destructive modes will be of consequence, however, mostly at liftoff, or initial engine startup, when the PRFs are low. The "ramp" function used on engine PRF to suddenly apply power will produce a wide spectrum of source excitation frequencies; a large amount of power will fall in the destructive frequency range (e.g., 3 - 50 Hz). In the future the structural response to different "ramp" functions should be carefully examined using the basic structural mode shapes and resonant frequencies.

In the "sectional" analysis, significant strut-dominated modes were found to exist.

The struts were found to oscillate in and out of the strut plane, with virtually no motion of the shroud section. These modes began to appear with mode 8 (see Table 5.3), at a frequency of 309.3 Hz for the lightened version. Higher frequency harmonics of the original “flap” mode were interspersed with shroud dominated modes (see Fig. 5.7).

These so-called “flap” modes could prove to be dangerous. It is quite likely that pulsejet frequencies capable of stimulating flap modes will be present during vehicle operation. Another aggravating effect would be due to air flow fluctuations around the strut. Hence, rigorous wind tunnel testing must be included as a part of the strut design validation process.

5.6 Mode Shapes

The graphic representation of mode shapes permits the designer to ascertain exactly what is happening at each of the mode frequencies. In the first analysis of the shroud vibrational characteristics, six unique mode shapes (and four orthogonal mode shapes) were obtained.

The greatest problem with earlier analytical solutions for the shroud vibrational dynamics was in discerning the relative behavior of the support struts and the annular shroud. With this “first order” analysis, two situations could be assumed: (1) Support struts have zero stiffness in relation to the shroud, or (2) support struts have infinite stiffness in relation to the shroud. These two assumptions made it possible to find global modes and local modes, independent of each other.

Predictably, the actual behavior was somewhere in between the two extremes, as evidenced by the intermingling of mode types. In addition, natural modes of the support struts themselves were readily evident. Two basic types of modes were evident. They were defined by the structural component which acts as the primary oscillator, either (1) the support struts, or (2) the annular shroud. Presented in Table 5.4 is a listing of the 6 unique modes, their structural component, and description of their behavior. After examining the results of the finite element analysis, one may note the absence of “in-plane” elliptical modes. Such modes are not present due to the inherent symmetry of the shroud and support struts, about the radial plane. Thus the first global modes of the annular shroud are “out-of-plane” bending modes. This again is another diagnostic feature that would not have been revealed by an analytical approach.

5.7 Conclusions of Dynamic Analysis

The main purpose of the dynamic analysis was to ascertain the frequencies of the natural vibration modes for the annular shroud/strut support structure. This is

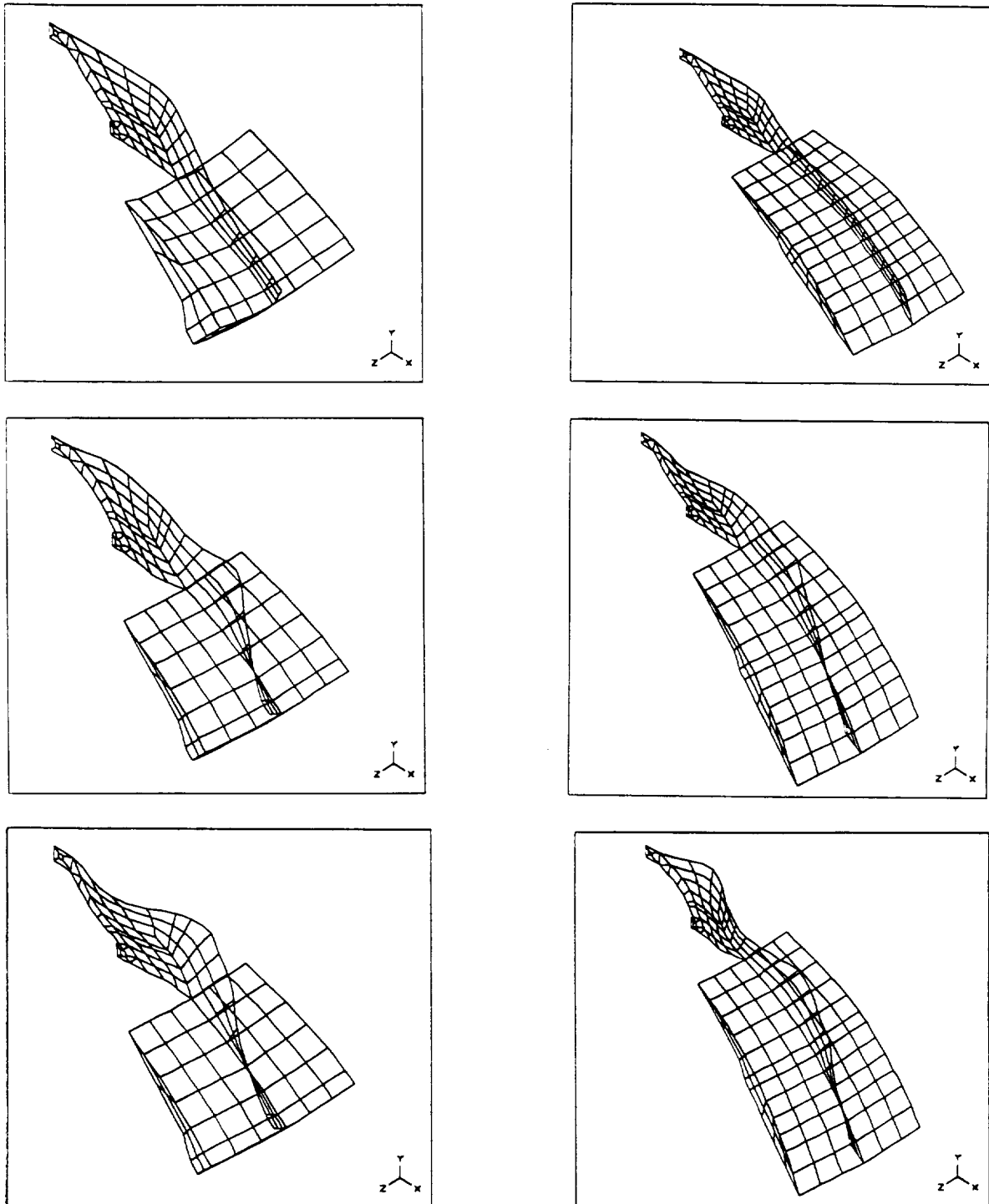


Figure 5.7: Various mode shapes for the T-tail Strut Assembly (deformations are exaggerated).

MODE No.	COMPONENT	PLANE	DESCRIPTION
1	ST	IP	TWIST MODE
2, 3*	ST	OOP	ROCK MODE
4, 5*	SH	OOP	1st BENDING MODE
6, 7*	SH	OOP	2nd BENDING MODE
8	ST	OOP	HEAVE MODE
9, 10*	SH	OOP	4th BENDING MODE
* = ORTHOGONAL MODE		ST = STRUT	SH = SHROUD
IP = IN-PLANE		OOP = OUT-OF-PLANE	

Table 5.4: Mode Shapes and Description

critical because of the pulsed nature of the LTD engine, for which the shroud/support strut is the major structural component.

It was determined that the first six unique global modes ranged from 3.0 to 34.5 Hz. Maximum structure displacement (and therefore maximum induced stress) in an oscillating system is inversely proportional to the excitation frequency. Therefore, the induced stress at kilohertz "source" frequencies projected for the LTD pulsejet engine will not excite destructive vibration modes in the engine/vehicle structure.

Although the current engine PRF will not present a design problem for the shroud-support strut structure, future lightened versions of the craft (with their higher modal frequencies) could potentially be damaged by destructive modes of vibration excited by engine PRF's in the 100 to 1000 Hz range. The lower-frequency spectral content of engine excitation frequencies must be examined to insure that strut dominated "flap" modes do not occur. Such modes exhibit extremely high lateral displacements which are highly stressing to the strut member. Fatigue effects must also be taken into consideration.

The shroud and support struts appear to have relatively equivalent stiffnesses; thus, their frequencies of natural vibration are interspersed. Since various mode numbers for the struts and shroud are of the same magnitude, the response to a given input frequency are qualitatively equivalent. For example, destructive modes will be excited in both the struts and shroud at excitation frequencies between 3 and 50 Hz;

however, neither will undergo destructive modes between 10,000 and 20,000 Hz. This is found to be a desirable characteristic of the structure.

A basic and sound understanding of the strut dynamic behavior has now been obtained. Several key design points have been clarified, and the groundwork has been laid for future structural analysis. Static (stress) analysis may now be accomplished using the existing model.

5.8 Static Analysis

As mentioned earlier the shroud and support structure of the LTD acts as the pulsejet engine of the craft. The high pressure, laser-heated gases push on the underside of the shroud to produce thrust. This repetitively-pulsed thrust is transmitted to the craft via the twenty-four radial support struts.

Both the shroud and the struts must be able to withstand the forces induced during maximum engine thrust and vehicle acceleration. Under this load, the integrity of the structure must be maintained, and the struts must not permit the shroud lower surface to be deflected away from the focal region of the incident laser beam.

5.9 Static Analysis Model

The purpose of the static finite element analysis was to evaluate the strut design (see Fig. 5.8) to uncover stress concentration areas. Since the load case is axisymmetric, only one individual section was used for the analysis. This allowed use of a denser mesh with parabolic elements. For this initial stress analysis, the shroud was considered solid, and the strut was fixed at the mounting holes.

Loads were defined as distributed pressure forces upon the flattened lower face of the shroud (i.e., the ERH thruster surface). the maximum thrust on each strut was found to be 4167 Newtons, which translates into a pressure load of 3.16 MPa across the shroud surface.

5.10 Results of Static Analysis

Of primary concern was the prediction of the stress fields throughout the strut structure. The Von Mises stress was considered such that, for no plastic deformation:

$$\sigma_{vm} < S_y \quad \begin{array}{l} \sigma_{vm} = \text{Von Mises Stress} \\ S_y = \text{Yield Strength of Nickel 200} \end{array}$$

for no plastic deformations (failure).

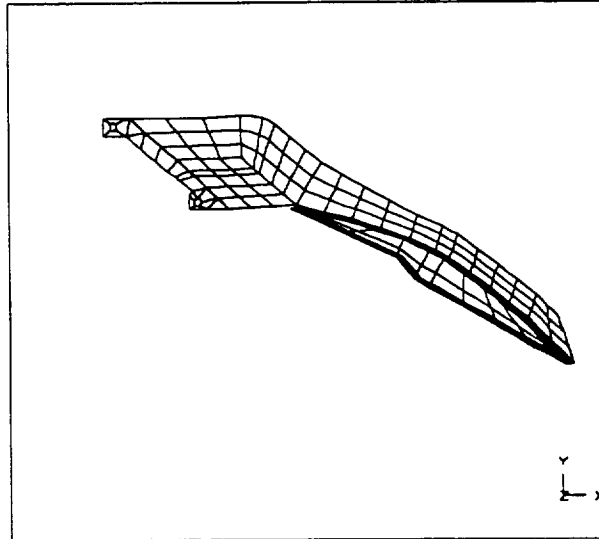


Figure 5.8: Static Stress Analysis of Strut Assembly.

Figure 5.9 displays the resulting stress contours for the given load case. The maximum stress was found at the outer edge of the strut to be 1457 MPa. The deflections under load were found to be significant. The maximum deflection at the trailing edge of the shroud was 4.625 mm; at the beam focus, the average deflection was 2.01 mm.

As in most engineering analysis, the actual behavior of the strut system could only be approximated, due to inherent limitations of the approach. For example, in reality the trailing edge of the strut is attached to a carbon-carbon ring that encircles the LTD vehicle centerbody. However, for this analysis it was necessary to consider it discontinuous. Had a continuous structural ring been used, the bending moment imposed on the strut would have been significantly lowered. This, in turn, would have greatly reduced the stress concentration that appeared on the outer edge of the strut and the strut/shroud interface.

Two very important results became evident from this analysis. First, the shroud section is very rigid and unstressed compared to the strut. This will permit removal of the excess, unloaded material at the center of the shroud; design mass limits can then be met. Secondly, the analysis shows that the current strut mounting hole pattern (for two bolts) is entirely capable of handling engine operating stresses. The critical stress concentration areas are located at the outboard edge of the strut, and at the point where the strut joins the shroud.

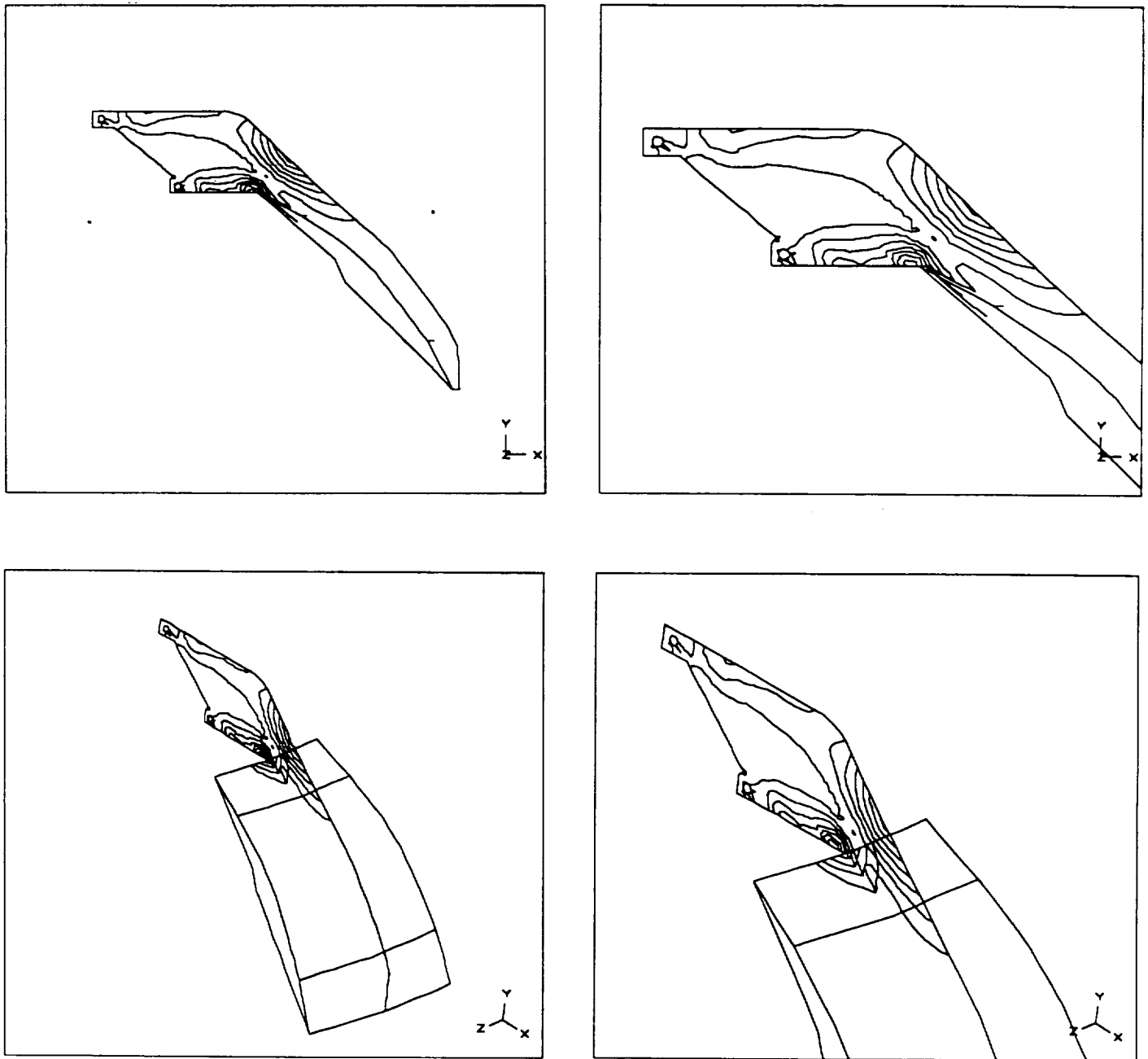


Figure 5.9: Stress contours for a loaded shroud strut assembly.

Since the strut is loaded in almost pure bending, the stress concentration at the outer edge of the strut may be easily reduced by increasing its cross sectional area (i.e., moment of inertia, I). This can be accomplished by either thickening the strut or by increasing its height. While increasing strut height increases I faster than by increasing strut thickness, the former alternative will tend to lower modal frequencies. Thus it will be necessary to evaluate dynamic response as well as stress handling abilities. Finally, it has been proposed that the stress concentration at the intersection of the strut and the leading edge of the shroud will be reduced by adding a "stress reliever".

5.11 Conclusions of Static Analysis

The static stress analysis examined the integrity of the strut/shroud section, and revealed areas that needed further refinement. The shroud itself was found to be excessively strong and can easily sustain the applied loads; thus, some material can be removed from the shroud interior to permit further weight reduction. Also, the two mounting holes provide sufficient strength for attaching the struts securely to the internal LTD support frame. Two areas are in need of further refinement: (1) the outer strut edge, and (2) the intersection of the strut and the shroud. A revised strut section with a higher moment of inertia and a stress reliever must be considered in future design and analysis.

REFERENCES

- [1] Myrabo, L.N., et al., Apollo Lightcraft Project Annual Report, NASA/USRA University Advanced Design Program 4th Annual Summer Conference, Kennedy Space Flight Center, Florida, 1988.
- [2] Halse, J., "CAEDSTM, an Introduction to Finite Element Analysis," Center for Interactive Computer graphics, Rensselaer Polytechnic Institute, Troy, N.Y.
- [3] Halliday, D., and Resnick, R., *Physics, Part One*, John Wiley and Sons, New York, 1977.
- [4] Liepmann, H.W. and Roshko, A., *Elements of Gasdynamics*, John Wiley and Sons, Inc., New York, 1957.
- [5] Rockwell International Rocketdyne Division; "The Space Shuttle Main Engine."

Chapter 6

OPTICAL SYSTEM FOR SENSING MISSION

6.1 Introduction

The Lightcraft Technology Demonstrator (LTD) represents not only a novel form of spacecraft propulsion, but also a different concept of launch vehicle integration with payload. Each part of the craft is designed with multiple functions in mind, and the same components may serve various applications at different times during the flight. For example, the liquid nitrogen is carried primarily as propellant for the laser heated rocket boost to orbit; however, a small amount will (i.e., 10%) also be used to cool both the primary mirror and the impulse thruster faceplates during the airbreathing propulsion mode. Also, where the cooling system is not regenerative, some liquid nitrogen could be vented over the impulse surfaces thereby providing a "film" cooling effect and perhaps helping to refresh the surrounding air before the next laser pulse arrives. It is this close integration of launch and mission components which makes the LTD so cost-efficient; this design approach is a logical extension of the so-called "lightsats", a class of small, lightweight satellites designed to perform specialized functions [1].

One of the most expensive elements of the LTD design is the high quality primary mirror, which is essential to the launch phase. Once the vehicle has reached orbit, it seems reasonable to apply the onboard optical system to other mission applications. It has been proposed that the LTD could serve as an orbiting satellite telescope; a similar mission was proposed for the Apollo Lightcraft [2]. Once the LTD has established orbit, a sensor array (or retina) will be deployed using hydraulic arms as illustrated in Fig. 6.1. The telescopic arms will extend a sensor array to the focal plane of the primary mirror, which will measure 1 cm in height and extend around the full circumference (1.2π m) of the craft. The LTD may be used for imaging applications at a variety of wavelengths to observe ground targets, the upper atmosphere, or outer space.

However, the main mirror has been designed primarily for propulsion applications.

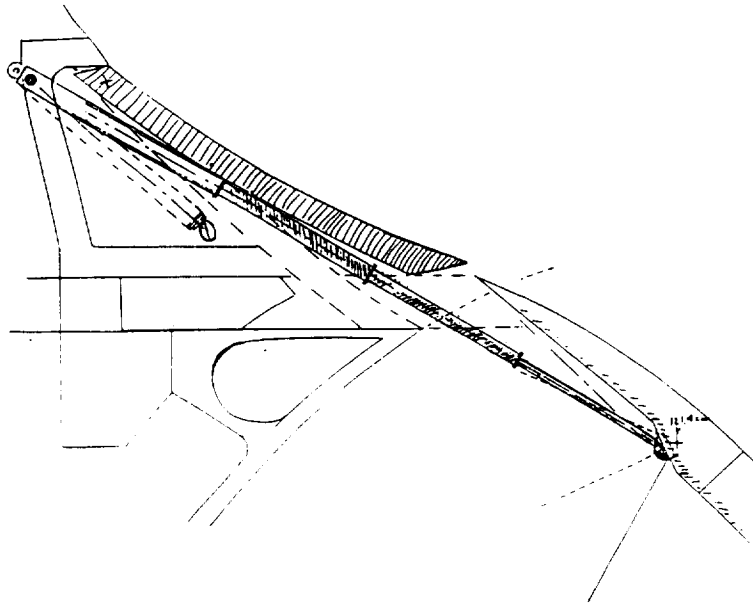


Figure 6.1: Deployment mechanism for LTD retina.

While the mirror is of large diameter and diffraction limited surface quality, the LTD telescope consists of a single refractive element with no corrective optics. The performance of this system is limited by geometric aberrations (reflective systems are free of chromatic aberration). The resolution limits of the primary optic under various conditions will be calculated, and the extent of significant aberrations will be evaluated. Several candidate devices for the sensor retina will be considered.

6.2 Characteristics of the primary mirror

The primary mirror is designed to be highly reflective in the infrared, although it should also exhibit good reflectivity in the visible, UV, or microwave regions of the spectrum. Multi-layer dielectric films may be designed for high reflectivity across a wide spectral range; thus, the mirror could serve as an antenna for microwave or laser communications. For such applications, the optical characteristics of the mirror become important. Several parameters of interest will be calculated, following the analysis given in a previous Apollo Lightcraft report [2]. The resolution of an imaging system, in general, is determined by the Rayleigh criteria [3]. The minimum angular separation between two points which can just be resolved is given by:

$$\Delta\theta = 1.22\lambda/D \quad (6.1)$$

where λ is the operating wavelength and D is the input aperture diameter. The quantity $(\Delta\theta)$ is referred to as the resolving power of the system, while $2(\Delta\theta)$ gives the diffraction limit angular spot size (to be compared with spot size in the presence of aberrations). The Rayleigh criteria may also be expressed in terms of the minimum separation between two points which can be resolved at a distance l ,

$$d(l) = 1.22\lambda l/D \quad (6.2)$$

This quality is taken to be a measure of the system's resolution limits when it is evaluated at $l = f$, the focal length of the system.

Another important property is the numerical aperture of the system, N.A., which measures light gathering power [3]; it is related to the f -number ($f/\#$) by:

$$f/\# = f/D = 1/2(\text{N.A.}) \quad (6.3)$$

The $f/\#$ determines the amount of light which reaches the final image plane; its reciprocal is known as the relative aperture. A smaller $f/\#$ allows more light to reach the final image; the $f/\#$ squared is a measure of exposure time. It is known as the speed of a system and smaller $f/\#$'s imply higher speeds.

The LTD mirror has a focal length of 7.916 cm and is characterized by a numerical aperture of 3.158 and $f/0.158$; the system is therefore very fast and exhibits high light gathering power, due to its short focal length. By comparison, the 200 in. diameter telescope at Mount Palomar Observatory has a focal length of 666 in., a numerical aperture of 0.150 and $f/3.33$ [4]. Similarly, one of the world's largest refracting telescopes at Yerkes Observatory has a 40 in. diameter main mirror and focal length of 63 ft., yielding a numerical aperture of 0.026 and $f/18.9$ [5]. However, the LTD will not out-perform either of these systems because it is poorly corrected for aberrations that limit image quality.

Table 6.1 gives calculated values of resolution at various ranges for upper and lower limits of the visible spectrum, as well as two infrared wavelengths. If the system is to be used in flight, the image could be blurred by any mechanical vibration or flight turbulence greater than these values. In practice, resolution limits will be set not by the diffraction limit of the optics, but by the mechanical stability of the optical support structure. Pointing accuracy from orbit will be limited by the LTD attitude control system. The calculations of Table 6.1 do not account for geometric aberrations. In the following section, a general description will be given of the five monochromatic aberrations involved; a more detailed description may be found in Ref. [3,4]. Aberrations are more pronounced for rays far from the optic axis and for oblique angles of incidence. Coma and astigmatism are expected to dominate in the formation of a final image; the analysis begins with a description of the weaker aberrations.

Resolution limits for LTD mirror at various wavelengths
(all angles in radians, all distances in meters)

	400 nm	700 nm	1 μ	10.6 μ
$\Delta\theta$	4.88×10^{-7}	8.54×10^{-7}	1.22×10^{-6}	12.93×10^{-6}
$d(f)$	38.63×10^{-9}	67.60×10^{-9}	96.57×10^{-9}	102.37×10^{-6}
$d(36,000 \text{ km})$	17.56	30.74	43.92	465.55
$d(360 \text{ km})$	0.17	0.30	0.44	4.65
$d(180 \text{ km})$	0.08	0.15	0.22	2.33

Table 6.1: Resolution limits for LTD mirror at various wavelengths (all angles in radians, all distances in meters).

Spherical aberration corresponds to a dependence of focal length on aperture size for rays far from the optic axis. This effect is well corrected by parabolic mirror sections [4,5]. Off-axis rays may also experience distortion, because transverse magnification is a function of distance from the optic axis. A ray trace indicates that the mirror has a very narrow angular field of view, so distortion is not expected to be a significant problem. Finally, the principal focal plane of the mirror is actually only a plane in the paraxial region; for off-axis rays, it takes on a finite amount of curvature. This is not significant because of the narrow field of view. It would be possible to correct for this effect by using a curved detector surface to match the wavefront profile, although our analysis suggests that this is not necessary.

The dominant monochromatic aberration for the LTD mirror is coma, or comatic aberration. In an optic system, the effective focal lengths and the transverse magnifications will be different for rays passing through off-axis regions of the system. This effect appears even for very small angles of incidence, affecting object points only a short distance from the optic axis. The formation of a comatic image is illustrated in Fig. 6.2; the final image forms a circular focus for paraxial rays, but off-axis rays form a comet-like tail in the image (hence the name coma). Slightly more than half the optical energy appears in the roughly triangular region between points 0 and 3.

Coma is defined as positive if the marginal rays focus farther away from the optic

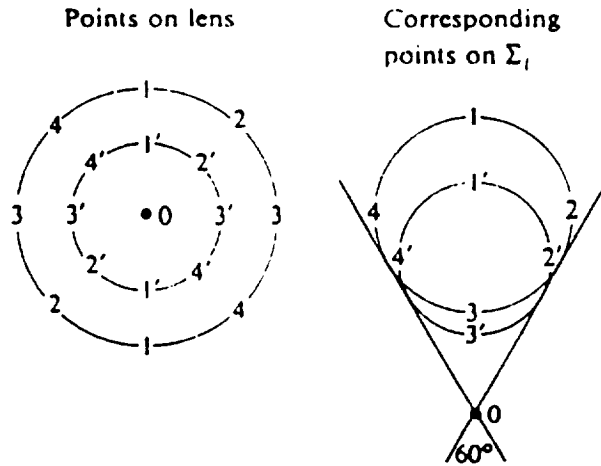


Figure 6.2: The geometric comatic image formed by an off-axis object point (Ref.3).

axis than the paraxial rays; if they focus closer to the axis, it is termed negative coma. A conservative estimate of the image spot size due to coma may be calculated from the angle of incidence, θ , and the primary mirror $f/\#$ as follows [5] :

$$\beta_c = \theta/16(f/\#)^2 \quad (6.4)$$

where β_c is measured in radians. The comatic spot size for the LTD mirror at various angles of incidence is given in Table 6.2; for comparison, the diffraction limited spot size is also shown. Image quality will be limited by the aberration, even for a mirror with ideal figure and surface quality. The ray traces indicate that coma will be positive for one half of the LTD mirror and negative for the other.

A detailed analysis of comatic aberration must account for the separate effects of tangential or meridional coma (the distance between image point 0 and 1 in Fig. 6.2), and sagittal coma (the distance between points 0 and 3). [3]. The ray traces apply only to meridional rays (a cross section cut through the primary mirror). From such traces, we may evaluate a meridional error plot [4]; Fig. 6.3 illustrates the graphical interpretation of such plots.

A representative meridional error plot for the LTD is given in Figure 6.4. An equation which fits the curve and characterizes the aberrations is given; coma is the dominant effect. A 1 cm high detector array was assumed for the LTD retina design; this means that most of the rays will miss the detector plane entirely for incident angle much greater than 0.5 degrees, which is the upper limit on angular field of view. While a larger detector surface would intercept more rays at larger angles, the coma becomes

angle of incidence (degrees)	coma spot size (radians)	astigmatism spot size (radians)
0.1	4.37×10^{-3}	9.64×10^{-6}
0.5	21.84×10^{-3}	0.24×10^{-3}
1.0	43.67×10^{-3}	0.96×10^{-3}

Table 6.2: Spot size due to aberrations in coma at oblique incidence (wavelength = 1 micron; diffraction limit = 4.88×10^{-6} radians).

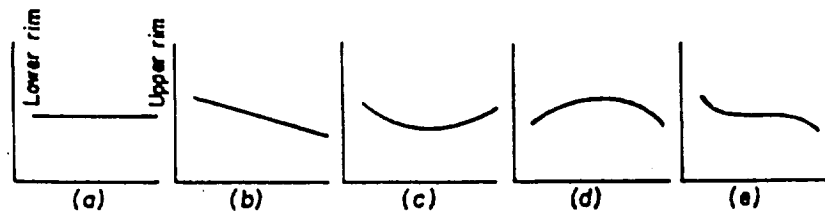
dramatically worse and the final image would be distorted beyond recognition. Since additional corrective optics can not be included in the LTD mirror system, the field of view limit must be tolerated; it is assumed that the pointing systems for the LTD in orbit are sufficiently accurate to track a desired object within this limitation.

Because of the limited capabilities of the ray trace software, no sagittal ray traces were performed and it was not possible to generate a sagittal error plot. However, theoretical limitations due to sagittal coma may be calculated; Kingslake [4] gives the following relation for sagittal coma as a function of off-axis distance, h , for a small aperture mirror:

$$coma_s = h/16(f/\#)^2 \quad (6.5)$$

Using this expression, a sagittal coma can be predicted for the LTD mirror of 50 mm for a point 20 mm from the axis. By comparison, the sagittal coma for the Mount Palomar telescope at the same distance off-axis is 0.115 mm [4].

Despite its large diameter and high quality surface, the LTD does not perform as well as conventional telescope systems because of aberrations. It is possible to reduce coma by using an aperture stop at the focal plane [3]; the rays far off-axis are removed from the image. The image intensity will decrease sharply as the object points move off-axis; this is known as vignetting [3]. Since the LTD retina is composed of



- (a) an ideal optical system
- (b) inward-curving field
- (c) positive coma
- (d) negative coma
- (e) spherical aberration

Figure 6.3: Sample meridional error plots (Ref. 4).

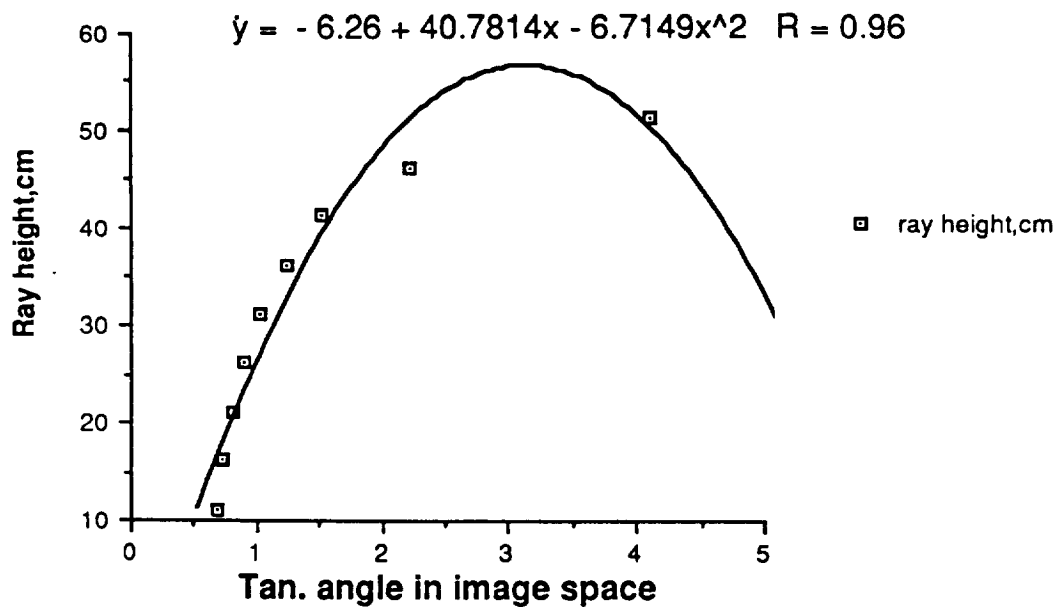


Figure 6.4: Meridional error plot for right side of the LTD primary mirror at 0.1° angle of incidence.

electronic detectors, the sensors could be apertured electronically to reduce coma; sensitive detectors could decrease the effects of vignetting. Electronic image processing techniques may significantly increase the fidelity of images generated by the LTD; aberrations could be compensated by electronic post-processing of the image.

Astigmatism occurs when an object point lies a considerable distance from the optic axis, so that a cone of incident rays strikes the mirror asymmetrically. The tangential and sagittal rays focus at two different points; the separation between these points is known as the astigmatic difference. The spot size of an image due to astigmatism may be calculated [5] from the relation:

$$\beta_a = \theta^2/2(f/\#) \quad (6.6)$$

where β_a is measured in radians. Values are given in Table 6.2; astigmatism is only pronounced for large angles, and coma still dominated image formation over the entire field of view.

The proposed mirror design represents a compromise between several possible mirror contours, and was selected for its propulsion applications. Different contours for the parabolic mirror will possess slightly different focal lengths [6], as shown in Fig. 6.5. The $f/\#$ for each of these designs is given in Table 6.3, which also shows the calculated spot sizes due to coma and astigmatism. Both aberrations may be improved by using larger $f/\#$ mirrors; the remaining aberrations would not be substantially affected. It is feasible to consider designing customized LTD satellites which trade off propulsion efficiency for improved imaging performance on certain mission applications.

The ray tracing program defines a figure of merit called root mean square (rms) blur. It is defined as the perpendicular rms distance between the mirror focal point and the intercept of actual rays with the focal plane. The rms blur is thus an estimate of the final image spot diameter. The normal distance from each ray to the focus and the corresponding rms blur is given in the Appendix; the blur increases linearly with incident angle.

6.3 Sensors for the LTD retina

Current designs call for a 1 cm high sensor retina to be deployed from the LTD forebody to the focal plane of the primary mirror. Several different types of sensors could be deployed around a single vehicle, enabling it to perform multiple missions. The devices would be lightweight, rugged, compact, and require minimal power; this suggests a solid state detector array. Such a device must be sensitive enough to observe faint, more distant objects or scan brighter objects in less time. This translates into high quantum efficiency (ratio of electrons generated to number of incident photons) combined with a low readout noise level. The detection of faint objects can be

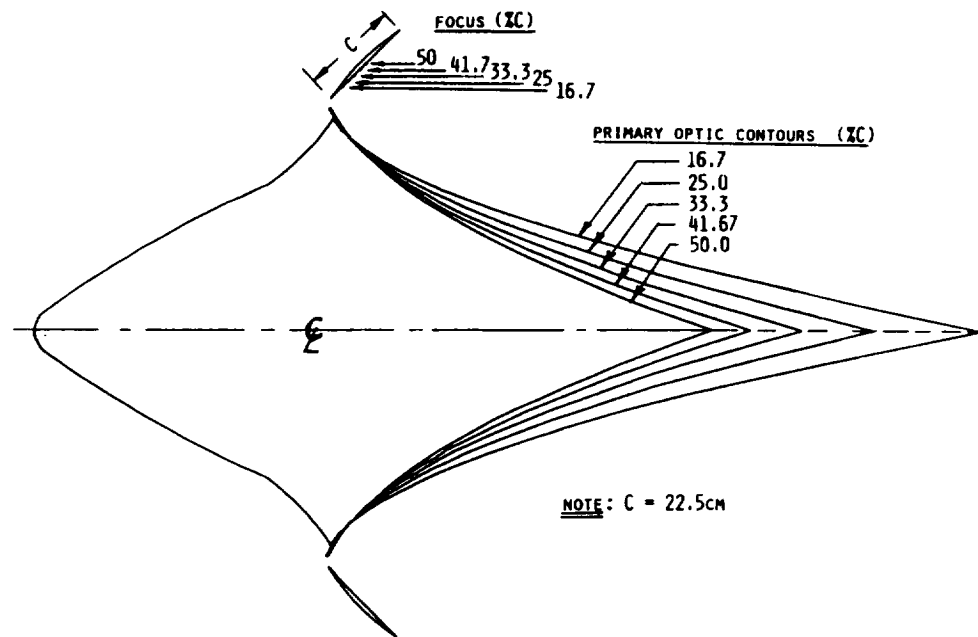


Figure 6.5: Alternative primary optic contours and focal lengths.

f/#	coma spot size (milliradians)	astigmatism spot size (microradians)
0.225	10.77	0.169
0.187	15.59	0.203
0.149	24.56	0.255
0.112	43.48	0.339
0.075	96.96	0.507

Table 6.3: Aberration spot size for various primary optic contours at incident angle = 0.5° (diffraction limit at 1 micron length = 4.88×10^{-6} radians).

enhanced by increasing the exposure time, assuming that the mirror system could be held sufficiently stable; this technique is also used to observe video images of a changing scene. Electronic detectors generate noise over prolonged exposures. The flow of thermally generated electrons (dark current) saturates the detector over time, even when no light is present. Low dark current is thus an important requirement; since dark current is smaller at reduced temperatures, cryogenically cooled detectors are sometimes used (especially for infrared sensors).

Solid state detectors saturate when exposed to very bright objects; the optically generated signal overflows into adjacent pixels, causing an effect known as blooming. The LTD sensors will be exposed to space with very little shielding; cosmic rays or high energy particles may pass through the detector and blind large areas of the retina. Other factors to consider include wide spectral response and a large number of pixels for high resolution. The sensors should collect as much raw data as possible, since many of the details could be recovered by electronic post-processing of the image; it should also be possible to electronically aperture the detector, in order to concentrate on details of a scene or reduce coma.

Only commercially available sensors such as the charge coupled device (CCD) and charge injection device (CID) [7,8] will be considered. Charge coupled devices represent a mature technology for space systems applications; a CCD system was included as part of the optical instrumentation on the Voyager spacecraft. The same company that developed these sensors, EG&G Reticon, has recently demonstrated a new CCD detector for astronomy applications [7]. It consists of a 400×1200 matrix of pixels, each measuring 27 microns square. Readout noise has been reduced to 4 electrons rms. Dark current is very low, only 20 electrons per pixel per hour at -100°C . Operating unshielded in space, the detector could reach low temperatures which would improve performance. The device has superior anti-blooming performance; only three adjacent pixels saturate when enough light is applied to generate 1.5 million electrons (over three times the saturation level). Figure 6.6 shows the effect of a cosmic ray passing through pixel 792 of the device; only a few adjacent pixels are blinded. The number of electrons generated by the interaction is plotted for each column of the device. The temperature of the device was -111°C (ref. 7). The spectral response extends from 400 to 1100 nm. Small portions of the device can be scanned independently, making it possible to aperture the device.

Another candidate device offered by CIDTEC Corp. [8] does not transfer accumulated charge from site to site. Collected charge is shifted between capacitors within each pixel, and the displacement current (which is proportional to the stored signal charge) is detected. Unlike the CCD, which clears itself whenever a new image is read out, the charge remains intact within a CID detector's pixels so that readout is non-destructive. In order to clear the array for a new image, the pixel electrodes switch briefly to ground, "injecting" the stored charge into the device substrate. The nonde-

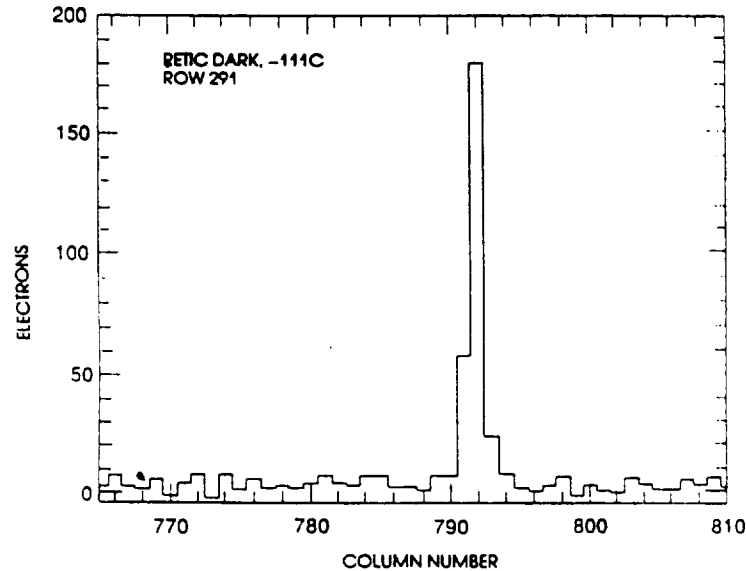


Figure 6.6: Effect of a cosmic ray on Reticon CCD.

structive readout capability makes it possible to control a time exposure accurately, and to check the image as it develops without erasing it.

Since charge does not transfer between individual pixels as in a CCD device, there are no paths between pixels along which charge overloads can propagate. This makes the device very tolerant to blooming, since illumination overloads are confined to each pixel and excess charge is drawn off into the substrate; cosmic rays only blind individual pixels. Because there is no need for opaque electrical contacts between pixels to transfer charge, the CID has a continuous pixel structure for higher resolution. Since each pixel can be addressed individually, electronic apertures are possible. A signal to noise ratio of 46 dB has been achieved, and detectors of 512×776 pixels are available in sizes suitable for the LTD.

6.4 Conclusions

The use of the LTD as a sensor satellite has been explored. The primary mirror could serve a dual purpose on each mission; however, since the mirror is designed primarily for propulsion applications, its performance in other respects is limited. A ray trace analysis of the primary optic indicates that it has superior light gathering ability, but the angular field of view is limited to only about 0.5 degrees. Coma is the dominant aberration over the entire field of view; a small amount of astigmatism is present for the larger angles of incidence, while other aberrations are essentially negligible. Several candidate sensors, including CCD and CID technology, are com-

mercially available and meet the requirements of the LTD retina.

REFERENCES

- [1] J.R. French, "Very Small Spacecraft for Planetary Exploration Missions", USRA Lightsat Conference, 1988.
- [2] L. Myrabo and W. Smith, editor, Apollo Lightcraft Project Annual report, NASA/USRA 4th Annual Summer Conference, Kennedy Space Flight Center, Florida, 1988.
- [3] E. Hecht and A. Zajac, *Optics*, Addison-Wesley, Reading, Mass., 1979.
- [4] R. Kingslake, *Lens Design Fundamentals*, Academic Press, N.Y., 1978.
- [5] G.C. Paraskos, J.H. Ward, "Taking Advantage of Reflective Aspherics", *Photonics Spectra*, p. 159-166, 1988.
- [6] J.C. Richard, C. Morales, W.L. Smith, L.N. Myrabo, "Laser-Boosted Lightcraft Technology Demonstrator", Proc. First Int. Conf. on Hypersonic Flight in the 21st Century, Grand Forks, N.D., Sept. 20-23, 1988; ISBN no. 0-9608700-1-6, University of North Dakota, Dept. of Space Studies, p. 353-365, Jan. 1989.
- [7] R. Hylkema, L. Robinson, "Tailoring CCD's for Astronomy", *Photonics Spectra*, p. 187-192, 1988.
- [8] CIDTECH Product Literature, CID Technologies, Inc., Liverpool, NY, 1988.

Chapter 7

OPTICAL SYSTEM FOR LASER PROPULSION

7.1 Introduction

The following chapter describes design considerations for the Lightcraft Technology Demonstrator (LTD) propulsive optical train. Design and fabrication techniques are considered for the LTD primary optic (PO), as well as characteristics of the ground based laser uplink. Using a ray trace of the PO, the effects of beam steering error on the propulsion system performance are evaluated for near, intermediate and far field intensity profiles. A proposal for the control system necessary to accurately track pointing error will be given.

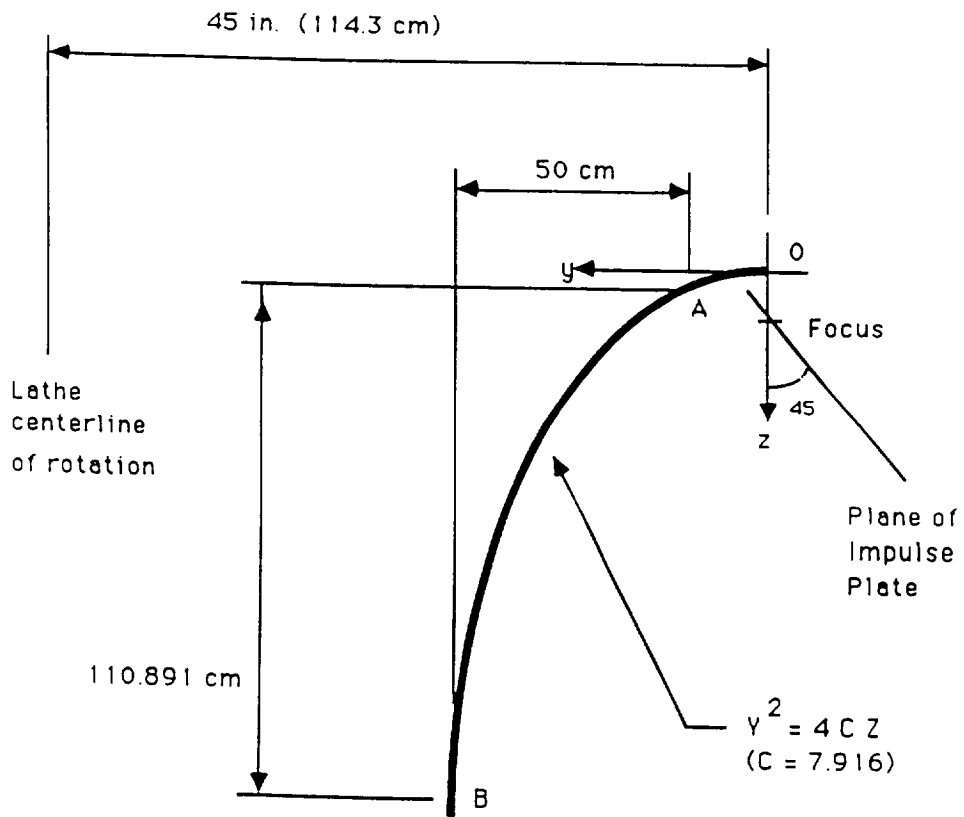
The LTD represents a novel concept in satellite self-deployment, although laser powered launch vehicles have been under study for several years. Small, lightweight (ten to several hundred kg), unmanned missions for specific applications have received increased attention as both equipment and launch costs continue to rise [1]. These so-called "lightsats" or "microspacecraft" have been considered for many diverse applications including communications satellites, lidar systems, and satellite laser ranging, among others [1,2]. As microelectronics technology continue to reduce payload size and weight, lightsat systems have been recognized as the means to fill a vital market niche in space science [2]. Laser propulsion itself has also received increased attention; NASA has even considered manned spacecraft based on huge (10 GW) orbital laser power stations (the Apollo Lightcraft [3]). Lawrence Livermore National Laboratory (LLNL) is currently engaged in a program to develop the LTD for launch within the next six years, funded under the SDIO Laser Propulsion Program.

7.2 Design and manufacture of the LTD primary mirror

The design of the 1.0 m diameter primary mirror is critical to the successful launch of the LTD. This mirror will be an off-axis paraboloid with a short focal length, designed for high light gathering capability. Such mirrors are commonly made by cutting several off-axis sections from a large on-axis parabola mirror blank; however, the cost increases with the off-axis mirror diameter [4,5]. Since the LTD calls for a mirror cut 45 in. off-axis, this technique would be prohibitively expensive, and other methods must be employed. Large diameter, high quality mirrors may be manufactured by diamond-turning, a technique using a specially designed high precision lathe with a single crystal diamond cutting tool. Computer controlled milling procedures are employed to machine certain metals (e.g., aluminum, copper, etc.) to exceptionally close dimensional tolerances. Pioneering efforts at LLNL have developed a 96 in. diameter diamond-turning lathe, which would be able to cut the LTD primary optic in a single processing step. An aluminum substrate would be used, because of its machining properties and its high reflectivity in the infrared. The LLNL equipment has already produced annular resonator optics for the Alpha ground-based chemical laser experiment to a surface figure accuracy of 12.5 nm rms [6]. The design of the LTD mirror is shown in Figure 7.1.

In order to achieve the necessary optical quality, the mirror figure (large-scale flatness) should be kept to at least $1/10$ of the operating wavelength. Reflectivity exceeding 99.9% must be maintained due to the high laser intensities required during launch; this cannot be achieved with bare metal mirrors because their intrinsic absorption is too high. Instead, high reflectivity multi-layer dielectric coatings must be applied over the mirror substrate, as illustrated in Figure 7.2. While these coatings are currently available, they set limits on the surface quality which can be realized. For example, a figure of $1/40$ wavelengths requires coatings with thickness uniformity of 0.1 nm, which is less than the diameter of an atom. The outer surface roughness should be kept within 1 nm rms to minimize scattering of the incident beam.

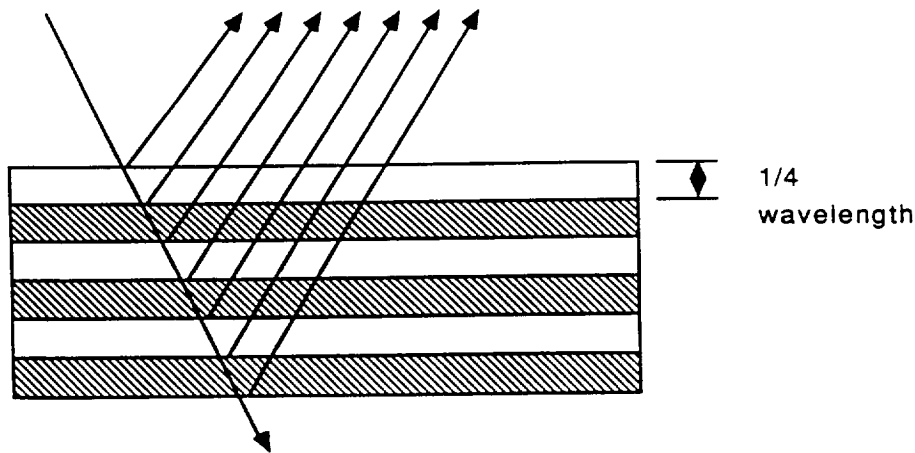
Another important issue is the stability and survivability of such a precision optic during a hostile launch and orbital environment. Since mirror systems can be supported from behind (as opposed to transmissive optics, which must be supported only along the edges), this could be achieved by using a carbon composite backing for structural support. The high intensity laser tends to produce isolated spot damage in the optical coatings; laser heating also causes thermal distortion in the mirror figure, and accelerates mechanical creep effects [7]. To address these problems, heat exchangers may be incorporated in the mirrored face plate, as shown in Fig. 7.3. A face plate on the order of 30 mils (0.5 mm) thick would incorporate coolant channels



Coordinates of Parabolic Mirror in x-plane (cm)

	Y	Z
O	0.000	0.000
Focus	0.000	7.916
A	10.109	3.227
B	60.109	114.107

Figure 7.1: Cross sectional view of LTD primary optic in the y-z plane.



Multi-layer dielectric coating for high reflectivity; thickness of each layer is one-quarter wavelength of the illuminating light, so that light is reflected in phase from all interfaces in the coating. Dark layers represent higher refractive indices, light layers represent slightly lower refractive index

Figure 7.2: Multi-layer dielectric coating for high reflectivity.

about 20×60 mils square. The performance of these channels at high pressures and flow rates is still under investigation, although the theoretical potential exists for an active cooling system to improve the mirror performance.

This same cooling system would also circulate coolant behind the shroud impulse surface, where laser intensities of 500 MW/cm^2 must be maintained for useful thrust generation. The system would be largely regenerative, but could also be used for transpiration cooling at the shroud and support strut leading edges. Also, a small amount of coolant could be vented over the impulse surfaces between laser pulses to provide a film cooling effect and perhaps assist in the convection of refresh air [8,9].

The mirror surface could be protected from dust and impacting particles with a several hundred angstrom coating of diamond-like carbon; this coating would also discourage thermal damage, and act as an electrical insulator to shield the metallic mirror from high electric fields of the laser beam [10]. Diamond coatings are also highly transmissive in the infrared.

Research into the physics of high energy beam interactions is continuing, and may have implications for the LTD experiments. For example, intense laser interactions with metal targets may lead to photoelectric effects. This would cause the PO to steadily lose electrons during flight and accumulate a net positive charge, which could attract small particles damaging to the mirror surface. Assuming single photon/atom interactions to be the dominant mechanism, the critical wavelength of light required

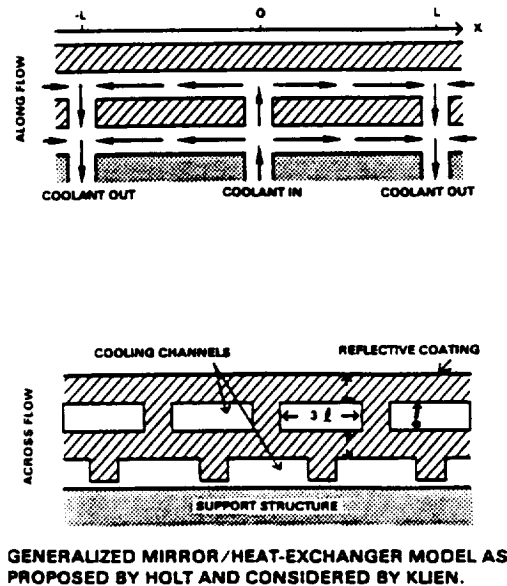


Figure 7.3: Proposed models for mirror face cooling channels.

for photoelectric emission is given by [11]:

$$\lambda = hc/\varphi \quad (7.1)$$

where Planck's constant, $h = 4.136 \times 10^{-15}$ eV/s, c is the speed of light, and φ is the work function of the metal target. Since the mirror substrate may consist of aluminum, whose typical work function is 4.28 eV, photoelectric emission does not occur below wavelengths of 0.29 microns. Thermionic emission of electrons, however, does not depend on the incident wavelength but on laser heating of the mirror; the total current per unit area generated, J , is given by [11]:

$$J = 2AT^2 e^{-\varphi/kT} \quad (7.2)$$

where T is the temperature of the target in Kelvin, Boltzman's constant, $k = 1.3805 \times 10^{-23}$ J/K, and the constant $A = 120.4$ amp/(cm² deg²). For a worst case analysis, one could take $T = 600^\circ$ C, which is just below the melting point of aluminum; for this case, the emitted current density is 17.9×10^{-18} amps/cm², which is negligible for our purposes.

It has also been reported [7] that multi-photon interactions may play a significant role in high energy laser interactions. For laser wavelengths of 1 micron, a single infrared photon energy is 1.24 eV; thus, a 4 photon interaction is required to overcome

the work function and produce electron emission. While this is highly unlikely in the infrared, recall that approximately 50×10^{30} photons/laser pulse are incident on the mirror during flight, so multi-photon interactions may become significant. Recent experiments [12] have demonstrated 7 to 12 photon interactions with xenon gas at wavelengths of 10.6 microns and beam intensities of the order 10^{13} W/cm². This suggests that multi-photon absorption during atmospheric propagation of the power beam may also be significant. Both of these effects are dependent on factors such as the laser power beam intensity profile, incident angle, and polarization; thus, it is expected that such factors could be controlled in the LTD system.

7.3 Power beam system analysis

Several transmission models have been proposed for free space high power laser propagation [3,13]. To be presented here is a first-order analysis for the LTD system based on some aspects of these models, assuming a ground-based laser and using the primary optic of the LTD as the receiver antenna. The power beam diameter will spread as it propagates through the atmosphere; the significant effects have been identified as diffraction from the source aperture, atmospheric turbulence, pointing jitter, and thermal blooming [13]. In practice, the effects of thermal blooming can probably be reduced or eliminated by using adaptive optics at the transmitter [13] and the judicious choice of a laser frequency that coincides with an "atmospheric window". The three remaining sources are expected to contribute almost equally to total beam spread. The maximum tolerable beam spread, σ , (in steradians) is given by:

$$2\sigma = r/R \quad (7.3)$$

where r is the radius of the receiver aperture (0.5 m) and R is the range between transmitter and receiver. The maximum effective range encountered by the LTD depends on the path taken to low Earth orbit; several possible trajectories have been calculated [3, 8, 9]. Assuming a trajectory of 30° inclination with respect to the horizontal, the maximum range is 560 km. This leads to a maximum tolerable spread of 446.42×10^{-9} steradians, if we are to prevent excess spillage of light around the vehicle. The contributions of diffraction, turbulence and jitter are all approximately 258×10^{-9} steradians.

Given the maximum beam spread due to diffraction, we may estimate the size of the transmitter aperture from:

$$\text{transmitter diameter} = 0.45\lambda\beta/\sigma \quad (7.4)$$

where λ is the optical wavelength and β is the beam quality (assumed equal to 1 for the diffraction limited case). The minimum required transmitter diameter is thus

7.3. POWER BEAM SYSTEM ANALYSIS

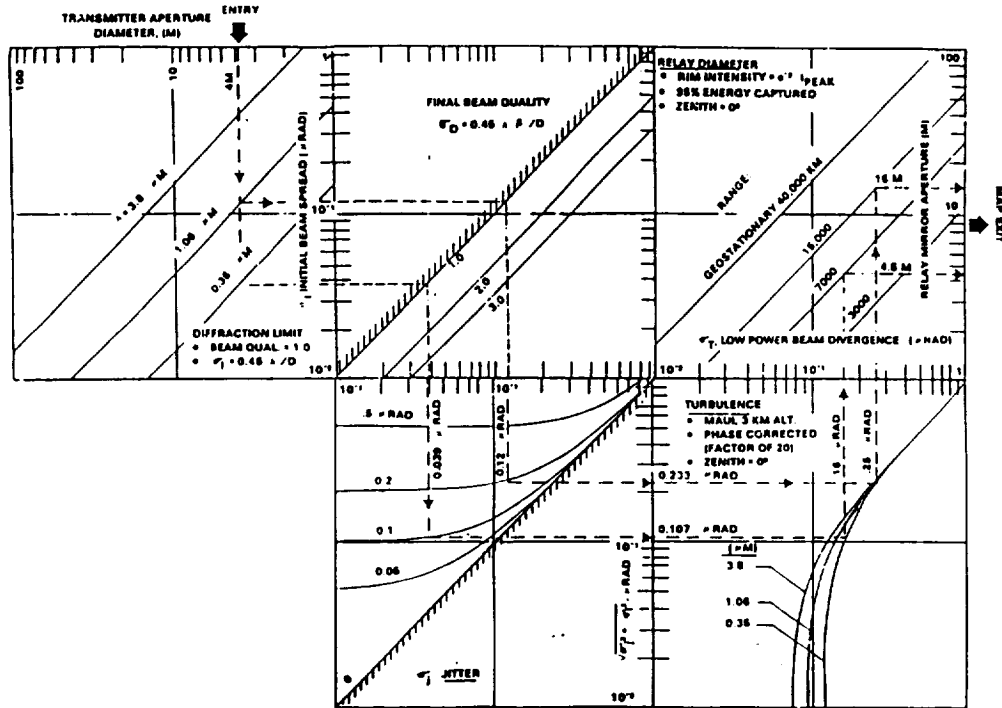


Figure 7.4: Graphic map of laser uplink propagation parameters (ref. 3).

1.74 m. The relationship between transmitter and receiver size depends in detail on factors such as the operating wavelength, beam quality, orbit range, and tolerable spread due to jitter and turbulence; these relationships have been calculated [13] and are displayed graphically in Figure 7.4. An example showing how a given transmitter aperture and wavelength might map into different receiver diameters at different ranges is given (diffraction limited performance is assumed). In a similar manner, it is possible to map a 1.7 m diameter source into a 2 to 3 m diameter beam in low Earth orbit, depending on the assumptions made regarding jitter and turbulence. Current SDIO plans involve the construction of a 4 m diameter adaptive primary mirror for a ground based telescope system which would also track a laser boosted launch vehicle; an adaptive 4 m mirror recently produced by Itek Corp. [14] may be considered as a point design for the transmitter.

For the present LTD vehicle, the propulsive power beam is assumed to deliver several hundred megawatts; an ultralight LTD would require 10 times less power. These figures represent time-average levels, including both the pulse duration and the interval between successive pulses. Each laser pulse is expected to last only 25 - 50 ns, with an energy of 30 - 40 kJ per pulse. A square pulse is assumed at the transmitter; for this case, each pulse is transmitted peak power, P , of 1×10^{12} W.

The intensity received at the LTD primary mirror, I , may be calculated from [13];

$$I = PT_r/2\pi(\sigma R)^2 \quad (7.5)$$

The quantity T_r is the atmospheric transmittance, which is about 0.85 for an operating wavelength of 1 micron [13]. This yields an intensity of 2.16×10^8 W/cm² at the primary mirror. Assuming a pulse duration of 35 ns, the mirror must be designed to tolerate a fluence level F of

$$F = I\Delta t = 7.57 \times 10^4 \text{ J/m}^2 \quad (7.6)$$

Although this is higher than currently available mirrors have obtained, the use of cooled mirrors should make it possible to achieve this level of fluence without inducing substantial laser heating damage to the main mirror.

7.4 Effects of pointing error

In order to determine the performance of the LTD receptive primary mirror under various conditions, a computerized ray trace study of the primary mirror has been generated, as described in the Appendix. Characteristics such as the mirror figure have been estimated previously; the primary purpose of this analysis was to determine the effects of pointing error and oblique incidence on the propulsive laser beam. Three possible beam intensity profiles were considered: near, medium, and far field. Actual ranges corresponding to these three regimes are not given, since they would depend on the specific trajectory to orbit [3, 8, 9]. Since the laser will be directed by the large aperture telescope, with the minor beam steering performed by adaptive optics, the near field irradiance is taken to be a torus. The central obscuration due to a secondary telescope optic is assumed to be of maximum radius 50 cm, which would obscure the central 25% of the PO area. Not performed, was a detailed fractional active area analysis for the LTD, as reported for the Apollo Lightcraft [3], because of the small diameter primary optic and narrow field of view permitted. The remainder of the toroidal beam is assumed uniform in intensity.

At intermediate ranges, this central portion fills in by diffraction to yield a uniform or 'top hat' intensity distribution. This case may also be encountered in the near field of a telescope with no central obscuration; the total power delivered is assumed to be the same for both toroid and uniform distributions. In the far field, the beam assumes a Gaussian profile, which is assumed to be truncated when the intensity in the Gaussian tails has fallen by e^{-2} (or 0.1353) from its peak value [13]. This allows for 95% of the power beam to be intercepted by the LTD mirror. A small amount of light spillage is thus tolerated, and may even prove to be useful as shall be illustrated later.

If there is a small pointing error in the power beam, the rays focus at a different point from the ideal focus; some rays miss the focus entirely for large angles of incidence. This corresponds to a loss of incident optical power. The spot size near the focus spreads out over a larger area, reducing intensity at the focus. These two effects combine to decrease the effective thrust generated by the LTD; the effect is worse for the larger incident angles and for the rays further off the parabolic mirror centerline. The effects of oblique incidence are shown in the Appendix. Each of these figures represents the case of uniform illumination; in the near field, rays 1-5 would not exist. In the far field, rays 1-5 would carry over 68% of the incident power, while the remaining rays convey about 27% (recall that about 5% beam spillage around the ship is permitted). The intensity at the focal point may be calculated at different angles for each of the three intensity distributions; the results are summarized in Table 7.1. Note the different intensities generated on either side of the craft. For the cases considered, a sufficient intensity to provide useful thrust was always maintained. The focal point moves in opposite directions on either side of the ship for small angles. This creates asymmetric thrust, which tends to push the craft back towards normal incidence; thus, for errors of 0.5 degrees or less, the LTD remains stable. However, it is still important that the LTD detects errors of this magnitude (or greater) and takes corrective action.

A system to sense and correct for large pointing errors is also proposed for the LTD. Even for the torus and uniform intensity distributions, a small amount of light leaks around the vehicle due to scattering; in the far field, the light in the Gaussian tails of the pulse becomes significant. A set of corner cube retroreflectors could be placed around the shroud trailing edge to intercept this light and reflect it back to the source. A detector array distributed around the transmitter source aperture (i.e., on the ground) could sense these reflected signals, and the distance to different parts of the shroud could be calculated by laser rangefinding techniques. Adaptive optics at the source would then be able to compensate for pointing errors before subsequent laser pulses were delivered to the vehicle. A total of 24 retroreflectors could be placed on the LTD (one for each shroud support strut), each with an area of about 1 cm². The maximum laser intensity assumed to exist at this point is about 6.08% of the peak intensity in the far field; this should not damage the highly reflective corner cubes, and still provides a sufficient signal for rangefinding. If the ranging signal proves to be too weak in the near or medium field, the power beam can be tailored to spill slightly more light around the LTD for this purpose. Typical satellite laser rangefinding systems exhibit range accuracies of 1 cm. If the retroreflectors are placed at the shroud edge, 0.7 m from the vehicle centerline, then a difference of 1 cm between either side of the ship corresponds to a pointing error of 0.477°, which is adequate resolution for our purposes.

Assuming the same maximum range used in the beam spread calculations, the

power beam would take 1.867 ms to reach the vehicle at maximum range. This provides a round trip time for the ranging signal of 3.733 ms. If the laser power beam is assumed to operate at 100 Hz, this provides 6.267 ms between successive laser pulses to adjust parameters of the beam. Recall that current designs call for a 4 m diameter transmitter aperture, which is estimated to require of the order 10^4 individual adaptive elements, each of which could be adjusted at rates of 1 to 3 kHz [3]. Accounting for the actuator response time, this leaves between 5.267 and 5.937 ms for the rangefinding and beam control systems to operate. This is within the realm of adaptive computer control systems; however, if the laser power beam operates at 1000 Hz the control system only has time to adjust every 4th pulse. This time is set by the round trip propagation time for the rangefinding signals, and cannot be overcome by more efficient adaptation algorithms or faster actuators. However, an adaptive computer controller might estimate the correction required for successive (i.e., future) laser pulses; this would allow the continuous adjustment of the source, with fine adjustments provided by rangefinding data whenever it was available.

7.5 Conclusions

This chapter describes the design and fabrication of the LTD primary receptive mirror. Although some of the physics behind propagating the high energy laser beam through the heated exhaust plume is not fully understood, the concept is shown to be within reach of current technology. The primary optic could be manufactured using existing diamond-turning lathe facilities; development of multi-layer high reflectivity coatings and microchannel cooling systems are the main technical problems encountered. The mirror must exhibit high figure quality and minimal surface roughness throughout the launch trajectory. Calculations of beam divergence indicate that a 4 m diameter adaptive ground based transmitter is entirely sufficient for a 1.0 micron wavelength. The effects of pointing error were evaluated using a computer ray trace routine; errors of 0.5 degrees, or less, shifts the focus asymmetrically on either side of the annular engine, but the effect is self-correcting and the LTD vehicle is therefore stable. At incident angles up to 1 degree, the power loss and spot size increase but do not cause a critical loss of thrust for near, intermediate, or far field beam profiles. An adaptive pointing error correction system is proposed, using retroreflectors to sample the power beam edges at 24 azimuthal locations and feed data back to the ground power source via laser rangefinding.

REFERENCES

- [1] J.R. French, "Very Small Spacecraft for Planetary Exploration Missions," USRA Lightsat conference, 1988.

- [2] A.E. Fuhs, M.R. Mosier, "A Niche for Lightweight Satellites," *Aerospace America*, 1988.
- [3] L. Myrabo and W. Smith, editor, Apollo Lightcraft Project Annual Report, NASA/USRA Advanced Design Program, 4th Annual Summer Conference, Kennedy Space Center, Florida, 1988.
- [4] R. Kingslake, *Lens Design Fundamentals*, Academic Press Inc., N.Y. (1978)
- [5] G.C. Paraskos, J.H. Ward, "Taking Advantage of Reflective Aspherics," *Photonics Spectra*, p. 159-166, 1988.
- [6] D.C. Thompson, B.L. Fix, "Tighter Tolerances at Lower Cost," *Mechanical Engineering*, p. 36-42, 1988.
- [7] BDM Corp., Assessment of Materials and Coating Requirements of UV Laser Optics, August, 1981.
- [8] J.C. Richard, C. Morales, W.L. Smith, L. Myrabo, "Laser-Boosted Lightcraft Technology Demonstrator," Proc. First Int. Conf. on Hypersonic Flight in the 21st Century, Grand Forks, N.D., Sept. 20-23, 1988; ISBN no. 0-9608700-1-6, Univ. North Dakota, Dept. of Space Studies, p. 353-365, January 1989.
- [9] J.S. Meltzer, W.L. Smith, M. Antonison, L. Myrabo, "Multi-Cycle engines for the Apollo Lightcraft," Proc. First Int. Conf. on Hypersonic Flight in the 21st Century, Grand Forks, N.D., Sept. 20-23, 1988; ISBN no. 0-9608700-1-6, Univ. North Dakota, Dept. of Space Studies, p. 489-494, January 1989.
- [10] A.S. Brown, "Diamonds Shine Brightly in Aerospace's Future," *Aerospace America*, p. 12-15, 1987.
- [11] G.P. Harnwell, J.J. Livingood, *Experimental Atomic Physics*, McGrawHill, N.Y. (1961)
- [12] R.R. Friedman, T.J. McIlrath, P.H. Bucksbaum, M. Bashkansky, "Ponderomotive Effects on Angular Distribution of Photoelectrons," *Phys. Rev. Lett.* Vol. 57, no. 23, p. 3156-3159 (1986)
- [13] L. Myrabo and J.A. Solomone, editor, "Advanced Beamed Energy and field Propulsion Concepts," final report of BDM Corp., submitted to Cal. Inst. Tech. and NASA Jet prop. Lab. (1983)
- [14] J.A. Adams, "SDI in Transition," *IEEE Spectrum* p. 32-38 (1988)

Chapter 8

MODELING OF LASER-GENERATED IMPULSE

8.1 Introduction

The focus of this chapter is to model the laser-heated blast wave and impulse-generation process using an axi-symmetric representation, that excludes radiation and conduction. Chapter 9 will review the particular methods used to remove some of the more restrictive assumptions of this case, as applied to the Lightcraft Technology Demonstrator engines in the airbreathing propulsion mode.

For the most part, air within the laser-generated blast waves is modeled as an ideal gas, throughout the expansion process. Note that the initial state (i.e., pressure, temperature, density, etc.) prior to laser-heating, is a direct function of flight Mach number and altitude (see chapter 9); hence, the graphical results in this chapter are also presented versus flight Mach number and altitude.

8.2 Initial State of an LSD Wave

The equations developed by Raizer [1,2] to describe the state of the laser-induced blast wave, were used in modeling the "line-source" blast wave expansion and impulse-generation process. The derivation is briefly presented below.

Raizer begins with the control volume in Figure 8.1, and assumes that the laser supported detonation (LSD) wave moves steadily towards the left at constant strength with no losses. He then applies the mass, momentum, and energy conservation equations in their integral forms, as reproduced below:

$$\rho_0 V_{LSD} = \rho u \quad (8.1)$$

$$p_0 + \rho_0 V_{LSD}^2 = p + \rho u^2 \quad (8.2)$$

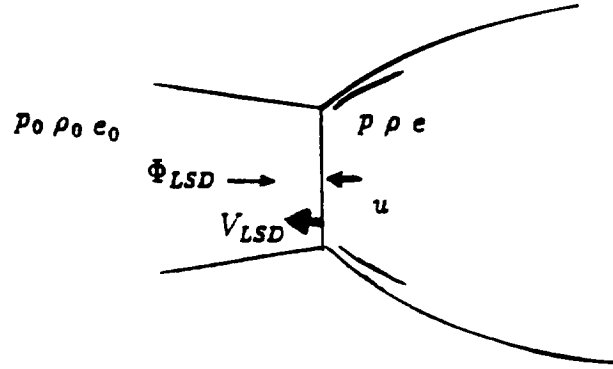


Figure 8.1: The control volume used by Raizer in modeling an LSD wave.

$$e_0 + \frac{p_0}{\rho_0} + \frac{V_{LSD}^2}{2} + \frac{\Phi_{LSD}}{\rho_0 V_{LSD}} = e + \frac{p}{\rho} + \frac{u^2}{2} \quad (8.3)$$

where ϕ_{LSD} is the laser radiation intensity, V_{LSD} is the LSD wavefront velocity, u is the gas velocity behind the LSD wavefront (measured relative to that front), p is the pressure of the fluid, and ρ is the density. Also, e represents the internal energy of the gas, which is defined as $e = RT/(\gamma - 1) = p/[(\gamma - 1)\rho]$, where R is the gas constant and T is the temperature (i.e., ideal gas assumption). The subscript '0' denotes the ambient values of a given quantity. These equations may also be obtained in other ways (i.e., see Ref. 3).

The shock adiabat is then found to be:

$$e - e_0 = \frac{(p - p_0) \left(\frac{1}{\rho_0} + \frac{1}{\rho} \right)}{2} + \Phi_{LSD} \sqrt{(p - p_0) \left(\frac{1}{\rho_0} + \frac{1}{\rho} \right)} \quad (8.4)$$

Using the equation of state, ($p = \rho RT$), an explicit expression for the shock adiabat, $p(\rho)$, of the wave can be obtained:

$$p = \left\{ \frac{2 \sqrt{1 - \frac{\rho}{\rho_0} \Phi_{LSD} \rho_0^{1/2}}}{\left[\frac{\gamma+1}{\gamma-1} \right] \left[\frac{\rho_0}{\rho} - 1 \right]} \right\}^{2/3} \quad (8.5)$$

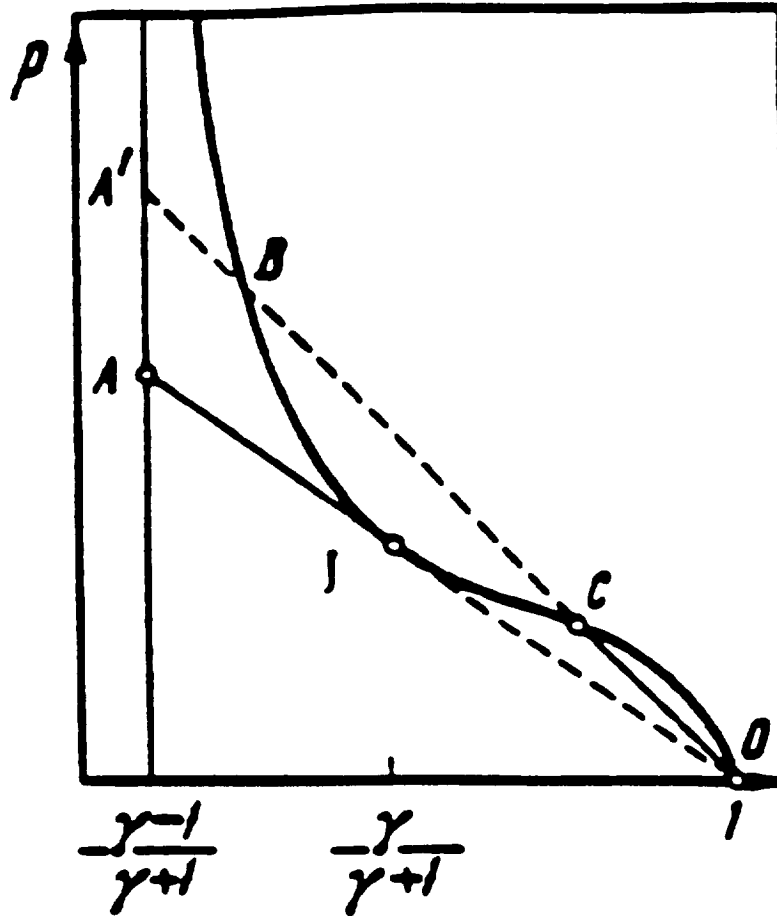


Figure 8.2: Raizer's shock adiabat for a laser radiation absorption wave (Ref. 2).

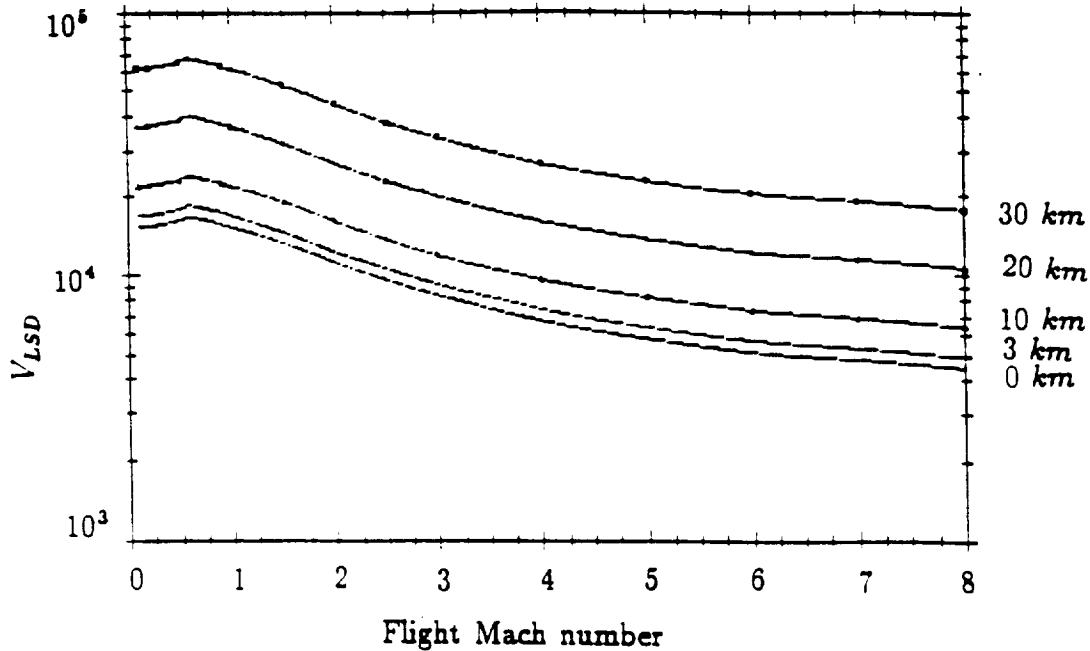


Figure 8.3: Peak *LSD* wavefront velocity vs. flight Mach number and altitude.

For a full discussion of the shock adiabat plotted in Figure 8.2, see Raizer [2].

The curve B-C-O in Figure 8.2 represents Eqn. 8.5. The point J gives the pressure for a strong detonation wave, according to Chapman-Jouguet theory (see Thompson, Ref. 4). The point C represents a deflagration wave. *LSD* waves are expected to be strong detonation waves.

With the CJ values much greater than ambient, and $c_{s,CJ} = \sqrt{(\gamma p/\rho)_{CJ}} = V_{LSD} - v_{r,CJ}$, it is found that $c_{s,CJ} = \gamma v_{r,CJ}$. However, with γ close to 1, $c_{s,CJ} = v_{r,CJ}$ so that $c_{s,CJ} = V_{LSD}/2$, in agreement with Chapman-Jouguet theory (i.e., a resultant local Mach number of $M_{CJ} = 1$). Also, the velocity of the wavefront is found to be:

$$V_{LSD} = \left[2(\gamma^2 - 1) \frac{\Phi_{LSD}}{\rho_0} \right]^{\frac{1}{3}} \quad (8.6)$$

and the pressure directly behind the *LSD* wavefront is:

$$p_{DW} = \frac{\rho_0 V_{LSD}^2}{\gamma + 1} \quad (8.7)$$

The *LSD* wavefront Mach number (through ambient air, and right after initiation), can be defined as $M_{LSD} = V_{LSD}/\sqrt{\gamma RT_{ambient}}$, using the local ambient gas temperature. This Mach number can be as high as 250.

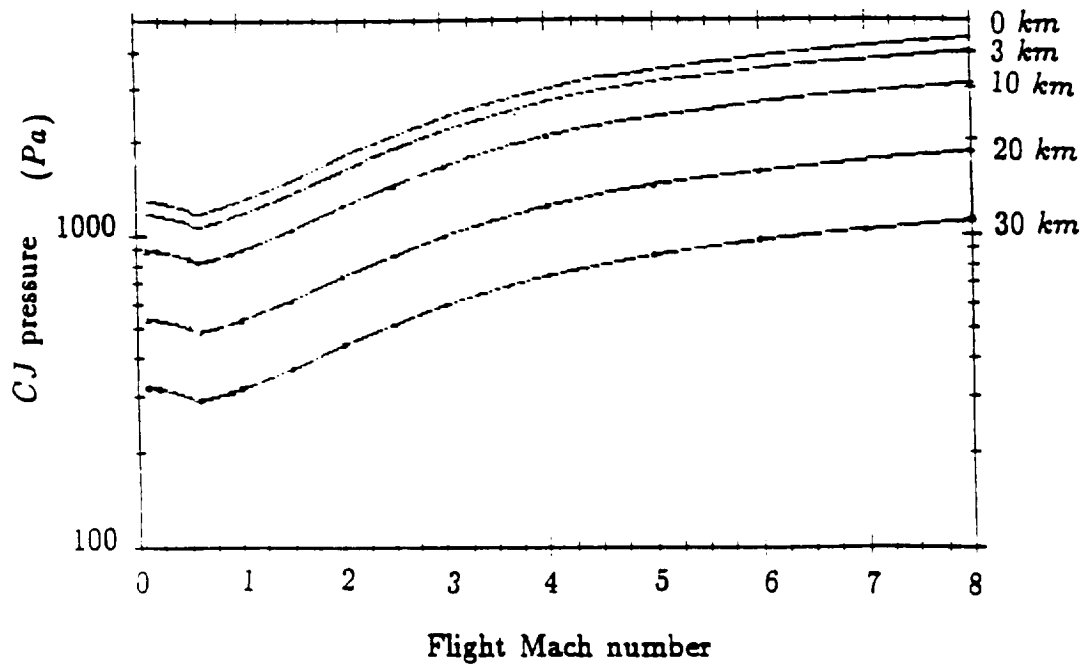


Figure 8.4: *CJ* pressure vs. flight Mach number and altitude.

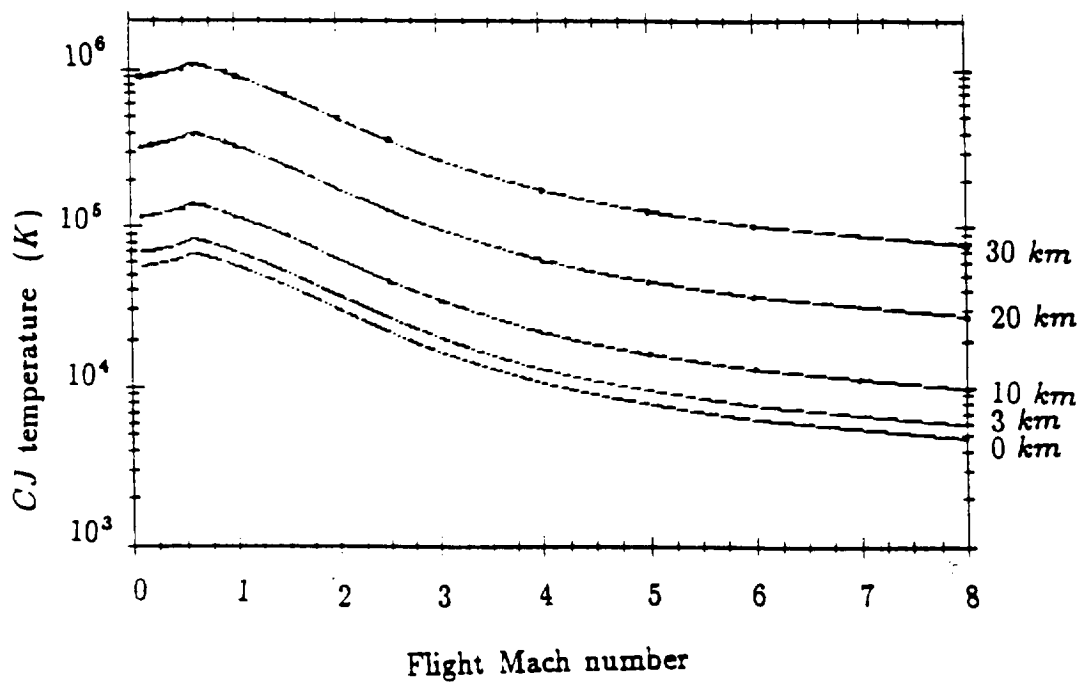


Figure 8.5: *CJ* temperature vs. flight Mach number and altitude.

While plasma temperatures can be very high, these conditions exist only for cycle times on the order of a millisecond. Peak plasma temperatures occur over shorter time intervals within small volumes that are somewhat removed from material surfaces. Due to the pulsed nature of the impulse generation process and the feasibility of including active cooling systems for material surfaces, these thermal problems appear surmountable. This report does not examine external-radiation-heated (ERH) thruster heat transfer characteristics, but such aspects certainly need further study.

It is noted that Raizer's equations do not incorporate real gas behavior, which is complicated because of the dissociation and ionization effects. Hence the extreme plasma temperatures predicted in Figure 8.5 would never be realized; peak values of 10,000 K to 30,000 K are more in agreement with reality.

8.3 Application of the Method of Characteristics

The method of characteristics may be used with Raizer's equations to describe the blast wave expansion process. The following is based on such a model as similarly discussed by Holmes *et al* (Ref. 12), and is covered in greater depth by Liepmann and Roshko [5].

The key equations are:

$$\frac{\partial \rho}{\partial t} + v_r \frac{\partial \rho}{\partial r} + \rho \frac{\partial v_r}{\partial r} + \frac{\rho v_r}{r} = 0 \quad (8.8)$$

$$\frac{\partial v_r}{\partial t} + v_r \frac{\partial v_r}{\partial r} = -\frac{1}{\rho} \frac{\partial p}{\partial r} \quad (8.9)$$

$$\frac{dp}{d\rho} = c_s^2 \quad (8.10)$$

which are basically the same expressions presented earlier. Information from the energy and state equations is contained in Eqn. 8.10. As before, ideal gas behavior and isentropic flow conditions are assumed.

If the radius, r , of the shock front is much greater than its thickness, the wave can be assumed to move out with a planar front; hence, the $1/r$ term can be neglected.

If Eqns. 8.8 and 8.9 are multiplied by the speed of sound, c_s , then Eqn. 8.10 can be used to remove p from these expressions. After addition and subtraction of the resulting equations one obtains:

$$\left[\frac{\partial}{\partial t} + (v_r \pm c_s) \frac{\partial}{\partial r} \right] \left(v_r \pm c_s \frac{d\rho}{\rho} \right) = 0 \quad (8.11)$$

which is equivalent to

$$\left[\frac{\partial}{\partial t} + (v_r \pm c_s) \frac{\partial}{\partial r} \right] \left(v_r \pm 2 \frac{c_s}{\gamma - 1} \right) = 0 \quad (8.12)$$

using the ideal gas assumption of $\gamma = \text{constant}$.

From this, it is reasonable to write

$$\frac{D^\pm}{Dt} \left(v_r \pm 2 \frac{c_s}{\gamma - 1} \right) = 0 \quad (8.13)$$

as a differential if

$$\frac{dr}{dt} = v_r \pm c_s \quad (8.14)$$

From these relations, it can be said that

$$v_r \pm 2 \frac{c_s}{\gamma - 1} = \text{constant} \quad (8.15)$$

along the paths

$$\frac{dr}{dt} = v_r \pm c_s \quad (8.16)$$

Equation 8.15 yields the Riemann invariants, so called because these do not vary along the *characteristic* paths given by Eqn. 8.16. The Chapman-Jouguet condition which detonation must also satisfy, includes the requirement that $(v_r + c_s)_{CJ} = V_{LSD}$ (see Courant and Friedrichs [6]).

Thus, the “+” characteristic path is the path of the shock; The “-” characteristic is the path of a rarefaction wave which travels at the velocity, $v_r - c_s$. The latter carries information from the blast wave initiation point towards a direction opposite that of the shock, if $v_r < c_s$.

As illustrated in Figure 8.6 (from Liepmann and Roshko), both shock and rarefaction waves start out with a high pressure region bounded at, say, $r = 0$ and $t = 0$; the gas starts to move for $t > 0$.

Holmes uses the above results to calculate the pressure at the surface, where $v_r = 0$. The “surface” pressure has been misleadingly denoted by many researchers as p_{LSD} , which is different from the other parameters associated with *CJ* conditions and using the subscript *LSD*. The actual surface pressure is found to be:

$$p_{LSD} = \left(\frac{\gamma + 1}{2\gamma} \right)^{\frac{2\gamma}{\gamma - 1}} p_{DW} = \left(\frac{\gamma + 1}{2\gamma} \right)^{\frac{2\gamma}{\gamma - 1}} p_{CJ} = \left(\frac{\gamma + 1}{2\gamma} \right)^{\frac{2\gamma}{\gamma - 1}} \frac{\rho_0 V_{LSD}^2}{\gamma + 1} \quad (8.17)$$

which is plotted in Figure 8.7.

Barnard and Bradley [7] have noted that real chemical detonations depart from ideal theory in that pressure, temperature and density distributions may appear as in Figure 8.8 (planar detonation wave front). Note that the gas conditions remain constant over a short induction period immediately behind the detonation front. For an *LSD* wave, it is possible to have the pattern pictured in Figure 8.9.

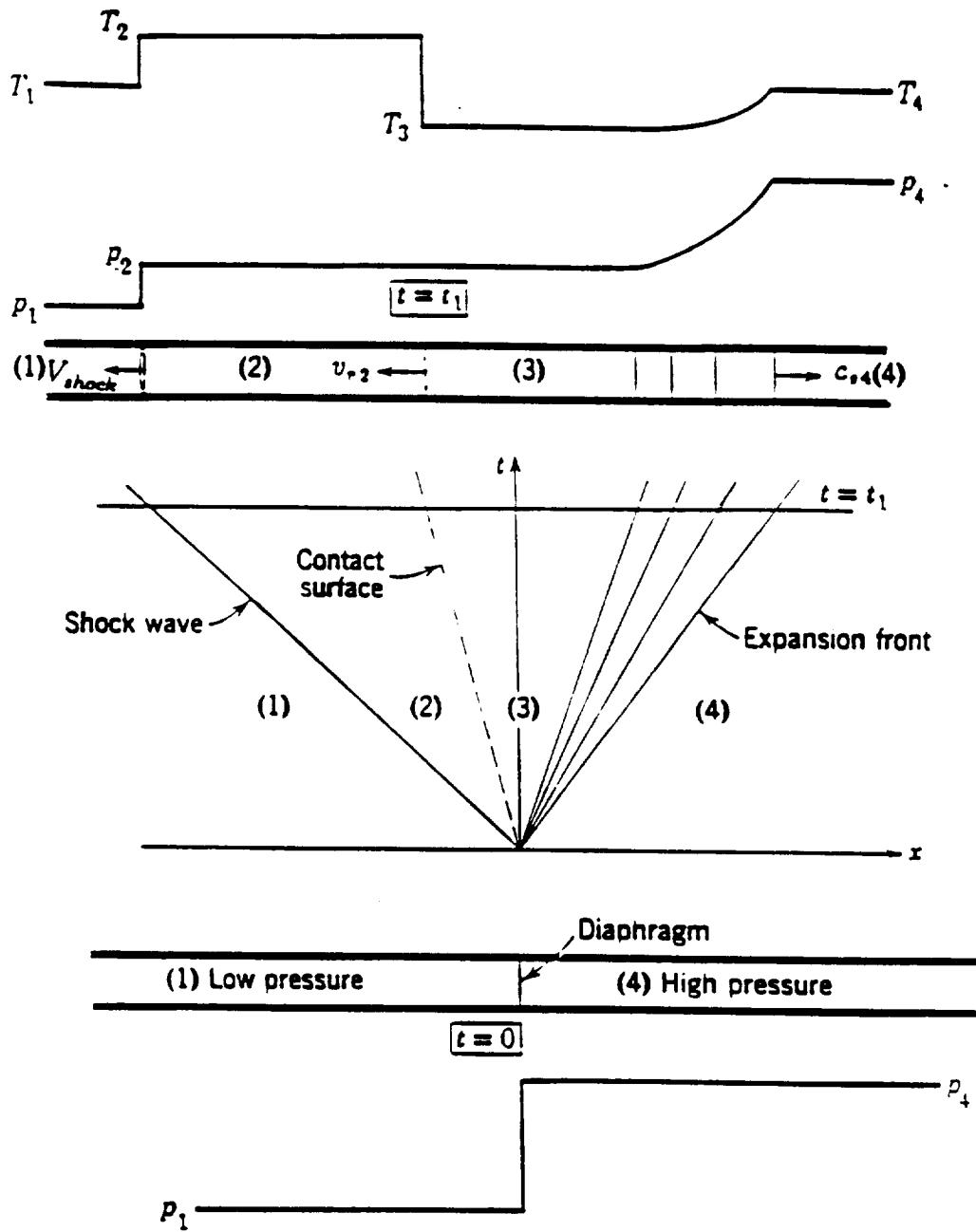


Figure 8.6: Shock tube gas dynamics.

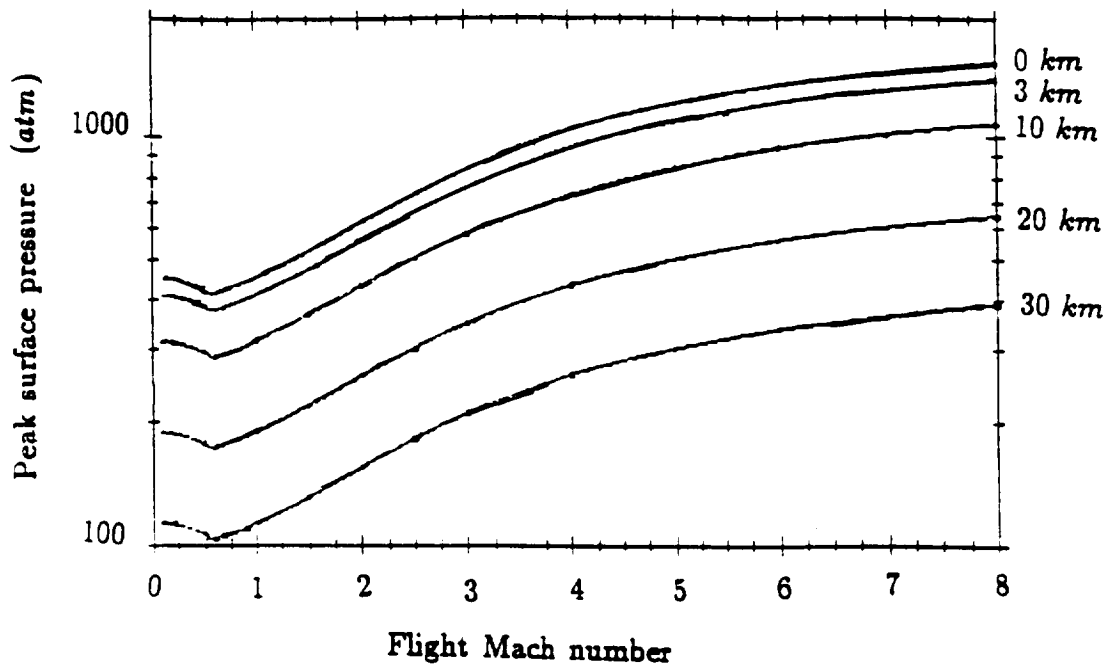


Figure 8.7: Peak surface pressure, before cylindrical blast wave decay.

8.4 Sedov's Solution of the Equations

The self-similar solutions for the above-mentioned differential equations (under axisymmetric and isentropic assumptions) were analyzed by Sedov [8] and also reviewed by Whitham [9]. These solutions are applied in the laser-generated blast wave and impulse model for the LTD engine.

The term "self-similar" describes a type of flowfield in which the value of a certain dependent variable (e.g., p , ρ , T , v_r , etc.) is scaled by its value at some specific reference point. This reference point may coincide with the given initial conditions, or another point where the value must be determined. In any case, a relationship must exist between the dependent variables such that the flow parameters exhibit a similar pattern along the flow field.

The method of characteristics is used only for that portion of the blast wave evolution which is assumed planar (for $t \approx t_p$); the Sedov equations are applied afterwards, when the blast wave has evolved into a cylindrical shape. The method of characteristics is unnecessarily complicated for the simple one-dimensional problem being studied, since one must track the rarefaction and compression waves with this approach. Although much could be learned about the blast wave structure using the method of characteristics, only one specific item (surface pressure) is pursued here; full knowledge of the effects of the rarefaction waves' motions and reflections must

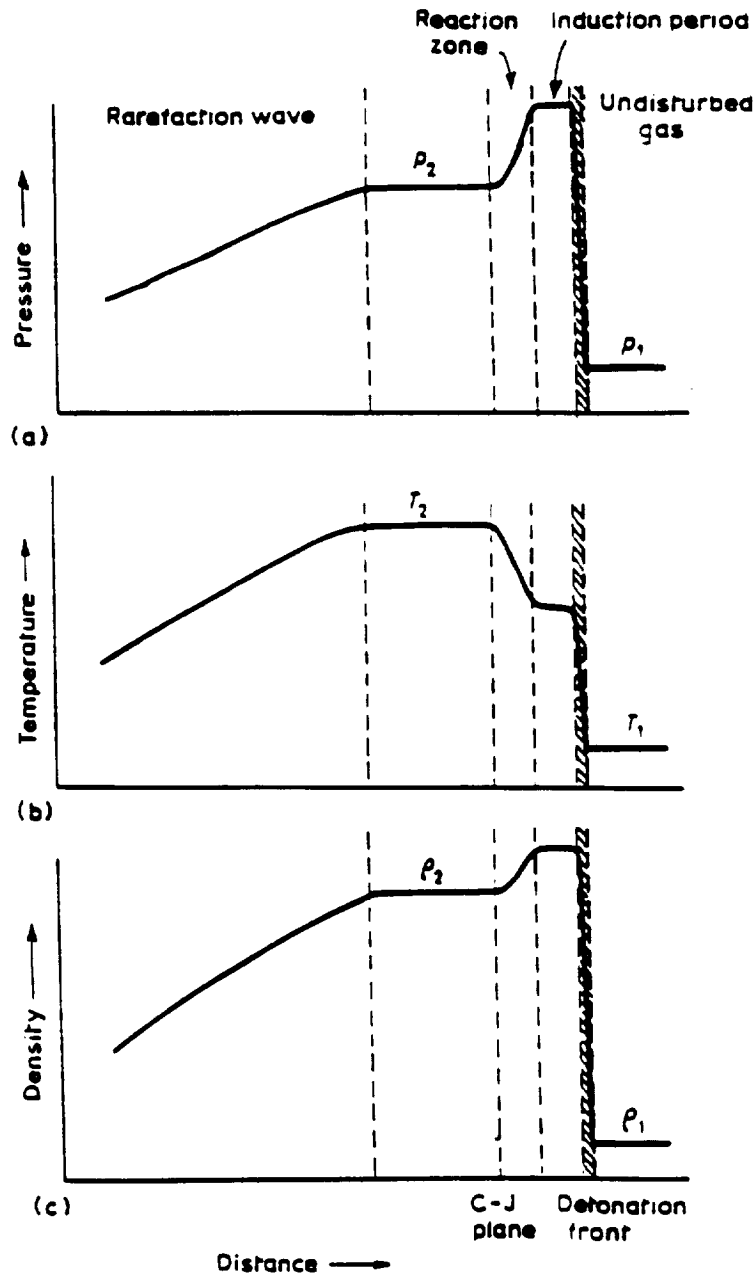


Figure 8.8: A real chemical detonation (Ref. 7).

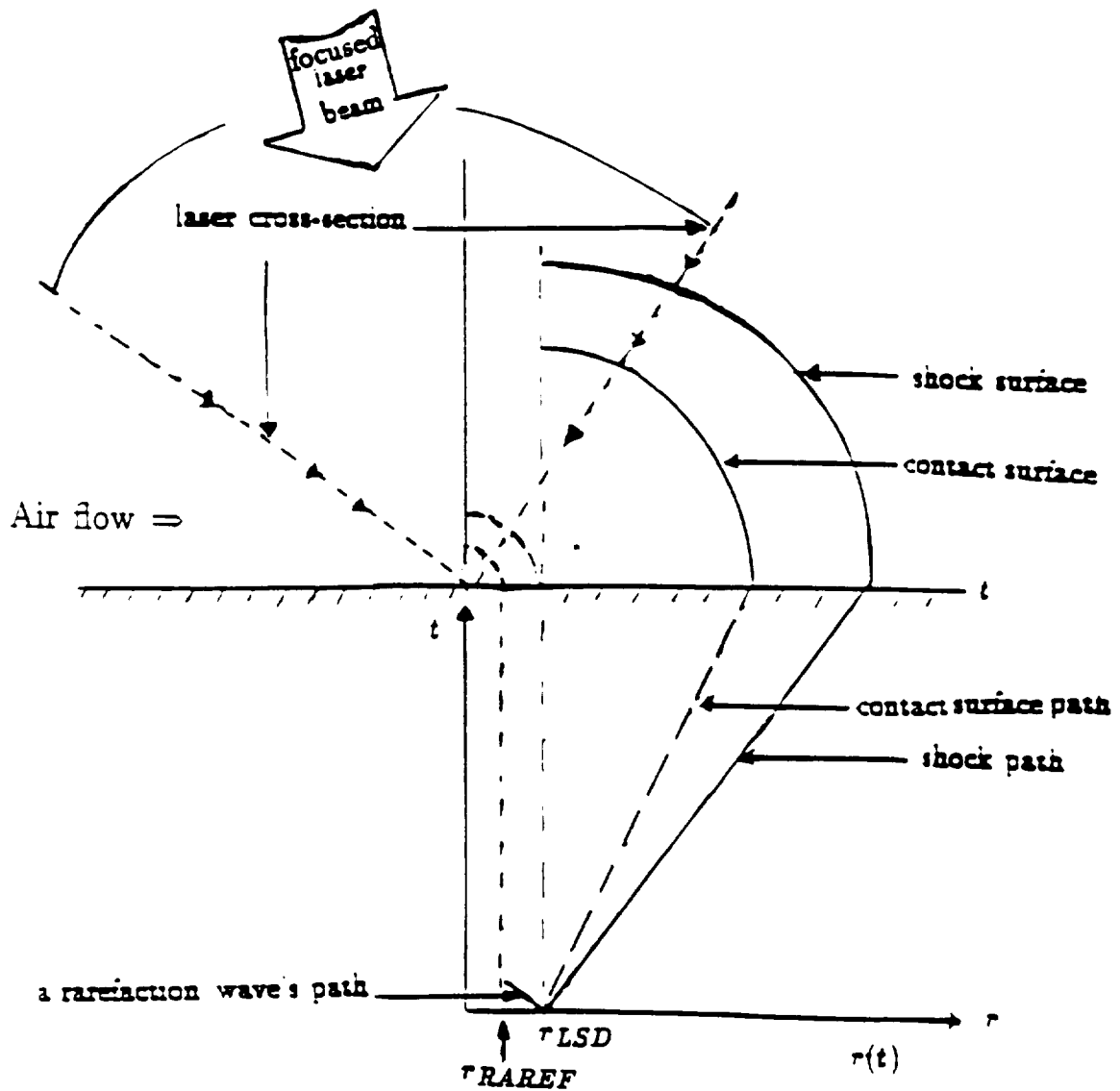


Figure 8.9: Dynamics of a propagating Laser Supported Detonation.

await a future study.

Sedov had also considered the case of a one-dimensional, axially propagating blast wave and a radially propagating, spherically-symmetric blast wave. These additional cases are mentioned here for comparison; Sedov's scaling laws are all presented in Table 8.1 (Reilly [10], and Sedov [8]). Sedov is generally recognized as the first to derive closed-form, self-similar solutions for the blast wave problem.

Because of the scaling relationship used in self-similar solutions, it is assumed that variables can be arranged into a non-dimensional form. Sedov's approach uses dimensional analysis. He claims that since the dimensions of p and ρ contain 'mass', there is at least one constant, a , whose dimensions also contain 'mass'. This constant must then be a characteristic parameter of the problem. Hence, the arrangement of the dimensions for a can be arbitrarily chosen, and Sedov assumes

$$[a] = ML^kT^s \quad (8.18)$$

This is a definition which outlines a 's dependence on 'mass'. Here 'mass' is denoted by M , T is 'time' and L is 'length'. The exponents k and s are to be determined.

The dependent variables are non-dimensionalized by setting

$$v_r = \frac{r}{t} v'_r, \quad \rho = \frac{a}{r^{k+3t^s}} \rho', \quad p = \frac{a}{r^{k+1t^s+2}} p' \quad (8.19)$$

with the non-dimensional, 'prime' variables as yet unknown. However, they are generally dependent on two non-dimensional variables.

If another characteristic parameter b is introduced with dimensions independent of a , the number of independent variables which can be formed by combining a and b is reduced to one. Since the dimensions of a include M , it can be excluded from the units chosen for b ; hence,

$$[b] = L^m T^n \quad (8.20)$$

The single non-dimensional independent parameter in this case is thus $r^{m/n} t^n / b$ which for $m \neq 0$ can be written as

$$\zeta = \frac{r}{b^{m/n} t^\beta} \quad (8.21)$$

where $\beta = -n/m$.

In generalizing his analysis, Sedov writes Eqns. 8.22, 8.23 and 8.24 as

$$\frac{\partial \rho}{\partial t} + \frac{\partial \rho v_r}{\partial r} + (\nu - 1) \frac{\rho v_r}{r} = 0 \quad (8.22)$$

$$\frac{\partial v_r}{\partial t} + v_r \frac{\partial v_r}{\partial r} = -\frac{1}{\rho} \frac{\partial p}{\partial r} \quad (8.23)$$

$$\frac{\partial}{\partial t} \left(\frac{p}{\rho^\gamma} \right) + v_r \frac{\partial}{\partial r} \left(\frac{p}{\rho^\gamma} \right) = 0 \quad (8.24)$$

where $\nu = 1$ for plane flow, $\nu = 2$ for flow with cylindrical symmetry, and $\nu = 3$ for flow with spherical symmetry.

Sedov claims that the solutions of Eqn's 8.22-8.24, may contain a number of arbitrary constants, depending on the independent variable. When the characteristic parameters include two constants with independent dimensions (in addition to r and t), he shows that the partial differential equations for v_r , ρ and p can be replaced by ordinary differential equations for v'_r , ρ' and p' . The solutions of these ordinary differential equations can, for some cases, be found in closed form while others can only be solved approximately.

The ordinary differential equations are very complicated and need not be solved to obtain the information required. It is noted that the total energy between two moving surfaces represented by r' and r'' respectively, is given by

$$E \propto \int_{r'}^{r''} \left(\frac{v^2}{2} + e \right) \rho r^{\nu-1} dr \quad (8.25)$$

and that the dimensions of E are $ML^{\nu-1}T^{-2}$. The change in fluid energy between the two surfaces mentioned equals the pressure work, which is proportional to

$$(p'' v''_r (r'')^{\nu-1} - p' v'_r (r')^{\nu-1})$$

A possible functional form of E is

$$E = ab^{\nu-1-k} t^{\beta(\nu-1-k)-2-s} f(\zeta'', \zeta', \dots) \quad (8.26)$$

Assuming also that $r'(t)$ and $r''(t)$ are determined from $\zeta' = \text{const}$ and $\zeta'' = \text{const}$, then generally

$$\frac{dE}{dt} = [\beta(\nu - 1 - k) - 2 - s] \frac{E}{t} \quad (8.27)$$

From the energy integral

$$[s + 2 - \beta(\nu - 1 - k)] f(\zeta'', \zeta', \dots) \propto \left\{ \zeta^{\nu+2} \left[p' v'_r + (v'_r - \beta) \left(\frac{\rho' v'^2_r}{2} + \frac{p'}{\gamma - 1} \right) \right] \right\}_{r'}^{r''} \quad (8.28)$$

which can be made independent of $f(\zeta'', \zeta', \dots)$ if

$$s - \beta(\nu - 1 - k) = -2 \quad (8.29)$$

yielding

$$\zeta^{\nu+2} \left[p' v'_r + (v'_r - \beta) \left(\frac{\rho' v'^2_r}{2} + \frac{p'}{\gamma - 1} \right) \right] = \text{const} \quad (8.30)$$

Table 8.1: Sedov's Scaling Laws

	Unpowered	Powered
PLANAR	$p/p_{ref} = (t/t_{ref})^{-2/3}$ $z/z_{ref} = (t/t_{ref})^{2/3}$	$p/p_{ref} = const.$ $z/z_{ref} = (t/t_{ref})$
CYLINDRICAL	$p/p_{ref} = (t/t_{ref})^{-1}$ $r/r_{ref} = (t/t_{ref})^{1/2}$	$p/p_{ref} = (t/t_{ref})^{-1/2}$ $r/r_{ref} = (t/t_{ref})^{3/4}$
SPHERICAL	$p/p_{ref} = (t/t_{ref})^{-6/5}$ $r/r_{ref} = (t/t_{ref})^{2/5}$	$p/p_{ref} = (t/t_{ref})^{-4/5}$ $r/r_{ref} = (t/t_{ref})^{3/5}$

The condition of constant energy may be used to evaluate the constants in ζ . Using ρ_0 (as defined earlier) and E/ρ_0 as the fundamental constants in ζ , the exponents and constants in ζ are evaluated and thus,

$$\zeta = \frac{r}{\left(\frac{E}{\rho_0}\right)^{1/(2+\nu)} t^{2/(2+\nu)}} \quad (8.31)$$

A reference radius can be used with a specific reference time such that ζ remains constant, — all of which leads directly to the equations of Table 8.1. Note that this outcome allows for variations in γ within the partial differential equations. In fact, with the self-similar solution, all points throughout the blast wave expansion behave *the same*, so that the 'ref' point can be arbitrarily chosen. Naturally, this would not occur in a flow regime with complex reflections.

The powered scaling laws are supplements to Sedov's original equations, and are useful in modeling laser energy deposition. The powered scaling laws assume an energy deposition that is linear in time (see Reilly et al., [10]). Although the exponents are different, the problem is still self-similar. The 'powered' laws are valid only while the laser is on; when the laser is off (i.e., after t_p , the laser pulse duration), the unpowered scaling laws become valid.

With Sedov's scaling relations, the ordinary differential equations for v'_r , ρ' and p' do not have to be solved. Since $p = 2V_{shock}^2/(\gamma + 1)$ and $V_{shock} = dr/dt$, Raizer's equations give the initial values needed to calculate the impulse. An expression for the laser-generated impulse imparted to a thrust surface, based on a model which employs both Sedov's and Raizer's equations will now be presented. The analysis applies Sedov's equations to the LTD's cylindrically symmetric ERH thruster geometry. Table 8.1 lists pressure relationship with time and radius of the blast wave for the unpowered cylindrical case. Given these relations, the impulse can be determined in a straightforward manner.

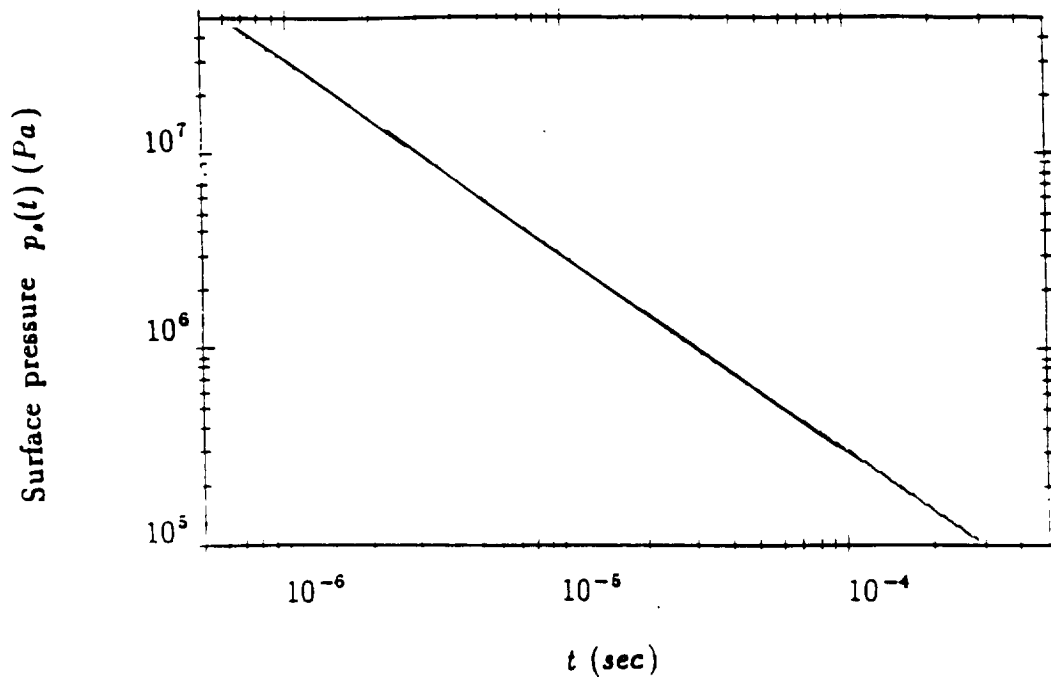


Figure 8.10: Surface Pressure vs. time using Sedov's equations ($\Phi_{LSD} = 500 \text{ MW/cm}^2$, $r_{LSD} = 0.5 \text{ cm}$, $M_\infty = 0.1$, 0 km , with P_{LSD} at t_{2D} .)

For example, using $p_{LSD} = p_{ref}$, $r_{LSD} = r_{ref} = 0.5 \text{ cm}$ and $t_{ref} = t_{2D}$, (for the conditions of $\phi = 500 \text{ MW/cm}^2$, $M = 0.1$, and $h = 0 \text{ km}$), Sedov scaling relationships give the values plotted in Figs. 8.10-8.13. Note that c_s , the speed of sound, is calculated as $V_{shock}(t)/2$, in accordance with the literature (e.g., see Reilly, [10]) while $V_{shock}(t) = dr(t)/dt$, $\rho = \gamma p/c_s^2$ and $T = p/(\rho ZR)$. The values of $\gamma = 1.2$, $Z = 3$ were assumed in this calculation. As before, the plasma temperatures indicated in Figure 8.12 greatly exceed the reasonable peak values of 10,000-30,000 K.

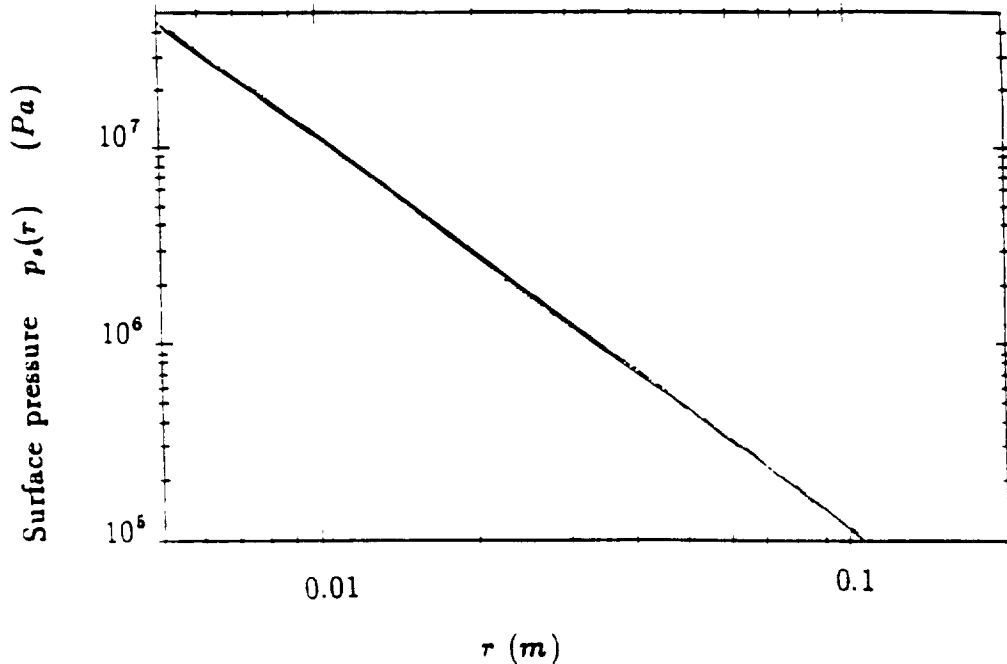


Figure 8.11: Surface Pressure vs. radius using Sedov's equations ($\Phi_{LSD} = 500$ MW/cm², $r_{LSD} = 0.5$ cm at t_{2D} , $M_\infty = 0.1$, 0 km, with P_{LSD} at t_{2D}).

8.5 Calculating the Impulse with Sedov's Scaling Laws

To enable the derivation of the impulse, a control volume is first drawn around the thrust surface as sketched in Figure 8.13. This semi-cylindrical control volume is taken to the outer edges of the ERH thruster surface and is centered on this plate. On the blast wave side of the surface, the pressure is set equal to $p_s(t)$ which is a function of the peak LSD wave pressure (given by Eqn. 8.18) via the pressure scaling relationship. On the other side of the thruster surface, the pressure is assumed to be at ambient value. Figure 8.14 shows an end view of the control volume drawn around the thrust surface. Within this context, the following equation can be derived to relate the time-resolved blast wave pressure at the surface, $p_s(t)$, the affected thruster area and the resultant impulse.

$$\int_0^{t_{final}} \int_{A(t)} [p_s(t) - p_a] dA dt =$$

$$\int_0^{t_0} \int_0^w \int_0^{r(t)} [p_s(t) - p_a] dr dz dt =$$

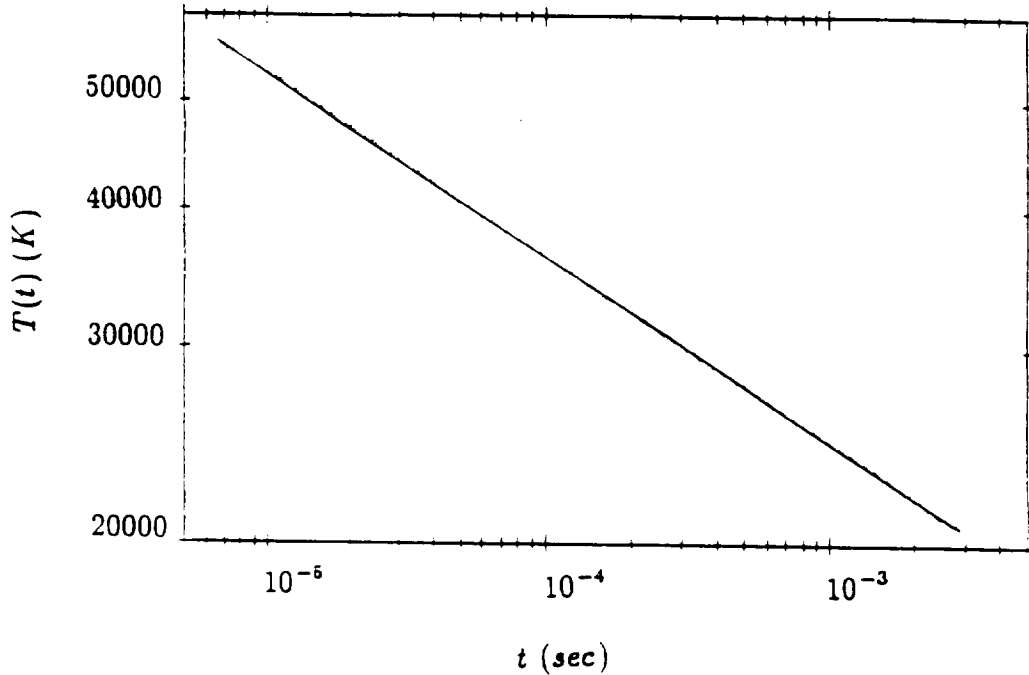


Figure 8.12: Wavefront temperature vs. time using Sedov's equations ($\Phi_{LSD} = 500$ MW/cm², $r_{LSD} = 0.5$ cm at t_{2D} , $M_\infty = 0.1$, 0 km, with T_{LSD} at t_{2D}).

$$w \int_0^{t_0} \int_0^{r(t)} [p_s(t) - p_a] dr dt \quad (8.32)$$

Equation 8.32 is the total impulse integral which depends on the time for the blast wave pressure to fall to ambient (i.e., $t_{final} = t_0 = t_a$), and on the radius of the blast wave, $r(t)$. The blast wave radius relation, $r(t)$, corresponds directly to the pressure scaling law in Table 8.1. The width, w , of the ERH thrust surface in the streamwise flow direction (see Fig. 8.15) is given by:

$$w = 2\pi(r_{ceol} + r_{ciol}) \quad (8.33)$$

where r_{ceol} and r_{ciol} are the thrust plate *exit outer lip* and *inlet outer lip*, respectively.

The LSD wave is assumed to start at the line focus of the laser beam (i.e., virtually at $r = 0$), and then propagate radially outwards at a fairly constant pressure (P_{LSD}) until the laser pulse is ended (at r_{LSD} and t_p). In reality, a very high laser intensity may be used to trigger air breakdown and ignite the LSD wave; then a lower intensity beam would sustain a relatively constant LSD wave pressure, during which the LSD wave moves at constant velocity, V_{LSD} (given by Eqn. 8.6). At $t = t_p$, (where t_p is the laser pulse duration), the wave reaches a radius defined by r_{LSD} . Hence, r_{LSD} is a convenient reference radius which is then used for the blast wave decay process (after

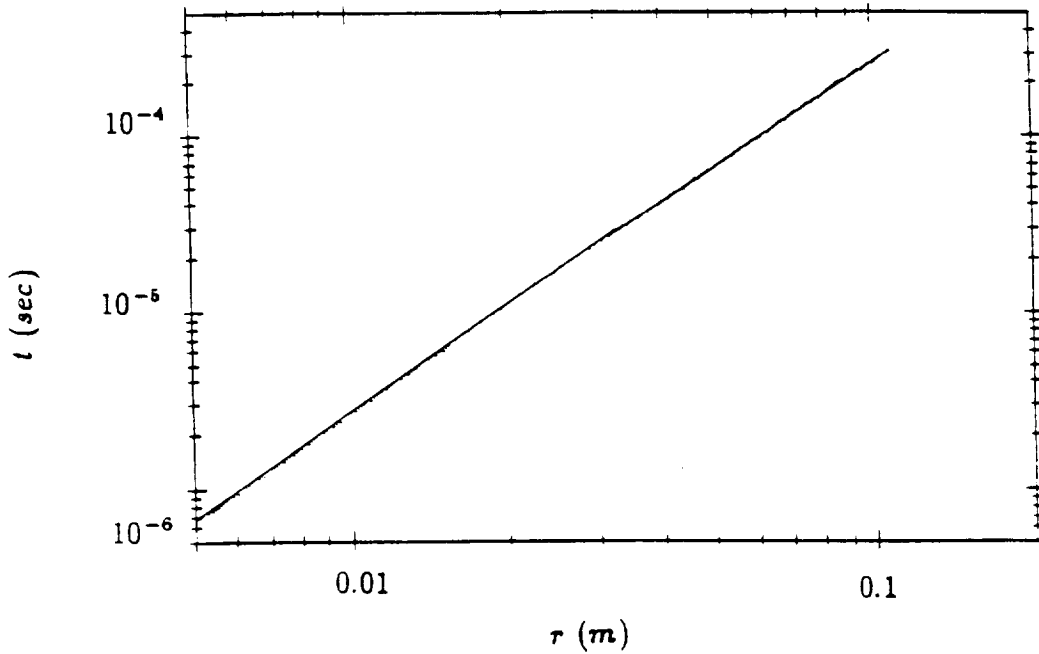


Figure 8.13: Blast wave radius vs. time using Sedov's equations ($\Phi_{LSD} = 500$ MW/cm², $r_{LSD} = 0.5$ cm at t_{2D} , $M_\infty = 0.1$, 0 km).

the laser is shut off at t_p), which is modeled with the unpowered cylindrical scaling law. If, for example, the LSD wave propagates to a height h off the surface, then

$$t_p = h/V_{LSD} \quad (8.34)$$

In this case, $h = r_{LSD}$ (although h may be small enough to be neglected in the semi-cylindrical blast wave calculation).

Shortly after the laser pulse terminates, a rarefaction wave comes in from the edges of the blast wavefront of the wave, according to method of characteristics analyses [12], at an average plasma speed of c_{LSD} , given by:

$$c_{LSD} = \frac{V_{LSD}}{2} \quad (8.35)$$

When this rarefaction fan first arrives at the centerline of the impulse surface in Figure 8.14, (at a time t_{2D}), the blast wave geometry is assumed to evolve into a completely cylindrical geometry. The time t_{2D} is given by:

$$t_{2D} = \frac{r_{LSD}}{c_{LSD}} \quad (8.36)$$

Therefore, t_{2D} may be taken as the reference time in the cylindrical unpowered scaling law. Once t_{2D} is known, the expansion (or impulse generation) time, t_0 , of the blast

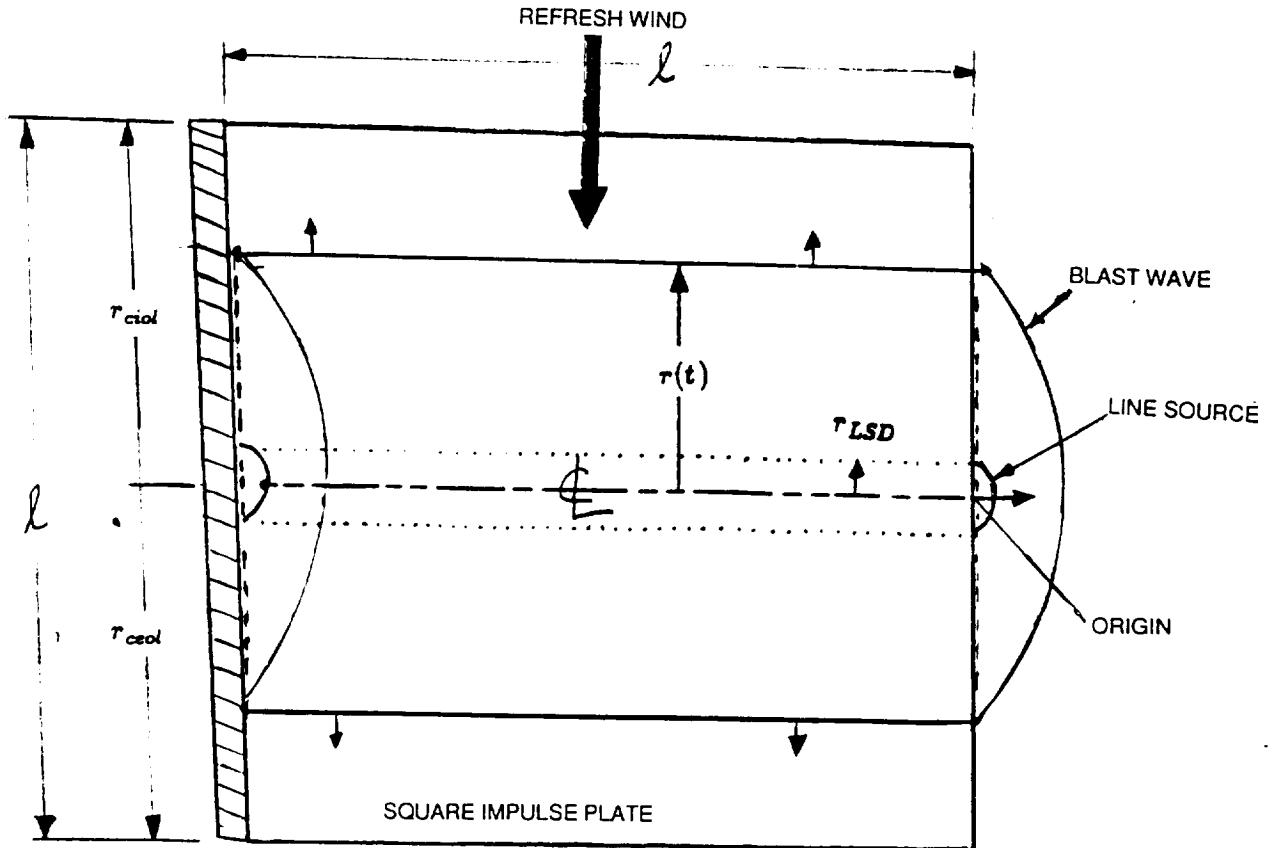


Figure 8.14: Top view of the line source showing the semi-cylindrical control volume.

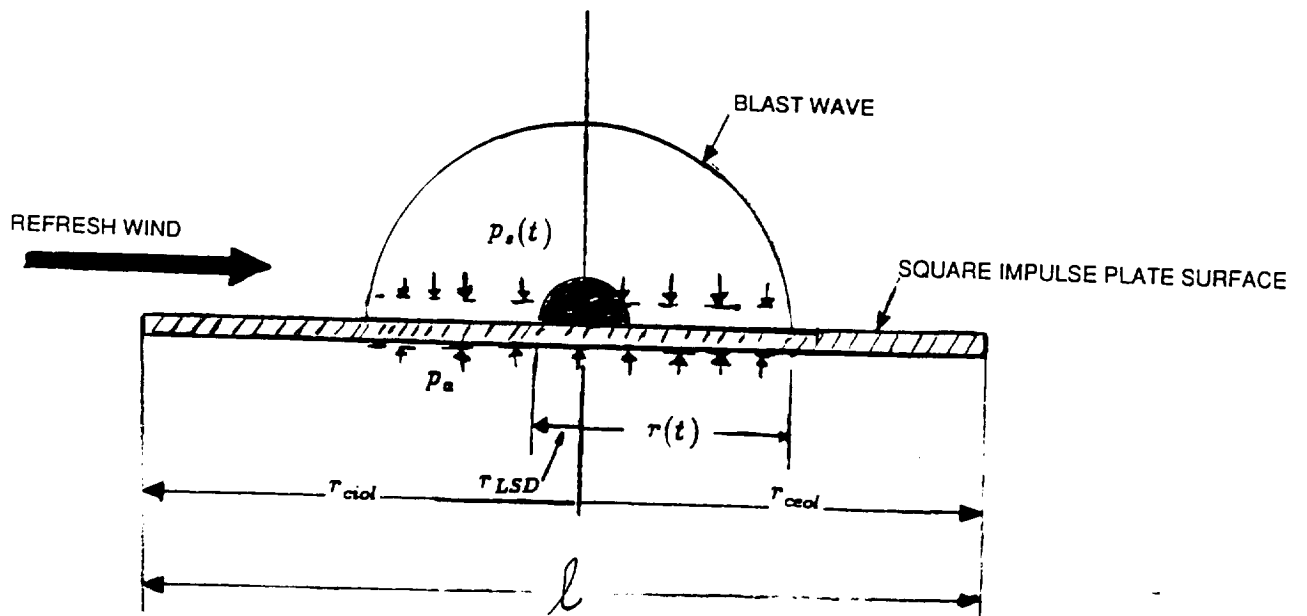


Figure 8.15: End view of the control volume drawn around the thrust surface.

wave may be calculated as:

$$t_0 = t_{2D} \frac{P_{LSD}}{p_a} \quad (8.37)$$

while the fully expanded radius, r_0 , of the wave at t_0 is:

$$r_0 = r_{LSD} \sqrt{\frac{t_0}{t_{2D}}} \quad (8.38)$$

Prior to the time t_{2D} , impulse delivered by the 'powered' planar LSD wave is treated the same as by Pirri, [11]. Thus, the first 'powered' portion of the impulse delivered to the square plate in Figure 8.14 is given by:

$$I_{pprp} = \int_0^{t_{2D}} \int_0^w \int_0^{r_{LSD}} [p_{LSD} - p_a] dr dz dt = 2\pi(r_{ceol} + r_{ciol})r_{LSD}(p_{LSD} - p_a)t_{2D} \quad (8.39)$$

Without subtracting the ambient pressure (p_a) term, one has,

$$I_{pp} = 2\pi(r_{ceol} + r_{ciol})r_{LSD}P_{LSD}t_{2D} \quad (8.40)$$

The final "laser-off" contribution of the impulse, I_{uc} , from the 'unpowered' cylindrical phase, delivered to the $l \times l$ square plate, can now be calculated.

$$\begin{aligned} I_{uc} &= wP_{LSD}r_{LSD}t_{2D} \int_{t_{2D}}^{t_0} \int_{r_{LSD}}^{r(t)} \left(\frac{p}{P_{LSD}} - \frac{p_a}{P_{LSD}} \right) d\left(\frac{r}{r_{LSD}}\right) d\left(\frac{t}{t_{2D}}\right) \\ &= 2I_{pp} \left[\left(\sqrt{\frac{P_{LSD}}{p_a}} - 1 \right) - \sqrt{\frac{P_a}{P_{LSD}}} \right] \end{aligned} \quad (8.41)$$

The total impulse is then:

$$I_{total} = 2\pi(r_{ceol} + r_{ciol})r_{LSD}P_{LSD}t_{2D} \left\{ 1 + 2 \left[\left(\sqrt{\frac{P_{LSD}}{p_a}} - 1 \right) - \sqrt{\frac{P_a}{P_{LSD}}} \right] - \frac{P_a}{P_{LSD}} \right\} \quad (8.42)$$

A computer program is used to compute through the procedure outlined above. Further details are presented in the next chapter. Note that the maximum radial extent of the thrust region (over the impulse plate) is denoted by $l/2$. If the r_0 calculated exceeds $l/2$, then the impulse calculation is terminated. This is a conservative assumption since the blast wave could be convected downstream across the impulse plate by the inlet airflow, effectively yielding larger thrust area in the upstream direction (i.e., r_{ciol}); on the other hand, r_{ceol} would be shortened. Since the wave is assumed axi-symmetric and the inlet air velocity is much smaller than that of the blast wave, this effect was not considered here. However, the experimental results obtained by Woodroffe *et al* suggest that significant beneficial effects may exist with a supersonic inlet airstream (see Ref. 13).

The peak laser power delivered into the LSD wave across a square plate of dimensions $l \times l$ is:

$$P = 2\pi r_{LSD}(r_{ceol} + r_{ciol})\Phi_{LSD} \quad (8.43)$$

From this, the peak laser energy can be obtained as follows:

$$E_p = Pt_p = 2\pi r_{LSD}(r_{ceol} + r_{ciol})\Phi_{LSD}t_p \quad (8.44)$$

The time required for fresh, unprocessed air to convect into the impulse region (in preparation for the next blast wave) is defined as $t_{refresh}$, given by:

$$t_{refresh} = \frac{l/2}{v_{r\,initial}} \text{ or } \frac{r_0}{v_{r\,initial}} \quad (8.45)$$

whichever is smaller, because this fresh air is assumed to enter after the blast wave expansion process is complete. Thruster performance is optimized with the smaller refresh time. A total engine cycle time can then be defined as:

$$t_{cycle} = t_0 + t_{refresh} \quad (8.46)$$

The engine pulse repetition frequency, PRF , is:

$$PRF = \frac{1}{t_{cycle}} = \frac{1}{t_0 + t_{refresh}} \quad (8.47)$$

Next the engine duty factor, DF , which can be interpreted as that portion of the total cycle time, over which laser energy can be applied, is:

$$DF = t_p PRF \quad (8.48)$$

Then, the time-averaged laser power spent over the cycle is:

$$\bar{P} = P_{ave} = P \times DF \quad (8.49)$$

Finally, the time-averaged thrust delivered to the $l \times l$ square plate is:

$$\bar{T} = T_{ave} = I_{total} PRF \cos \delta_c - D_{total} \quad (8.50)$$

where δ_c is the orientation angle for the shroud lower impulse surface of the LTD. Another important parameter concerns the efficiency of impulse delivery to the thruster surface: the *Coupling Coefficient*, CC , or efficiency of thrust production from the available input laser power, defined as:

$$CC = \frac{\bar{T}}{\bar{P}} = \frac{T_{ave}}{P_{ave}} \quad (8.51)$$

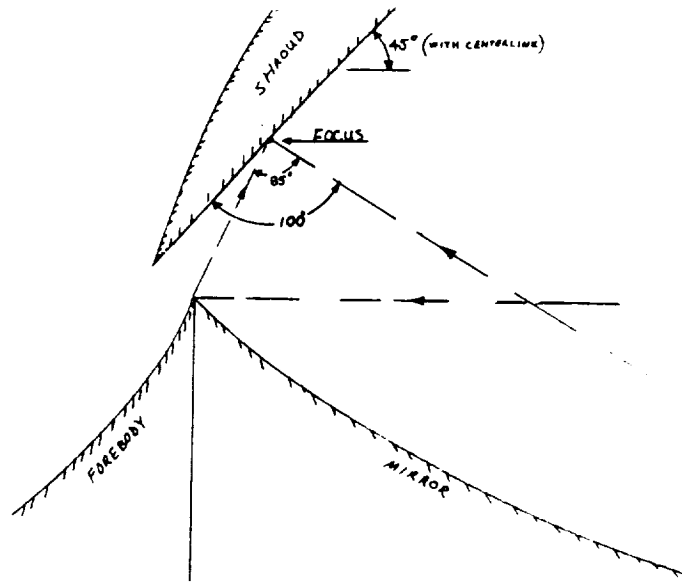


Figure 8.16: Cross sectional view of LTD ERH thruster surface

As shown in Figure 8.16, the LTD primary optic focuses the laser beam to an angle of 85° upon the ERH thruster surface, and into a LSD wave cross-section that is roughly semi-circular. Hence, it is necessary to scale the 'actual' LSD-wave plasma geometry and input laser pulse energy to the one-dimensional assumption treated above (i.e., E_p in Eqn. 8.44). Thus, only $((180/360)\pi)/2 = 78.54\%$ of the 1-D model laser pulse energy is really absorbed into the gas; this scaling ratio is incorporated in the computer code.

The principal results of the comprehensive engine performance analyses for the Lightcraft Technology Demonstrator, are presented in the next chapter — after the LTD aerodynamic inlet model is introduced. Finally, note that the important parameters described above are all plotted for the sample case of $r_{LSD} = 0.5\text{cm}$, and $\Phi_{LSD} = 500\text{MW}/\text{cm}^2$.

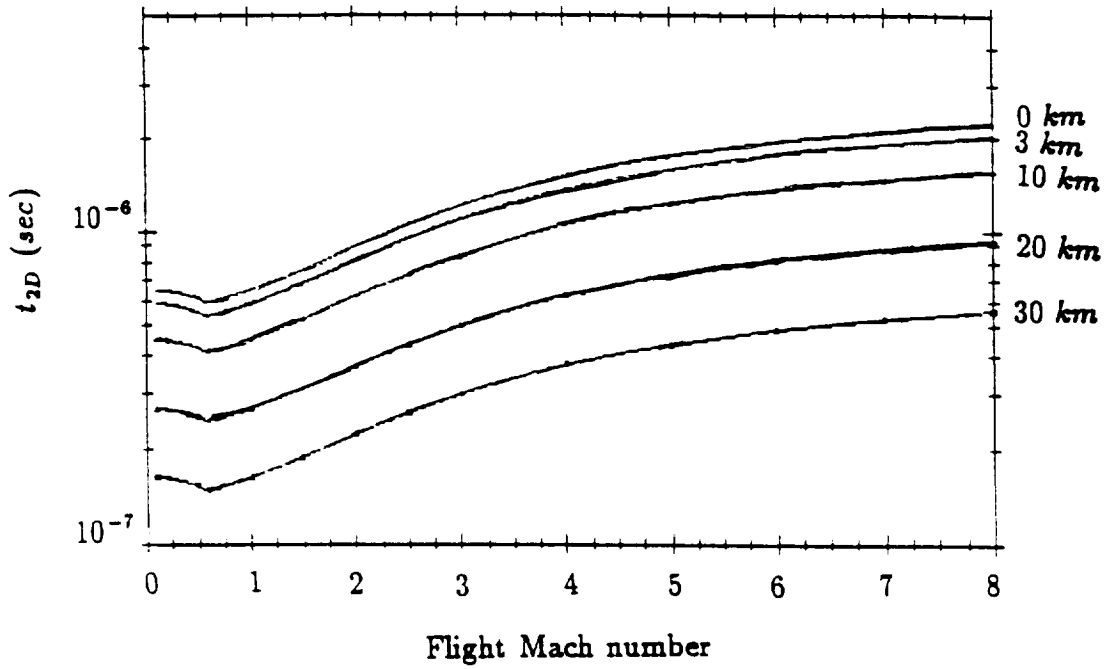


Figure 8.17: The delay time, t_{2D} , after which the blast wave assumes a semi-cylindrical shape ($\Phi_{LSD} = 500 \text{ MW/cm}^2$, $r_{LSD} = 0.5 \text{ cm}$)

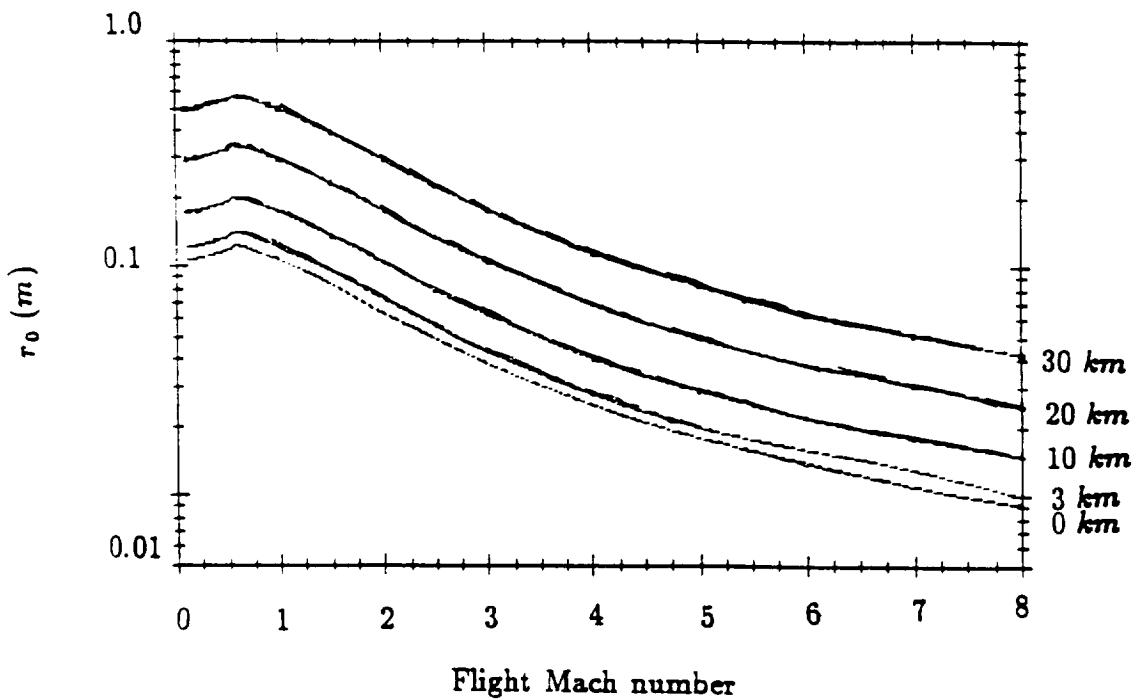


Figure 8.18: Blast wave radius after complete expansion to ambient pressure ($\Phi_{LSD} = 500 \text{ MW/cm}^2$, $r_{LSD} = 0.5 \text{ cm}$)

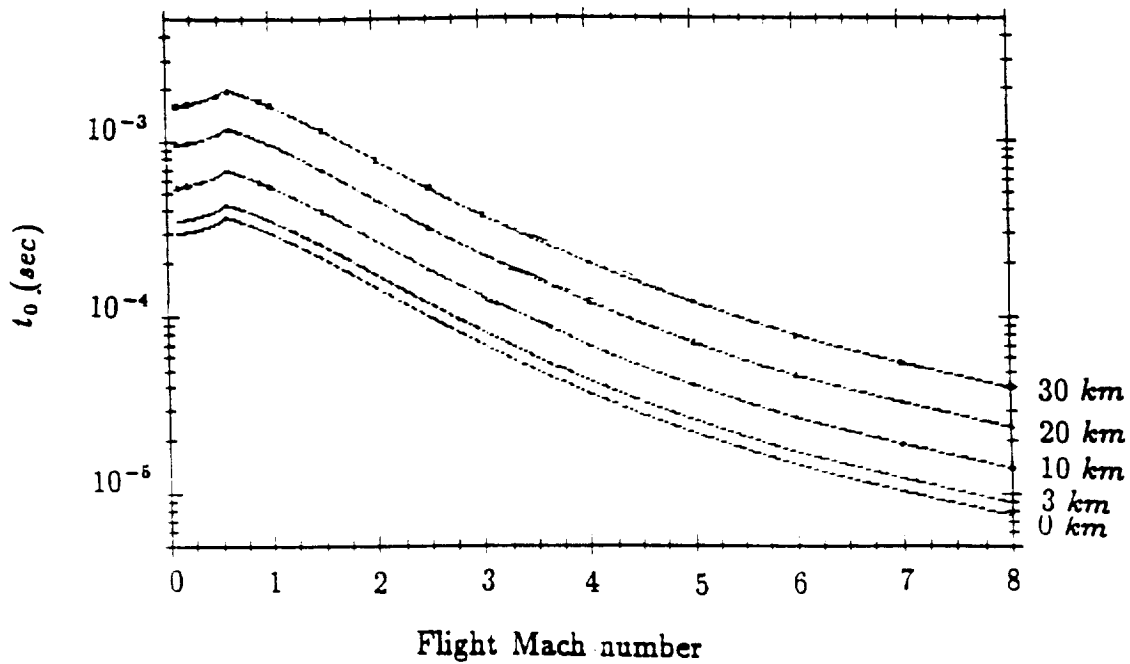


Figure 8.19: The time required for blast wave expansion to ambient pressure ($\Phi_{LSD} = 500 \text{ MW/cm}^2$, $r_{LSD} = 0.5 \text{ cm}$)

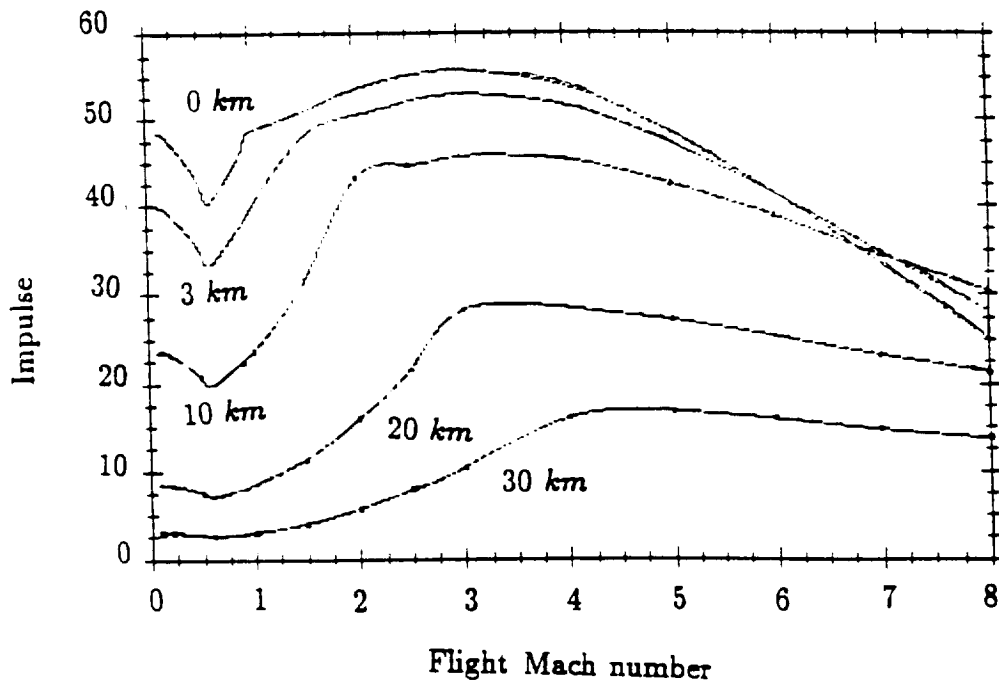


Figure 8.20: Gross impulse produced by the laser-generated blast wave for one complete engine cycle (with units of $N - sec$), for various vehicle flight conditions ($\Phi_{LSD} = 500 \text{ MW/cm}^2$, $r_{LSD} = 0.5 \text{ cm}$)

REFERENCES

- [1] Raizer, Yu P., "Heating of a Gas by a Powerful Light Pulse," *Soviet Physics, JETP*, Vol. 21, No. 5, Nov. 1965.
- [2] Raizer, Yu P., *Laser Induced Discharge Phenomena*, Consultants Bureau (Div. of Plenum Publishing), N.Y., 1977.
- [3] John, Fritz, *Partial Differential Equations*, Springer-Verlag, N.Y., 1982.
- [4] Thompson, Phillip A., *Compressible Fluid Flow*, Advanced Engineering Series, Shames, Irving H., Consulting Editor, Thompson, 1978.
- [5] Liepmann, Hans Wolfgang and Roshko, Anatol, *Elements of Gas Dynamics*, John Wiley and Sons, N.Y., 1957.
- [6] Courant, Richard and Friedrichs, Kurt Otto, *Supersonic Flow and Shock Waves*, Applied Math. Sciences Series, No. 21, John, Fritz, Sirovich, L. and Marsden, J.E., Series Editors, Springer-Verlag, N.Y., 1976.
- [7] Barnard, J.A. and Bradley, J.N., *Flame and Combustion*, 2nd ed., Chapman and Hall, N.Y., 1985.
- [8] Sedov, L.L., *Similarity and Dimensional Methods in Mechanics*, 4th Russian ed., Academic Press, N.Y., 1959.
- [9] Whitham, G.B., *Linear and Non-Linear Waves*, John Wiley and Sons, N.Y., 1974.
- [10] Reilley, J.P., Ballantyne, A. and Woodroffe, J.A., "Modeling of Momentum Transfer to a Surface by Laser-Supported Absorption Waves," *AIAA Journal*, Vol. 17, No. 10, Oct. 1979, p. 1098.
- [11] Pirri, Anthony N., "Theory for Momentum Transfer to a Surface with a High Pulse Laser," *Phys. Fluids*, Vol. 16, No. 9, Sept. 1973, p.1435.
- [12] Holmes, B.S., Targer, C., Erhlich, D., and Lindbergh, H.E., "The Mechanical Loads from LSD Waves and their Simulation, Vol. 1, Analysis and Pressure Measurements," Report No. AFWL-TR-75-285, Vol. 1, Stanford Research Institute, Stanford, Cal., July, 1976.
- [13] Woodroffe, J.A., Stanevics, J.O.A., Ballantyne, A., and Rielly, J.P., "Pulsed Laser-Generated Impulse on a Surface in Supersonic Flow," *AIAA Journal*, Vol. 18, No. 1, January, 1980, p. 94.

Chapter 9

THE LTD ENGINE PERFORMANCE ANALYSIS

9.1 Analysis of LTD Inlet Flow Aerodynamics

A simple LTD inlet flow model was developed in order to determine the state of the inlet air (pressure, temperature, velocity, etc.) which refreshes the lower annular shroud impulse surface. This aerodynamic model model* was needed not only for the refresh air state, but also for defining external drag characteristics of the entire vehicle. In the latter, it is important to distinguish between the drag produced by engine-related vs. airframe-related components, so as not to double penalize overall vehicle performance.

9.1.1 Investigative Procedure

Several basic assumptions in modeling the flow over the LTD vehicle forebody were made to simplify the aerodynamic inlet analysis. The primary objective of this model was to adequately specify fresh air flow conditions over the ERH thruster impulse area. The flow around the vehicle was assumed to be inviscid. It is also dominated by compressible flow effects since the flight regime of interest can extend to Mach 8.

A number of important considerations enter in the design of the vehicle forebody, shroud and inlet configuration. First, the inlet must provide a reasonable compromise between subsonic, supersonic and hypersonic performance. Conventional wisdom for efficient hypersonic inlets dictates a slender conical spike with a sharp point; potential pitfalls for this approach include an excessive inlet weight penalty, large boundary layer buildup and extreme heat transfer rates at the point. For certain hypersonic inlets, the boundary layer can grow thick enough to fill the entire inlet gap; temperatures within this boundary layer can be very high.

The LTD geometry in Figure 9.1 is designed to automatically bleed this hot hypersonic boundary layer; also, the shroud inlet gap is placed at a sufficiently large

radius to prevent the bow shock from being swallowed below the design Mach number (e.g., Mach 5). In addition, the inlet is fairly short so that the boundary layer does not grow large at hypersonic speeds. Although the total pressure recovery will be somewhat lower than a slender cone inlet could provide, aerodynamic heating will be much reduced for the blunt geometry, and passive thermal protection systems should be adequate; in contrast, a pointed cone would require active cooling of the tip at hypersonic speeds. Finally, the blunt inlet should give superior performance in subsonic flight. Clearly, the best compromise for the above mentioned inlet requirements can only be derived from a thorough experimental testing program. The LTD's engine is designed for the acceleration role and must exhibit a good measure of performance over a wide Mach number range; it attempts this goal with a fixed inlet geometry, but a minimally variable geometry (e.g., a translating shroud, or variable "kicker" plates) could easily be included.

Perhaps the most important inlet parameter is the velocity of air convected across the thrust generation site. To determine the flow velocity at this location, the inlet gap velocity is determined by the aggregate flow conditions over each of the cone-shaped segments that make up the LTD inlet forebody. For example, in subsonic flight the conical LTD forebody will cause the external flow to accelerate into the inlet gap at a velocity greater than the freestream, which is typical of cones and/or spheres (e.g., see White [1]). Here, the ratio of inlet gap to freestream velocity was set equal to 5/3 — up until sonic inlet conditions are reached; thereafter, choked inlet flow was assumed to remain until a flight Mach number of 1. For subsonic flight, this inlet Mach number schedule and a fixed inlet gap area directly determines inlet mass flow rate and ram drag, required in thrust calculations.

In supersonic flight, a strong bow shock is formed over the LTD inlet forebody. The Mach number after this oblique conical bow shock was calculated using the conical shock relations for a semi-vertex angle of 30° (see Shapiro [2], Kuethe and Chow [3], Oates [4] and NACA 1135 [5]). These relations were also used to compute the stagnation pressure ratio, (p_{t_1}/p_{t_∞}) , static pressure ratio (p_1/p_a) , and bow shock angle, θ_1 .

Once the gas conditions behind the conical bow shock are known, a similar process is applied to obtain the flow state behind the shock which forms over the truncated second cone which has a semi-vertex angle of 51° . This flow transition point occurs sufficiently far back on the first cone, at which the oblique shock relations for a 21° wedge can be applied — to obtain M_2 , p_{t_2}/p_{t_1} and p_2/p_1 , and θ_2 .

Figure 9.3 shows the results of this analysis for M_1 , M_2 and M_{IN} (i.e., at the inlet gap). Note that M_{IN} is assumed to be *sonic* beyond a flight Mach number of 0.6.

The overall pressure recovery of the LTD inlet is the ratio of inlet gap stagnation pressure to the freestream $(p_{t_{IN}}/p_{t_\infty})$, which is obtained by multiplying the stagnation pressure ratios across the first and second shocks. Note in Figure 9.2 that the inlet gap

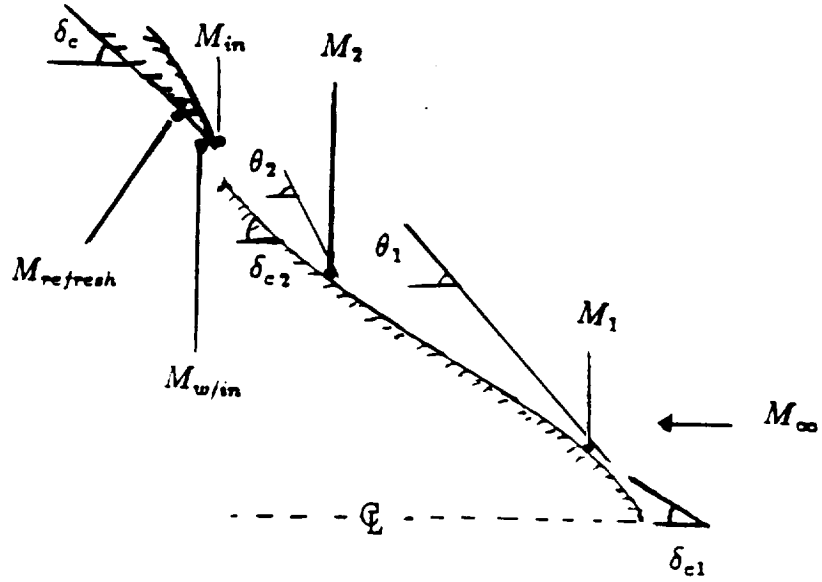


Figure 9.1: LTD forebody flow parameters.

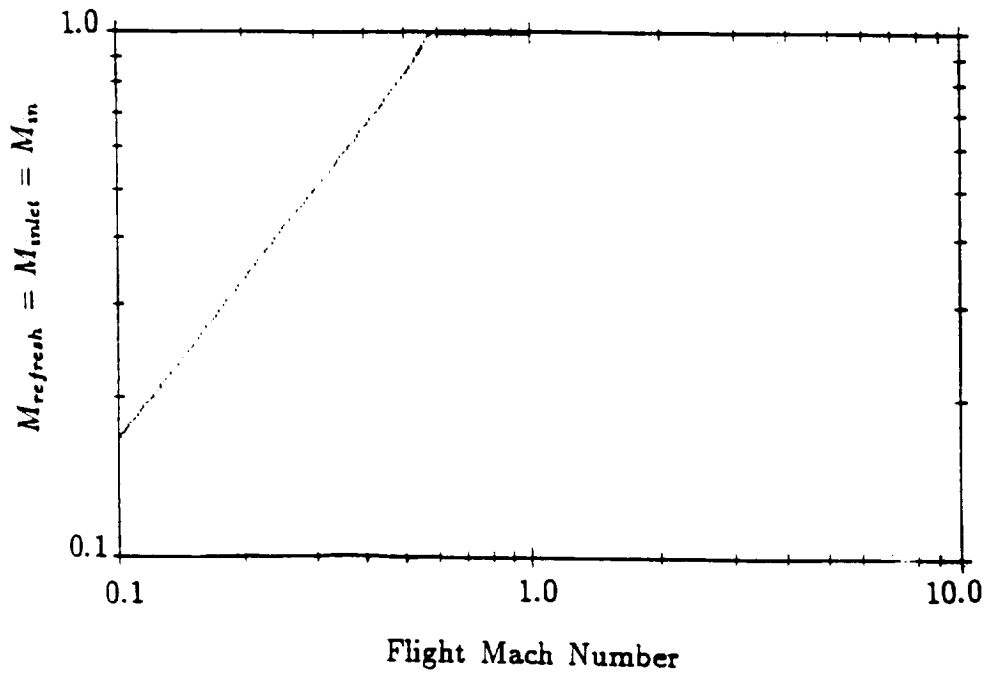


Figure 9.2: LTD inlet Mach number schedule for subsonic flight speeds.

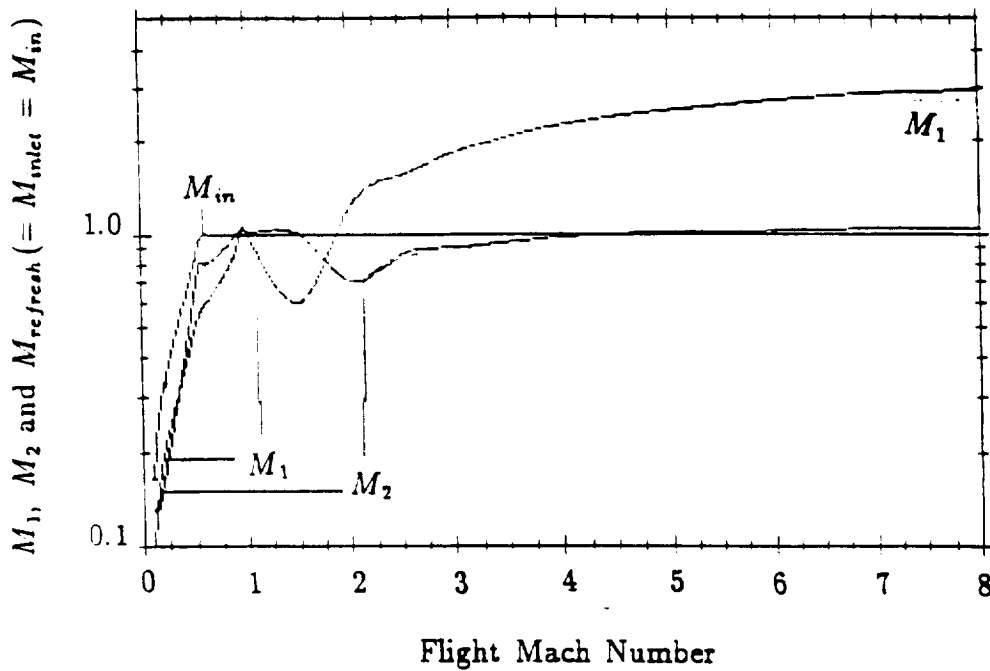


Figure 9.3: LTD forebody/inlet Mach number schedule assumed for supersonic flight speeds. 30° and 51° cones (semi-vertex angle) model the forebody geometry.

is choked beyond a flight Mach number of 0.6. The inlet pressure recovery schedule is plotted in Figure 9.4. No real gas effects have been included in this analysis.

With the above information, the inlet gap velocity can now be calculated as:

$$u_{in} = \sqrt{\frac{\gamma p_{in}}{\rho_{in}}} \quad (9.1)$$

where p_{in} is the inlet gap static pressure and ρ_{in} , the density. The inlet static pressure and temperature are plotted in Figures 9.5 and 9.6 (respectively) as a function of LTD flight Mach number and altitude.

First the stagnation temperature is calculated from

$$\frac{T_{t\infty}}{T_\infty} = 1 + \frac{\gamma - 1}{2} M_\infty^2$$

The stagnation temperature is constant across all shocks throughout the inlet flow; hence, ($T_{t\infty} = T_{tin}$). This fact is used with the following relationship to calculate T_{in} .

$$\frac{T_{tin}}{T_{in}} = 1 + \frac{\gamma - 1}{2} M_{in}^2$$

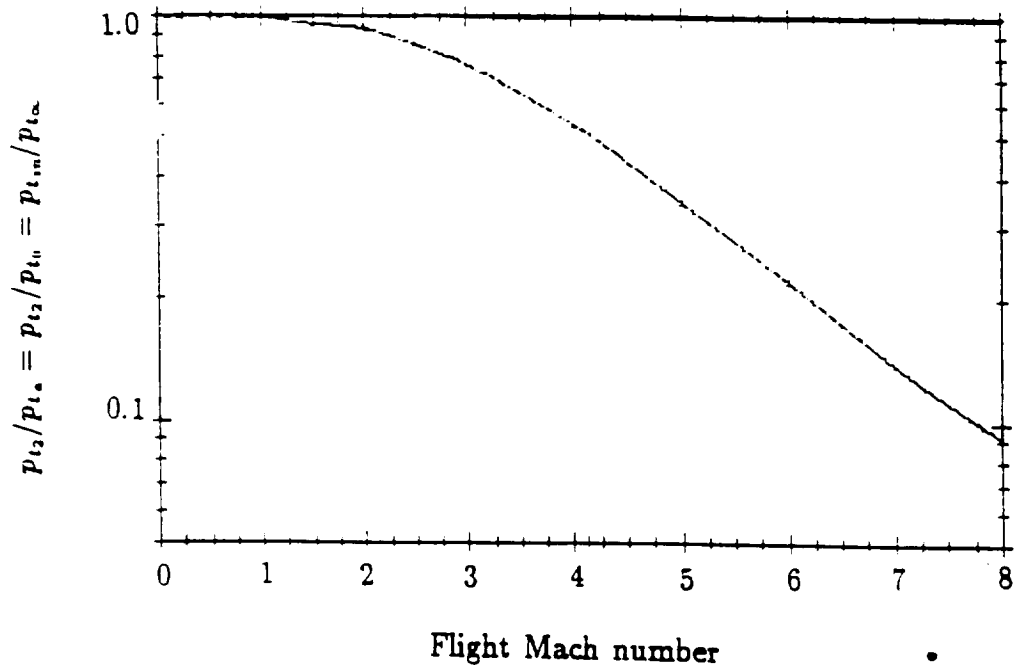


Figure 9.4: Stagnation pressure recovery schedule for the LTD inlet .

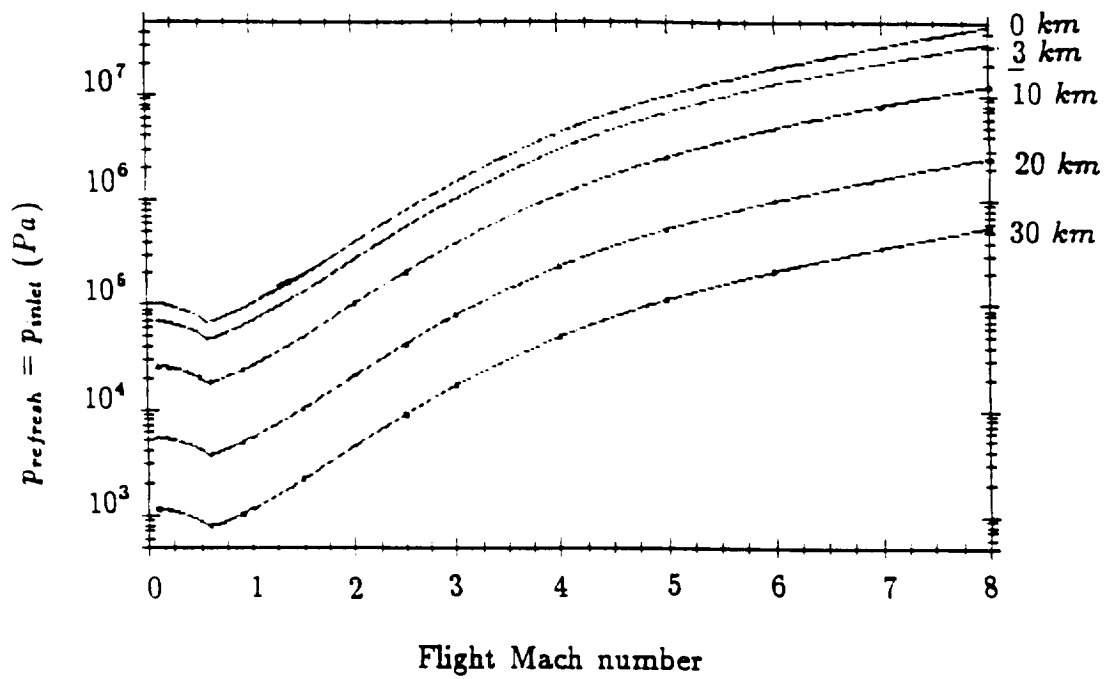


Figure 9.5: Inlet static pressure vs. Mach number and altitude.

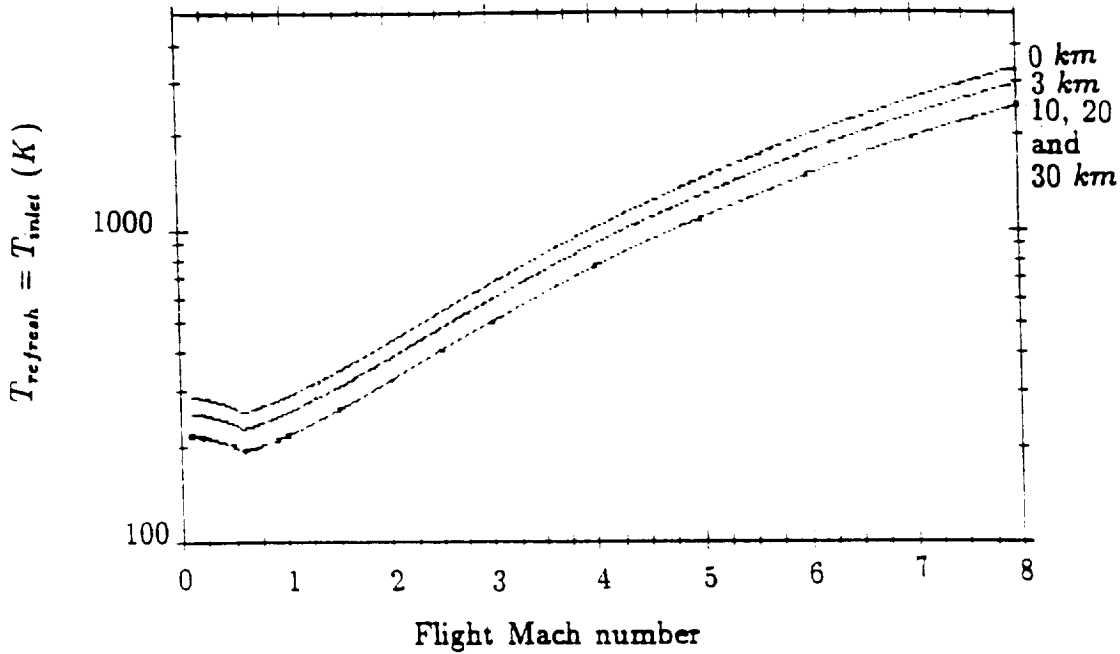


Figure 9.6: Inlet static temperature vs. Mach number and altitude.

In the free stream region,

$$p_{t\infty}/p_{\infty} = (T_{t\infty}/T_{\infty})^{\gamma/(\gamma-1)}$$

With the assumed inlet pressure recovery schedule, p_{tin} is then computed as

$$p_{tin} = \left(\frac{p_{tin}}{p_{t\infty}} \right) p_{t\infty}$$

The air density at the inlet is simply

$$\rho_{in} = \rho_{\infty} \left(\frac{p_{in}}{p_{\infty}} \right) \left(\frac{T_{\infty}}{T_{in}} \right)$$

In the analysis of overall LTD flight performance, the LTD centerbody is considered the “vehicle” component, and the annular shroud is treated as the “engine.” The total drag of the LTD vehicle includes viscous (or frictional) drag, pressure drag, spillage drag and inlet ram drag. The viscous drag is neglected because the effect is small. Pressure drag results from the differences in static pressure applied across the fore and aft surfaces of the vehicle centerbody. Spillage drag occurs when all the inlet air flow passing through the frontal “capture” area (i.e., within the circular

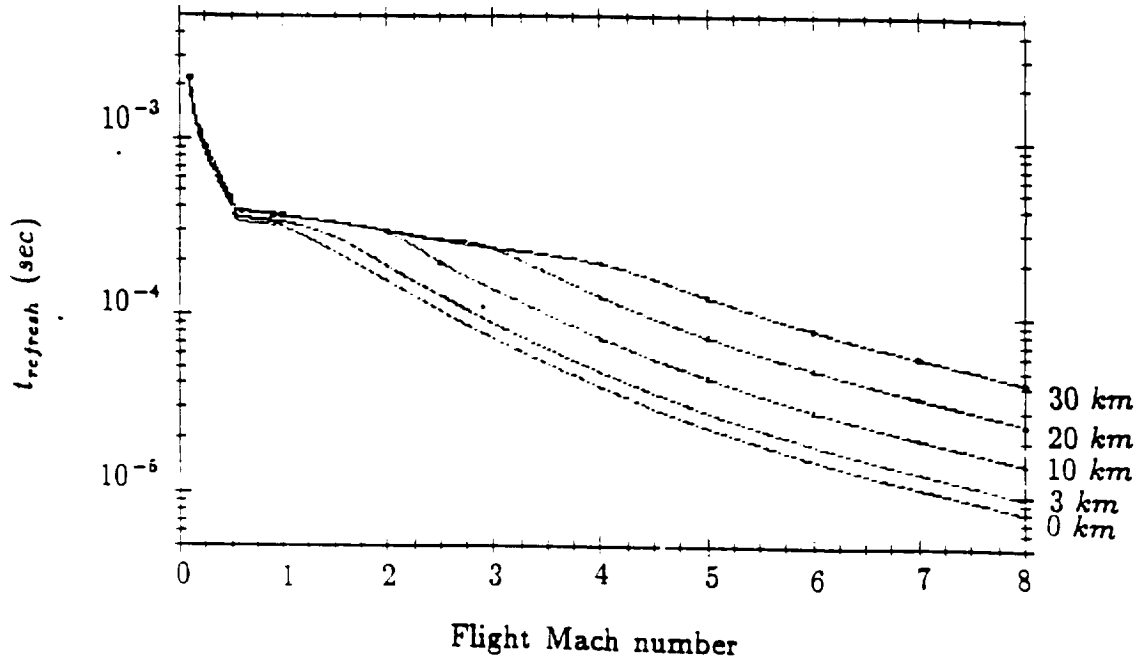


Figure 9.7: Refresh time vs. flight Mach number.

stream-tube cross-section defined the shroud leading edge, r_{ciol}) cannot be swallowed by the inlet gap and must be diverted out over the shroud upper surface.

One of the most important engine-related drag components modeled here is the inlet ram drag which is defined as:

$$D_{RAM} = \dot{m}_{in} u_{in} \quad (9.2)$$

where

$$\dot{m}_{in} = \rho_{in} u_{in} A_{inlet} = \rho_{in} u_{in} \pi (r_{ciol}^2 - r_{ciil}^2) \cos \delta_{cone2} \quad (9.3)$$

assuming that $M_{refresh} = M_{inlet}$, $u_{inlet} = u_{refresh}$ and that the distance from the inlet gap to the blast wave ignition point is $l/2$, the refresh time is simply given by

$$t_{refresh} = \frac{l/2}{u_{refresh}} \text{ or } \frac{r_0}{u_{refresh}} \quad (9.4)$$

whichever is smaller, as discussed earlier. The refresh time, based on this expression is plotted in Fig. 9.7 as a function of LTD flight Mach number and altitude.

Plotted in Figure 9.8 is the total ram drag coefficient, where $c_D = 2 D_{RAM} / \rho_{\infty} u_{\infty}^2 A_{total}$; note $A_{total} = \pi r_{ciol}^2$ is the maximum frontal "capture" area of the inlet.

An important parameter that checks accuracy of the aforementioned inlet assumptions is the ratio of the inlet gap mass flow rate at the choked flow condition, M_{IN}

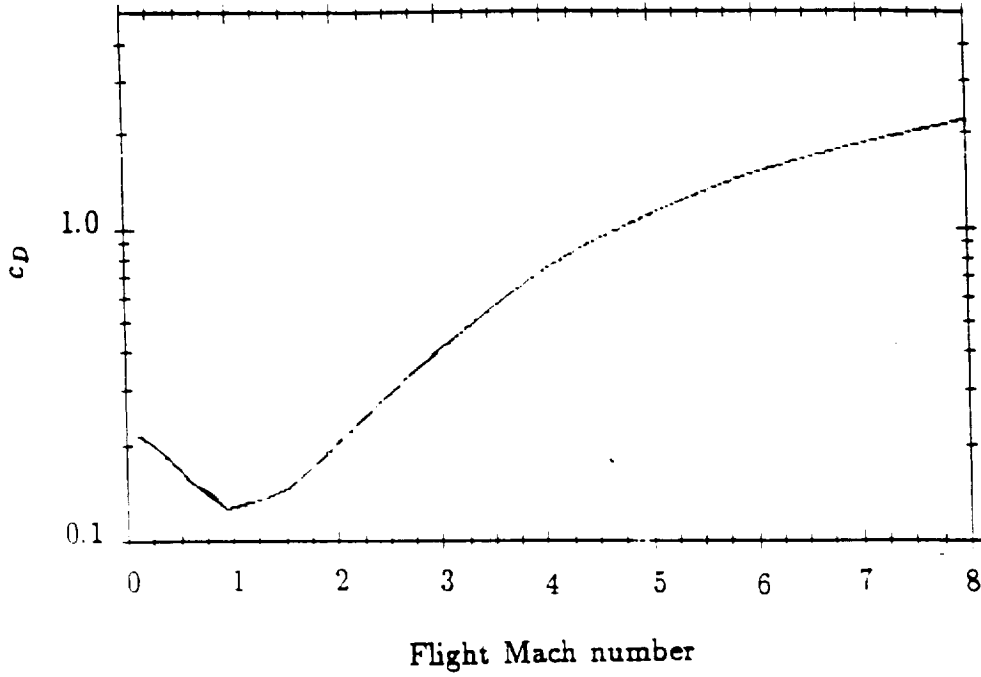


Figure 9.8: Ram drag coefficient for the LTD ERH thruster.

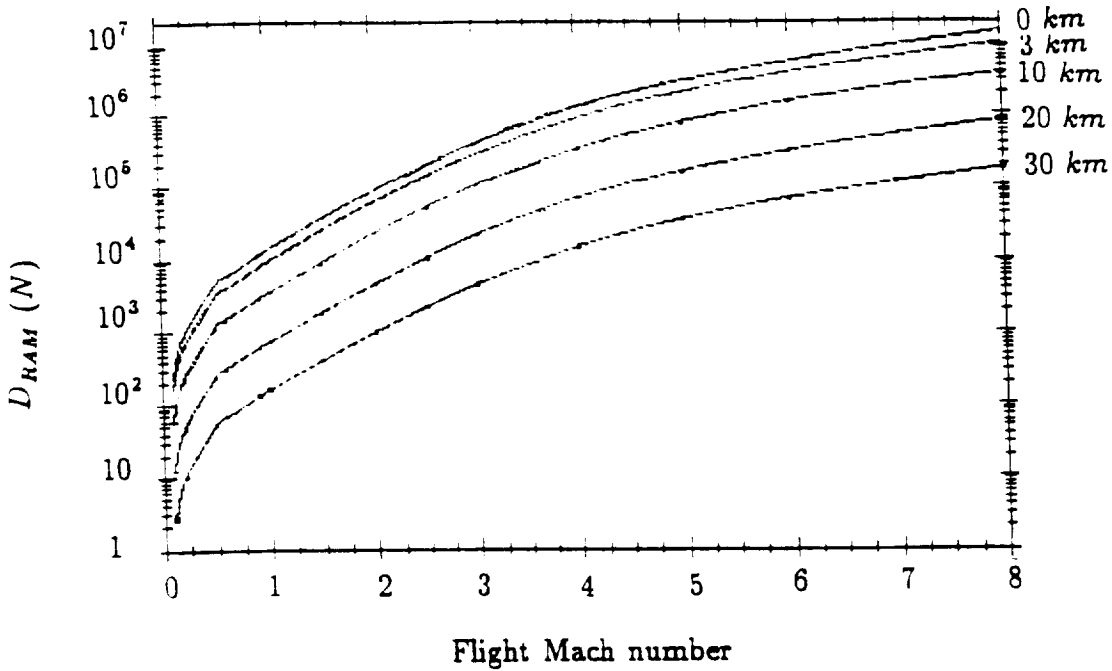


Figure 9.9: LTD inlet ram drag vs. Mach number and altitude.

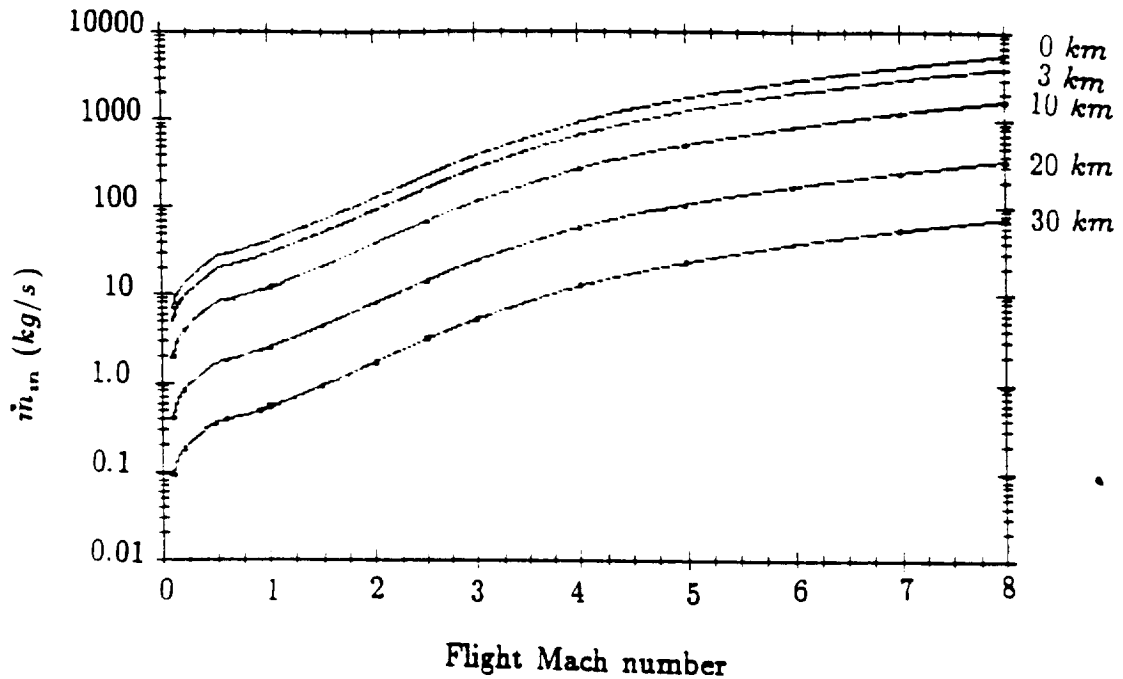


Figure 9.10: LTD inlet mass flow rate vs. Mach number and altitude.

$= 1$, to the maximum “capture” mass flow rate defined by the inlet lip (i.e., τ_{ciol}); the latter is given by $\dot{m}_{\infty} = \rho_{\infty} \pi r_{ciol}^2 u_{\infty}$. This ratio, which physically cannot exceed 1, is plotted in Figure 9.11. Note that present LTD inlet assumptions indicate a design Mach number of about 5. The actual LTD inlet characteristics are best left for experiments to confirm.

Another critical ERH thruster parameter is the resultant pressure at the inlet gap, produced by a decaying blast wave after it has expanded across the shroud lower impulse surface. Cylindrical blast wave characteristics are calculated (as described earlier) with Sedov and Raizer’s equations, and plotted in Figure 9.12. Note that blast wave pressure does not decay fast enough to avoid exceeding the inlet static pressure under certain flight conditions. Since fluids will generally tend to move from regions of high to low pressure, the inlet flow might reverse direction and separate from the forward lip. This might limit the engine operational flight regime to the higher dynamic pressure trajectories where the parameter in Figure 9.12 is always less than the stagnation pressure at the inlet gap. Again, experimental confirmation of this assumption is necessary.

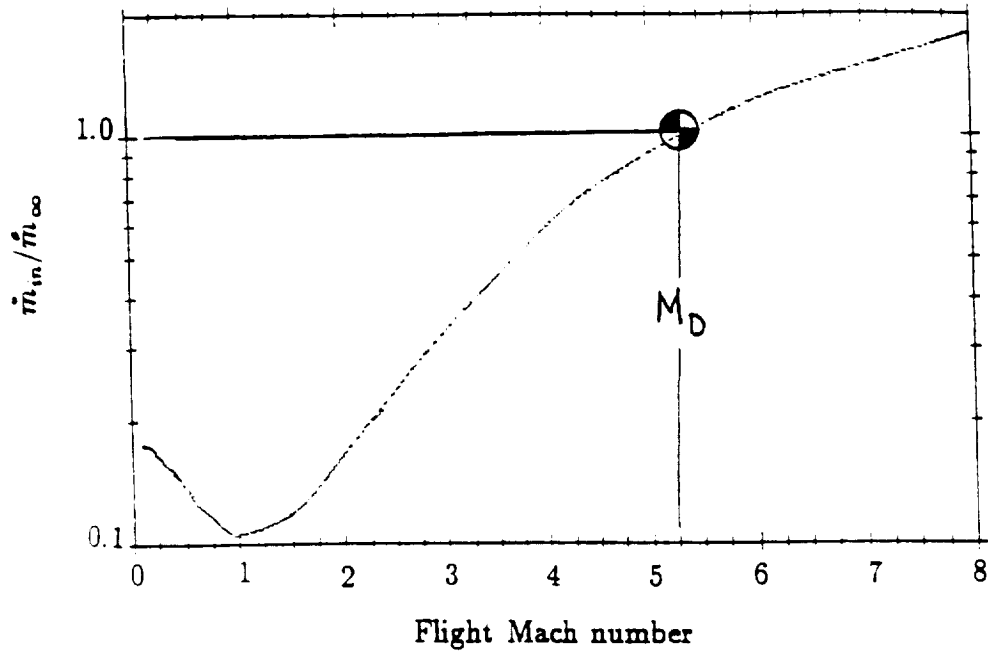


Figure 9.11: Ratio of inlet gap to maximum "capture" mass flow rate, vs. flight Mach number.

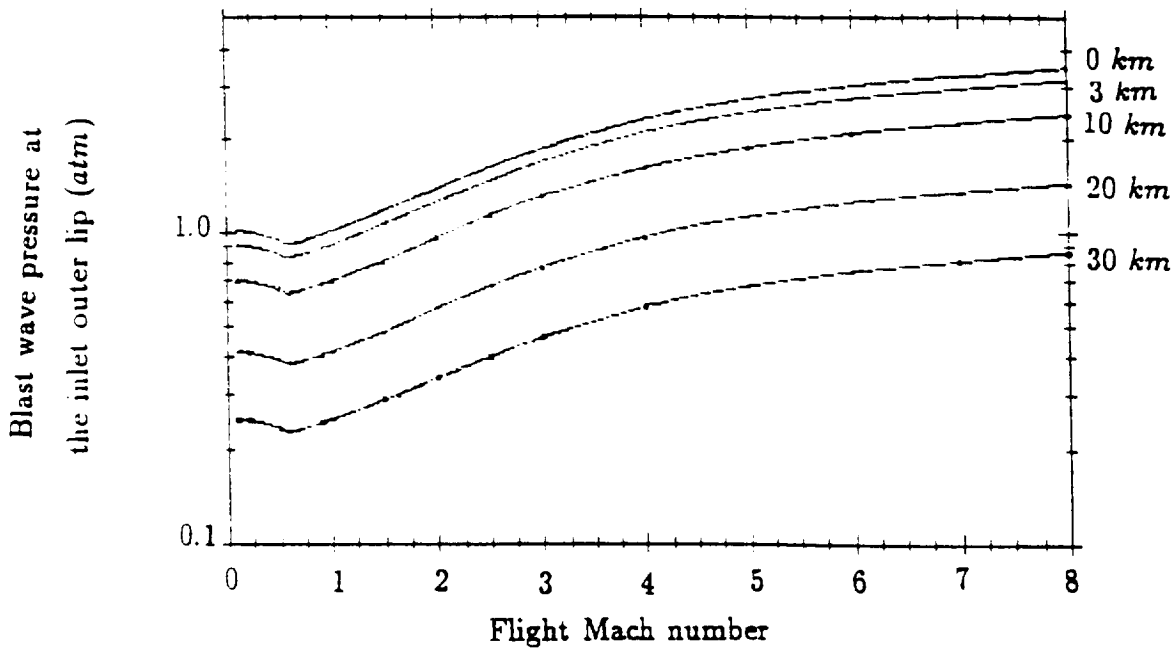


Figure 9.12: Blast wave pressure at the inlet outer lip (i.e., $r = 10.8$ cm), in bars, vs. flight Mach number and altitude, with $\Phi_{LSD} = 500$ MW/cm² using Raizer and Sedov's equations.

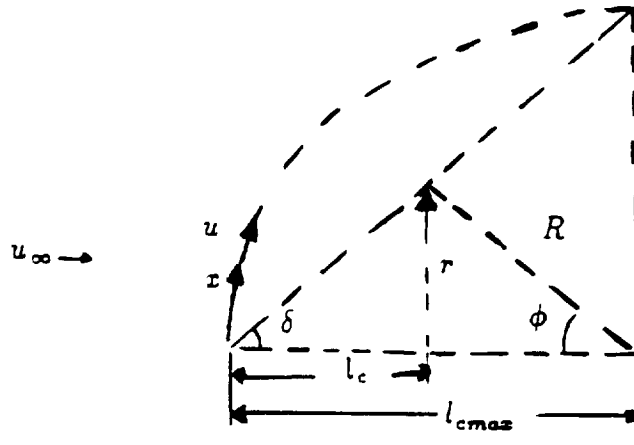


Figure 9.13: Model of subsonic flow over a cone.

9.1.2 Alternate Subsonic Inlet Model

This alternate procedure attempts to justify the above assumptions made in modeling the subsonic inlet flow to the LTD engine. The main objective is to obtain forebody pressure distributions for inlet and vehicle drag calculations.

The LTD forebody flow model for the subsonic case is based on the known aerodynamic flow field that occurs over a sphere; the inlet geometry is shown in Figure 9.13. The fluid velocity along a spherical surface can be obtained from inviscid potential flow theory (see Schlichting):

$$u/u_{\infty} = 2 \sin(x/R)$$

where the variables are noted in Figure 9.13. A factor of 3/2, instead of 2, is suggested for the cones. This gives a critical flight Mach number of 0.6 for the choked inlet condition (i.e., $M_{inlet} = 1$), in accordance with previous discussions. Note that the subscripts ∞ , a and 0 all represent the same ambient location far upstream of the vehicle inlet.

From Figure 9.13, it is observed that $x = \sqrt{r^2 + l^2}$ and $R = \sqrt{l_{cmax}^2 + r^2}$, where l_{cmax} is defined as $l_c = r_c$. Note also that $x \approx r/\sin \delta$, and $R \approx r/\sin \phi$. From these considerations, one can express the velocity, u_{c1} , at any point along the front

forebody cone as

$$\frac{u_{c1}}{u_{\infty}} = \frac{3}{2} \sin \sqrt{\frac{1 + (l_{cone1}/r_{cone1})^2}{1 + (1 - l_{cone1}/r_{cone1})^2}} \quad (9.5)$$

For the second cone,

$$\frac{u_{c2}}{u_{c1}} = \frac{3}{2} \sin \sqrt{\frac{1 + [l_{cone2}/(r_{cone2} - r_{cone1})]^2}{1 + [1 - l_{cone2}/(r_{cone2} - r_{cone1})]^2}} \quad (9.6)$$

By introducing the definition for the Mach number at any point along the cone, $M = u/c_s$, where $c_s = \sqrt{\gamma_0 p / \rho}$, one obtains

$$u = M_{\infty} \sqrt{\frac{\gamma_0 p_0}{\rho_0}} \frac{3}{2} \sin(\dots) \quad (9.7)$$

or

$$M = M_{\infty} \sqrt{\frac{p_0 \rho}{p \rho_0}} \frac{3}{2} \sin(\dots) \quad (9.8)$$

Also, from isentropic, steady, compressible flow equations,

$$M = M_{\infty} \sqrt{\left(\frac{1 + (\gamma_0 - 1)M^2/2}{1 + (\gamma_0 - 1)M_{\infty}^2/2} \right)^{\frac{\gamma_0}{\gamma_0 - 1}} \left(\frac{1 + (\gamma_0 - 1)M^2/2}{1 + (\gamma_0 - 1)M_{\infty}^2/2} \right)^{\frac{-1}{\gamma_0 - 1}} \frac{3}{2} \sin(\dots)} \quad (9.9)$$

which is simply:

$$M = M_{\infty} \sqrt{\frac{1 + (\gamma_0 - 1)M^2/2}{1 + (\gamma_0 - 1)M_{\infty}^2/2}} \frac{3}{2} \sin(\dots) \quad (9.10)$$

After solving for M ,

$$M = \frac{1}{\sqrt{\frac{1}{\frac{M_{\infty}^2}{1 + (\gamma_0 - 1)M_{\infty}^2/2} - \frac{\gamma_0 - 1}{2}}}} \quad (9.11)$$

By replacing u/u_{∞} with either u_{c1}/u_{∞} or u_{c2}/u_{c2} , M_2 (right in front of cone 2), or M_{in} (right in front of the inlet gap) can be calculated. Equation 9.11 may be used for any part of the flow that is subsonic.

Note that the results presented in Figure 9.14 basically serve to confirm the earlier subsonic inlet analysis, and may aid in the study of other forebody cone angles.

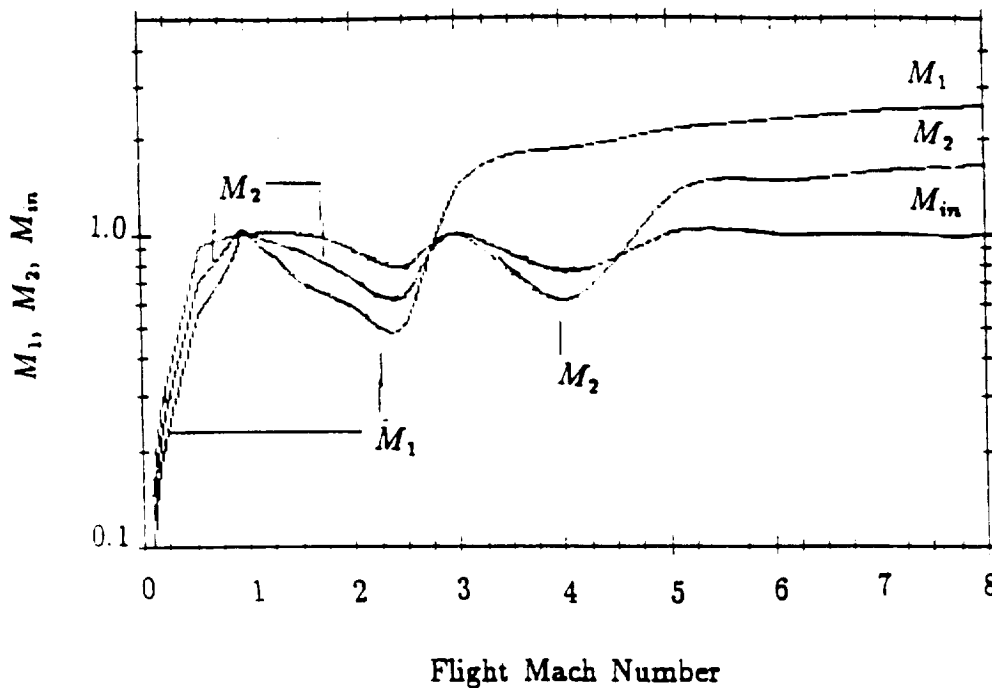


Figure 9.14: Alternate forebody/inlet Mach number schedule; 30° and 51° cones model the forebody.

9.2 LTD Performance Projections

The results in this section present a complete analytical performance projection for the Lightcraft Technology Demonstrator airbreathing engine. The impulse coupling coefficient, measured in units of Newtons of thrust per megawatt of input laser power, remains the principal measure of engine performance.

A base line case which assumes an inlet gap height of 3 cm, is the central focus of the analysis. Several engine-related parameters were varied in search of the optimum coupling coefficient regime and to understand the performance sensitivity to those parameters. The principal baseline case parameters consist of the following: $\tau_{LSD} = 0.5$ cm and $\Phi_{LSD} = 500 \text{ MW/cm}^2$ and $M_{refresh} = 1.0$ when $M_\infty \geq 0.6$. As described earlier, Raizer and Sedov equations are used in the impulse model, and a simple forebody/inlet model determines the air refresh conditions in the thruster. The baseline net coupling coefficient performance is displayed in Figure 9.15.

Also for the baseline case, Figure 9.16 gives the laser pulse duration; Figure 9.17, time-averaged input laser power; Figure 9.18, time-averaged thrust; Figure 9.19, pulse repetition frequency; and Figure 9.20, pulse energy. In figures 9.21 and 9.22, the gross time-averaged thrust and gross coupling coefficient performance are displayed, respectively. Note that gross time-averaged thrust minus inlet ram drag (Fig. 9.9)

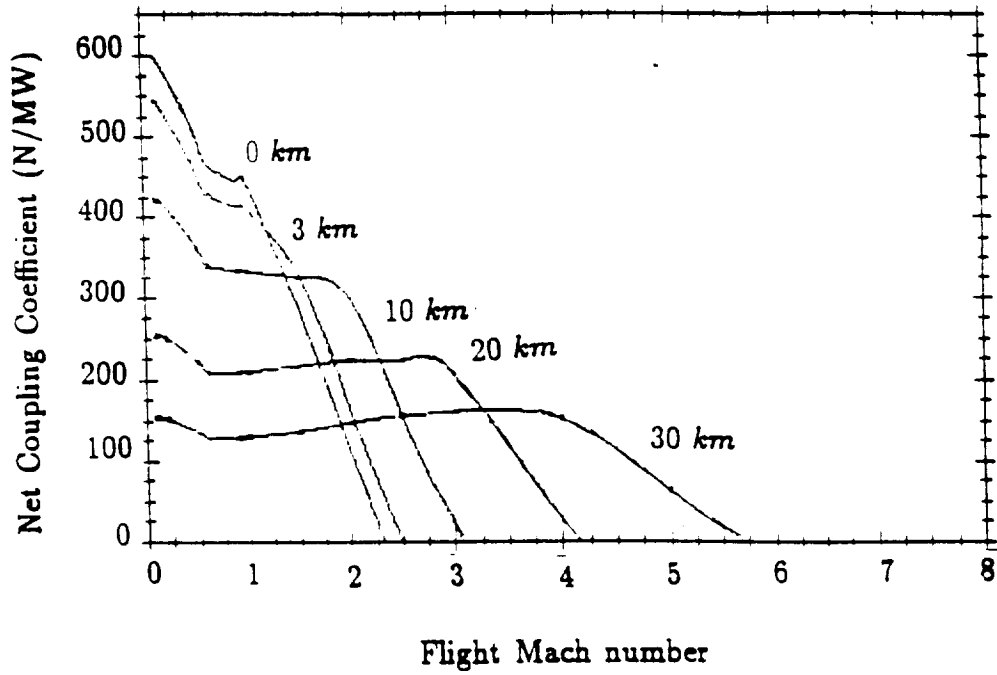


Figure 9.15: Net coupling coefficient vs. Mach number and altitude, for the baseline case (inlet gap = 3 cm, $\Phi_{LSD} = 500 \text{ MW/cm}^2$, $r_{LSD} = 0.5 \text{ cm}$, and $M_{refresh} = 1.0$ when $M_\infty \geq 0.6$).

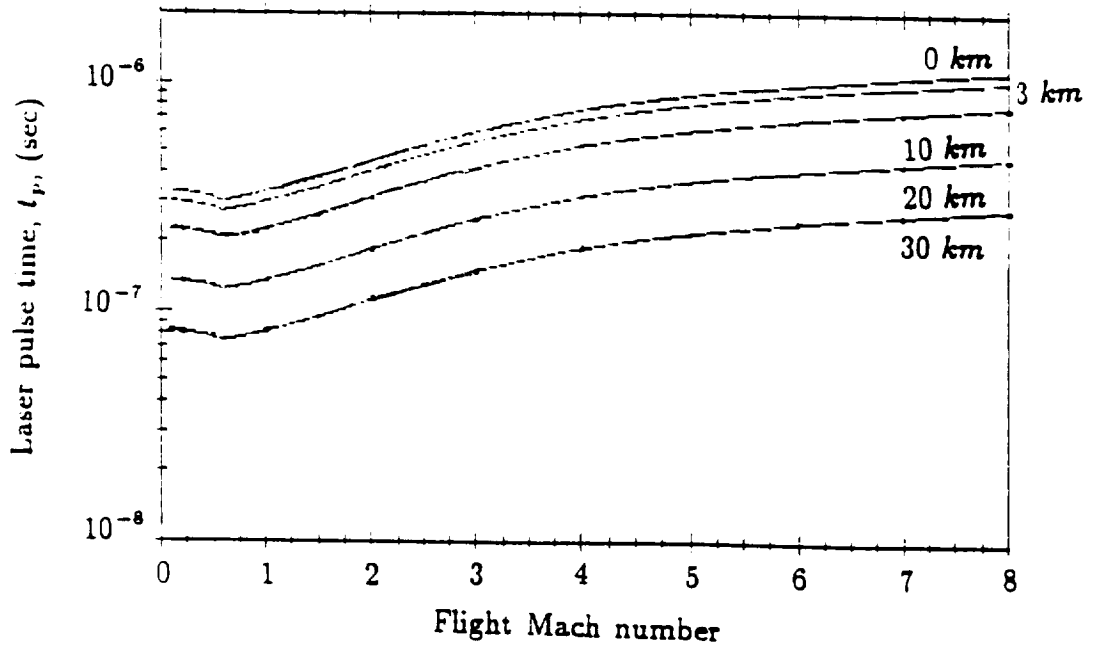


Figure 9.16: Laser pulse time vs. Mach number and altitude, for the baseline case.

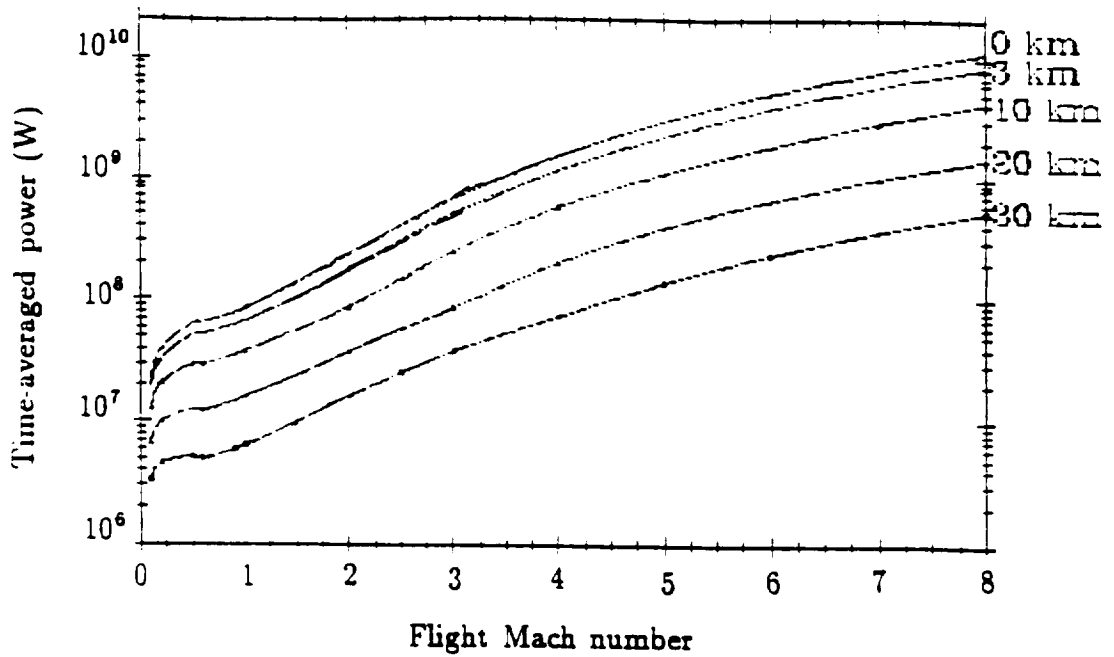


Figure 9.17: Time-averaged power vs. Mach number and altitude, for the baseline case.

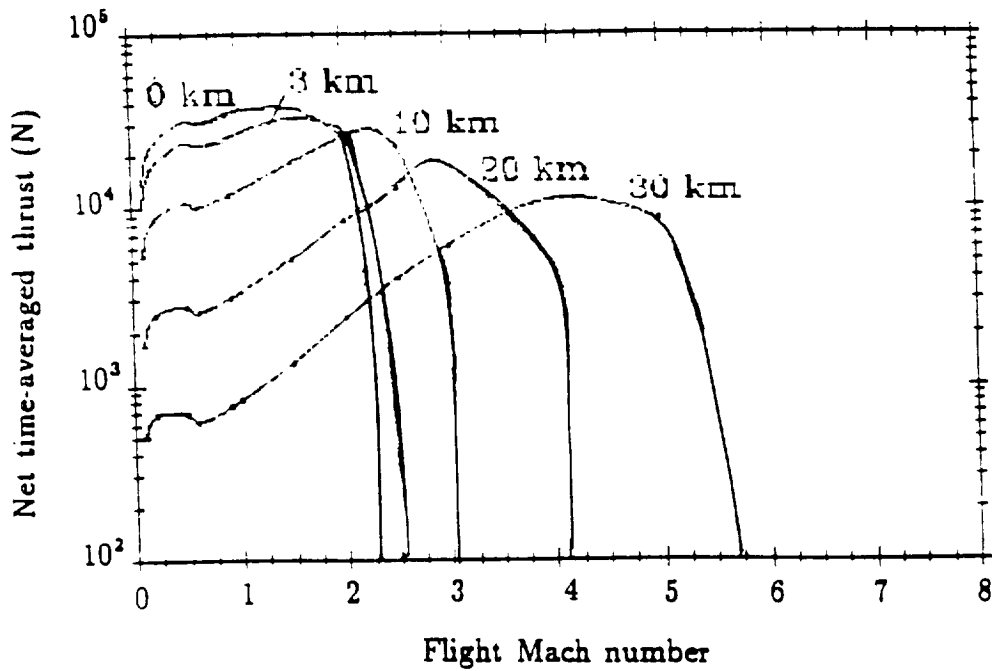


Figure 9.18: Net time-averaged thrust vs. Mach number and altitude, for the baseline case.

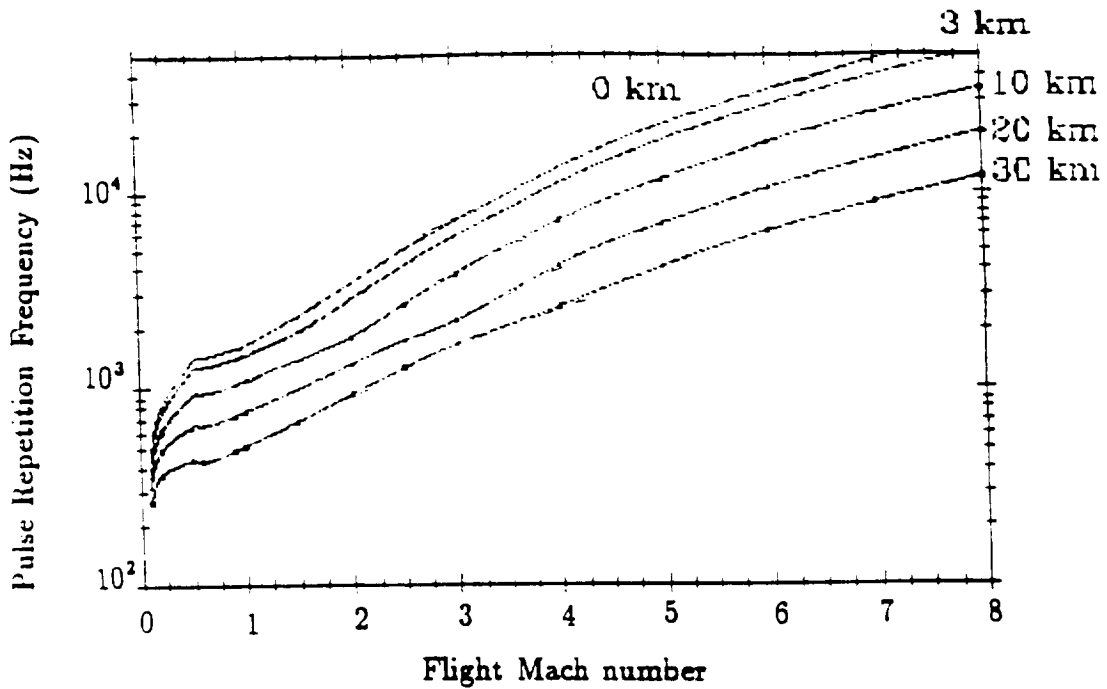


Figure 9.19: Pulse Repetition Frequency vs. Mach number and altitude, for the baseline case.

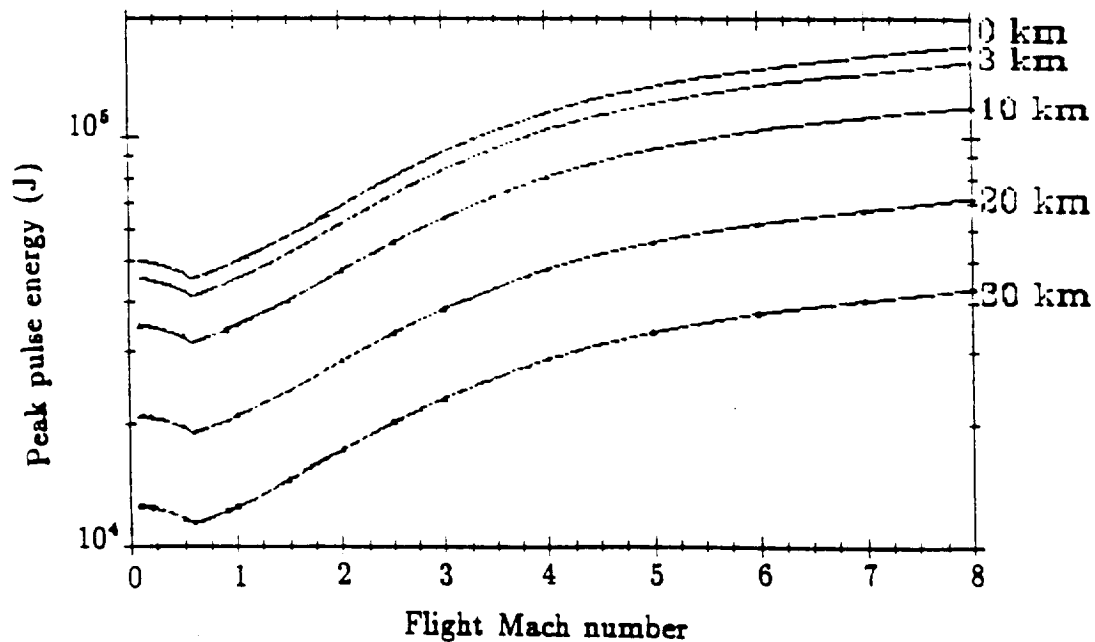


Figure 9.20: Pulse energy vs. Mach number and altitude, for the baseline case.

equals net time-averaged thrust (Fig. 9.18); also, time-averaged net thrust divided by time-average input power (Fig. 9.17) equals net coupling coefficient (Fig. 9.15).

Finally, Figure 9.23 displays an important parameter that gives some insight into the dynamics of the refresh process for the baseline case: $t_{refresh}/t_{expansion}$, where $t_{expansion} = t_0$.

Note from Figure 9.23 that it may be possible for the LTD to fly along a boost trajectory where this parameter is close to 1. At this condition, the time required for fresh air to refresh the ignition point ($t_{refresh}$) is exactly equal to the time necessary for the blast wave pressure to expand down to the local ambient level. This criteria has been employed to size the streamwise dimension (i.e., “ l ”) of the annular shroud impulse surface; hence the heated air-plasma annular “bubble” would relax to ambient pressure, just as the aft bubble edge meets the trailing edge of the shroud. At this point, the next laser pulse would be delivered, because fresh air has simultaneously reached the ignition site. It bears mentioning that the plasma bubble is assumed to convect aft, immediately following ignition; this contradicts limited experimental evidence to the contrary, which suggests the existence of an initial delay time — until the plasma bubble pressure drops almost to the local stagnation pressure level (i.e., the sum of both dynamic and static pressure components) — when the ‘bubble’ begins to move aft. All of this has direct implications on how large the annular shroud impulse area must be; however, the resolution of this issue must wait for an

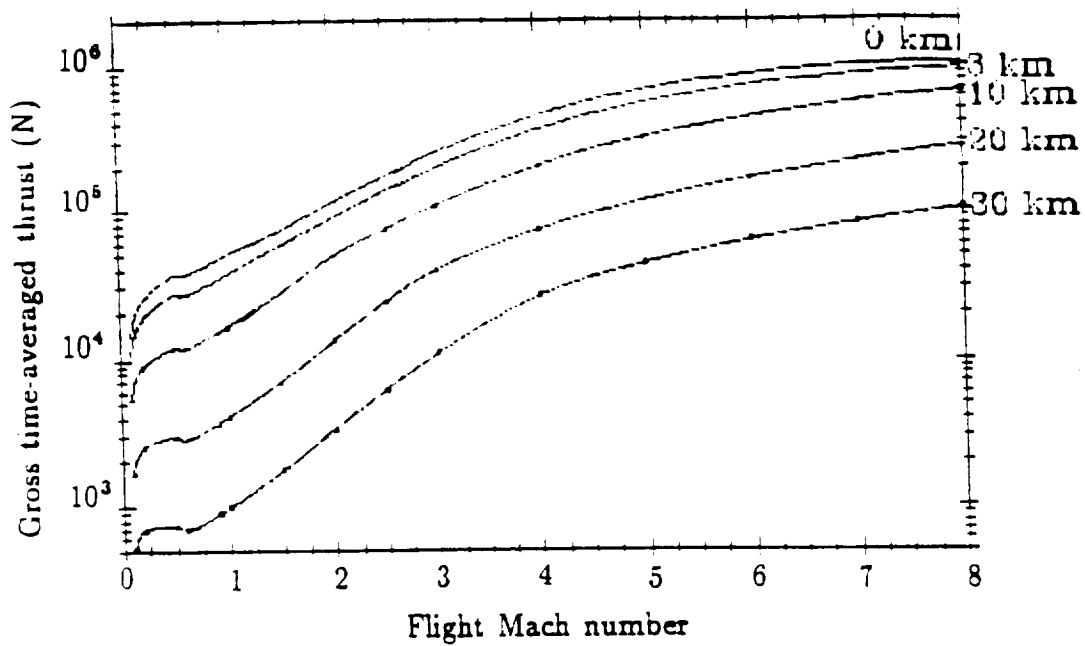


Figure 9.21: Gross time-averaged thrust vs. Mach number and altitude, for the baseline case.

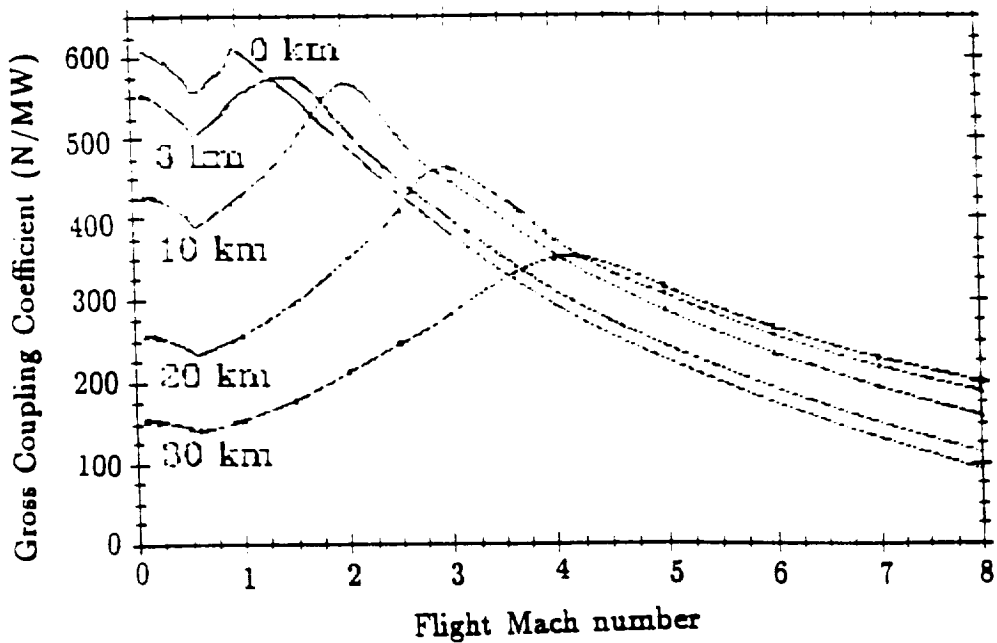


Figure 9.22: Gross coupling coefficient vs. Mach number and altitude, for the baseline case.

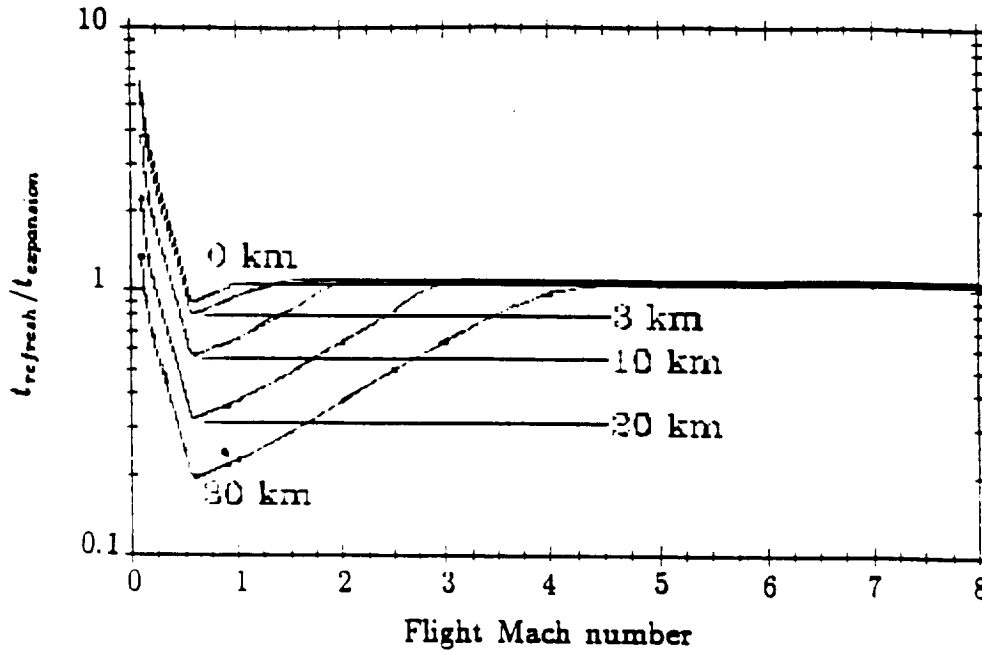


Figure 9.23: $t_{refresh}/t_{expansion}$ vs. Mach number and altitude, for the baseline case.

experiment.

At the present state of knowledge, these combined air refresh flow and laser-heating effects are difficult to model analytically; hence, four variations in engine input assumptions (i.e., $M_{refresh}$, inlet gap height, τ_{LSD} and Φ_{LSD}) were run to determine their separate impact upon coupling coefficient performance.

First to be studied was the effect of refresh Mach number ($M_{refresh} = 0.75, 0.5$ and 0.25) at flight Mach numbers beyond 0.6 ; the flow velocity is assumed fixed from the inlet gap to the ignition site. All other parameters were held constant at the baseline values, including the aforementioned inlet flow velocity schedule from $0 \leq M_{\infty} \leq 0.6$ (wherein, inlet Mach number increases to 1.0 at flight Mach 0.6). In comparing the coupling coefficient (CC) performance for $M_{refresh} = 0.75$ with the baseline case, CC values are found to be significantly improved between $0.6 \leq M_{\infty} \leq 4$, with no decrease in top end performance. Also note that CC goes to zero at about $M_{\infty} = 5.6$ and 30 km altitude, just like the baseline case; these cases agree well with the inlet design Mach number 5.2 suggested in Figure 9.11. As $M_{refresh}$ is further reduced 0.5 in Figure B.2, low end CC performance is seen to increase somewhat beyond the $M_{refresh} = 0.75$ case, but the top end performance begins to suffer (with a zero CC at $M_{\infty} = 5.5$ and 30 km). This situation becomes unacceptably exaggerated for the $M_{refresh} = 0.25$ case in Figure B.3.

From this inlet Mach number sensitivity analysis, one concludes that the ERH

thruster will accept a wide range of $M_{refresh}$ values from 0.5 to 1.0; the lower refresh Mach numbers seem to indicate improved CC performance, but might degrade time-average thrust levels and PRF (this impact was not examined, however).

Examined next was the sensitivity to inlet gap height on CC performance. Figure B.4 illustrates the effect of reducing the gap height by 1 cm below the baseline value of 3 cm. Note that the CC performance increases significantly at the top end, where the CC at 30 km altitude goes to zero at $M_\infty = 7.4$; this may in part be due to a large reduction in ram inlet drag — associated with a reduced inlet mass flow rate. However, this inviscid analysis does not take into account the forebody boundary layer thickness, which might grow to a significant fraction of the inlet height, and viscous effects will reduce the air velocity there; note also that the top end performance greatly exceeds the M_D of 5.0 assumed for the inlet. If, on the other hand, the gap is increased by 1 cm to 4 cm total, the net coupling coefficients (see Fig. B.5) suffer at the top end, where they fall to zero at $M_\infty = 4.75$ at 30 km altitude.

The next variable to be varied was τ_{LSD} which had a baseline value of 0.5 cm. The additional values of 0.1, 0.25, 0.75 and 1 cm were investigated. As shown in Figures B.6 through B.9, shortening τ_{LSD} decreases the high flight Mach number ('high end') performance, but increases the low Mach number ('low end') performance. This is probably because the blast wave impulse dies off faster with shorter laser pulse times and smaller initial plasma volumes. Also, the laser energy available for the thrust cycle is less with shorter pulse times, which in turn is less with lower τ_{LSD} . For the lower flight Mach number range, however, the faster cycle times (which result from shorter laser pulses) allows more laser pulses to be delivered per second. Thus the effect of a higher PRF dominates the low end performance where the air density is higher (i.e., lower altitudes) with the lower Mach numbers. A τ_{LSD} of 0.5 cm seems to yield a good compromise between high end, and low end engine performance for the baseline Φ_{LSD} of 500 MW/cm².

The effect of different laser pulse intensities can also be very important. As mentioned earlier, 5×10^8 W/cm² was chosen as the baseline case; 3×10^9 and 10^{10} W/cm² were also run. While breakdown occurs at roughly 10^9 W/cm² for 10.6 μm wavelength, the breakdown threshold is a direct function of wavelength: $\Phi_{Breakdown} \propto \lambda^{-3/2}$. By using lasers in the shorter infrared (e.g., 1 μm) and visible (e.g., 0.7 μm to 0.3 μm) ranges, Φ_{LSD} can be greatly increased beyond the baseline value of 3×10^8 W/cm². However, higher Φ_{LSD} 's mean even greater plasma temperatures, which push the credibility limits of this straightforward ideal gas model. Hence the results of this sensitivity analysis on Φ_{LSD} which are presented in Figures B.10 through B.27, should be viewed in a qualitative sense only.

The principal effect of increasing laser intensity (Φ_{LSD}) appears to be a large associated reduction in laser pulse times; also, as τ_{LSD} is varied at a new higher Φ_{LSD} , the optimum CC performance is shifted to a shorter τ_{LSD} . Interestingly enough, there

is a value of r_{LSD} for which the original baseline case of $r_{LSD} = 0.5$ cm and $\Phi_{LSD} = 500$ MW/cm² seems to be almost duplicated: for example at $\Phi_{LSD} = 3 \times 10^9$ W/cm² it is $r_{LSD} = 0.25$ cm (see Fig. B.11); at $\Phi_{LSD} = 10^{10}$ W/cm² it is $r_{LSD} = 0.2$ cm (see Fig. B.20). Whereas the baseline laser pulse duration is roughly 0.3 μ s along a typical launch trajectory (see Fig. 9.16), at 3×10^9 W/cm² it shortens to 70 ns; with 10^9 W/cm², t_p falls to 40 ns.

In general, the time-averaged input laser power (see Figs. 4.17, B.18 and B.24) and net thrust (see Figs. 4.18, B.14 and B.25) for the three optimal cases mentioned above are nearly identical. The pulse energies (Figs. 9.20, B.16, and B.27), and the pulse repetition frequencies (Figs. 4.19, B.15, and B.26) fall in similar ranges also.

In summary, while much is known about laser-induced breakdown and impulse-generation within a static atmosphere, minimal experimental data exists on laser impulse coupling within a gasdynamic environment. Although this "refresh" aspect of the ERH thruster has a certain similarity to all airbreathing engines, a clear fundamental understanding must await critical proof-of-concept experiments. This chapter reveals analytical performance projections for the ERH thruster cycle that (taken as a whole) look exceedingly promising. The key parameters are clearly laid out such that a well conceived experimental program can now be planned.

REFERENCES

- [1] White, Frank Mangrem, *Viscous Fluid Flow*, McGraw-Hill, N.Y., 1974.
- [2] Shapiro, Ascher H., *The Dynamics and Thermodynamics of Compressible Fluid Flow*, Vol. 1 and 2, Ronald Press Co., N.Y., 1953.
- [3] Kuethe, Arnold M. and Chow, Chuen-Yen, *Foundations of Aerodynamics: Bases of Aerodynamic Design*, 3rd. Ed., John Wiley & Sons, N.Y., 1976.
- [4] Oates, Gordon C., *Aerothermodynamics of Gas Turbines and Rocket Propulsion*, AIAA Education Series, Przemieniecki, J.S., Series Editor-in-Chief, AIAA, 1984.
- [5] "Equations, Tables and Charts for Compressible Flows," NACA Report No. 1135, 1955.

Chapter 10

LASER-HEATED ROCKET MODE

As presently conceived, the LTD vehicle could be constructed using state-of-the-art components derived from current liquid chemical rocket engine technology, advanced composite structures, and high power laser optics developed for SDIO applications. In the rocket mode, the regeneratively cooled, 1 m diameter primary optic will also serve as a plug nozzle; hence, the parallel with liquid chemical rocket technology becomes obvious.

The LTD combined-cycle engine would start off in an airbreathing mode, then "shift" into the rocket mode at Mach 5 and 100 kft. Fourteen kilograms of LN_2 would be expended in the airbreathing mode (to cool the primary mirror), leaving 126 kg for the rocket mode. The rocket specific impulse will be ≥ 875 s (coupling coefficient, $\text{CC} \simeq 100$ N/mW), using LN_2 as the reaction propellant. This single-stage-to-orbit vehicle has a mass ration of 2.0, and the *entire* final mass of 124 kg (i.e., 120 kg dry mass, plus 2 kg of LN_2 and 2 kg of He ullage) becomes the payload.

Soon after arriving in orbit, the remaining 2 kg of LN_2 evaporates, helping to cool down the vehicle, while maintaining adequate propellant pressure. This compressed, cold N_2 & He mixture is then utilized by a simple 3-axis rocket attitude control system to accomplish fine pointing required for sensor satellite functions throughout its life-time.

A cutaway view in Fig. 10.1 shows the internal arrangement of hardware components for the LTD machine; the projected mass breakdown is given in Chapter 2. Note that the two most massive components are the 28 in. diameter LN_2 tank and the annular shroud engine. The LN_2 tank is a filament wound pressure vessel similar to the ones made by Brunswick Defense in Lincoln, Nebraska.

Figure 10.2 displays the range of primary optic (PO) contours considered for the LTD machine. These contours are generated by rotating a parabola about an off-center axis. Note that the annular shroud airfoil has a circular arc cross-section with a flat bottom, and a chord (C) length of 22.5 cm. Five PO contours are displayed with focal rings positioned at 16.67% C , 22.0% C , 33.33% C , 41.67% C , and 50.0% C . The

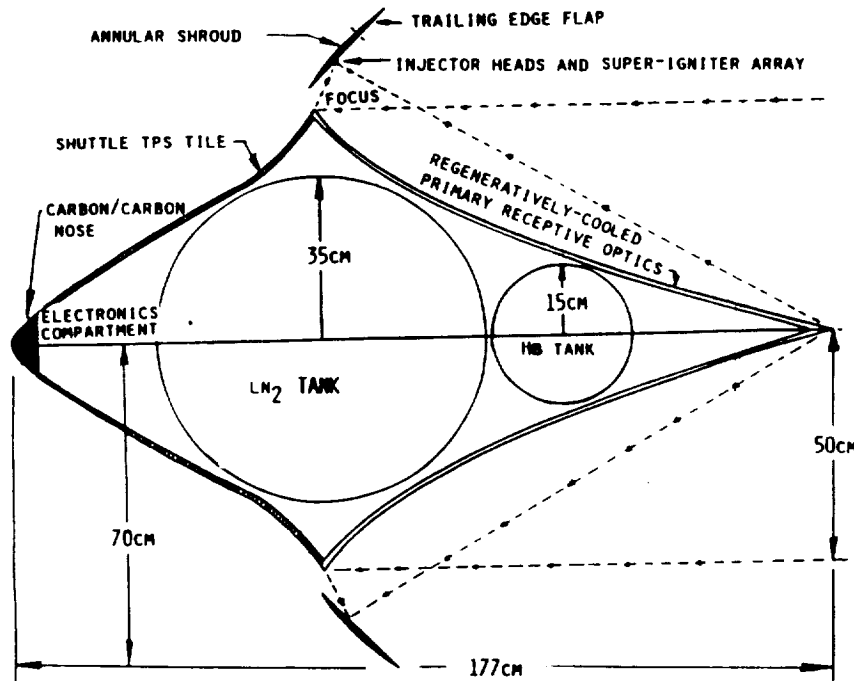


Figure 10.1: Cutaway View of LTD Aerospace Vehicle

longest PO afterbody has its focus at the 16.67% C chord point. As mentioned earlier, one wants to place the focus as far forward on the shroud as possible, yet at the same time minimize the PO weight penalty. For the LTD machine, this compromise was reached by placing the focus at 33.33% C . Note that the PO contours in Fig. 10.2 bear a striking resemblance to isentropic spike rocket engine nozzles.

10.1 Plug Nozzle Rocket Engines

Graham and Bergman were the first to build plug nozzle rocket engines back in the late 50's and early 60's while working for General Electric. Figure 10.3 shows their 16,000 lb (71.2 kN) thrust, H_2O_2 uncooled plug nozzle thrust chamber mounted in a test cell. (Incidentally, this engine developed a thrust level roughly equivalent to the LTD engine's maximum thrust in the airbreathing mode.) As indicated in Fig. 10.4, six H_2O_2 decomposers were arranged around the base of the plug to provide exhaust gases for hot tests. Two, of the many external expansion nozzles which were tested, are displayed in Figs. 10.4A and B; an isentropic plug, and a 20° foreshortened plug. This rocket engine demonstrated good performance at off-design pressure ratios, and proved the feasibility of thrust vector control by selective combustor throttling. Subsequent analysis of the test data revealed that full isentropic plug nozzles could

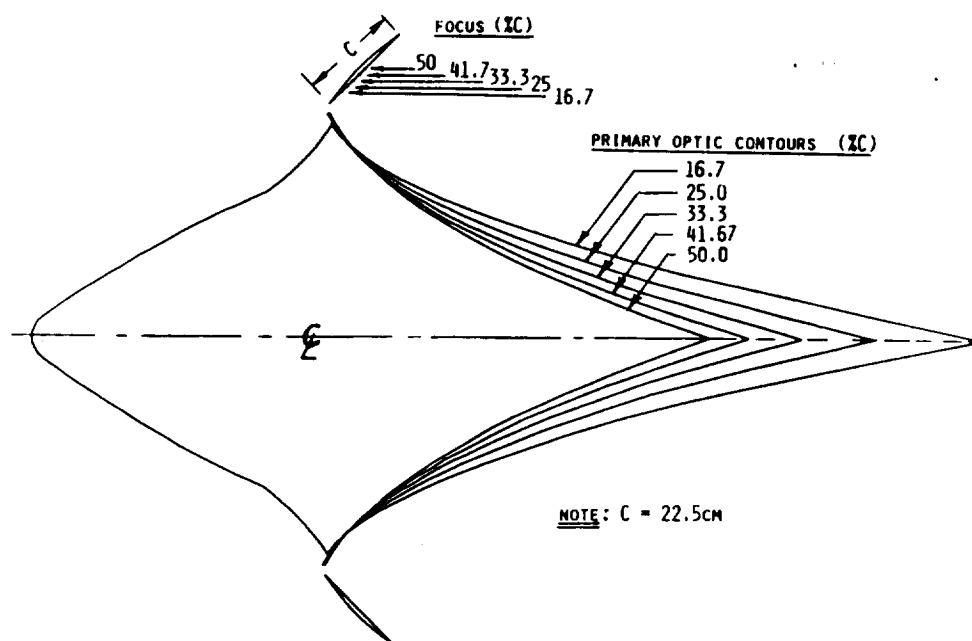


Figure 10.2: Primary Optic contours vs. Focal Locations.

be subjected to substantial truncation/foreshortening, without degrading the thrust performance to any large degree. Figure 10.5 indicates the method used to foreshorten the plug nozzles, by replacing the tip with a cone at the appropriate tangent location.

For the first flight-weight demonstration of a regeneratively cooled plug nozzle rocket engine, Graham and Bergman decided to completely truncate the isentropic spike nozzle, replacing it altogether with the 42° half-angle cone shown in Fig. 10.6. Calculations were carried out to determine the minimum size of plug nozzle that could cool itself with RP-1/LOX propellants. The result was the 50,000 lb thrust stainless steel engine displayed in Fig. 10.7. As indicated in Fig. 10.8, the plug nozzle had an exit nozzle diameter of 1.07 m (which is identical to that of the primary optic of the LTD machine). The overall maximum diameter of the 50,000 lb thrust engine was 1.34 m.

Figure 10.9 shows one of the eight cooled segments of which the engine is composed; each segment could be independently throttled to accomplish thrust vectoring. Pictured in Fig. 10.10 is an enlarged view of the lower cone segment, revealing RP-1 coolant flow passageways.

The lower cone segments were fabricated from two thin stainless steel faceplates separated by numerous vertical ribs that formed the coolant passageways, all fused together by an electron-beam welding machine. Each of the eight lower cone segments had a mass of 2.077 kg and an area of 1089 cm^2 ; this translates to a mass penalty of

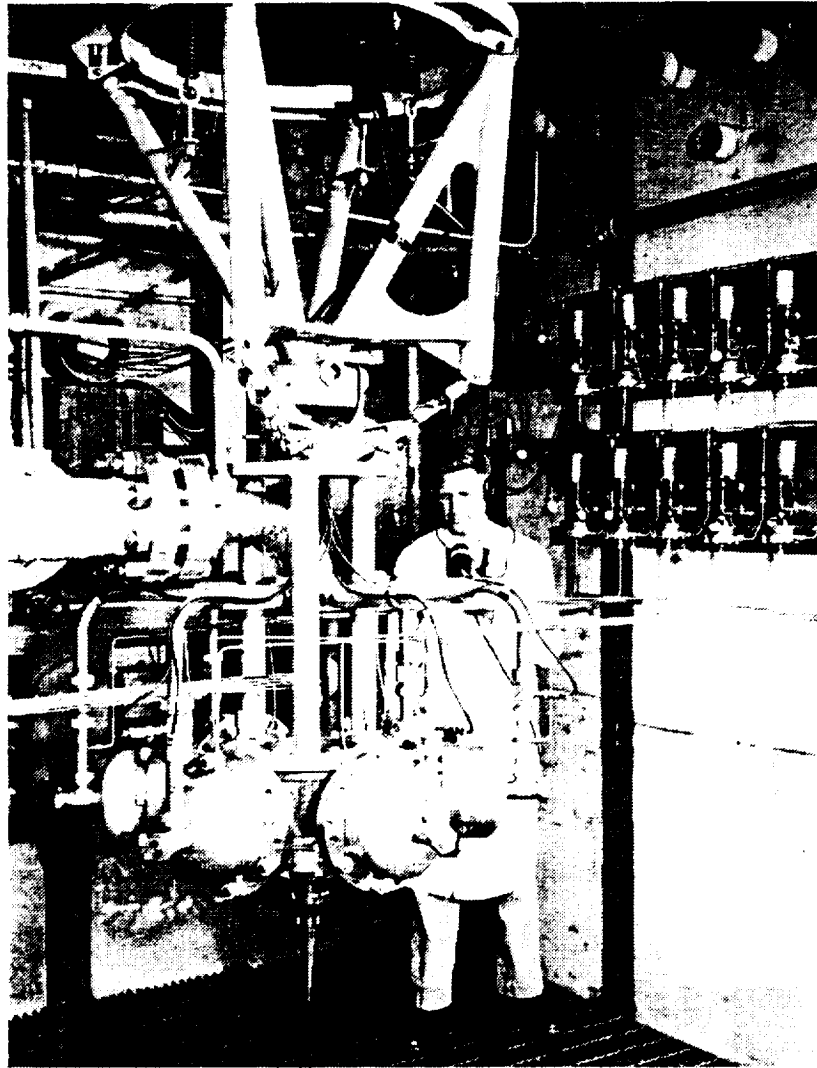


Figure 10.3: 16 Klb H_2O_2 Plug Nozzle Development Thrust Chamber in Test Cell
(After Graham and Bergman, Ref. 1)

ORIGINAL PAGE
BLACK AND WHITE PHOTOGRAPH

10.1. PLUG NOZZLE ROCKET ENGINES

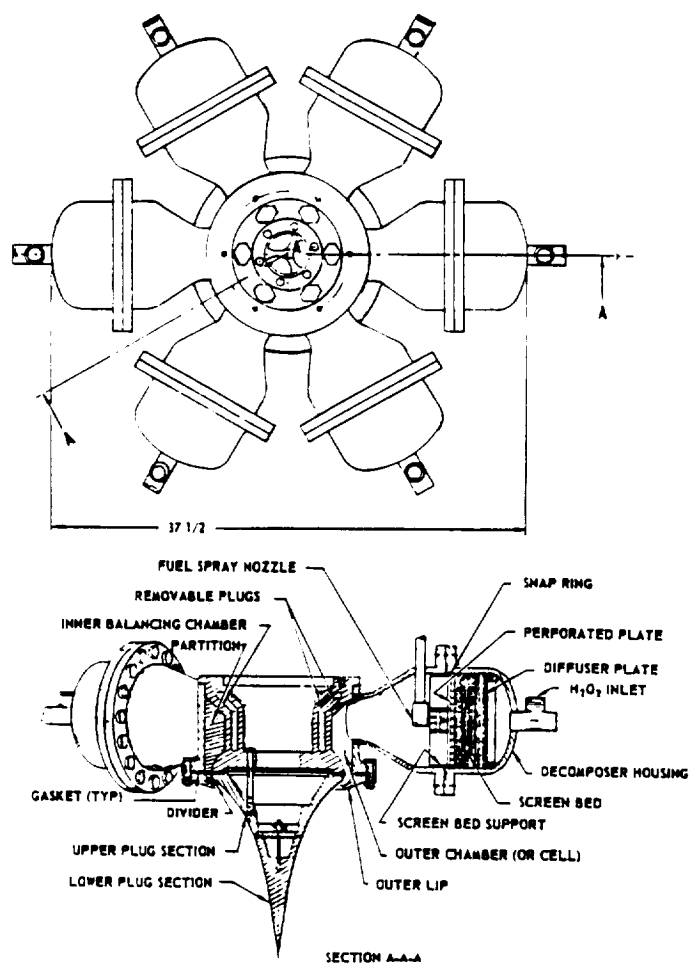


Figure 10.4: Detail of 16 Klb H₂O₂ Plug Nozzle Configuration (from Ref. 1)

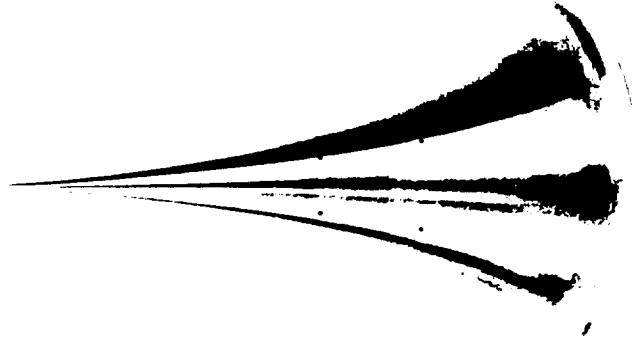


Figure 10.5: Isentropic Plug Nozzle, External Expansion (from Ref. 1)

1.9 grams for every 1 cm^2 of regeneratively cooled surface area.

It is interesting to imagine how this method of construction might be applied to the design of a cooled primary optic for the LTD spacecraft. Similar techniques are no doubt being investigated for large cooled optics in SDI power-beaming applications. The shortest primary optic contour in Fig. 10.2 (i.e., focus at $50\%C$) has a total surface area of $17,370 \text{ cm}^2$; at 1.9 g/cm^2 , a stainless steel mirror might come in at 33 kg. Using a thin lightweight metal faceplate with a carbon fiber composite sandwich substructure, perhaps the $33.3\%C$ optic could be built for 22 kg. A schematic diagram showing the internal details of an isentropic plug nozzle rocket engine with a geometry that is similar in shape to this primary optic design is given in Fig. 10.11.

10.2 Injector Head Design

Pictured in Fig. 10.12 is one of the eight ring injectors that forms a complete annulus at the top of the 50 Klb thrust rocket engine designed by Graham and Bergman. One might envision a similar injector head, reduced in width to 0.5 cm, for the LTD spacecraft at the mirror's annular focus region. Laser supported detonation (LSD) waves must be ignited at this location with absolute reliability. Therefore, these injector heads must be united with a tuned ignition array [2,3] or other mechanism to minimize the laser energy (and time) required to ignite LSD waves. Other "hot section" surface areas within the LTD engine which must be actively cooled (see Fig. 10.1) include the shroud support struts, and entire lower surface of the shroud — which is the principal impulse coupling region. The secondary impulse coupling surface is, of course, the primary receptive mirror, which serves to turn the rocket exhaust flow back towards the axial direction.

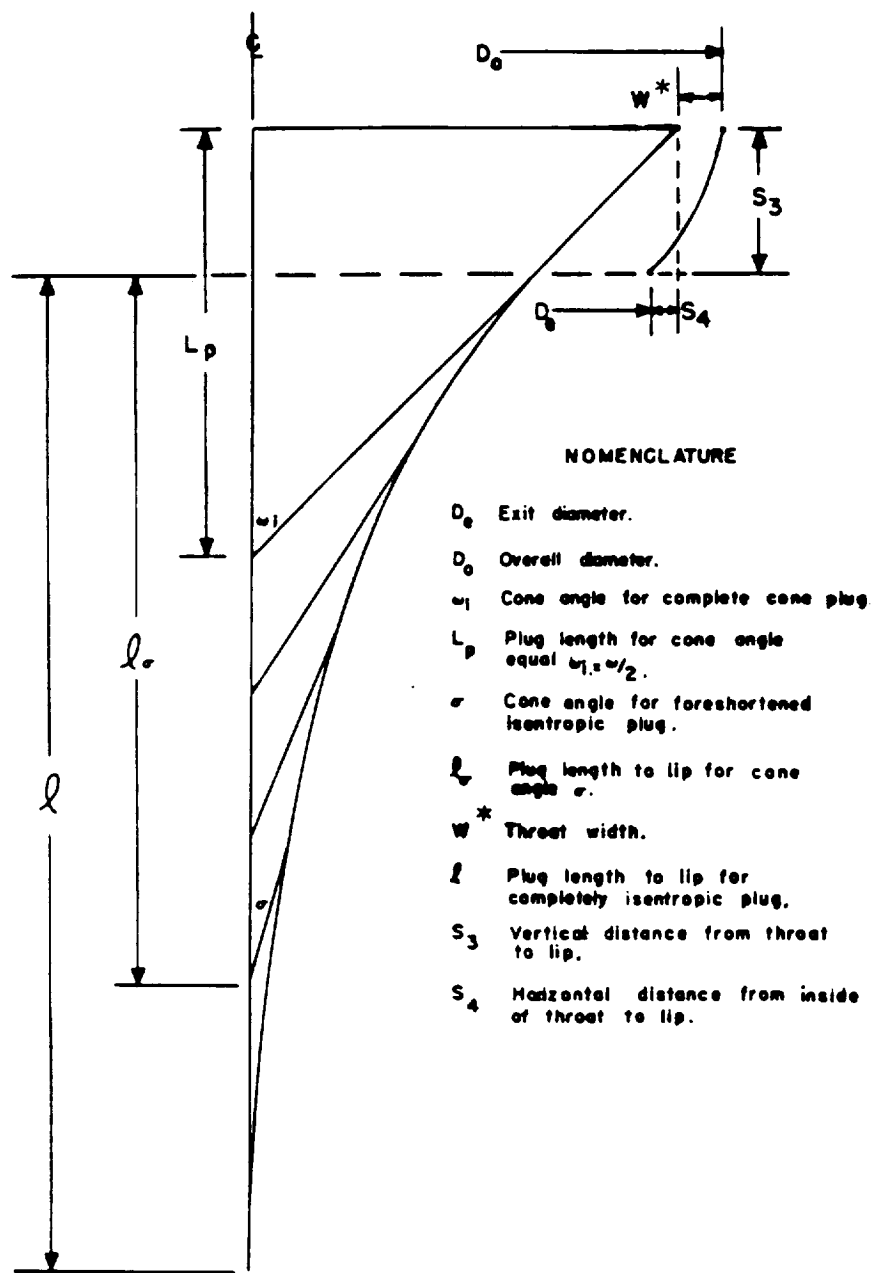


Figure 10.6: Outline of 50% Internal Expansion Plug Nozzle (from Ref. 1)

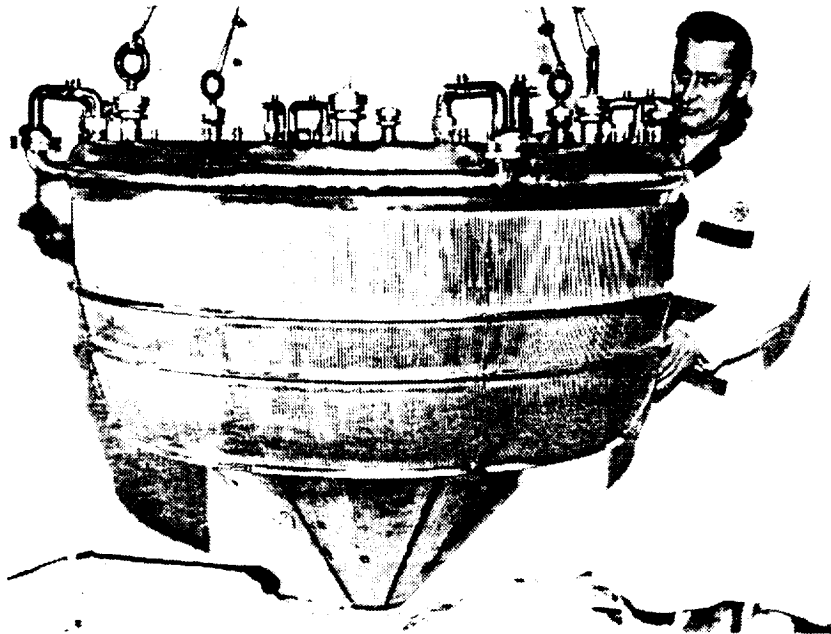


Figure 10.7: Cooled Engine Prior to Wire Wrapping and Thrust Mount Installation (from Ref. 1)

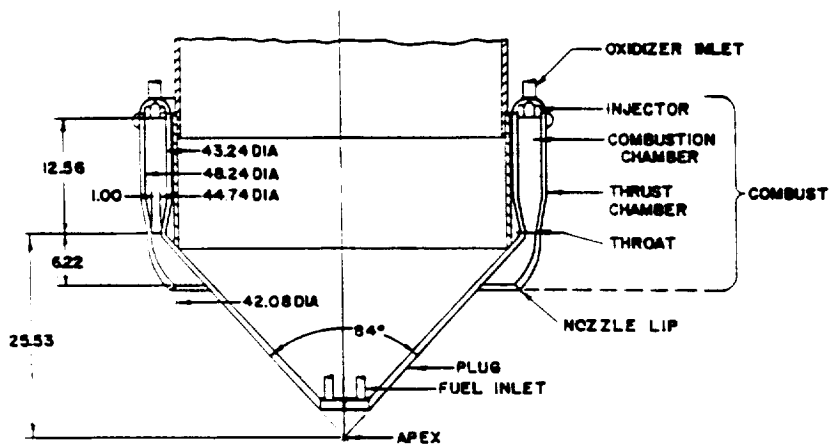


Figure 10.8: 50 Klb Plug Nozzle Configuration (Dimensions in Inches)(from Ref. 1)

10.2. INJECTOR HEAD DESIGN

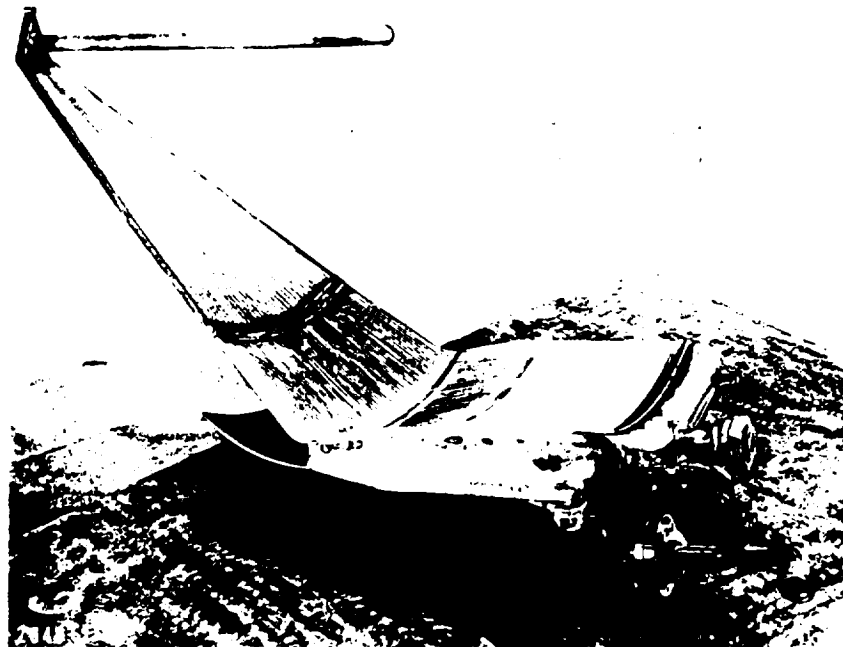


Figure 10.9: Cooled Segment (from Ref. 1)

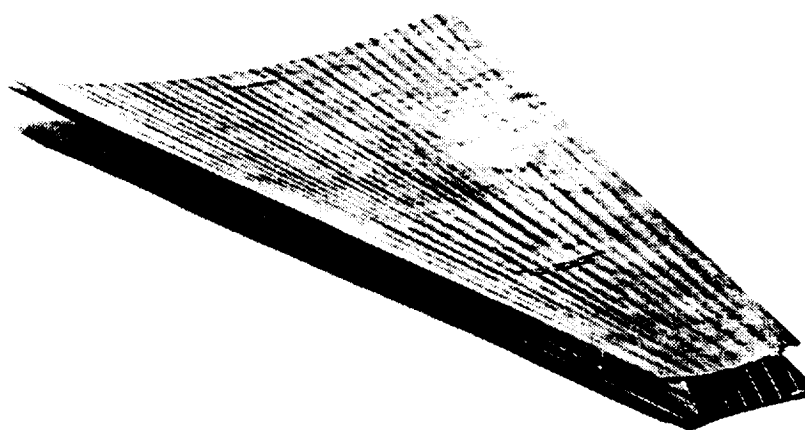


Figure 10.10: Cone Segment Assembly (from Ref. 1)

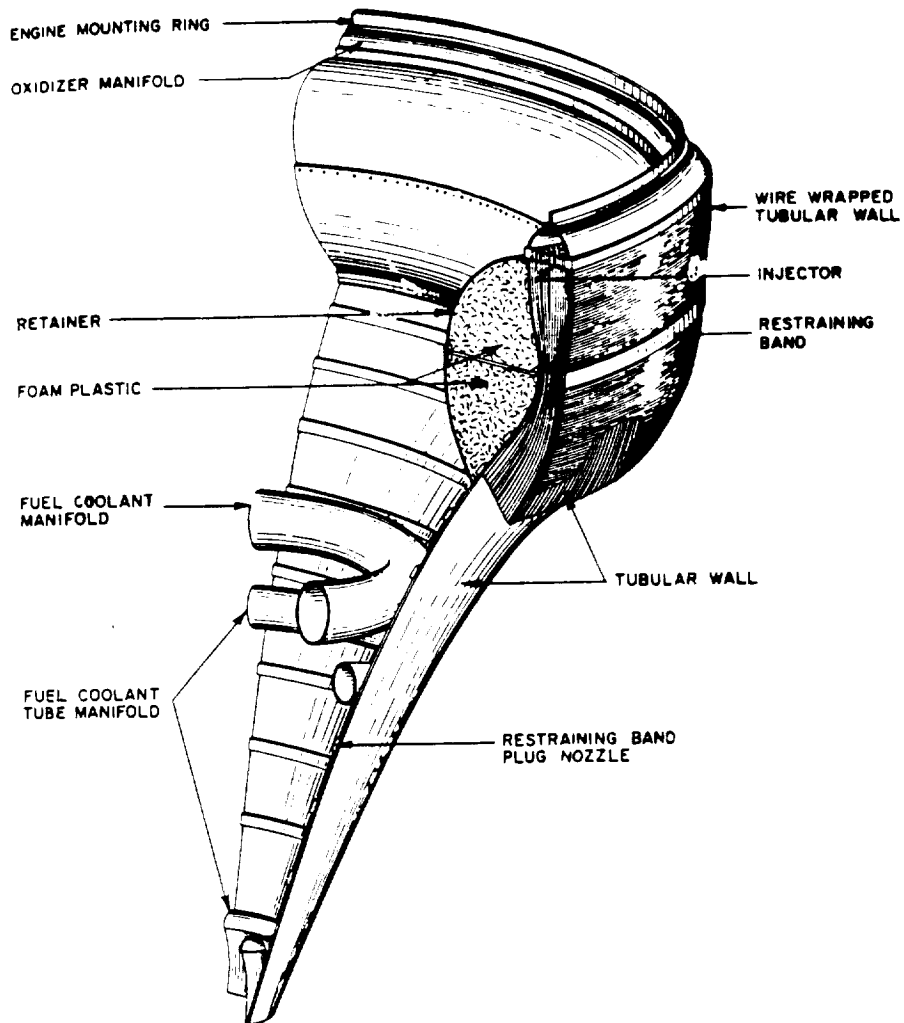


Figure 10.11: Quarter Sector of 33.33%C Primary Optic (from Ref. 1)

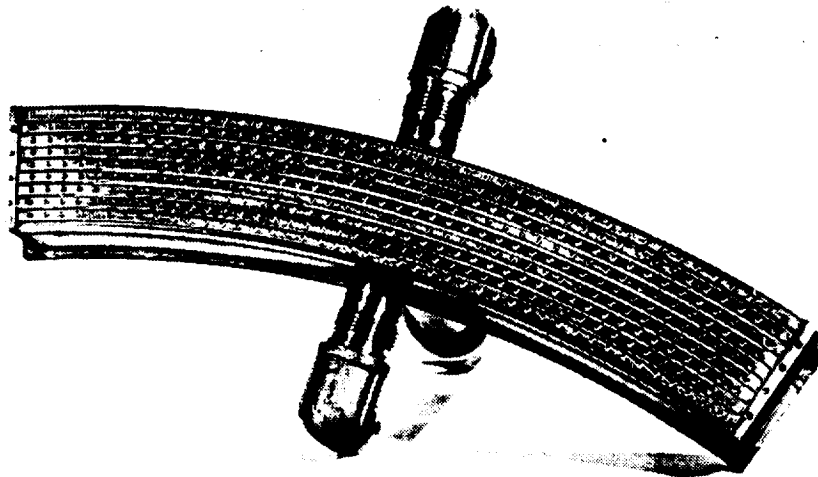


Figure 10.12: Injector Model III (from Ref. 1)

REFERENCES

- [1] Graham, A. R., "NASA Plug Nozzle Handbook," Contract NAS9-3748, General Electric Co., for the New York State Atomic and Space Development Authority, circa 1970.
- [2] Reilly, D. A., "Advanced Propellant for Laser Propulsion," presented to the 1987 SDIO Workshop on Laser Propulsion, Los Alamos National Laboratory, Los Alamos, NM, September 14-18, 1987.
- [3] Rollins, C., and Weyl, G., "Issues for Laser Propulsion: Progress in Theory and Modeling," presented to the 1987 SDIO Workshop on Laser Propulsion, Los Alamos National Laboratory, Los Alamos, NM, September 14-18, 1987.

Chapter 11

EARTH-TO-ORBIT TRAJECTORY SIMULATION

The trajectory analysis of any launch vehicle becomes a critical step in the overall system integration process. Many important engine/vehicle related characteristics of the craft must come together for the final product: *performance*. Launch vehicle performance is typically measured in terms of payload capability which for the LTD is the entire dry mass and ullage gas, totaling 124 kilograms. This vehicle must be capable of attaining low Earth orbit with the available amount of propellant while minimizing the total laser energy consumed along the insertion trajectory.

The trajectory was evaluated using a computer tool called SORT (Simulation and Optimization of Rocket Trajectories) which was written by McDonnell Douglas Astronautics Co. for NASA to design space shuttle trajectories [1]. The code is sufficiently general such that it can analyze any trajectory (even those for other planets), and model all important environmental parameters that affect the vehicle dynamics. Engine performance, vehicle aerodynamics, guidance algorithms, and mass histories interact with atmosphere and gravity models.

The capability of the SORT program is quite extensive in its use of these sophisticated vehicle and environmental models. The program can iterate on trajectory parameters to optimize performance, achieve a desired criteria, or constrain the solution to avoid some specified limit. These capabilities make SORT one of the most powerful trajectory analysis tools available in the world.

Even with all of the generality built into SORT certain modifications were required for the Lightcraft Technology Demonstrator vehicle. The most significant software modification involved the unique energy source, a laser. A new vehicle steering option was encoded so that the Lightcraft could always point at the ground-based laser power station or laser satellite which initially passes overhead (see Fig. 11.1). Since the use of laser propulsion was not anticipated by the authors of SORT, software changes were also needed in the engine model in order to evaluate the total amount of laser energy expended along the trajectory. After these modifications to the code were

included, SORT was capable of modeling Lightcraft performance to a high degree of accuracy.

11.1 Vehicle and Environmental Models

11.1.1 Aerodynamics

For this preliminary performance analysis, vehicle drag was the only aerodynamic force (or moment) that was modeled. Since the Lightcraft is axisymmetric, it produces no lift at zero angle-of-attack. During flight, the vehicle's angle-of-attack stays fairly small due to the restrictive steering requirements and high thrust to weight ratios. It is suspected that aerodynamic lift can possibly be used to benefit Lightcraft performance along the trajectory.

The vehicle drag profile is shown as the dashed line in Fig. 11.2 (from Ref. 2). The conservatively high drag coefficients indicated for the LTD are the result of the blunt vehicle configuration. In the analysis of hypersonic airbreathing launch vehicles, it is not always immediately evident as to what should be classified as "engine" versus "airframe" — especially when large portions of the vehicle forebody provide the hypersonic inlet function. Hence careful inventory must be kept to avoid penalizing the engine for what might be more appropriately accounted against the vehicle airframe.

In the LTD, the annular shroud is classified as the "engine," and the double-coned center body is treated as the "airframe." This is a conservative approach that results in very high vehicle drag coefficients. As portrayed in Fig. 11.3, the LTD conical forebody serves to turn the external inlet airflow so that it "blows" in a direction parallel to the annular shroud. Here it is assumed that the unstalled annular shroud airfoil produces negligible lift and drag. In sharp contrast, flow over the conical centerbody is assumed to separate at the sharp outer edge (see Fig. 11.3), so that the entire afterbody primary optic is immersed in a turbulent wake. Hence, the theoretical and experimental drag coefficient data for a 30° conical head (half-angle) presented in Fig. 11.2 would be appropriate. Note that the subsonic drag coefficient was taken to be 0.45 which closely agrees with the data in Fig. 11.4, also from Ref. 2, for a 30° half-angle cone.

11.1.2 Engine

Detailed discussions for the two engine modes are presented in earlier chapters of this report. The flight performance for the airbreathing mode was calculated for a wide range of altitudes, Mach numbers, and power settings. These values were then loaded into trivariate tables accessible to the program. The SORT program interpolated this

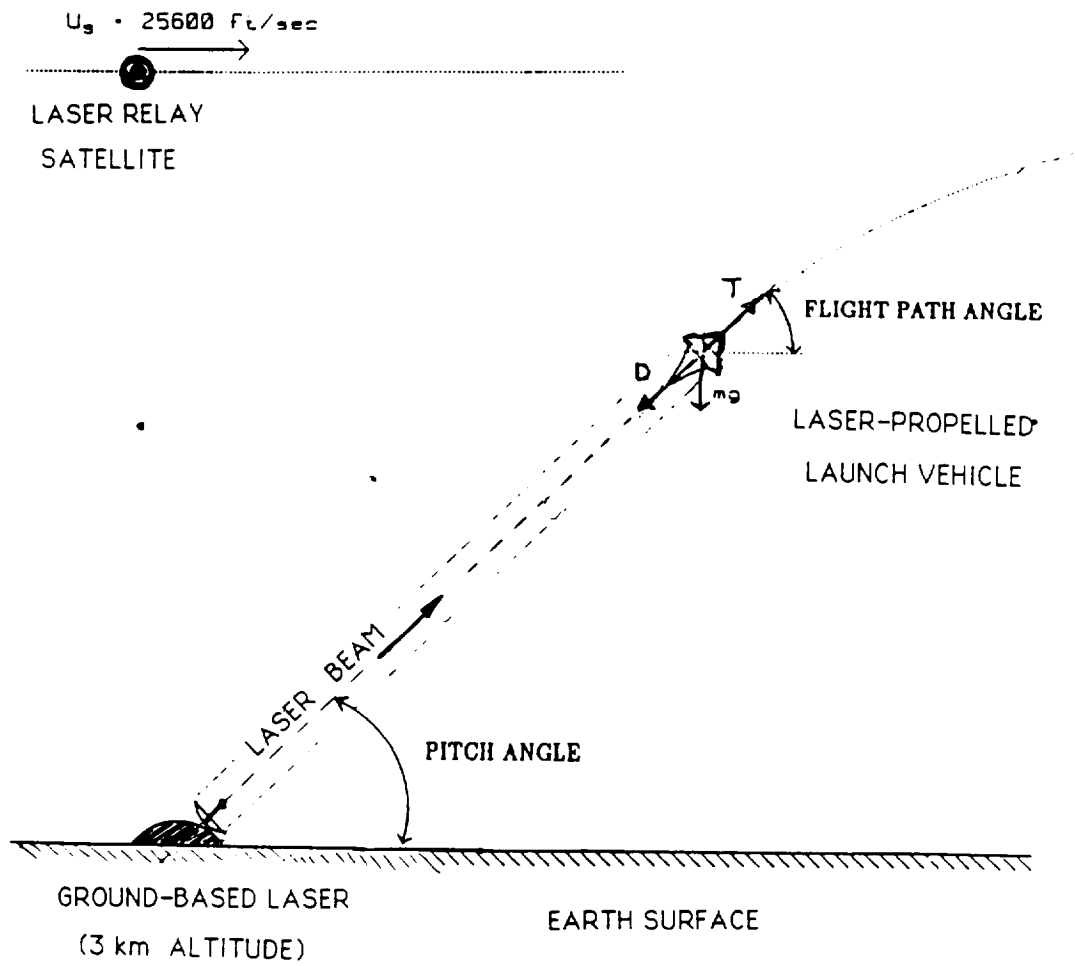


Figure 11.1: Ground-Based Laser Launch

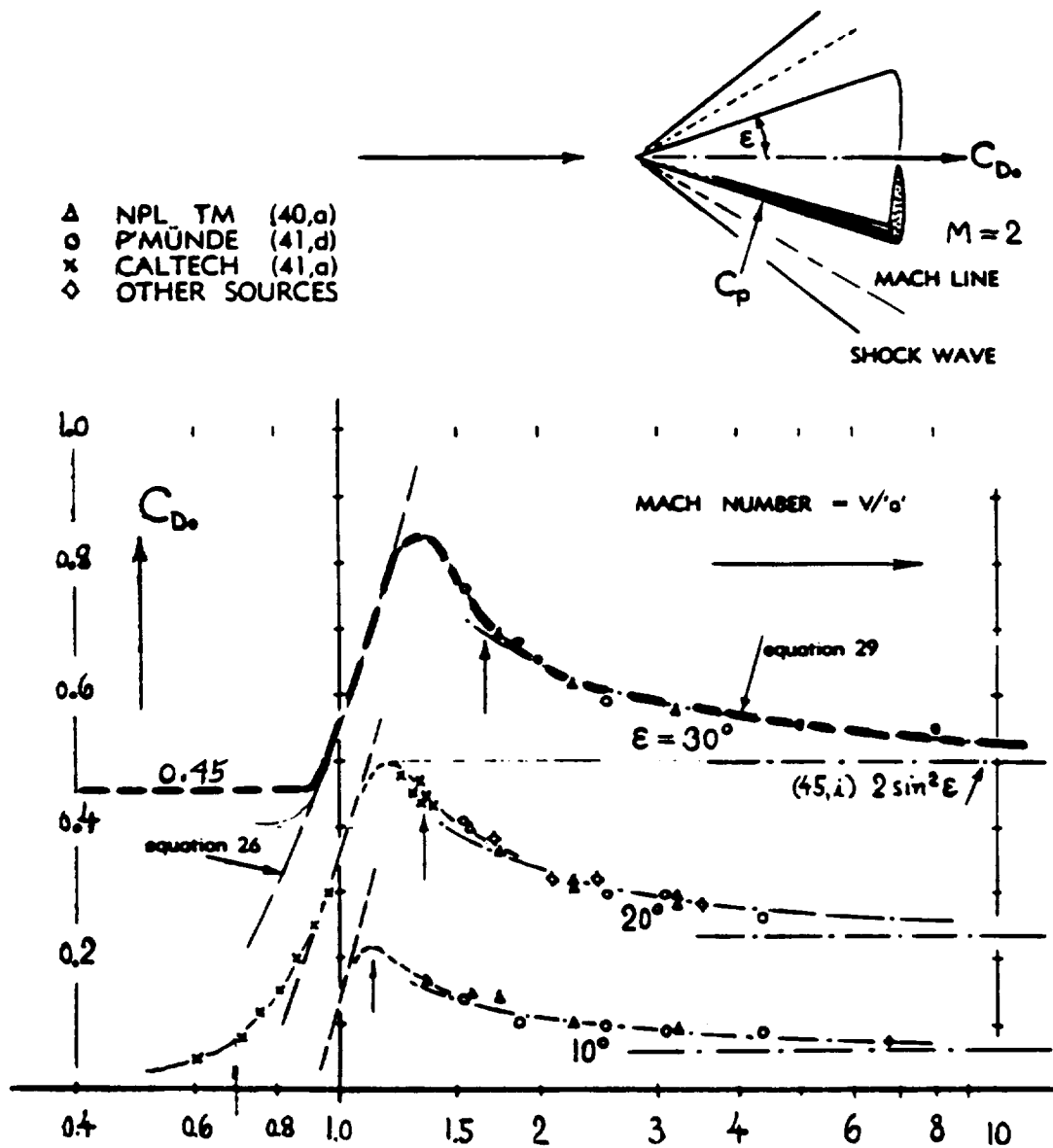


Figure 11.2: Theoretical and experimental drag coefficients of various conical heads at transonic and supersonic Mach numbers (from Ref. 2).

ORIGINAL PAGE IS
OF POOR QUALITY

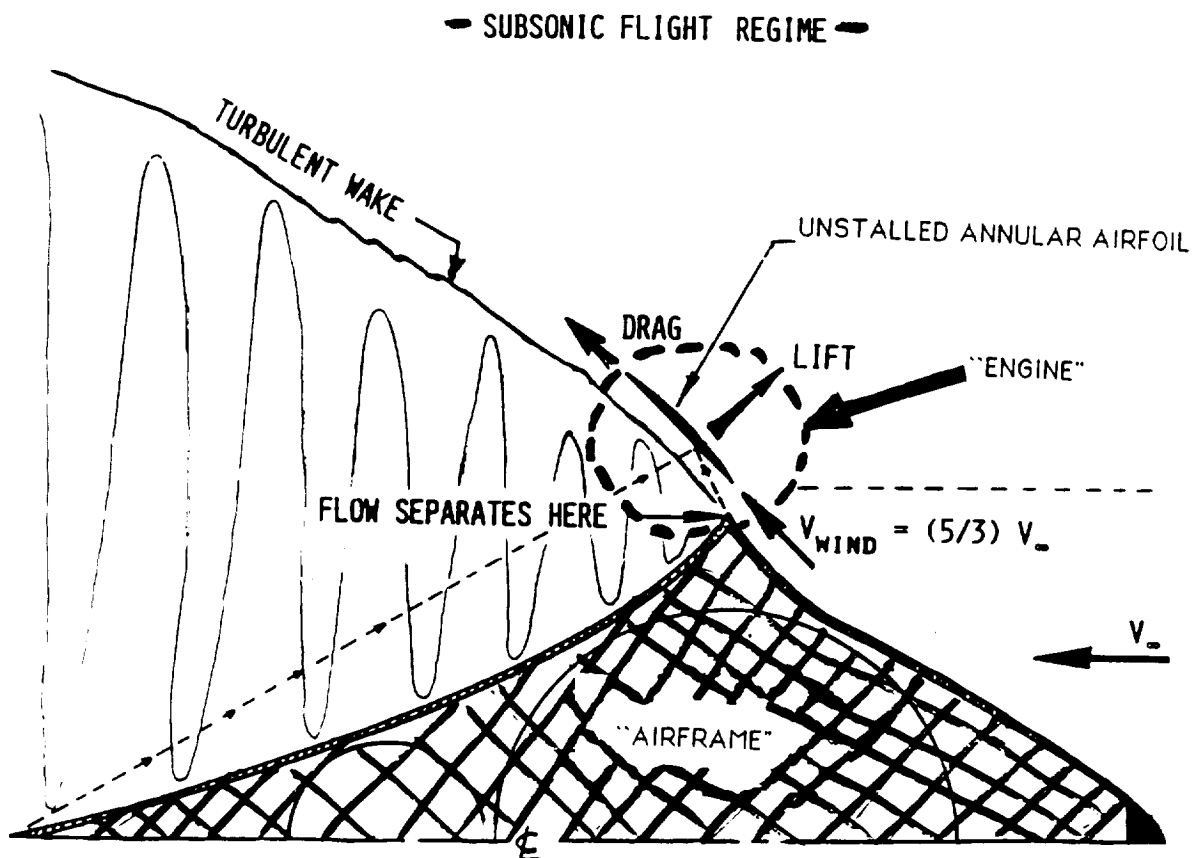


Figure 11.3: Classification of "engine" and "airframe" components, for the purpose of determining vehicle drag profile.

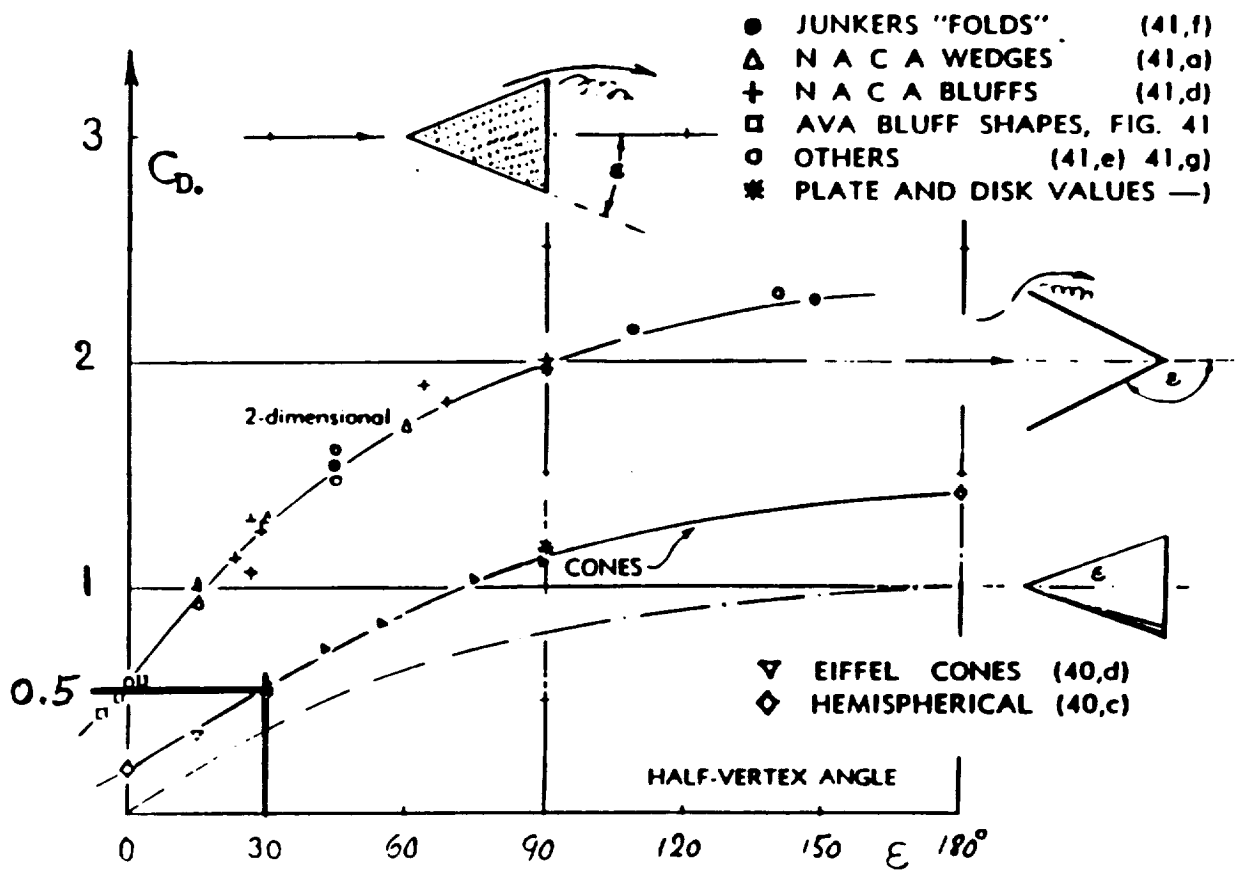


Figure 11.4: Drag coefficients of wedges, cones and similar shapes as a function of their half-vertex angle (from Ref. 2).

data to find the thrust, specific impulse and power consumption at any point along the trajectory. The engine model also calculates the cumulative laser energy used throughout the launch trajectory, which also can include atmospheric attenuation of the laser beam.

11.1.3 Steering

The Lightcraft Technology Demonstrator must point directly at the ground-based laser (GBL) or the relay satellite at all times during powered flight. Two laser power transmission geometries were assumed for the four trajectory simulation cases which have been carried out on the LTD. The geometry used in Case I is portrayed in Fig. 11.5. The stationary ground-based laser is assumed to have an elevation of 3 km (density altitude). The LTD is accelerated to an initial velocity of 100 m/sec by a compressed air cannon, which ejects the vehicle at an initial launch angle of 30°. One-half second later the GBL is switched on, and the "shroud-lift" ERH thruster begins the laser powered ascent.

As shown in Fig. 11.6, a boost reference angle of 30° is maintained until 50 seconds into the flight, whereupon this restriction is relaxed. When orbit velocity (8 km/sec) is attained, the boost reference angle has fallen to 19.5°, and the power beam is switched off. This launch trajectory (Case I) will place the vehicle into a highly elliptical orbit that might cause the vehicle to re-enter the atmosphere before one revolution of Earth is completed. Hence, this launch option may require the addition of a small chemical rocket, as shown in Fig. 11.7, for orbit circularization. The Case I launch geometry, with the chemical "kick" rocket, should enable circular satellite altitudes of up to 2000 km.

For the last three trajectory simulation cases, a different laser power transmission geometry and steering algorithm were used (see Fig. 11.8). As before, the LTD is ejected by the compressed air cannon at an initial velocity of 100 m/sec, density altitude of 3 km and initial launch angle (measured from horizontal) of 30°, 45° or 60° for Cases II, III, and IV, respectively. Again, the laser powered boost begins 0.5 seconds later, and the initial LTD pitch angle is maintained constant until the airbreathing engine phase terminates at Mach 5-7 and 100-115 kft density altitude. Thereafter, the craft is allowed to coast in a ballistic trajectory until apogee is reached (≈ 150 km), whereupon the craft is pitched over to roughly 0°, measured with respect to the horizon (see Fig. 11.9). At this point, the GBL is turned back on, and the beam is bounced off a laser relay satellite (200 km altitude orbit) and redirected toward the LTD, as shown in Fig. 11.8. Upon arrival of the beam, the LTD's laser heated rocket mode is engaged, and the LTD accelerates to orbital velocity (8 km/s) in a matter of 80-100 seconds of firing time. Currently, the steering model works only for satellites passing directly over the launch site, and further improvements should permit the

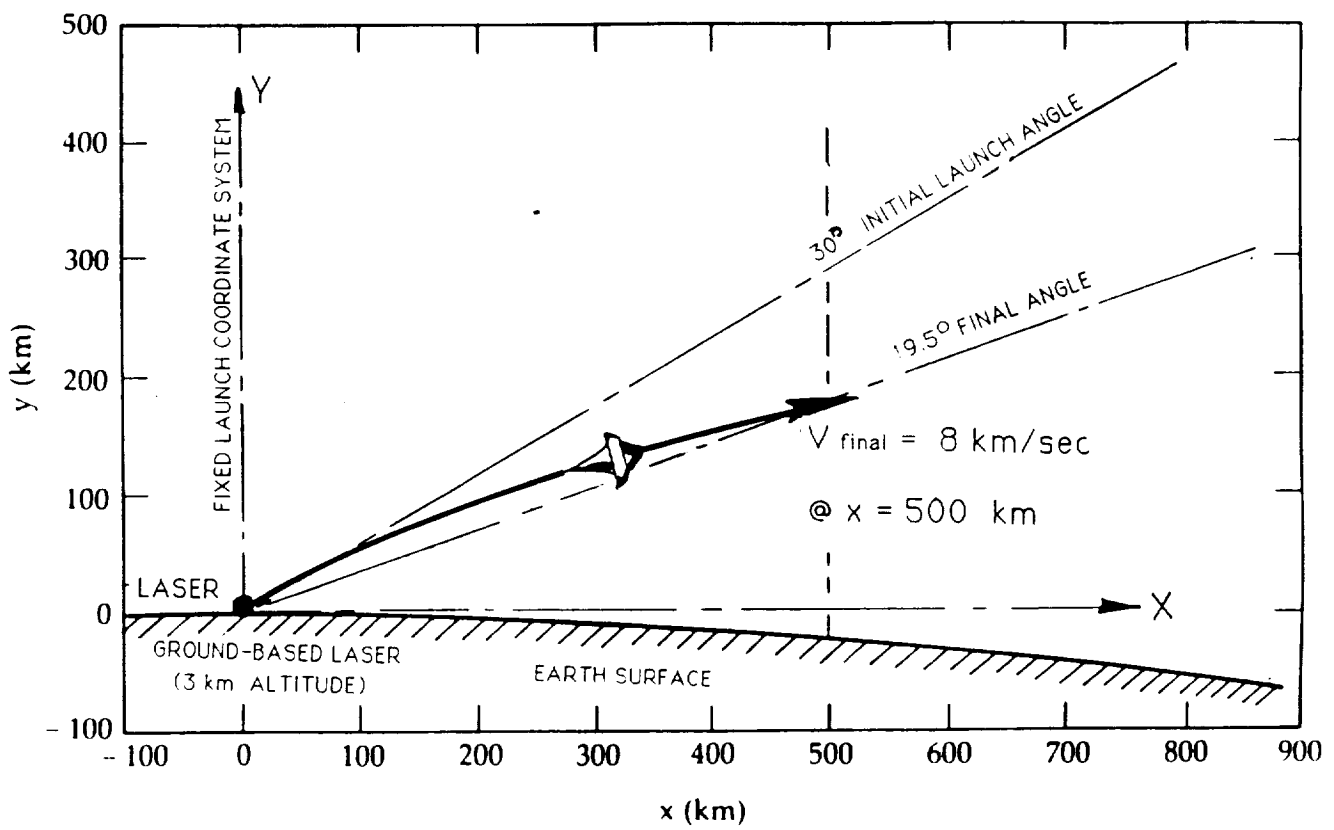


Figure 11.5: "Case I" Launch Trajectory (No Relay Satellite)

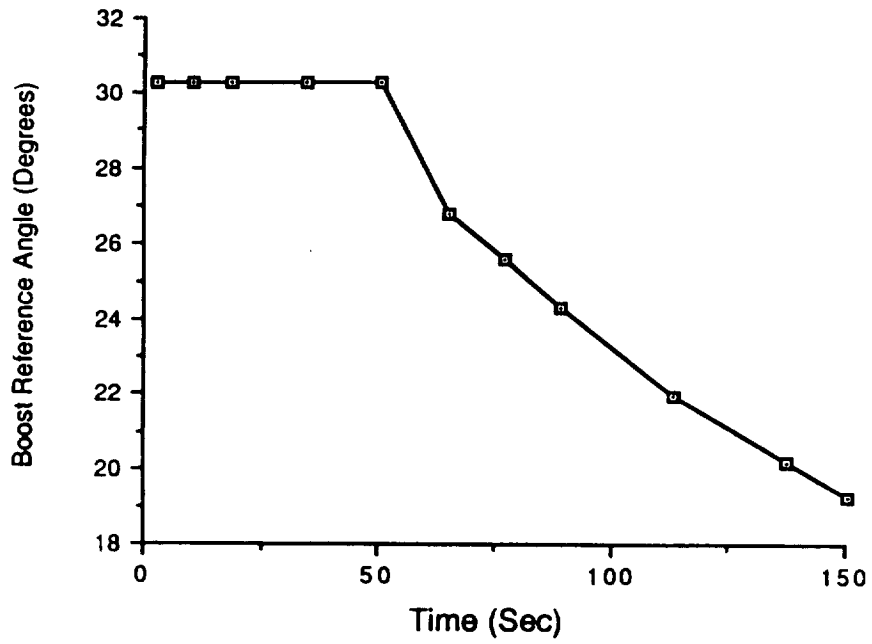


Figure 11.6: Boost Reference Angle vs. Time for Case I

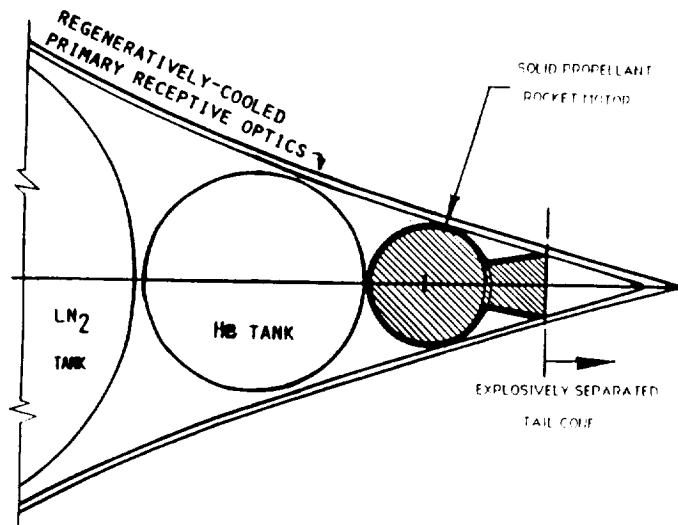


Figure 11.7: Chemical "Kick" Rocket Option (for orbit circularization)

inclusion of relay satellites with a more general ground track.

11.2 Simulation Parameters

The preliminary weight breakdown for the LTD can be found in Chap. 2. The SORT program can model variations in the center-of-gravity (CG) location, but the present analysis placed the vehicle CG on the centerline (along with the engine) to simplify the thrust-pointing requirements.

A complete Earth gravity model exists in the SORT code which includes J2, J3, and J4 effects. The program continuously calculates the orbital parameters throughout the boost trajectory.

The atmospheric data loaded into SORT was the ARDC Model Atmosphere [3]. Although wind can be a significant aerodynamic perturbation, none was included at this stage of the analysis.

The SORT program treats the trajectory as a specified sequence of maneuvers of phases. Each event is defined by the user at appropriate places in the simulation so that new inputs can be assembled into the trajectory. The launch vehicle flies from event to event until, finally, it obtains the orbital parameters necessary to achieve the desired orbit altitude. The craft then coasts until it reaches apogee, and performs a final orbit-insertion burn. The SORT program has iteration capability that can be used to optimize total propellant weight (or laser energy) used during ascent. A typical trajectory sequence for Cases II, III, and IV is described below.

11.3 Trajectory Sequence

The LTD is given an initial velocity of 100 m/s at a precise launch pitch angle, by a compressed air cannon. While accelerating within the cannon, a lightweight sabot is used to cradle the LTD and also to prevent the escape of compressed gasses around the LTD. After emerging from the barrel, the sabot quickly separates from the LTD, leaving it free and clear — ready to accept the laser power beam.

At 0.5 sec, the shroud lift ERH thruster is engaged and the LTD climbs out at a fixed boost reference angle. Since the ERH thruster mode is completely airbreathing, only a small amount ($\approx 10\%$) of the liquid propellant is consumed as expendable coolant for the primary mirror and engine hot sections. This mode effectively initiates the acceleration portion of the flight. As the vehicle climbs out, the pulse frequency of the ERH engine is increased to accelerate the craft through the transonic region, toward Mach 5. As the ram drag increases, net effective thrust of the ERH thruster decays. At 100–115 kft, the engine is shut off.

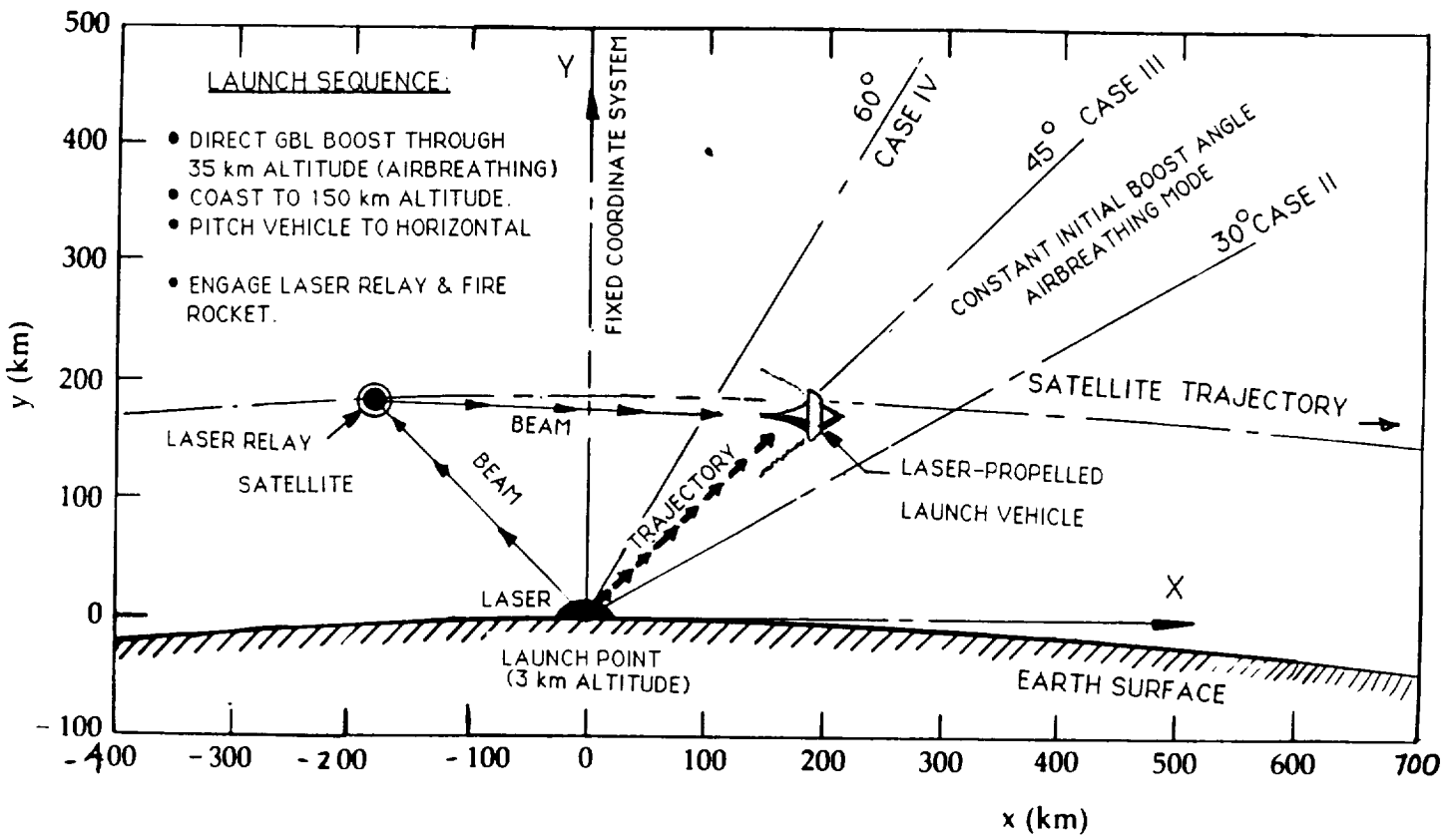


Figure 11.8: Use of Laser Relay Satellite for Orbit Circularization (Cases II, II and IV)

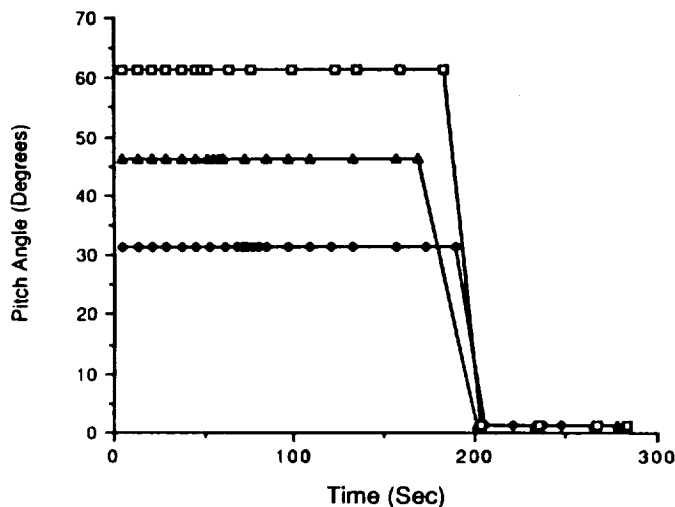


Figure 11.9: LTD Pitch Angle vs. Time (for Cases II, III, IV)

The vehicle continues to coast upward along a ballistic trajectory toward apogee. At the specified (or optimized) altitude, the vehicle pitches over just prior to receiving power from the low altitude relay satellite. The exact zenith angle (measured from vertical at the GBL site) at which to engage the relay satellite is determined iteratively to achieve maximum performance. Severe atmospheric absorption is suffered by high power laser beams transmitted beyond zenith angles of 70.5° ; i.e., three vertical atmosphere path lengths (at a 60° zenith angle, two atmospheric path lengths are incurred). Hence, for a 200 km relay satellite, the maximum slant range (GBL to relay satellite) is ≈ 600 km; this equates to an orbital path length of about 565 km to the 0° zenith position. At 8 km/s, the relay satellite will take 70 seconds to arrive at a position directly over the GBL.

The rocket mode is started as the vehicle reaches apogee. This burn is terminated as the inertial velocity reaches the necessary value for circular orbit at that altitude. The available laser power of 250 MW, translates to a rocket thrust of ≈ 17.5 kN ($CC = 70$ N/MW), and a firing time of 80–100 seconds to reach 8 km/sec orbital velocity. Also, as mentioned earlier, the LTD optical axis must be aligned with the relay satellite to an accuracy of $\pm 0.5^\circ$ or better. The LTD launch window must be exactly synchronized such that the LTD is approaching apogee when the relay satellite is at a zenith angle of 70.5° (or 60° , etc.).

If the 200 km relay satellite is engaged when it is too high overhead (e.g., zenith angle of 0°) and the LTD is still at a much lower altitude (e.g., 150 km), the rocket mode will drive the LTD back into the atmosphere before it has a chance to accelerate

to orbital velocity. The trajectory will not climb high enough to prevent increased aerodynamic drag, which is associated with additional expenditures of fuel or laser energy, from terminating the mission.

The final velocity desired at rocket termination is a function of the relay satellite and LTD apogee positions, altitude, LTD flight path angle and the drag experienced (i.e., ΔV) as the vehicle coasts up to the desired apogee altitude to make the final rocket burn. There is no easy analytical solution to this targeting problem. Many trajectories are run in an optimizing attempt. Typically the performance indicator "propellant weight" was optimized, although total laser energy could also be run. Analysis in the future will focus on the minimization of laser power. The key parameters which were varied in the attempt to optimize propellant weight were the initial position of the relay satellite, power available to the engines (throttle setting), and apogee altitude for the pitchover maneuver. Trajectory optimization is a never-ending task (e.g., engineers are still fine-tuning Space Shuttle trajectories to discover more payload capability), but the results so far give a baseline indication of the LTD microspacecraft performance potential.

11.4 Results

The trajectory analyses to date using SORT have just barely scratched the surface of the comprehensive performance optimization problem. However these simulations do give highly accurate answers for the selected models and input data. Assuming the vehicle models (engine, drag, etc.) are fairly accurate, the resultant performance reported here would certainly be attainable. Although not optimal, the current results indicate the types of problems to be encountered, and present conservative performance capabilities (within the accuracies of the models and assumptions). Further, more detailed analyses can be expected to improve upon these results.

11.4.1 Case I

As mentioned above, Case I doesn't use a laser relay satellite, and was run at a 30° initial launch angle with the craft switching from the "shroud lifter" ERH thruster mode directly to laser-heated rocket mode at about 65 seconds into the flight. This transition occurred at about Mach 7 and 35 km altitude. The rocket specific impulse was set at 875 seconds, or in the middle of the range projected for nitrogen propellant (e.g., 725-1025 sec). Figures 11.10 through 11.17 show the projected performance of the LTD machine for this case. Note that the rocket "burn" lasts for approximately 85 seconds, and accelerates the vehicle to 8 km/sec at $t = 150$ seconds. The trajectory in Fig. 11.12 indicates that this point is reached at a down range distance of 500 km and an altitude of about 185 km, where the boost reference angle is 19.5° . If the

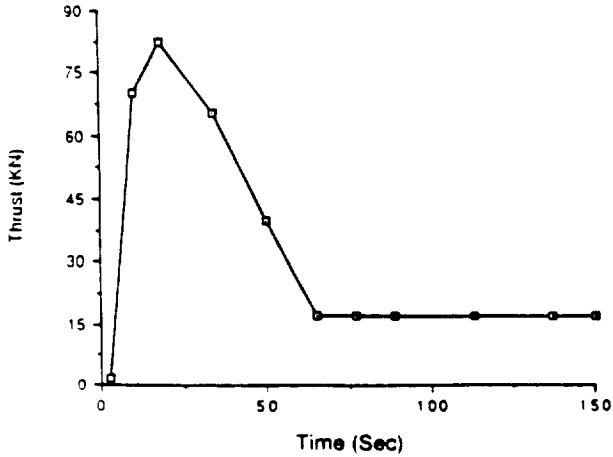


Figure 11.10: Thrust vs. Time (Case I)

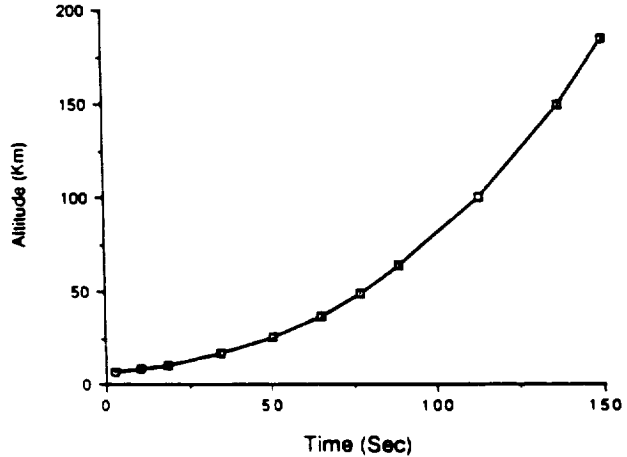


Figure 11.11: Altitude vs. Time (Case I)

LTD is equipped with a small chemical rocket for orbital insertion (see Fig. 11.7), this mode could possibly enable circular orbits of up to 2000 km in altitude. Note in Fig. 11.14 that acceleration varies from 2 to 3 G's in the airbreathing mode, and reaches a peak of 10 G's at the end of the rocket mode. In Fig. 11.16, the peak power requirement is 350 MW which occurs in the ERH thruster mode and significantly exceeds the 250 MW baseline power level set for the rocket mode.

The coupling coefficient reaches a peak of 525 N/MW early in the airbreathing mode and falls to a low of 70 N/MW in the rocket mode (see Fig. 11.17).

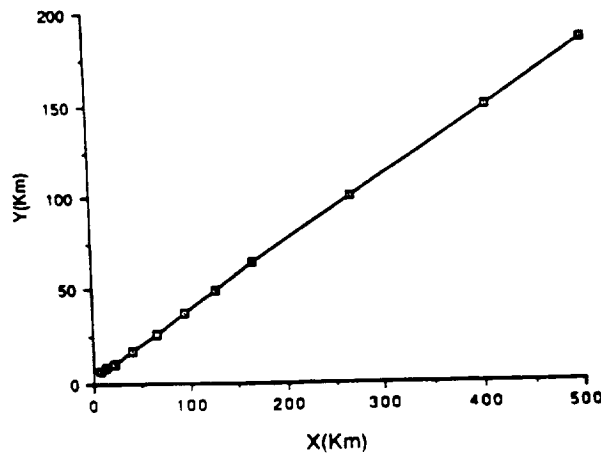


Figure 11.12: Altitude vs. Downrange Distance (Case I)

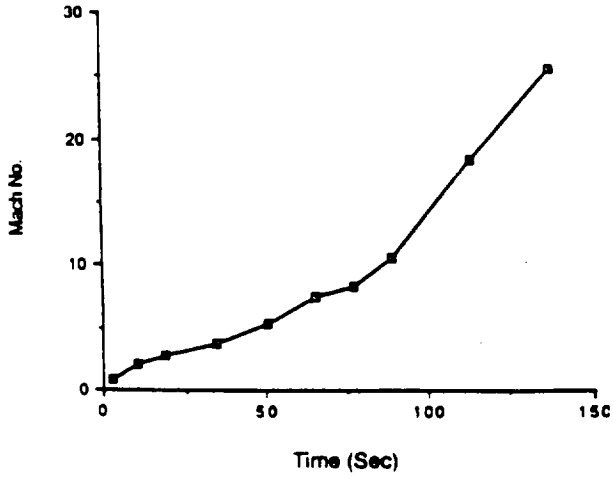


Figure 11.13: Flight Mach Number vs. Time (Case I)

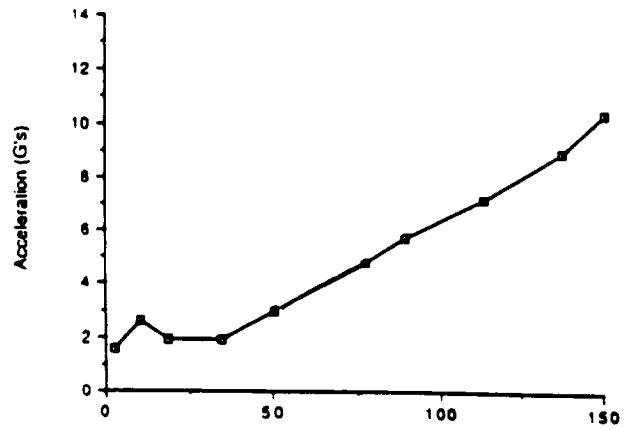


Figure 11.14: Acceleration vs. Time (Case I)

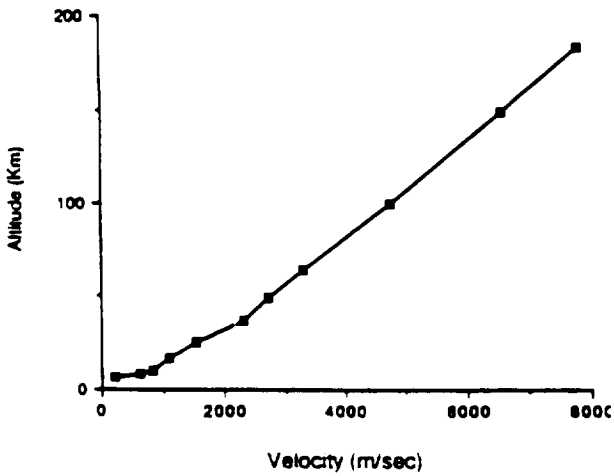


Figure 11.15: Velocity vs. Altitude (Case I)

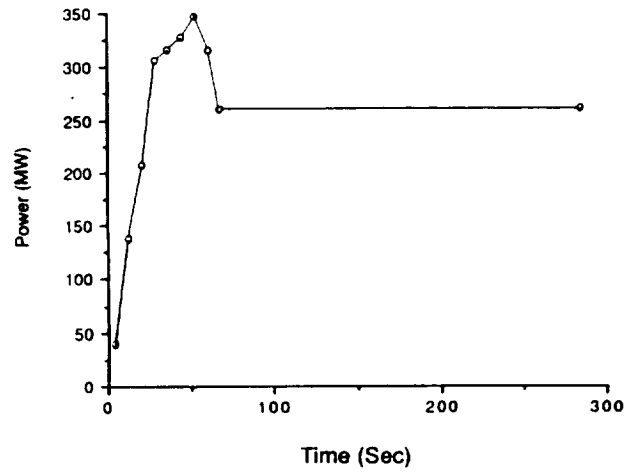


Figure 11.16: Power vs. Time (Case I)

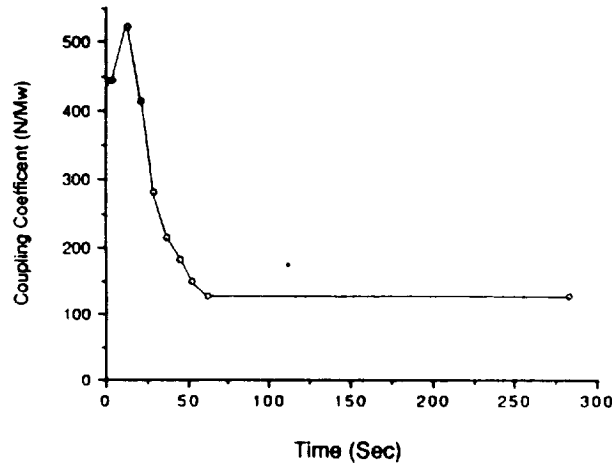


Figure 11.17: Coupling Coefficient vs. Time (Case I)

11.4.2 Cases II, III and IV

As before, cases II, III, and IV utilize the laser relay satellite, and assume initial boost reference angles of 30°, 45° or 60°, respectively. These cases are useful for low Earth orbit missions (e.g., around 200 km) and depend upon the laser relay satellite for orbital insertion. Figures 11.18 through 11.25 present the LTD performance for these cases. The rocket specific impulse was set at a conservative value of 650 seconds which allowed a coupling coefficient of 125 N/MW (see Fig. 11.25).

Note from Fig. 11.18 that the unpowered coasting phase lasted from 100–150 seconds in duration, which extended the total launch duration to 250–300 seconds total.

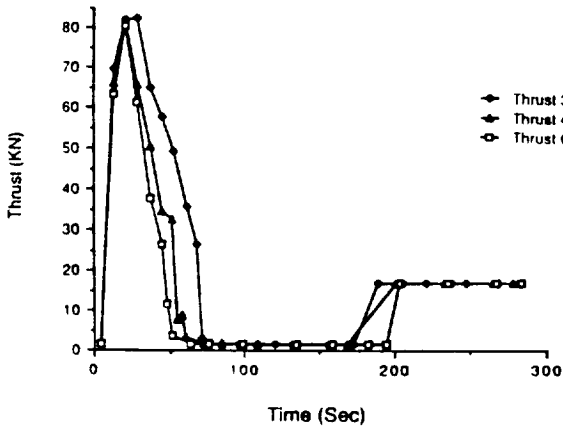


Figure 11.18: Thrust vs. Time (Cases II, III, & IV)

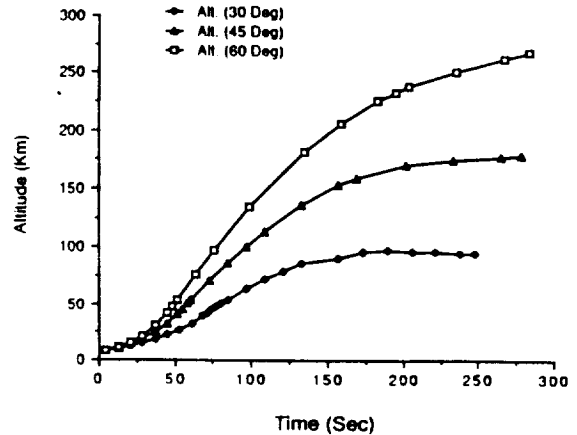


Figure 11.19: Altitude vs. Time (Cases II, III, & IV)

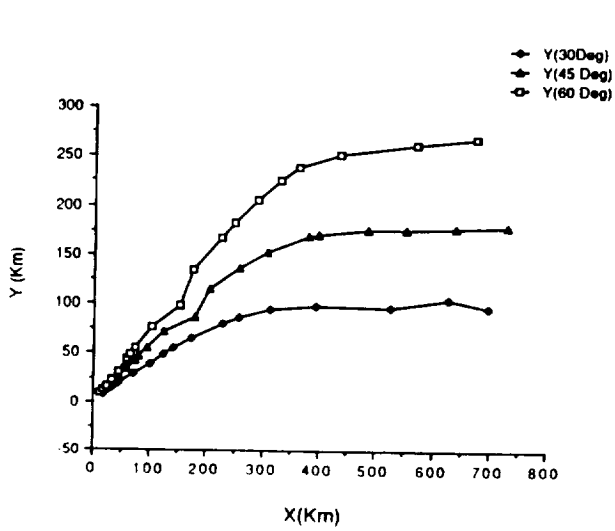


Figure 11.20: Altitude vs. Downrange Distance (Cases II, III, &IV)

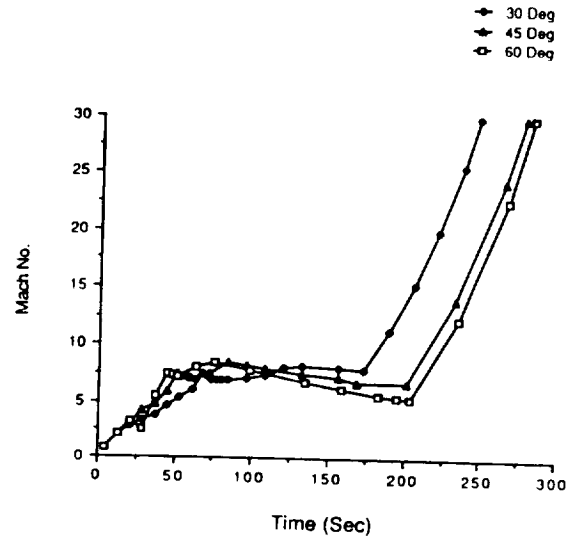


Figure 11.21: Flight Mach Number vs. Time (Cases II, III, &IV)

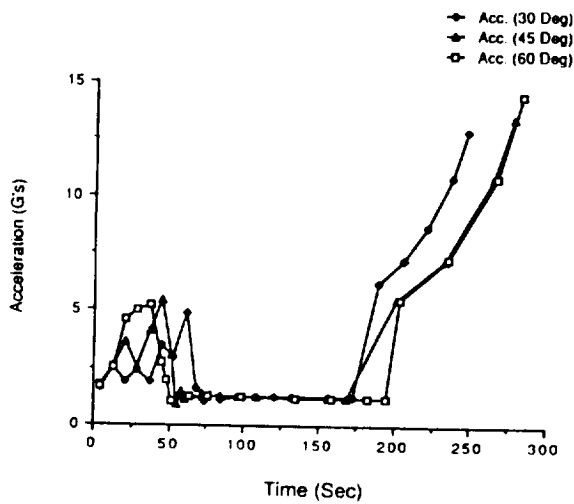


Figure 11.22: Acceleration vs. Time (Cases II, III, &IV)

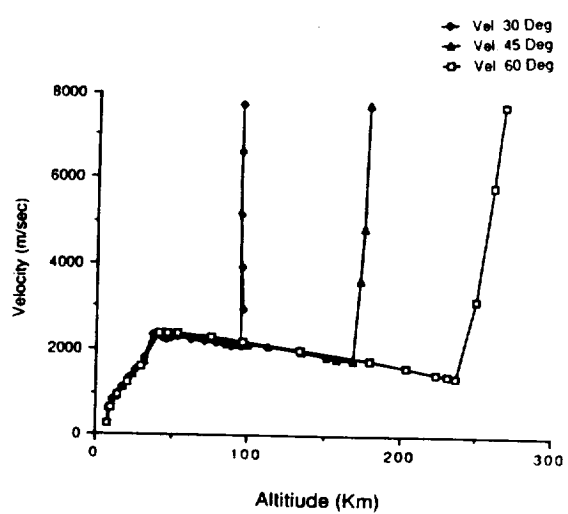


Figure 11.23: Velocity vs. Altitude (Cases II, III, &IV)

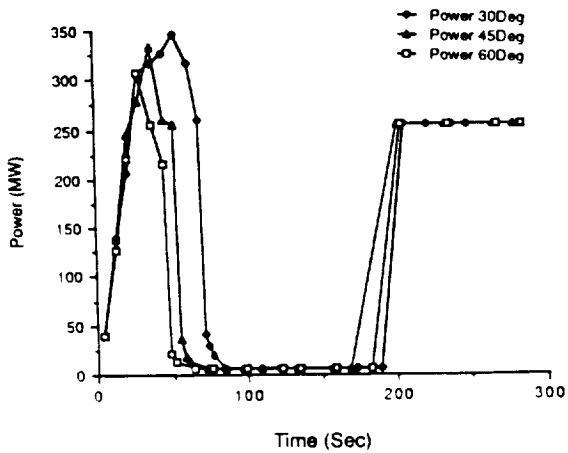


Figure 11.24: Power vs. Time
(Cases II, III, &IV)

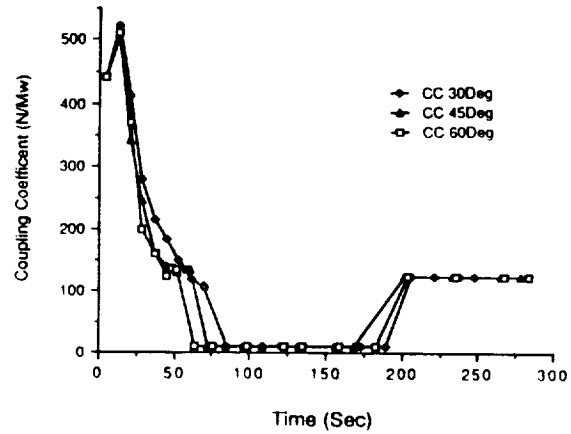


Figure 11.25: Coupling Coefficients vs. Time
(Cases II, III, &IV)

As indicated in Fig. 11.20, Case II (30°) resulted in a retrograde orbit and would immediately re-enter the atmosphere; in contrast, Case III (45°) produced a circular orbit at about 175 km altitude, and Case IV (60°) — a near-circular orbit at 265 km. From Fig. 11.23, it is apparent that, although Case III suffered the greatest ΔV loss due to drag in the coasting phase, 60° appears to be an excellent launch angle. Figure 11.24 indicates that the peak airbreathing engine laser power required for the 60° case is about 310 MW; for the 45° , 330 MW.

11.5 Summary

The trajectory analysis will need to continue as the engine and aerodynamic models evolve and the final results may end up considerably different than those presented here. This does not imply that the current analysis is crude or inaccurate, because it is quite precise within the confines of the models and inputs. The predicted performance for the Lightcraft Technology Demonstrator is undoubtedly revolutionary, and further analysis will continue to define this new frontier.

REFERENCES

- [1] Berning, M., "Version IV User's Guide for the Simulation and Optimization of Rocket Trajectories Program," McDonnell Douglas Astronautics Co., Houston, TX, Transmittal Memo No. 1.2-TM-FM86028-53, December 1985.
- [2] Hoerner, S.F., *Fluid Dynamic Drag*, Published by the Author, 1965.
- [3] Hill, P. and Peterson, C., *Mechanics and Thermodynamics of Propulsion*, Addison-Wesley Publishing, 1965.

Chapter 12

LIGHTSAT SYSTEMS DESIGN

As mentioned earlier, the Lightcraft Technology Demonstrator (LTD) is a microspacecraft that will not only demonstrate laser propulsion technology, but also serve as a lightsat. After attaining orbit, the LTD will become a low altitude (e.g., 200 km - 2000 km) sensor satellite, and have a nominal pointing accuracy of ± 0.5 deg (see Chapt. 6). Satellite hardware must be chosen to fulfill the LTD's role as a lightsat; i.e., weight, cost and size of electronics, attitude control systems, power supply, etc. must be minimized.

12.1 Lightsat Background

Small, lightweight (several kg), unmanned missions for specific applications have received increased attention as both equipment and launch costs continue to rise [1]. This was one of the underlying motivations behind the development of "get-away special" canisters for the Space Shuttle. A recent proposal by NASA and the University Corporation for Atmospheric Research involves housing scientific apparatus in the unpressurized sections of discarded Space Shuttle external fuel tanks [2]. Experiments could be housed in a cylindrical section 22.5 ft. long and 27.5 ft. in diameter; the apparatus would function like a high-flying sounding rocket to collect data for about an hour in suborbital space before the tanks re-enter the atmosphere and burn up. The program, known as Space Phoenix, is intended to recover some portion of the \$40 million cost for each shuttle fuel tank. Efforts such as these illustrate the importance of using small components for multiple mission purposes in order to provide economical access to space.

Many significant experiments may be performed in space without resorting to large, relatively expensive payloads. These so-called "lightsats" or "microspacecraft" have been considered for many diverse applications, including communications satellites, lidar systems, and satellite laser range finding. Several less obvious applications have been presented in Ref. [1, 2, 4]. Specifically, NASA's proposed Mission to Planet

Earth calls for a global network of small surface or atmospheric sensor satellites to monitor global climate trends such as ozone depletion, pollution, or continental drift. Another NASA program, Project Pathfinder, has suggested the use of many microspacecraft at different locations to act as distributed (phased) arrays for either radio or optical signals. Such an array directed towards space could provide the most accurate triangulation measurements of our galaxy ever made by astronomers. As microelectronics technology continues to reduce payload size and weight, lightsat systems have been recognized as the means to fill a vital market niche in space science [4].

Although the missions described above do not specifically require laser boosted spacecraft technology, it has been noted [4] that the development of appropriate launch systems is important to the success of lightsats. With these applications as motivation, both lightsats and laser propulsion are mentioned as future alternatives in the report of the National Commission on Space [5]. Small, multi-purpose payloads may also encourage the involvement of universities and the private sector in space technology (similar to the get-away specials) as the launch costs decrease. Although cost projections vary, Canavan [6, 7] has provided some interesting speculation in this regard. In a recent report on the laser deployment of sensor satellites [6], it is assumed that a ground based laser system could launch 1 kg per 1 MW of laser power, and that sensor satellites could be produced for as little as \$1,000/kg (advanced sensor hardware, however, can cost up to \$200,000/kg [4]). Taking the lower estimate, this implies performance of \$1,000/MW; a 10 MW laser facility is projected to cost \$100 million [6, 7], and would be able to launch a \$10,000 satellite under these assumptions. In order to recover its initial cost at this rate, the facility would have to launch 100,000 kg total payload. By comparison, a Space Shuttle flight to low earth orbit (250 km) costs about \$3000/kg [7], so that using the shuttle to launch the same total weight would cost about \$300 million - roughly three times the amortization cost of a ground based laser facility! Also, we have not made any assumptions concerning the launch rates required; a four shuttle fleet may launch 14 flights in a single year at best [6, 7], while the lightsats could launch at a much higher rate. It has been noted [7] that over three years, the laser facility would amortize to about \$1/second of launch time, making the technology highly competitive.

12.2 Orbital Positioning

For an Earth orbiting satellite to accomplish its objectives, it must maintain a specific attitude in relation to the planet. The spacecraft must also be able to determine its own position in orbit. Finally, it must then have the ability to correct its attitude, and possibly position, from sensed orbital deviations.

12.2.1 Attitude Determination

Since the LTD is to be a low Earth orbit (e.g. 200 km - 2000 km) satellite, a pointing accuracy of ± 0.5 degree will be sufficient for the mission. Attitude sensors which have been considered are star trackers, sun sensors, and Earth horizon sensors.

Star trackers employ a detector which searches for visual signals above a given threshold value and then tracks the signal until the star is lost, or until it resumes searching after a predetermined time interval. Although these sensors were originally considered for use in the LTD, after further investigation this type of sensor was deemed too accurate for mission requirements in relation to the cost of the component. The crudest model available is accurate to one arc minute, and its use would necessitate periodic compilation and uplinking of an ephemeris¹ to the satellite. Therefore, a star tracker would not be cost efficient.

Another useful method of attitude determination is the sun sensor. In this category there are three basic types: 1) an analog sensor, which continuously calculates the sun angle; 2) a sun presence sensor, which calculates the sun angle when the sun is in the field of view; 3) and a fine sun sensor, which is the most precise of the three. For LTD purposes, the analog sensor proved to be the most beneficial because continuous sun tracking is often useful, if not necessary, when utilizing a solar array. An example of an acceptable sensor is made by Lockheed Missiles and Space Company, located in Sunnyvale, California. Their wide angle sun sensor (WASS) weighs 0.155 kg and measures 6x5x5 cm. It is accurate to 0.5 degrees and has a 2π steradian field of view. Using the most popular output of 620 μ A, almost no power would be consumed. The voltage type of output would also use minimal power.

The third type of attitude sensor is the Earth horizon sensor. It uses infrared sensors to scan the Earth and measure rotation angles, thus defining the spacecraft attitude relative to the Earth from a constant altitude. The detector senses radiation between 13.5 to 25 μ m in the spectral band. A small sun detector is also utilized to identify sunlight intrusion. A circular orbit requires one horizon sensor while an elliptical orbit needs two sensors. These attitude sensors are cheaper than star trackers and do not need the added expense of an ephemeris. A representative example is made by Ithaco, located in Ithaca, New York. Their horizon crossing indicator (HCI) has a head that is 10.0 cm long and 5.9 cm in diameter with an electronics box measuring 12.8x10.3x4.3 cm. The combined weight of the system is 0.65 kg. The HCI has an accuracy of 0.1 degree and a power requirement of less than 0.7 watts.

Therefore a combination of an analog sun sensor and one or two Earth horizon sensors will be used in the LTD for attitude determination. The analog sun sensor will be the primary device while the Earth horizon sensor will be used for back up.

¹An ephemeris is an astronomical almanac or table of predicted positions of celestial bodies.

12.2.2 Orbital Position Determination

In addition to the attitude sensors for solar array positioning and antenna pointing, the satellite will need a method for determining its orbital position above the Earth's skies. Three common methods will be discussed: 1) the Global Positioning System (GPS); 2) the Tracking and Data Relay Satellite System (TDRSS); 3) and the Satellite Tracking and Data Network (STDN).

GPS employs several satellites, each of which continuously broadcasts its own ephemeris and time. A GPS receiver can then determine its own position from four separate simultaneous GPS observations. The system can provide receivers with a positional accuracy of 20 m, velocity accuracy of 0.06 m/s, and time accurate to 10 ms. It was determined, however, that the hardware required weighed far too much for the LTD.

Although TDRSS and STDN are primarily communications options², they each can be used for determining a satellite's orbital position. TDRSS has a tracking system much like that of the GPS, except that it involves a real time cost since calculations are done by TDRSS and not by one's own satellite. The TDRSS consists of only two satellites and one receiving station on the ground (see Figure 12.1). The STDN is a network of ground stations (see Fig.12.2) used mainly for communication purposes, but also from which ranging can be performed. Ranging is the process of sending radar waves to a satellite and having it reflect the waves back to the station. Knowing the wavelength and the velocity of the wave and the time it takes to travel to and from the satellite, the range (position) and range rate (velocity) can be determined. Both the TDRSS and the STDN require only a lightweight antenna as hardware.

Therefore the LTD will use the TDRSS as its primary means of determining its orbital position and velocity, because of its simpler system. When the orbit is less than 1200 km and the satellite falls within TDRSS's zone of exclusion (see Figure 12.3), STDN will be used. In any case, STDN will be used as a backup.

12.2.3 Attitude and Orbital Control

Once corrections are determined to be needed, whether because of deviations or command decisions, there are three methods to change the attitude of a satellite: momentum reaction wheels, magnetic torque bars, and thrusters. For communication applications, only the yaw and pitch axis need be controlled since the LTD is axisymmetric about its roll (longitudinal) axis. For satellite photography and remote sensing, however, "roll" stabilization about the longitudinal axis must be provided.

²Using TDRSS & STDN would give the added bonus of easy satellite housekeeping downlink and command uplink.

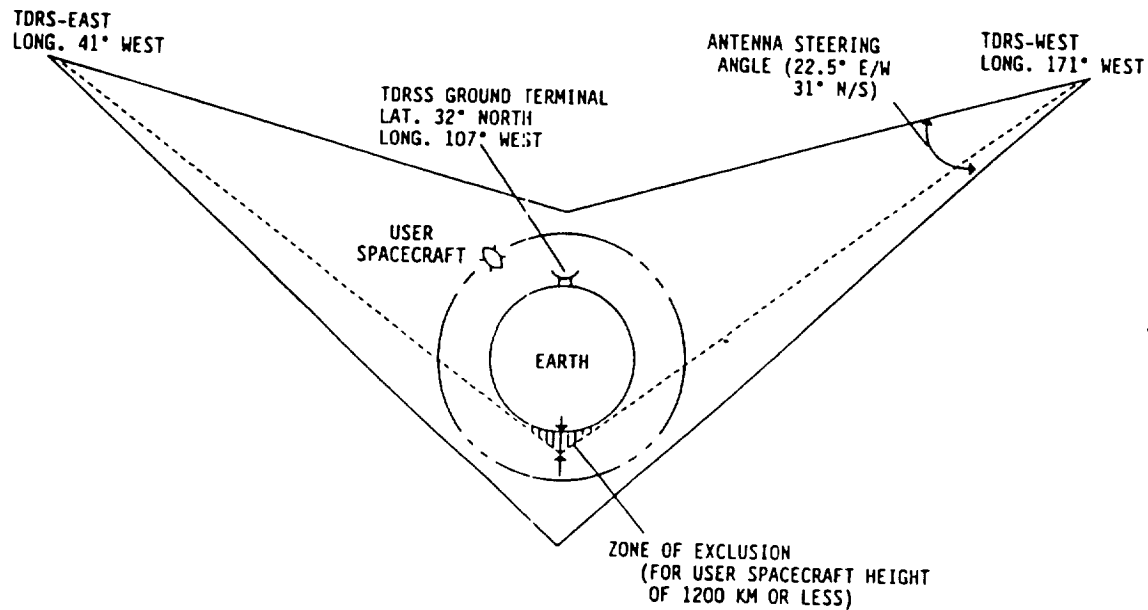


Figure 12.1: Tracking and Data Relay Satellite System

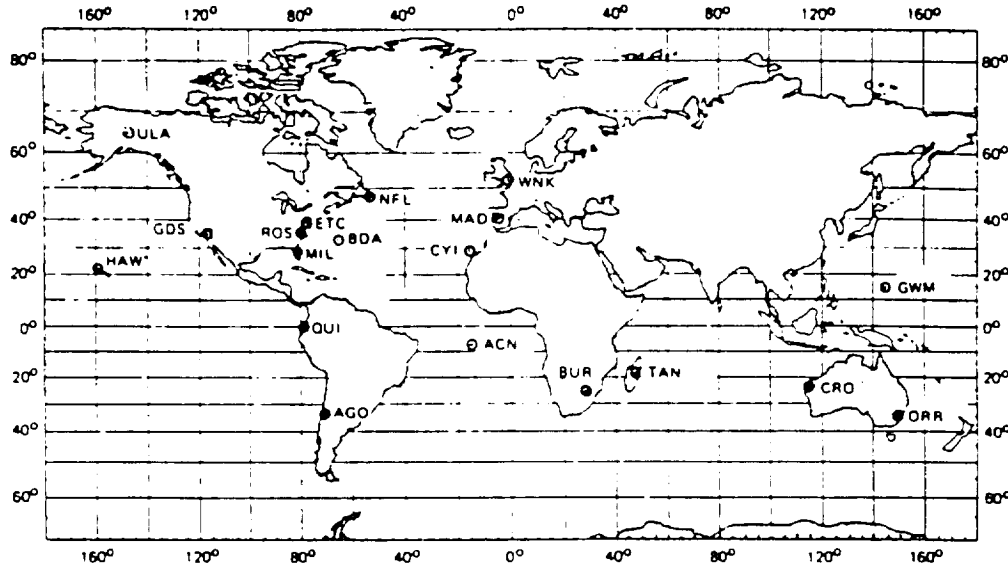
Finally, for orbital translations, only thrusters will work.

Momentum reaction wheels would not be a feasible option for the LTD because, although some of the more modern ones are small, they are still too heavy for a lightsat.

Ithaco of Ithaca, New York, manufactures a magnetic torque bar system called Torqrod. The Torqrod uses the readings from a magnetometer (which gives a three-axis measurement of the Earth's magnetic field) in determining which rod to energize to produce the desired attitude correction. Torqer bars, used in the Torqrod system, are inexpensive, weigh as little as 0.375 kg each, and measure less than 40 cm long. Two Torqer bars are needed; one in the yaw axis and one in the pitch axis. The major advantage of employing the Torqrod system is that the mission life becomes component dependent, because the system uses very little power and no consumables. The Torqrod system, however, compensates slowly.

Cold gas thrusters should be used for attitude control on the LTD for several reasons. First, although hot gas thrusters generate greater specific impulse, cold gas thrusters operate more consistently, with greater precision and are substantially cheaper. Also, no extra fuel need be lifted to orbit by the LTD because 2 kg of cold gas helium (and some LN_2) will already be on board, having been used to pressurize the liquid nitrogen propellant tank prior to orbit. Only four thrusters will be necessary, two in each direction along both the yaw and pitch axis.

CHAPTER 12. LIGHTSAT SYSTEMS DESIGN



STATION	SYSTEM	LATITUDE ¹	LONGITUDE (E)	HEIGHT ABOVE ELLIPSOID (METERS)
ASCENSION ISLAND (ACN)	9m USB	- 19°57' 17.37"	145°40' 27.57"	528
SANTIAGO CHILE (AGO)	9m USB	- 33°09' 03.58"	289°20' 01.08"	706
	VHF CRARR	- 33°09' 06.06"	289°20' 01.07"	706
	INTERFEROMETER	- 33°08' 58.10"	289°18' 54.20"	894
BERMUDA (BDI)	9m USB	32°21' 05.00"	795°20' 31.84"	- 33
	FPO-6 RADAR	32°20' 53.05"	795°20' 43.90"	- 35
GRAND CANARY ISLAND (CYI)	9m USB	27°45' 51.61"	144°21' 51.88"	167
ENGINEERING TRAINING CENTER MARYLAND (ETC)	9m USB	38°59' 54.84"	283°09' 26.23"	- 1
	9m USB (ERTS)	38°59' 54.08"	283°09' 29.21"	4
	INTERFEROMETER	38°59' 57.25"	283°09' 38.71"	5
GOLDSTONE CALIFORNIA (GDS)	26m USB	35°20' 29.66"	243°01' 35.06"	919
	9m USB (ERTS)	35°20' 29.64"	243°01' 37.45"	913
GUAM (GWM)	9m USB	13°18' 38.25"	144°44' 12.53"	116
HAWAII (HAW)	9m USB	22°07' 34.46"	200°20' 05.43"	1139
	FPS 16 RADAR	22°07' 24.37"	200°20' 04.02"	1143
MADRID SPAIN (MAD)	26m USB	40°27' 19.67"	355°49' 53.58"	808
MERRITT ISLAND FLORIDA (MIL)	9m USB NO. 1	28°30' 29.79"	279°18' 23.85"	- 55
	9m USB NO. 2	28°30' 27.91"	279°18' 23.85"	- 55
ORRORAL VALLEY AUSTRALIA (ORR)	INTERFEROMETER	35°37' 37.19"	148°57' 15.15"	926
QUITO ECUADOR (QUI)	INTERFEROMETER	- 00°37' 22.04"	281°25' 16.10"	3546
ROSMAN NORTH CAROLINA (ROS)	4.3m USB	35°11' 45.99"	277°07' 26.96"	810
	VHF CRARR	35°11' 42.02"	277°07' 26.97"	810
TANANARIVE MALAGASY REPUBLIC (TAN)	4.3m USB	- 19°01' 13.87"	47°18' 11.87"	1368
	VHF CRARR	- 19°01' 16.34"	47°18' 11.83"	1368
	INTERFEROMETER	- 19°00' 31.66"	47°17' 59.75"	1347
	FPS 16 RADAR	- 19°00' 05.52"	47°18' 53.46"	1307
FAIRBANKS ALASKA (JULA)	9m USB	64°58' 19.20"	212°29' 13.39"	339
	VHF CRARR	64°58' 17.50"	212°29' 19.12"	339
	INTERFEROMETER	64°58' 36.91"	212°28' 31.89"	282
WINKFIELD ENGLAND (WNK)	INTERFEROMETER	51°28' 46.12"	359°18' 08.13"	87

¹A MINUS SIGN (-) INDICATES SOUTH LATITUDE

Figure 12.2: Locations and Geodetic Coordinates of STDN Stations.

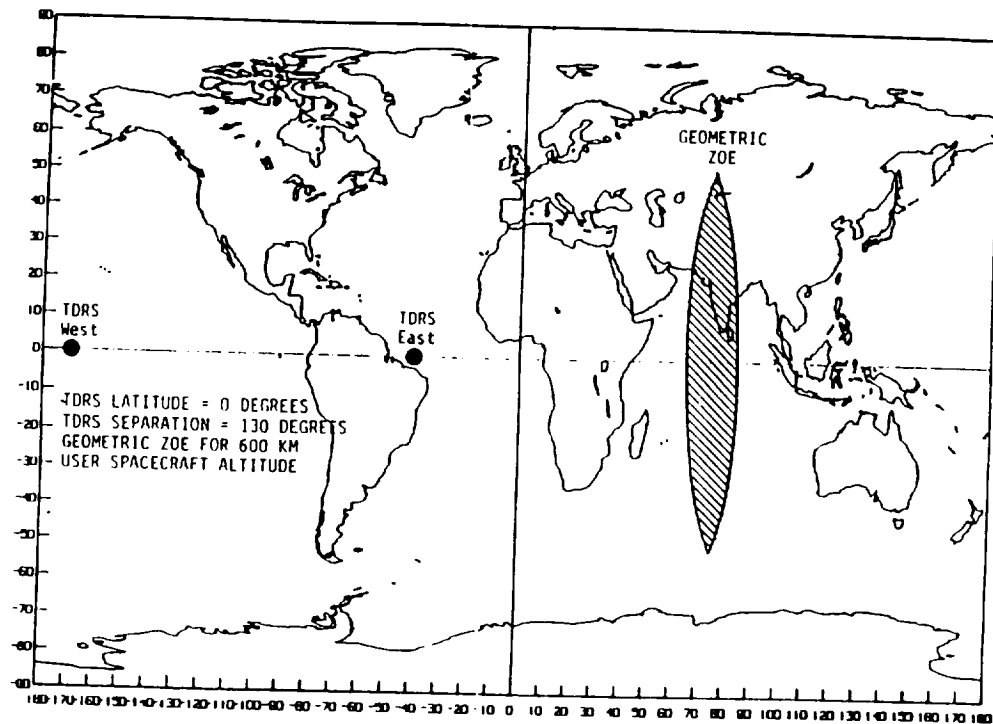


Figure 12.3: TDRSS Geometric Zone of Exclusion

Although orbital translations are not considered in the mission parameters, it has been suggested that the injector heads could be used in emergency orbital maneuvers. First the satellite would be pointed in the right direction, then the pressurized helium would enter the injector (see Chapt. 4) heads by way of the liquid nitrogen tank.

In summary, for primary attitude control, a magnetic torque bar system is chosen with cold gas thrusters being used when immediate corrections are needed. For any unforeseen translational motion required, the thrust could be provided by the injector heads used as thrusters.

12.3 Communications and Sensing

An effective sensor lightsat must be able to communicate with Launch Command to transmit its status, to send data it has gathered (from another source), and to receive command instructions. To accomplish this goal, specific orbital parameters, communication frequencies, and antenna options must be explored.

12.3.1 Orbital Parameters

There are three major orbital parameters associated with sensor satellite missions: 1) coverage area, or the portion of the Earth's surface that can be viewed by the

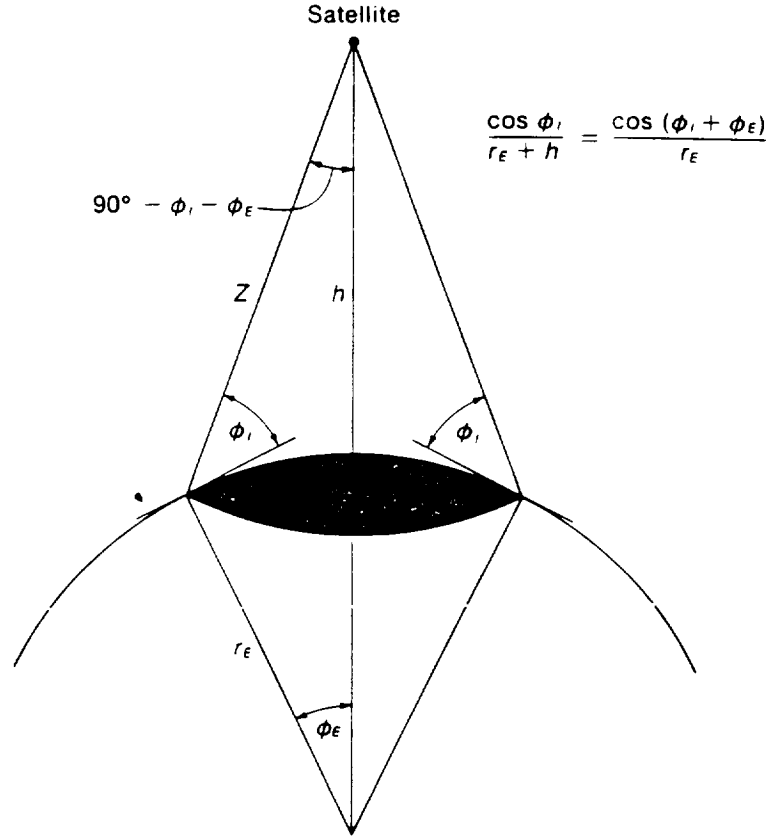


Figure 12.4: Satellite-Earth Angles

satellite, 2) slant range, or the distance from a fixed point on the Earth to the satellite, and 3) length of time a satellite can observe with a prescribed elevation angle (i.e., “window of opportunity”). The elevation angle is essential since a sensor satellite’s “vision” can be impaired if it is at too low an elevation angle, close to the horizon. An example of satellite-Earth angles is shown in Figure 12.4 (ϕ_1 = elevation angle from ground station, A_{cov} = shaded area)(see Ref. 8).

The coverage angle, A_{cov} , with an elevation angle, ϕ_1 , can be obtained from:

$$A_{cov} = 2\pi R_E^2 (1 - \cos \phi_E) \quad (12.1)$$

where,

$$\phi_E = \arccos \left(\frac{R_E \cos \phi_1}{R_E} + h \right) - \phi_1 \quad (12.2)$$

R_E is the radius of the Earth; and h is the altitude of the satellite above the Earth. Since the Earth’s total surface area is $4\pi R_E^2$, A_{cov} can be rewritten as a fraction of

the Earth's total surface:

$$\frac{A_{cov}}{4\pi R_E^2} = 0.5(1 - \cos \phi_E) \quad (12.3)$$

For example, with a ϕ_E of 0° and altitude of 1000 km, the maximum percentage of the Earth that the LTD can view is 6.78%.

The slant range between a point on Earth and a satellite at altitude h and angle ϕ_1 is calculated from:

$$z = \sqrt{(R_E \sin \phi_1)^2 + 2R_E \pi h + h^2} - R_E \sin \phi_1 \quad (12.4)$$

Before the LTD's sensor "window of opportunity" can be determined, one must first find the lightsat's orbital period t_s . Based on Kepler's 3rd law

$$t_s = \frac{2\pi \sqrt{a^3}}{\sqrt{\mu}} \quad (12.5)$$

where a is the semi-major axis of an elliptical trajectory, and μ is the product of the universal gravitational constant G and the sum of the mass of the Earth m_E and the satellite m_s . Since the mass of the satellite is negligible compared to that of the Earth,

$$\mu = G(m_E + m_s) = Gm_E \quad (12.6)$$

For an orbit of 1000 km, Earth radius of 6378.155 km, and μ of $3.986013 \times 10^5 \text{ km}^3/\text{s}^2$, the LTD's orbital period (t_s) is approximately 105 minutes.

For a satellite at altitude h , the "window of opportunity" (t_p) is

$$t_p = \left(\frac{2\phi_E}{360^\circ} \right) \left(\frac{t_s}{1 \pm \frac{t_E}{t_s}} \right) \quad (12.7)$$

where t_E is the rotation period of the Earth (one sidereal day, which equals 23 h, 56 min, and 4.09 s, or 86164.09 s). The \pm sign depends on whether the satellite is in a prograde (same direction with respect to Earth) orbit, or a retrograde (opposite direction) orbit. For a ϕ_E of 30.18° and an altitude of 1000 km, t_p is approximately 72 s.

12.3.2 Communication Frequencies

The typical frequencies allocated for satellite communications fall in the super high frequency (SHF) and extremely high frequency (EHF) bands (see Table 12.1). The frequency spectrum is divided into subbands which are listed in Table 12.2. The LTD's communications system will be chosen for low power requirements, minimal propagation distortions, and reduced noise and interference effects. The transponder must also be designed to function both as a receiver and transmitter for TDRSS and STDN purposes.

Table 12.1: Electromagnetic Frequency Spectrum

Frequency	Wavelength (m)	Designation
3 Hz – 30 kHz	$10^8 - 10^4$	Very Low Frequency (VLF)
30 kHz – 300 kHz	$10^4 - 10^3$	Low Frequency (LF)
300 kHz – 3 MHz	$10^3 - 10^2$	Medium Frequency (MF)
3 MHz – 30 MHz	$10^2 - 10$	High Frequency (HF)
30 MHz – 300 MHz	$10 - 1$	Very High Frequency (VHF)
300 MHz – 3 GHz	$1 - 10^{-1}$	Ultra High Frequency (UHF)
3 GHz – 30 GHz	$10^{-1} - 10^{-2}$	Super High Frequency (SHF)
30 GHz – 300 GHz	$10^{-2} - 10^{-3}$	Extremely High Frequency (EHF)
10^3 GHz – 10^7 GHz	$3 \times 10^{-5} - 3 \times 10^{-9}$	Infrared, Visible Light, and Ultraviolet

Table 12.2: Satellite Frequency Spectrum

Frequency	Range (GHz)
L	1 – 2
S	2 – 4
C	4 – 8
X	8 – 12
Ku	12 – 18
K	18 – 27
Ka	27 – 40
Millimeter	40 – 300

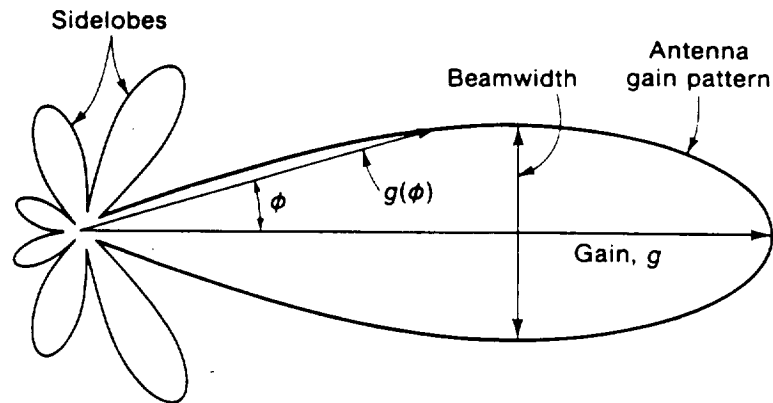


Figure 12.5: Antenna Gain Pattern (see Ref. 8)

12.3.3 Antenna Options

The most important antenna characteristics are its gain (maximum value of the gain pattern), beamwidth (a measure of the angle over which most of the gain occurs), and sidelobes (amount of gain in off-axis directions). Figure 12.5 shows a typical antenna gain pattern, with its essential features. The most desirable antenna patterns are those with high gain concentrations over a narrow beamwidth and small sidelobes. A list of typical antenna patterns are shown in Table 12.3. The LTD will be equipped with an erectable light-weight antenna for communicating with launch command, accessing the TRDSS (and STDN) network, and relaying data gathered from LTD sensors (see Fig. 12.6).

The maximum gain, g , and half power beamwidth, ϕ_b , in radians are given as:

$$g = A\rho_a \left(\frac{4\pi}{\lambda^2} \right) \quad (12.8)$$

$$\phi_b \approx \frac{\lambda}{d\sqrt{\rho_a}} \quad (12.9)$$

where A is the antenna area, d is the aperture diameter, and ρ_a is the antenna efficiency factor.

12.4 On Board Computer

The on-board-computer (OBC) will be located in the electronics payload compartment of the LTD. It will be encased in a radiation-shielded and thermal protective

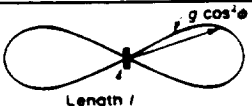
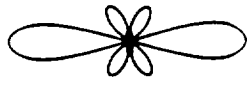
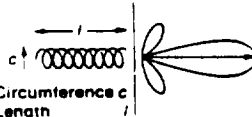
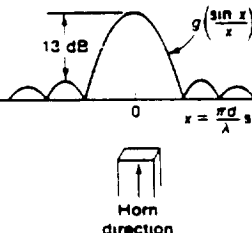
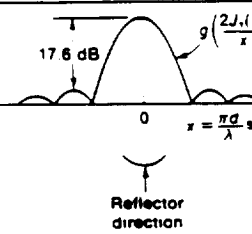
Antenna type	Pattern	Gain g	Half-power beamwidth
Short dipole $l \ll \lambda$		1.5	90°
Long dipole $l \gg \lambda$ $l = \lambda/2$		1.5 1.64	47° 78°
Phased array, phase difference $= \frac{2\pi s}{\lambda} \cos \theta_0$		$\frac{N\pi s}{1.4\lambda}$	$50^\circ \frac{\lambda}{Ns}$ $\theta_0 = 0$
Helix		$15 \frac{cl}{\lambda^2}$	$52^\circ \frac{\lambda}{c\sqrt{l}}$
Square horn, dimension d		$\frac{4\pi d^2}{\lambda^2}$	$\frac{0.88\lambda}{d}$
Circular reflector		$\frac{\pi d^2}{\lambda}$	$\frac{1.02\lambda}{d}$

Table 12.3: Typical Antenna Gain Patterns (see Ref. 8)

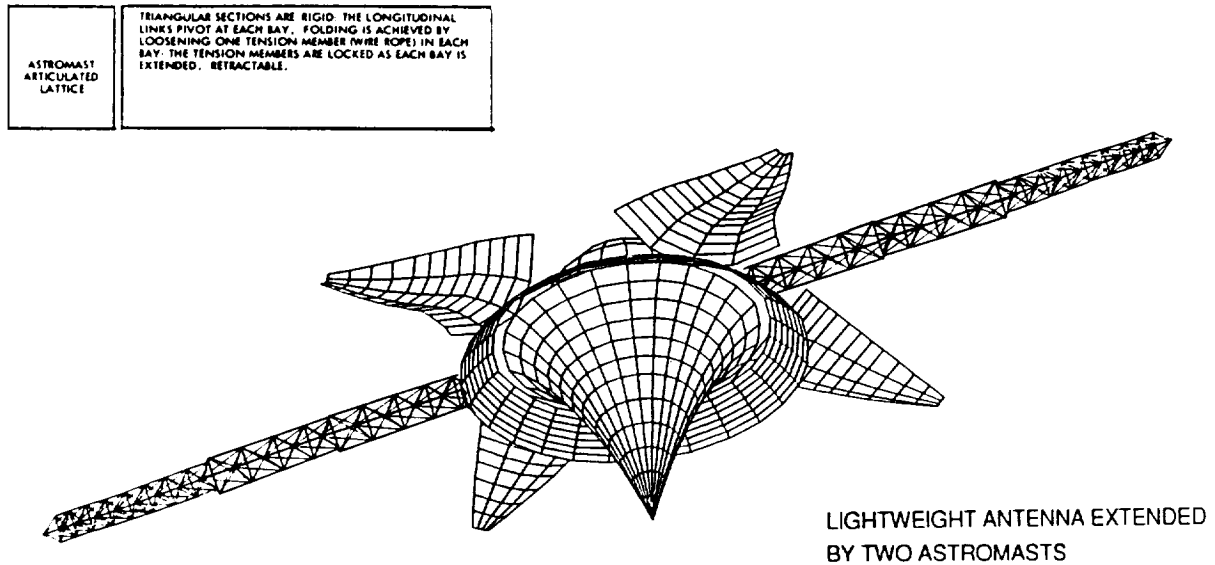


Figure 12.6: LTD will deploy an antenna for communications during satellite mode.

casing. The OBC will control the specific actions of all electrical and mechanical components. It will manage the antenna, transponder, temperature sensors, solar array, batteries, attitude system, and LN_2 propellant delivery.

The OBC will begin operation at liftoff and remain in operation throughout the life of the LTD. For example, in the boost mode temperature sensors that are distributed at critical areas on the mirror and thrust surfaces will advise the OBC so that adequate coolant flow rates are administered. Later, once orbit is achieved, the OBC will direct the LTD forebody to open up into four "petals," expose the solar array' and extend the antenna. These "petals" will be actively positioned by mechanical actuators that are programmed (and controlled by the OBC) to maximize solar power collection (see Fig. 12.7).

12.5 Power Systems

The LTD will primarily be powered and recharged by solar energy gathered by an array of solar cells. During launch and when the satellite is in the Earth's shadow, however, the LTD will have to rely on its batteries to power its electrical systems. Therefore, to design an adequate power system for the LTD, several areas must be considered; the shadow factor, solar array, and rechargeable batteries.

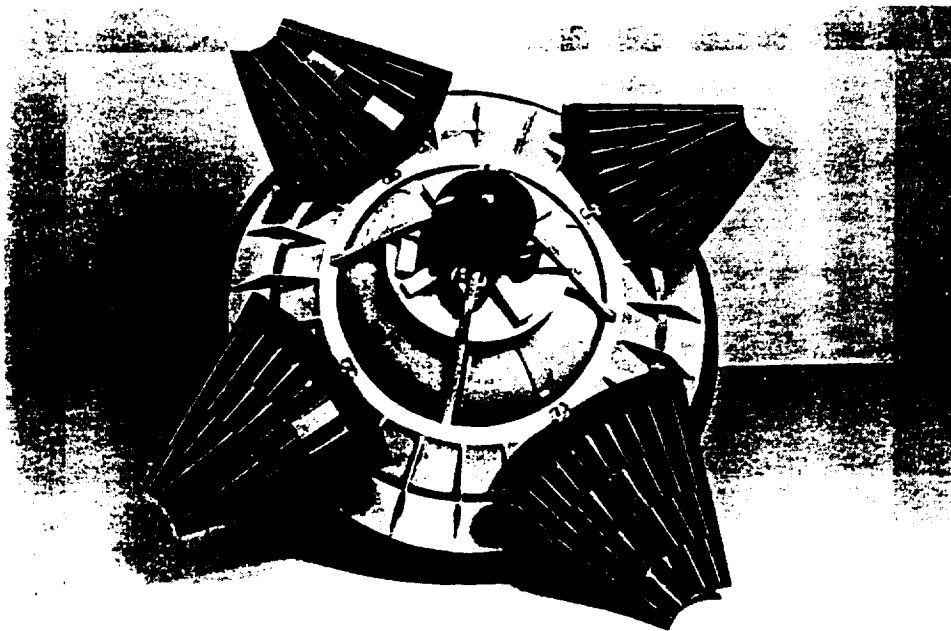


Figure 12.7: Solar cell array exposed during LTD satellite mode.

12.5.1 Shadow Factor

In Low Earth Orbit (LEO), a certain portion of the LTD's trajectory will remain unilluminated by the sun. Clearly, the craft will receive no solar energy while in the Earth's shadow. The eclipse period can be calculated from the maximum shadow angle:

$$\phi_{max} = 180^\circ - 2 \arccos \left(\frac{R_E}{a} \right) \quad (12.10)$$

For example, at an altitude of 1000 km, ϕ_{max} is 119.6°. Hence, 1/3 of the satellite's time is spent in the Earth's shadow. With a period of 105 minutes, the satellite would be in the sun for 70 minutes.

12.5.2 Solar Array

Since the LTD will be illuminated by the sun for only 2/3 of its orbital period, the actual power requirement must be increased by 50% to a total of 60.8 W from an initial requirement of 40.5 W (see Table 12.4). By allowing for an additional 25% safety margin, the solar array must be able to generate approximately 76 W of energy.

Table 12.4: Power Requirements for Solar Array

Solar Array Actuators:	20.0 W
Horizon Sensor:	0.5 W
On Board Computer (OBC):	5.0 W
Regulators (battery, gas/pressure), Sensors (temperature, optical), and Heaters:	15.0 W
Total:	40.5 W

The solar array surface area can then be calculated from the following equation:

$$A = \frac{P}{S * \eta * F * \cos \Gamma} \quad (12.11)$$

where P is the power load requirement (76 W), S is the average solar intensity (1353 W/m²), Γ is the compound angle between the sun line and the average array normal (45°), η is the solar cell efficiency (0.1771 at 64° C), and F is the sum-total of all array design and degradation factors (0.8). The compound angle, Γ , is an approximation of the average power angle that occurs over the array surface. The solar cell efficiency is obtained from:

$$\eta = \eta_{ref} [1 - \beta(T - T_{ref})] \quad (12.12)$$

where η_{ref} is the initial solar cell efficiency (0.22 for a silicon solar cell), β is the thermal calibration coefficient (0.005° C), T is the average temperature on a flat solar panel at 1000 km (64° C), and T_{ref} is 25° C. The needed solar array surface area is found to be 0.56 m².

12.5.3 Battery

The LTD battery must be rechargeable and be able to store enough energy to supply power needs through out the 35 minutes of darkness. From an initial power requirement of 40.5 W, less power needed for the solar cell actuators, approximately 20 W will be required during this period of darkness, which equates to a 11.7 W·h battery. Allowing for a 80% depth of discharge, a 20 W·h battery should suffice.

Microprocessors commonly operate at 5 ± 0.5 V, or about 6 V. The use of Nickel-Hydrogen batteries would be a logical choice, since they provide much greater energy densities, and volume reductions than conventional battery types. A weight of 0.5 kg,

length of 10 cm, diameter of 9 cm, and a capacity of 1 A·h are likely battery characteristics.

12.6 Conclusion

As mentioned above, once in orbit, the LTD will function as a light-weight sensor satellite, complete with all the requisite on-board electronics, communications, and attitude control systems. The LTD senses its attitude with a sun sensor and a Earth horizon sensor. To change attitude, it uses a combination of cold gas jets and/or magnetic torque bars. It will be equipped with an erectable, light-weight antenna for communicating with Launch Command, accessing the TRDSS (and STDN) networks, and relaying data gathered from LTD sensors. An on-board-computer will manage satellite electrical, mechanical and attitude control systems, coolant flow rates, and solar array actuators. The solar array is mounted onto the inner forebody surface, which opens into four "petals" to collect solar energy for recharging the on-board nickel-hydrogen battery. The battery is used primarily when the satellite traverses the Earth's shadow. This combination of satellite components is chosen for minimal cost and weight, so that the LTD can fulfill its primary objective of a self-launched lightsat.

REFERENCES

- [1] French, J. R., "Very Small Spacecraft for Planetary Exploration missions," USRA Lightsat Conference (1988).
- [2] Bell, T. E., "Jettisoned Shuttle Fuel Tanks to Harbor Atmospheric and Space Science Experiments," The Institute (supp. to IEEE Spectrum), p 4, May 1989.
- [3] Browde, A., "Shrinking Electronics Boost Satellite Utility," Aerospace American, pp 22-24, 1988.
- [4] Fuhs, A. E., Mosier, M. R., "A Niche for Lightweight Satellites," Aerospace American, pp 14-16, 1988.
- [5] Cohen, B. N., editor, *Pioneering the Space Frontier: The Report of the National Commission on Space*, Bantam Books, Inc., N.Y., 1986.
- [6] Canavan, G. H., "Laser Propulsion of Sensors and Interceptors," LA-UR-87-3208, Los Alamos National Laboratory, Los Alamos, NM, 1987.
- [7] Canavan, G. H., "Decoy Deployment with Laser Propulsion," LA-UR-88-1246, Los Alamos National Laboratory, Los Alamos, NM, 1988.

- [8] Gagliardi, R. M., *Satellite Communications*, Lifetime Learning Publications, Belmont, California, 1984.
- [9] Ha, T. T., *Digital Satellite Communications*, Macmillan Publishing Company, New York, 1986.
- [10] Husson, J. C., "Introduction to Space Systems," *Electrical Communication*, Volume 62, Number 1, 1988, pp 4-11.
- [11] Product Literature, Micro Mo Electronics, Inc., 742 Second Ave S., St. Petersburg, Florida, 33701.
- [12] O'Lone, Richard G., "U.S. Planning New Emphasis on Lightweight Satellite Systems," *Aviation Week & Space Technology*, August 10, 1987.
- [13] Patterson, R. E., Luft, W., and Dunlop, J. D., "Development of Spacecraft Power Systems Using Nickel-Hydrogen Battery Cells," Paper 76-288, AIAA/CASI 6th Communications Satellite Systems Conference, Montreal, Canada, April 5-8, 1976.
- [14] Rauschenbach, H. S., *Solar Cell Array Design Handbook*, Van Nostrand Reinhold Company, New York, 1980.
- [15] Product Literature, Solarex Corporation, 1335 Piccard Drive, Rockville, Maryland, 20850.
- [16] Wertz, James R., *Spacecraft Attitude Determination and Control*.
- [17] Product Literature, Whittaker-Yardney Power Systems, a division of Whittaker Technical Products, Inc., 82 Mechanic Street, Pawcatuck, Connecticut, 02891.
- [18] Williams, A. F., *The Handbook of Photovoltaic Applications*, The Fairmont Press, Inc., Atlanta, Georgia, 1986.

Chapter 13

FUTURE DIRECTIONS

For the following year, the Lightcraft Technology Demonstrator's combined-cycle engine will remain as the central focus of further research efforts. The preliminary conceptual design of this laser-boosted microspacecraft was performed last year. The study involved an analytical performance analysis of the LTD engine in its two modes of operation, including an assessment of propellant and tankage requirements, and a detailed design of the inner structure and external body shape. Also, a structural vibrational analysis was performed on the annular shroud pulsejet engine. Finally, the sensor satellite mission was examined to identify the requisite subsystem hardware (e.g., electrical power supply, optics and sensors, communications and attitude control systems).

13.1 Computer Modeling Efforts

In the upcoming year, efforts will be focused on the LTD's propulsion system and vehicle aerodynamics rather than on its mission as a sensor satellite. A 3-D computational fluid dynamics (CFD) model of the LTD's external inlet will be assembled, and run for a variety of different shapes and flight speeds. From these computer simulations, the boundary layer thickness, external surface pressure distribution, and transition point (from laminar to turbulent flow) can be determined. A 2-D blast wave code provided by the Naval Research Laboratory (NRL) may also be employed to model the impulsive thrust generated by laser-induced blast waves. In addition, a computer analysis of the radiation/convection heat transfer will be conducted to find the engine/vehicle thermal profile. All of this will enable the intelligent choice of appropriate spacecraft materials (specifically tailored to withstand the hypersonic transatmospheric environment) and also the design of active thermal cooling systems for the primary optics and engine hot-sections. Finally, a more detailed vibrational analysis will be performed using finite element models that will include not only the shroud/strut assembly, but also the spacecraft internal support structure.

13.2 Wind Tunnel Experiments

Several experiments will be performed to validate theoretical vehicle and engine inlet performance simulations. Hot and cold flow wind and shock tunnel tests are planned, with two different scale models (5 in. dia. and 1.25 in. dia.). The test flow conditions will be varied from subsonic to hypersonic. Flow visualization techniques, including smoke injection and schlieren photography, will provide details of flow dynamics around the vehicle, along with bow shock wave structure. Static and total pressures will be measured at critical positions on and around the test models. Heat transfer data will be obtained in high temperature flow experiments, using the RPI 24 in. diameter hypersonic shock tunnel.

13.3 Laser Impulse Experiment

Laser impulse experiments will also be conducted on a full-scale, 1/15th segment of the annular engine, in both static and dynamic wind conditions. These high power laser experiments will yield engine impulse and heat transfer data to prove technical feasibility of the propulsion concept. The proposed experiment is designed to verify the analytical performance for the airbreathing combined-cycle engine mode, referred to as the External Radiation-Heated (ERH) thruster (see chap. 9).

The experiment is specifically designed for the one kilojoule pulsed CO₂ laser shown in Figure 13.1, which was loaned to Rensselaer by the Naval Research Laboratory in Washington, DC. This laser is similar to the Lumonics 624-TEA commercial pulsed CO₂ laser. The high power NRL laser (now at RPI) will be set up with unstable resonator optics to produce a laser pulse duration of 50 ns. The 20 cm × 20 cm output laser beam will be focused by a special parabolic mirror to intensities exceeding 5×10^8 W/cm² at the impulse pressure plate, as shown in Figure 13.2 (note that the laser-induced clean air breakdown threshold is greater than 10^9 W/cm²). The resultant LSD wave will be roughly 20 cm long and 0.5 cm in diameter. The impulse pressure plate pictured in Figure 13.2 will measure 25 cm × 25 cm and represent a full-scale, 1/15th segment of the annular LTD engine. Finally, it should be noted that the four module NRL CO₂ laser will be set up to run at an effective PRF of 1200 to 12,000 Hertz — for two pulses only. With the latter interpulse time, the effective time-average laser power will be 5 megawatts. Only two pulses are required to exactly simulate the propulsive physics of a repetitively-pulsed engine.

Several statements regarding the diagnostics and instrumentation for the experiment are in order. First, schlieren photography and a TRW image converter camera with nano-second resolution will be employed to record the process of LSD wave ignition and the evolving cylindrical shock wave patterns as a function of time: framing rates of 50-100 nano-seconds are possible. Efforts will be made to ascertain the min-

imum flux and fluence required to start the LSD wave at a metallic "ignitor" plate. Also, the laser pulse shape will be correlated with temporal variations in the laser flux upon the LSD wave, and their effect upon the LSD wave velocity will be assessed.

Second, the 25 cm × 25 cm ERH thruster plate will be instrumented with at least six pressure transducers, and a number of thin (and thick) film platinum heat gauges for measuring convective and radiative heat transfer. This data will be recorded on a 4-channel Nicolet digital oscilloscope with nano-second resolution. Because of the high temperature engine environment, radiation losses from the cylindrical, high pressure air plasma must be studied. The chemistry and hydrodynamics of the pulsed thruster exhaust will be examined to assess the effects of "frozen flow" losses.

Also, the gas dynamics of refreshing inlet air will be documented. These experiments will provide clear insight to the pulse-by-pulse interaction process during impulse generation. As mentioned above, the experimental apparatus is designed to convect air across the thruster plate to enable the determination of the optimum "wind" velocity for adequate "clearing-time" between laser pulses — such that maximum impulse is delivered to the ERH thruster plate. (Incidentally, to calibrate the pressure-integrated impulse data system, the "pendulum" method of direct impulse measurement will be used for the *initial static* tests only.)

Portrayed in Figure 13.3 are the details of the air supply system (i.e., the wind tunnel) for the test section. Fresh air from the outside enters the large flow area "dryer," which is plugged into a 4 ft × 8 ft window in the laboratory. The air then accelerates through a converging/diverging nozzle and enters the test section which is supported by two adjustable jack stands. After flowing through the test section, the spent heated air is vented to a large dump tank, which turns the air flow 90° and then feeds it into a converging duct. The duct is connected directly to the vacuum line as shown in Figure 13.3.

Figure 13.4 gives an interior view of the dump tank and test section. Note that the laser beam enters from the left through a high power infrared "salt" window, and then falls upon the parabolic metal (uncooled) front surface mirror. This mirror is suspended by a three point adjustable mount, which can be aligned from the outside. The impulse plate is designed for easy removal and servicing. It is anticipated that numerous configurations will have to be tried before the best one can be identified. Note also that the test section is supplied with removable nozzle blocks so that the air inlet Mach number can be changed at will.

13.4 Systems-Integration Issues

Finally, additional systems-integration questions that were not addressed in this year's final report will be explored. Several critical areas include LTD range safety during launch, manufacturing cost analyses, and possible high power laser attenuation by the engine exhaust plume.

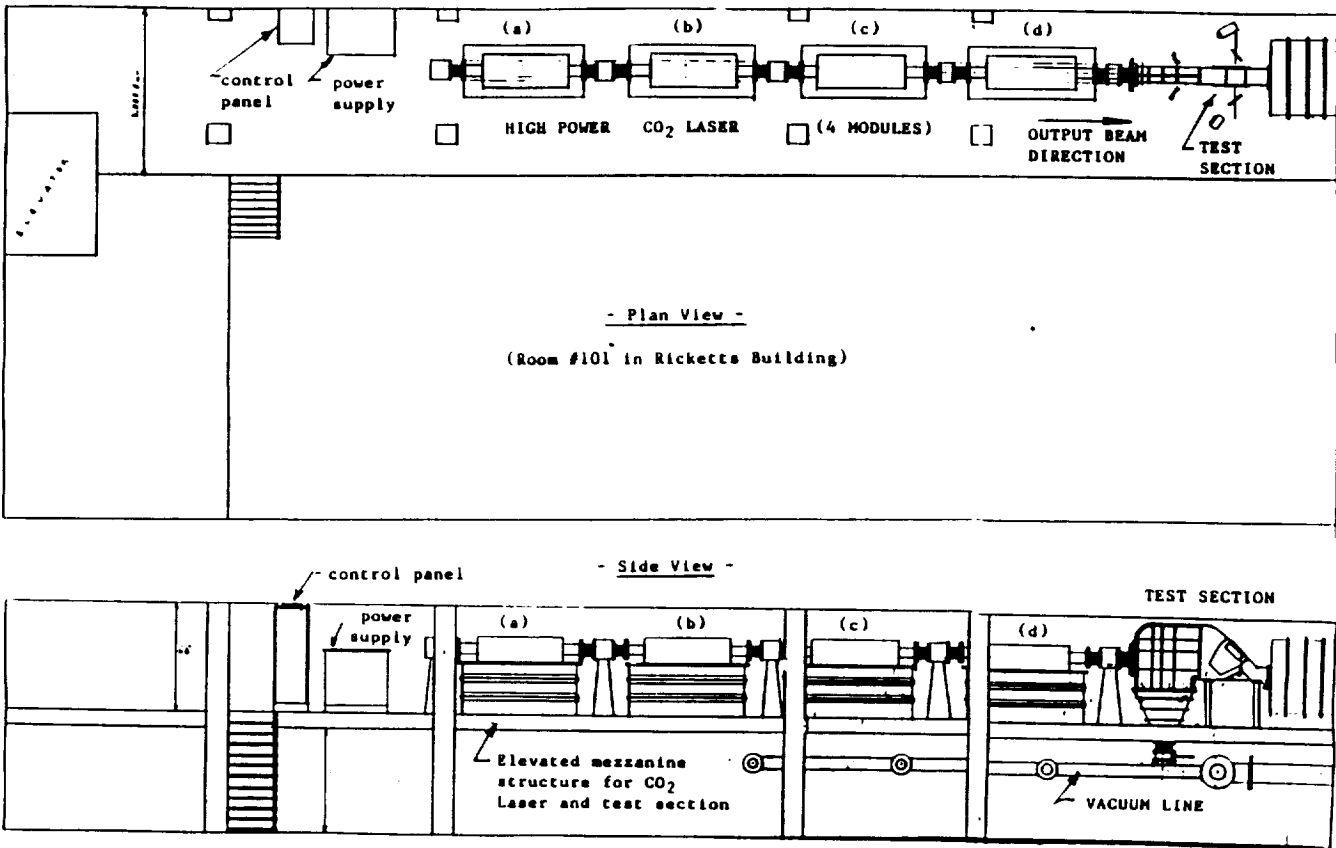


Figure 13.1 Layout of RPI Laser Propulsion Laboratory in Ricketts Building. (showing proposed location of NRL CO₂ Laser and Experiment Test Section)

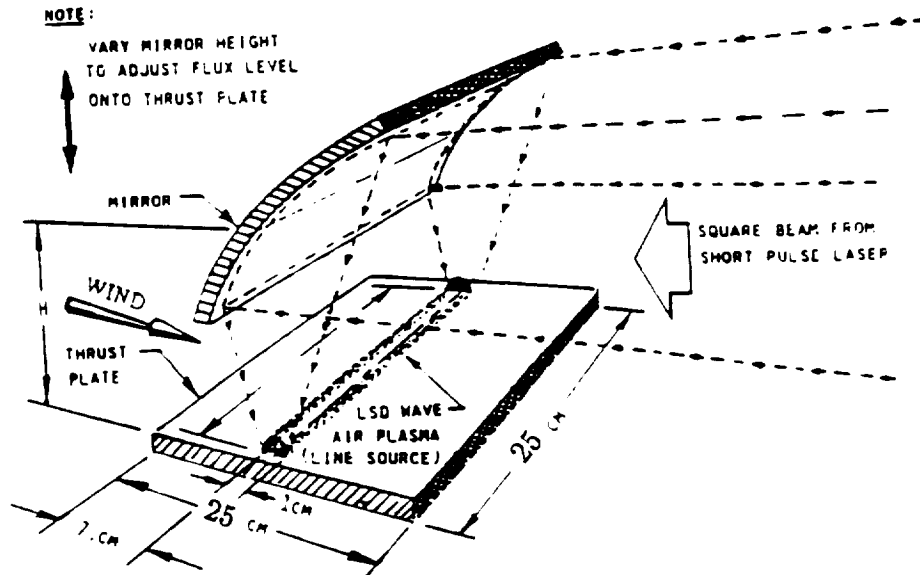
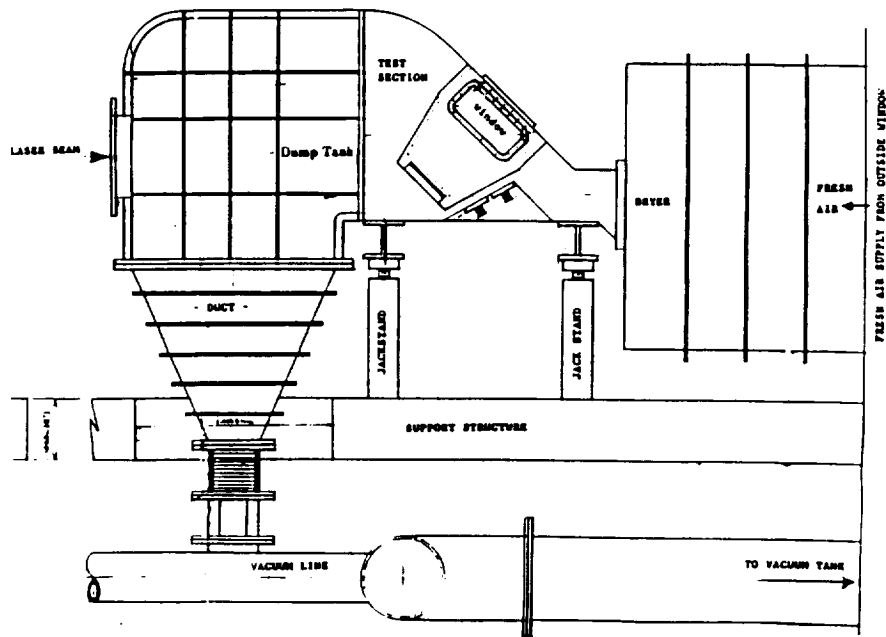


Figure 13.2 The impulse pressure plate will represent a full-scale, 1/15th segment of the annular LTD engine.



• Figure 13.3 Assembly drawing showing details of air supply system.
(Side View)

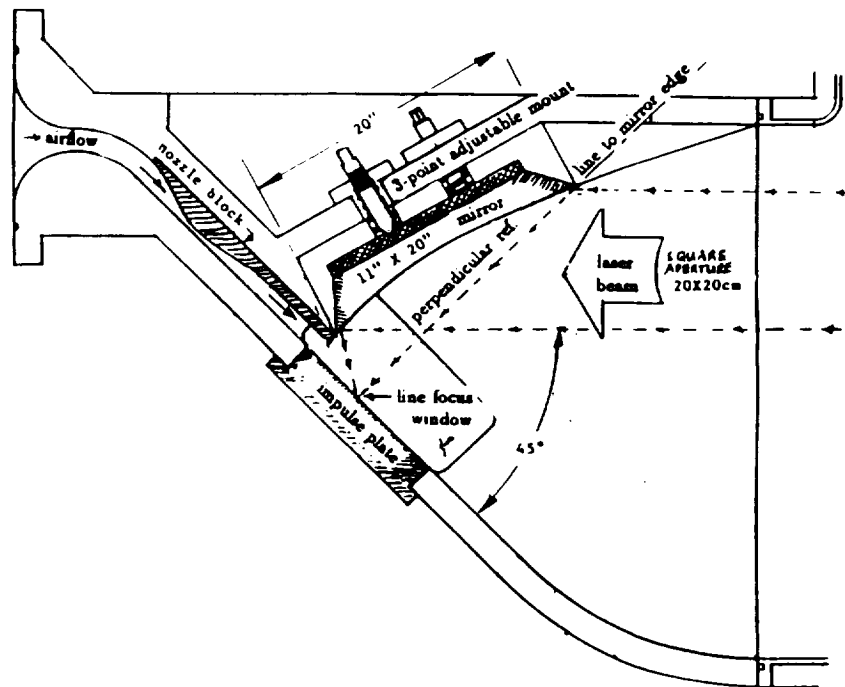


Figure 13.4 Test Section, showing impulse plate and parabolic mirror.

Appendix A

RESULTS OF COMPUTER GENERATED RAY TRACES

This appendix summarizes the results of a computer ray trace study performed on the LTD primary mirror. Calculations were performed using the program "Beam 2" from Stellar Software; the graphical ray traces were rendered in the CATIA interactive computer graphics program. In the following tables, individual rays were numbered for easy reference to the traces; ray 1 is defined as incident along the centerline of the LTD craft, and rays are consecutively numbered proceeding outward from the vehicle centerline on either side. A total of 11 rays were traced for each side of the LTD in the extreme cases of 0.1 and 1.0 degrees vehicle incidence. Only the odd numbered rays were traced for the remaining cases.

Tables 1 and 2 represent the perpendicular distances between incident rays and the ideal focus for various oblique angles of incidence. The corresponding rms blur is then calculated. Figure 1 illustrates graphically that the rms blur is linearly proportional to incident angle; the equation of the fitted line is also given. The remaining figures define the ray trace geometry, and present magnified views of the focal planes on either side of the vehicle for incident angles of 0.1, 0.2, 0.5, 0.7, and 1.0 degrees. All angles are measured counter-clockwise from the vehicle centerline; because the LTD is rotationally symmetric about this centerline, the same meridional ray traces are valid for any cross section view of the craft.

REFERENCES

- [1] CATIA Basic Three-Dimensional Design, User Manual, Vol. 1, prog. no. 5668-830, IBM Corp. dept. 43K/967, Kingston N.Y. (1985)

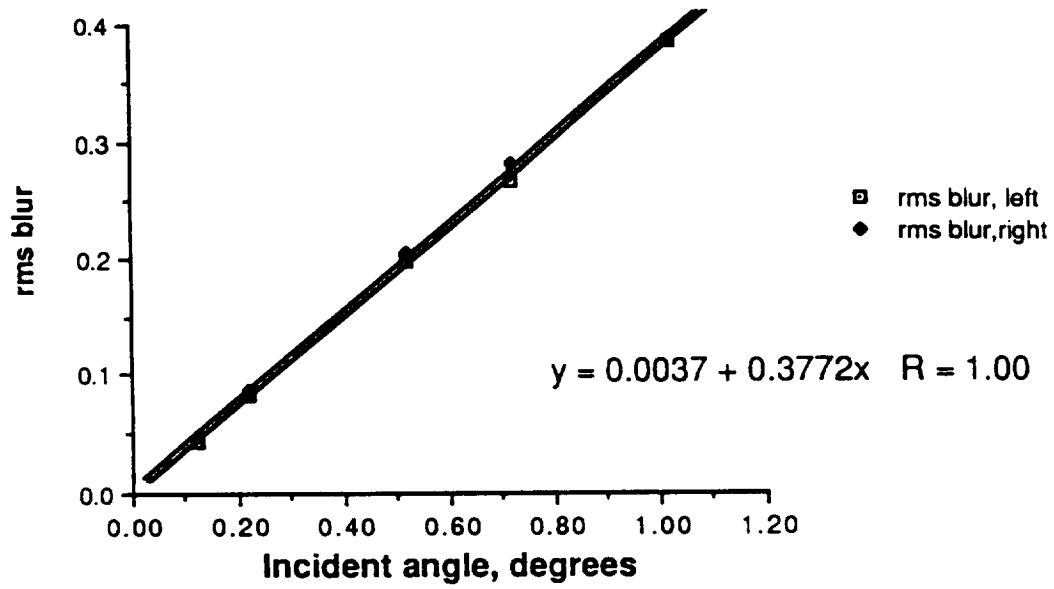


Figure A.1: RMS blur vs. angle of incidence.

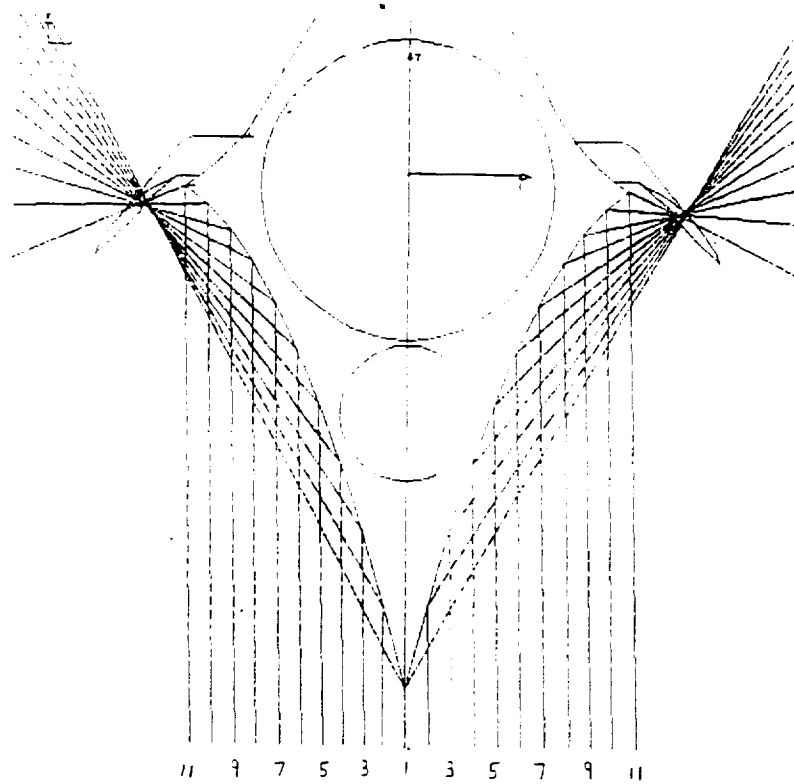


Figure A.2: Geometry for ray trace analysis, indicating the focus of parallel incident light rays.

ray	0.1 degrees		1.0 degrees	
	Left	Right	Left	Right
1	0.079133	0.085295	0.826300	0.840476
2	0.066513	0.073328	0.709123	0.715295
3	0.055705	0.061820	0.595425	0.601060
4	0.045750	0.051470	0.492471	0.497744
5	0.036709	0.042435	0.402163	0.405508
6	0.029108	0.034038	0.319032	0.323672
7	0.022621	0.027244	0.248805	0.253201
8	0.016225	0.020690	0.217250	0.189286
9	0.011627	0.016520	0.139714	0.144422
10	0.007704	0.012534	0.102291	0.105632
11	0.007278	0.008480	0.076231	0.077365
rms blur	0.034397	0.039441	0.375346	0.377605

Table A.1: Perpendicular distance from ray intercepts to focal point at oblique incidence, and RMS blur (all values in cm)

ray	0.2		0.5		0.7	
	Left	Right	Left	Right	Left	Right
1	0.162961	0.169128	0.414376	0.420642	0.582036	0.588282
2	0.114840	0.121739	0.295197	0.301620	0.415029	0.421443
3	0.077013	0.082779	0.196428	0.203807	0.278725	0.284490
4	0.046950	0.052352	0.120776	0.127849	0.172485	0.177886
5	0.025825	0.030647	0.068461	0.073368	0.046833	0.101790
6	0.014932	0.016135	0.037894	0.039097	0.053057	0.054404
rms blur	0.073753	0.078796	0.188853	0.194394	0.258027	0.271466

Table A.2: Perpendicular distances and RMS blur for intermediate angles.

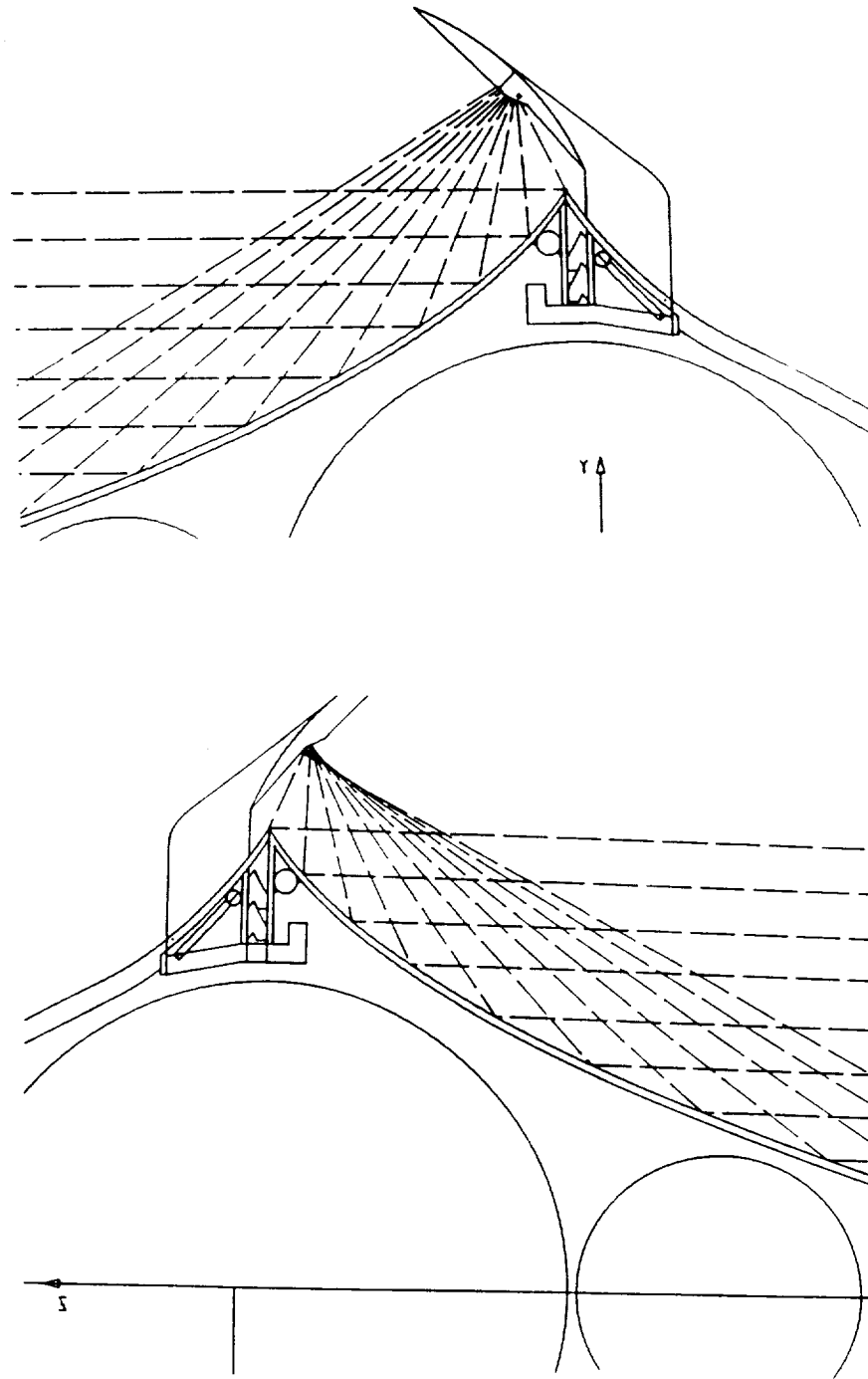


Figure A.3: Ray traces for oblique angles of incidence.

Appendix B

SENSITIVITY ANALYSIS: LTD ENGINE PARAMETERS

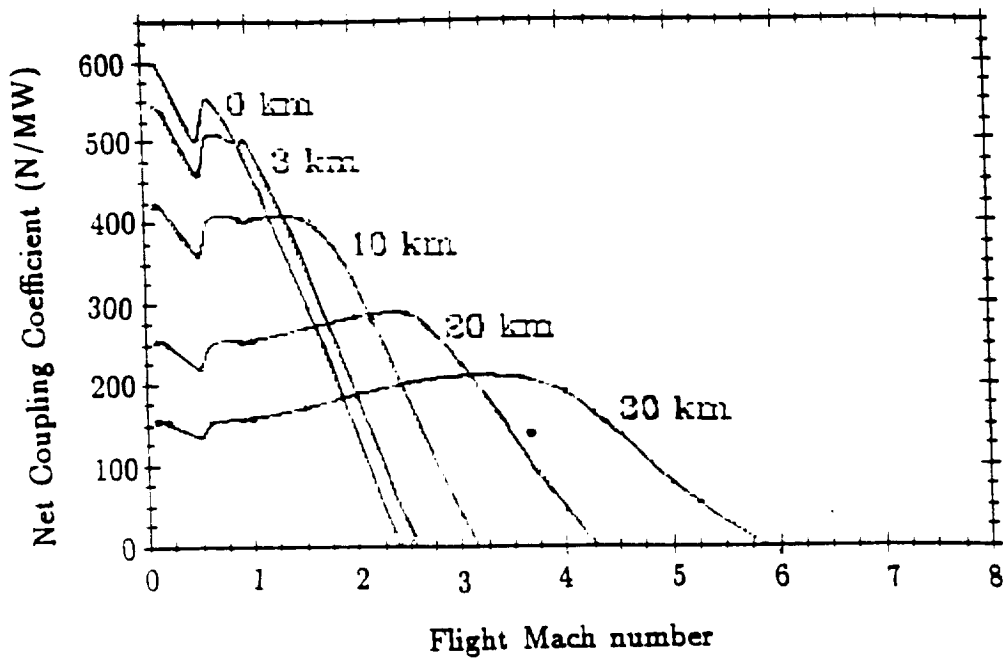


Figure B.1: Net coupling coefficient vs. Mach number and altitude using $M_{refresh} = 0.75$ for $M_{\infty} \geq 0.6$ (the only change from baseline case).

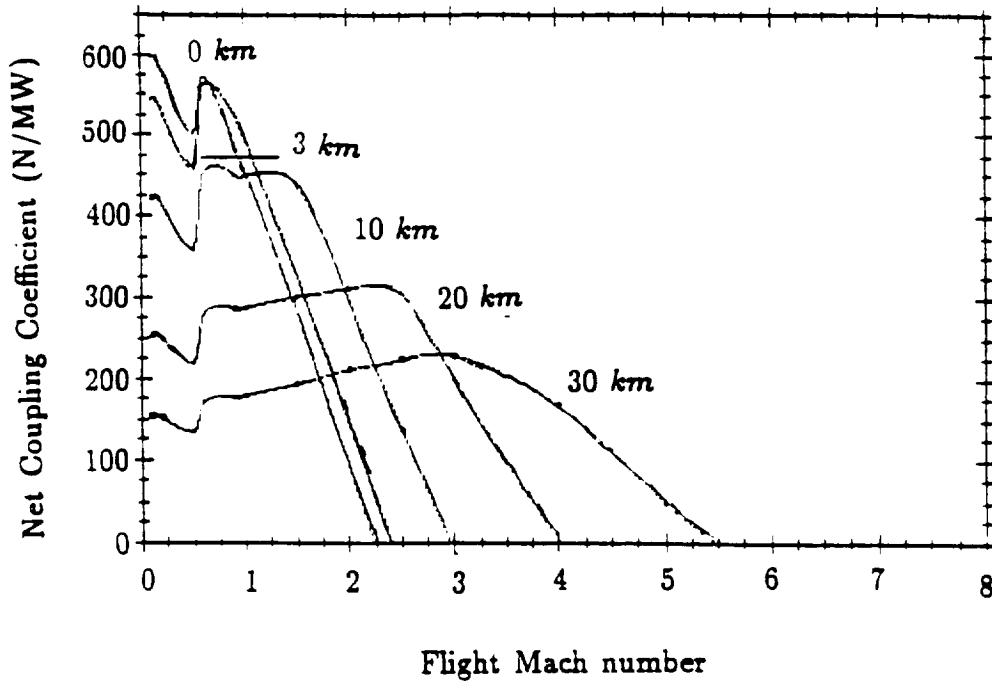


Figure B.2: Net coupling coefficient vs. Mach number and altitude, using $M_{refresh} = 0.5$ for $M_{\infty} \geq 0.6$ (the only change from baseline case).

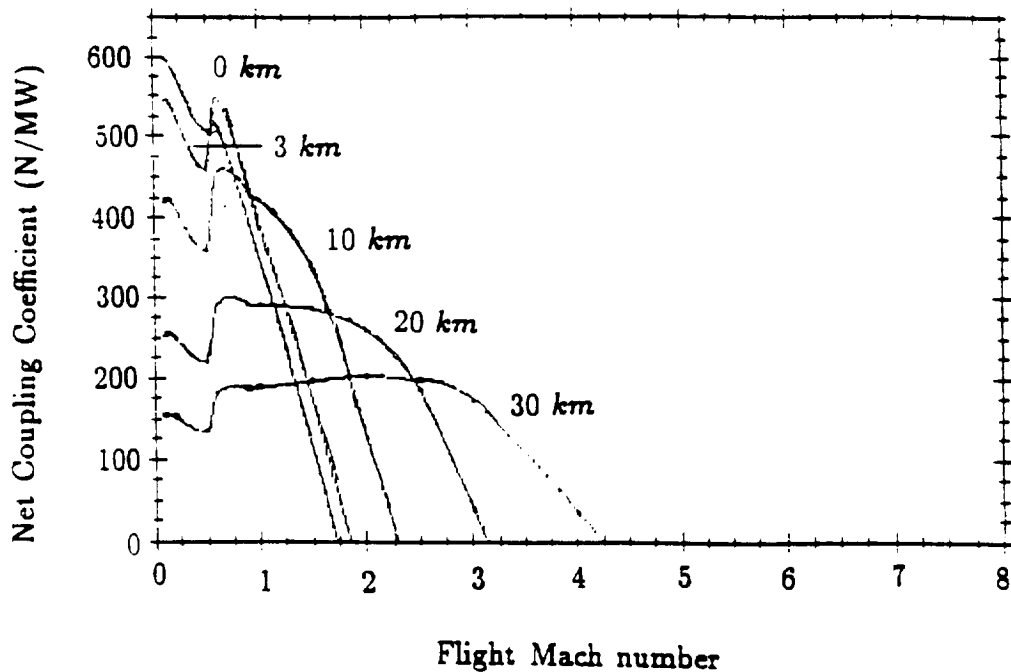


Figure B.3: Net coupling coefficient vs. Mach number and altitude, using $M_{refresh} = 0.25$ for $M_{\infty} \geq 0.6$ (the only change from baseline case).

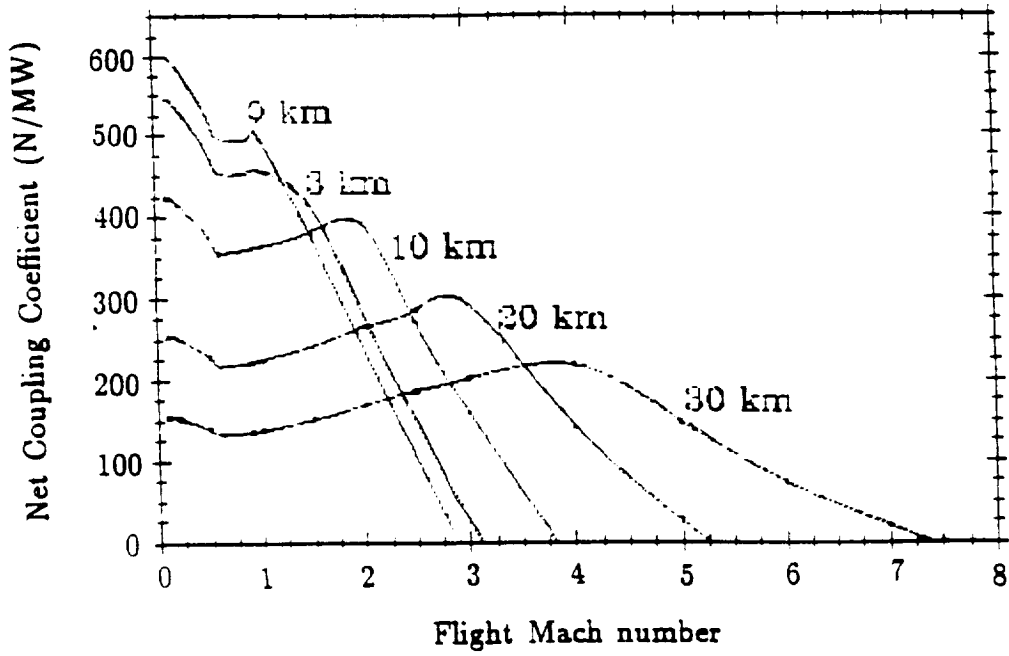


Figure B.4: Net coupling coefficient vs. Mach number and altitude, with the inlet gap reduced by 1 cm (the only change from baseline case).

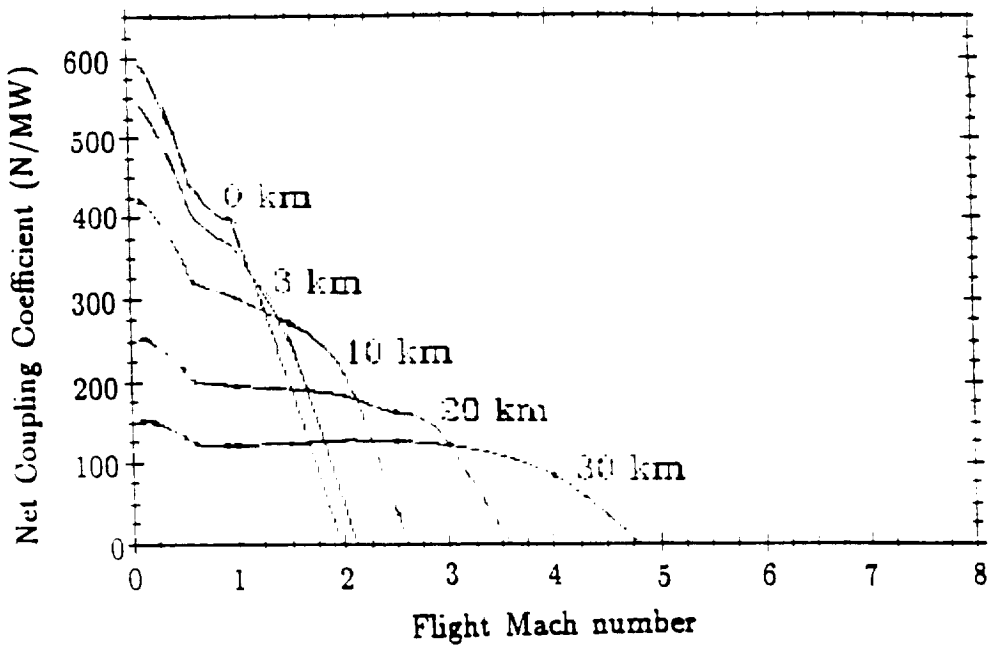


Figure B.5: Net coupling coefficient vs. Mach number and altitude, with the inlet gap increased by 1 cm (the only change from baseline case).

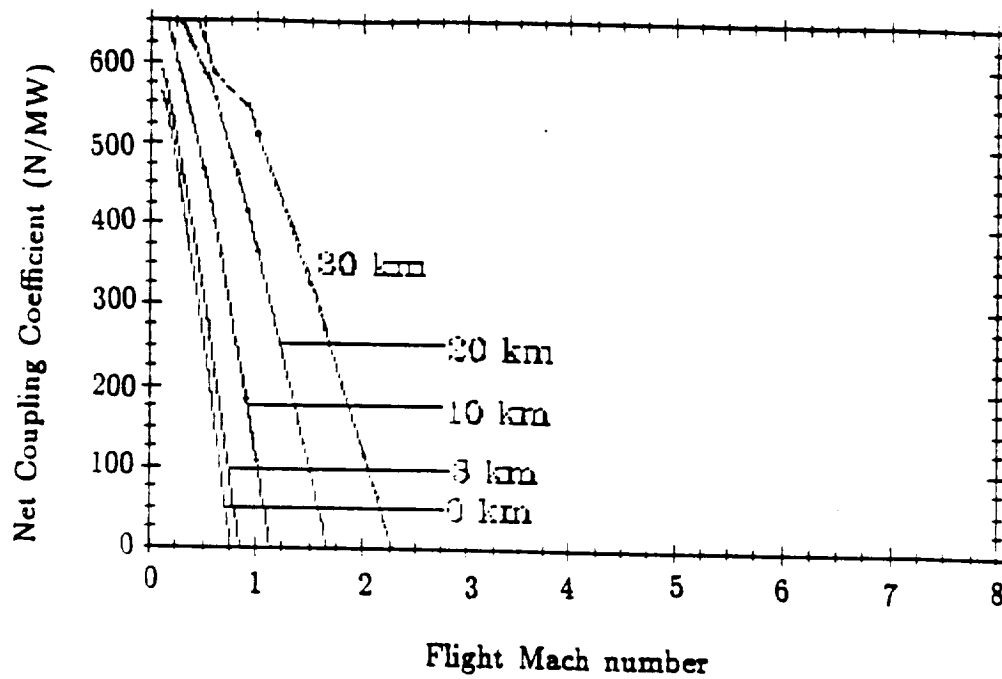


Figure B.6: Net coupling coefficient vs. Mach number and altitude, with r_{LSD} changed to 0.1 cm at t_p (the only change from the baseline case).

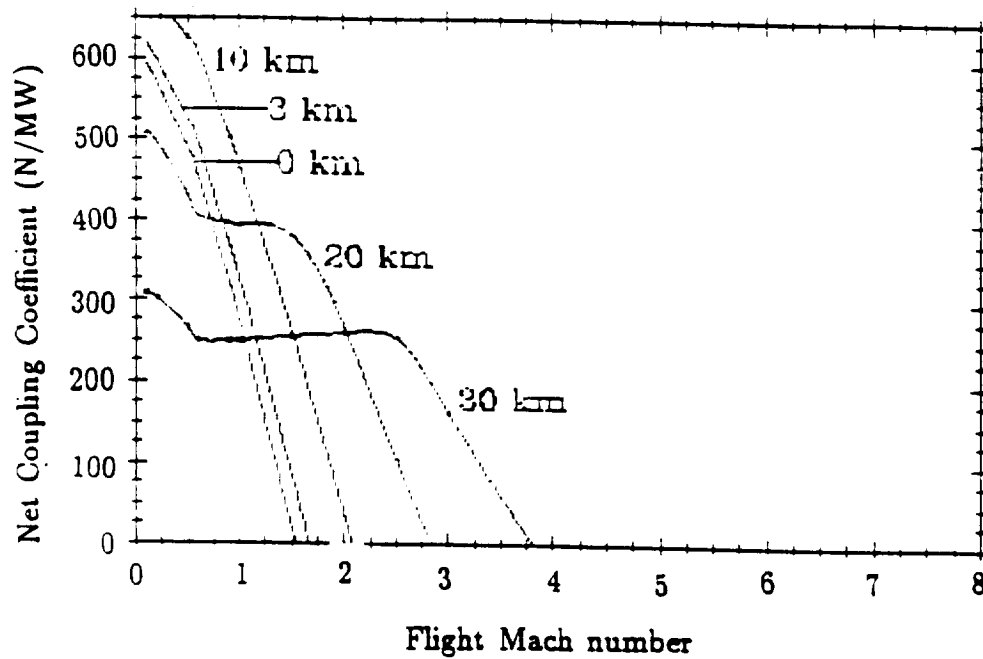


Figure B.7: Net coupling coefficient vs. Mach number and altitude, with r_{LSD} changed to 0.25 cm at t_p (the only change from the baseline case).

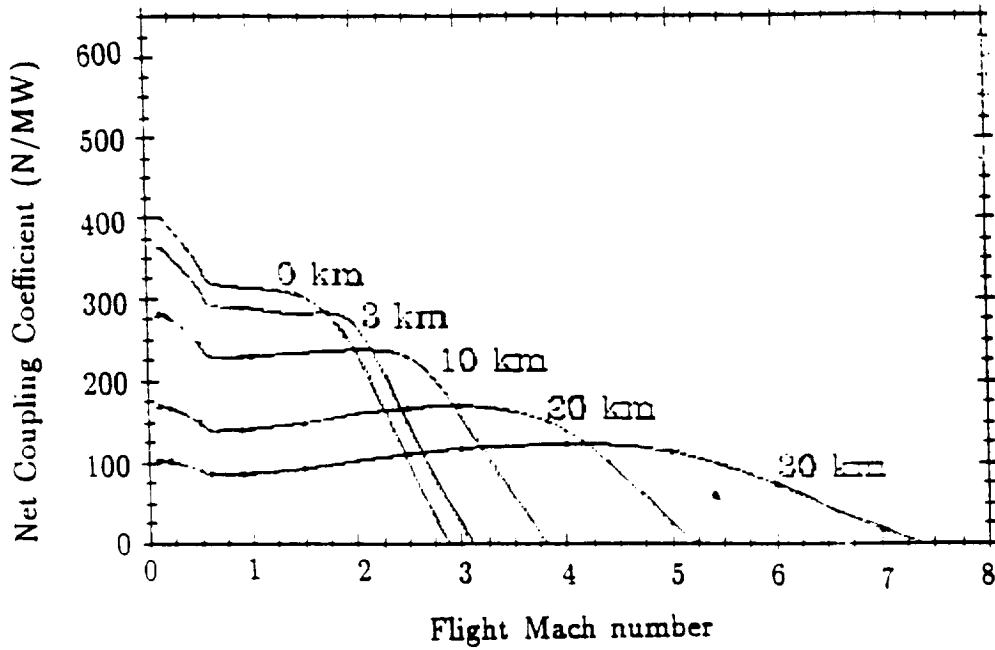


Figure B.8: Net coupling coefficient vs. Mach number and altitude, with r_{LSD} changed to 0.75 cm at t_p (the only change from the baseline case).

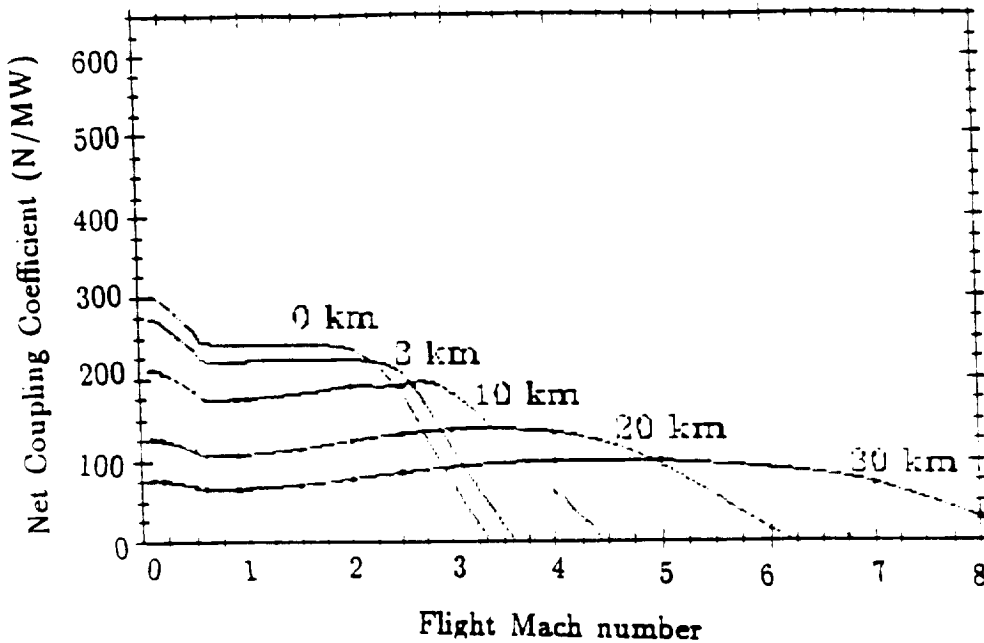


Figure B.9: Net coupling coefficient vs. Mach number and altitude, with r_{LSD} changed to 1 cm at t_p (the only change from the baseline case).

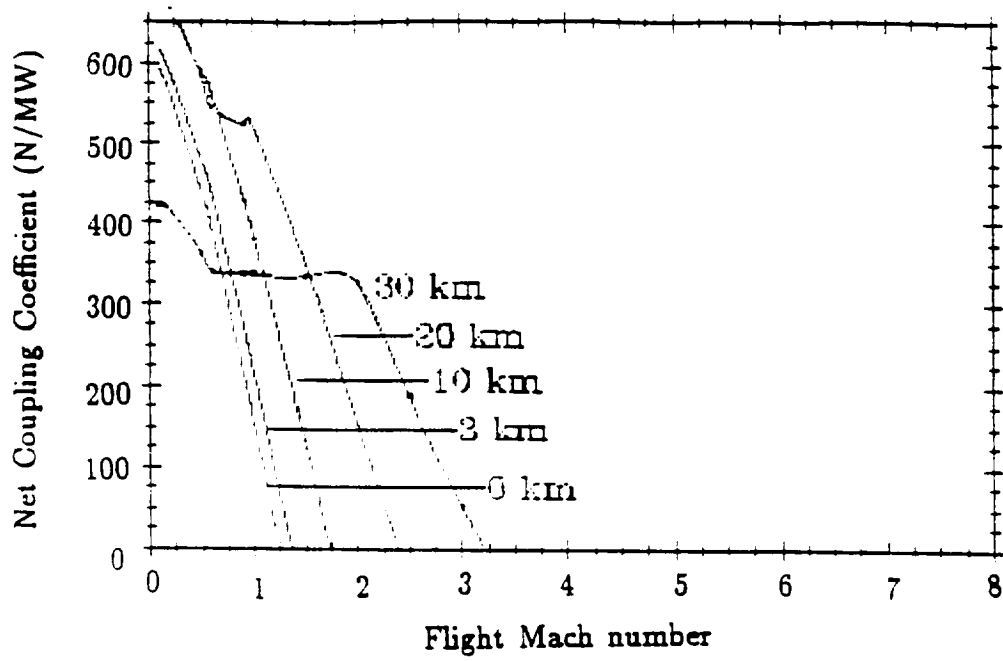


Figure B.10: Net coupling coefficient vs. Mach number and altitude, with $r_{LSD} = 0.1$ cm and $\Phi_{LSD} = 3 \times 10^9$ W/cm² at t_p .

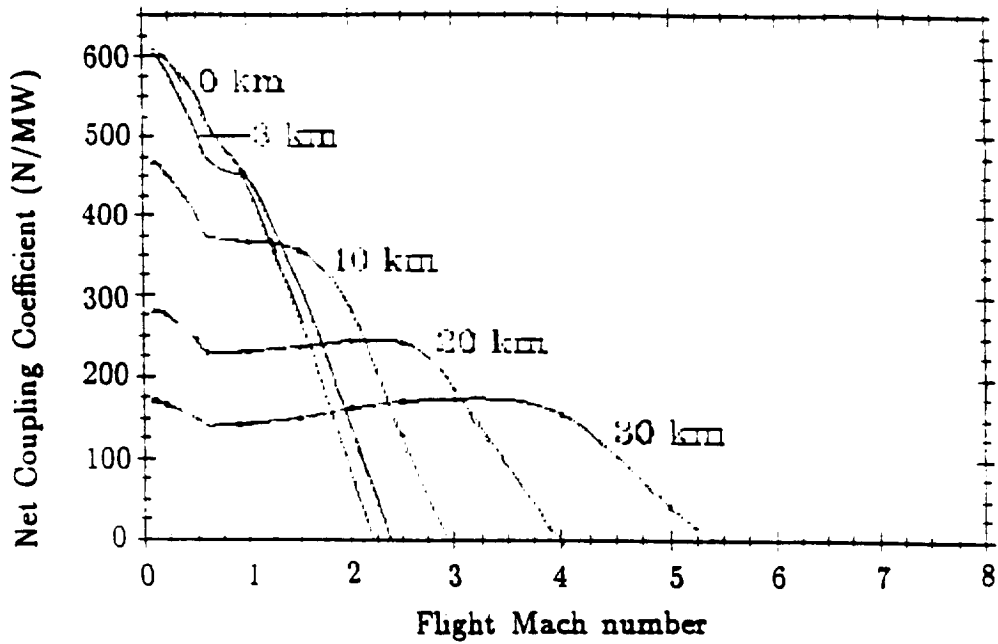


Figure B.11: Net coupling coefficient vs. Mach number and altitude, with $r_{LSD} = 0.25$ cm and $\Phi_{LSD} = 3 \times 10^9$ W/cm² at t_p .

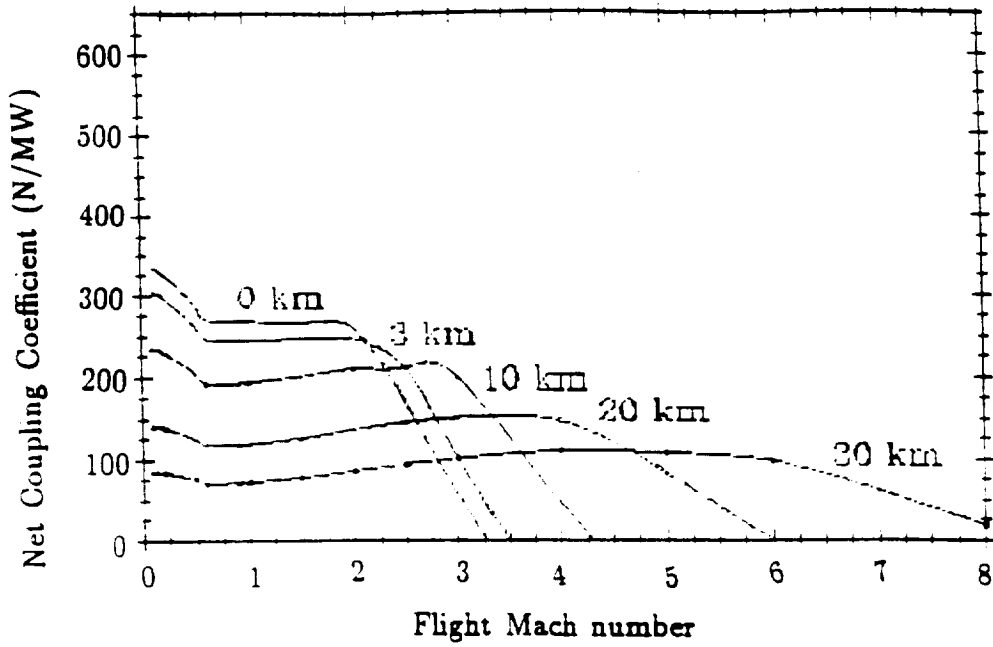


Figure B.12: Net coupling coefficient vs. Mach number and altitude, with $r_{LSD} = 0.5\text{cm}$ and $\Phi_{LSD} = 3 \times 10^9 \text{ W/cm}^2$ at t_p .

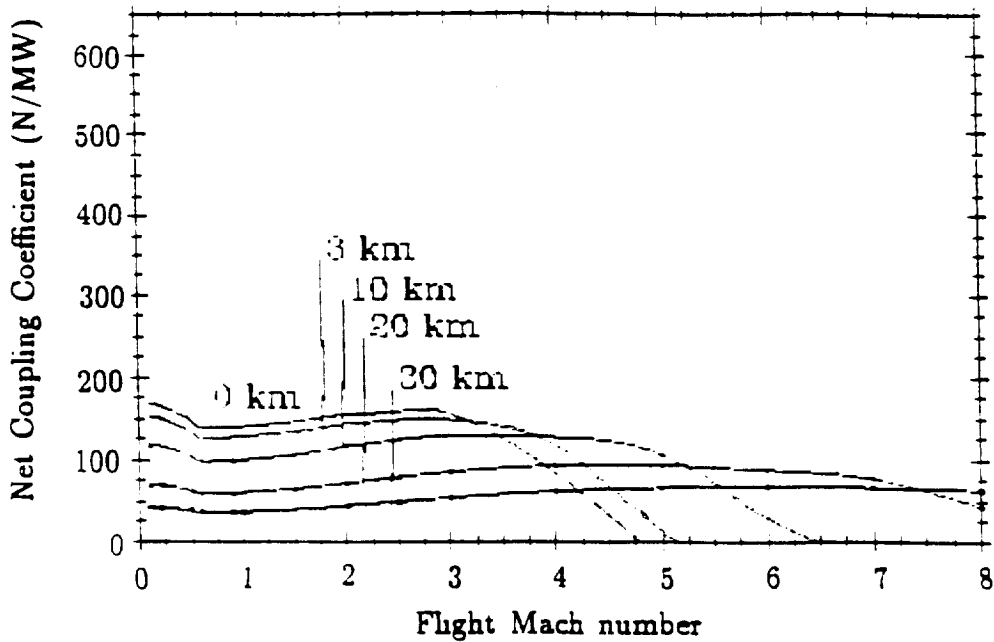


Figure B.13: Net coupling coefficient vs. Mach number and altitude, with $r_{LSD} = 1\text{cm}$ and $\Phi_{LSD} = 3 \times 10^9 \text{ W/cm}^2$ at t_p .

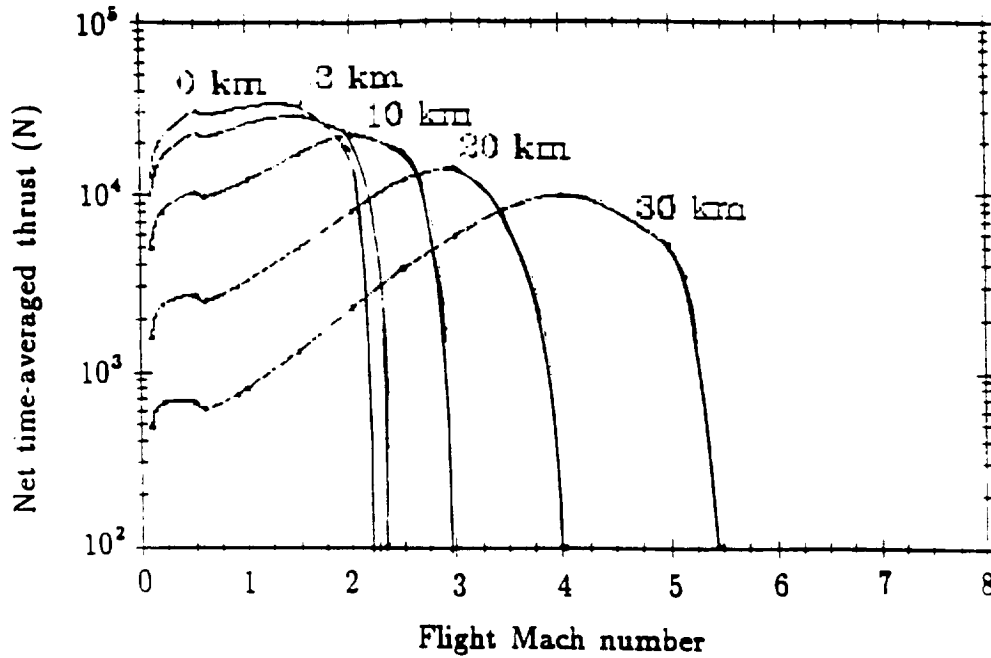


Figure B.14: Net time-averaged thrust vs. Mach number and altitude, with $\tau_{LSD} = 0.25$ cm and $\Phi = 3 \times 10^9$ W/cm² at t_p .

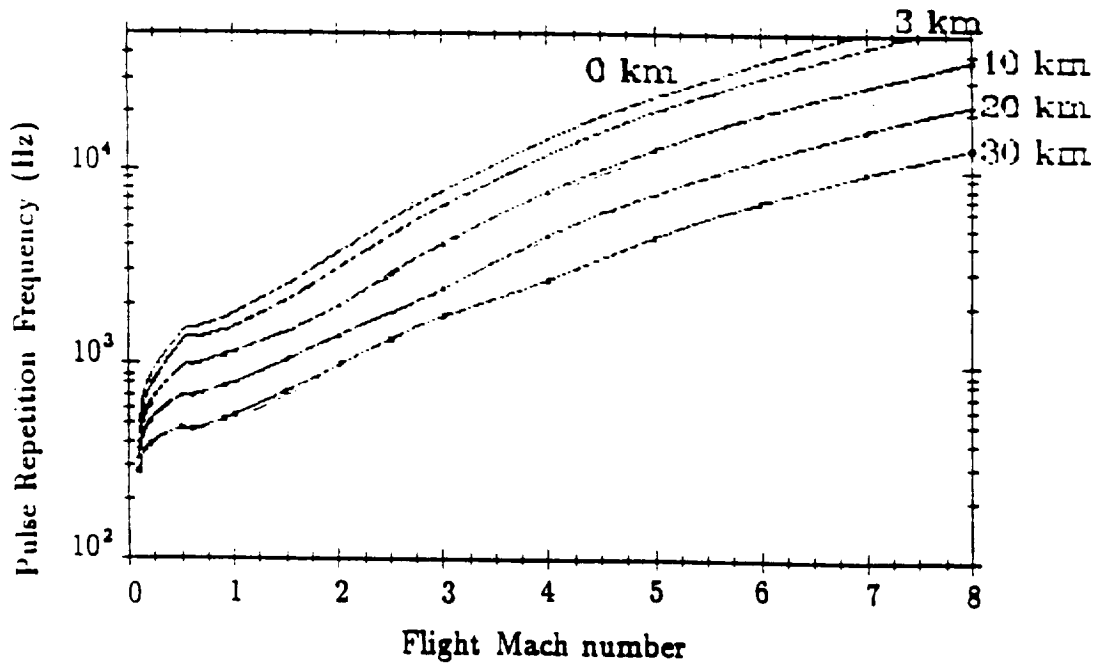


Figure B.15: Pulse Repetition Frequency vs. Mach number and altitude, with $\tau_{LSD} = 0.25$ cm and $\Phi_{LSD} = 3 \times 10^9$ W/cm² at t_p .

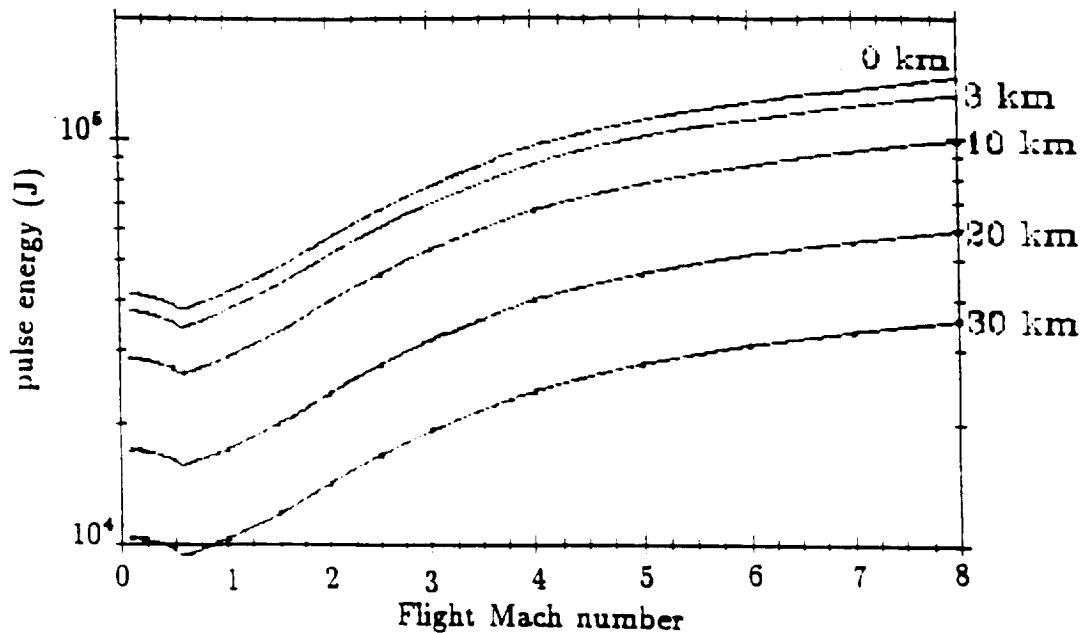


Figure B.16: Pulse energy vs. Mach number and altitude, with $\tau_{LSD} = 0.25$ cm and $\Phi_{LSD} = 3 \times 10^9$ W/cm² at t_p .

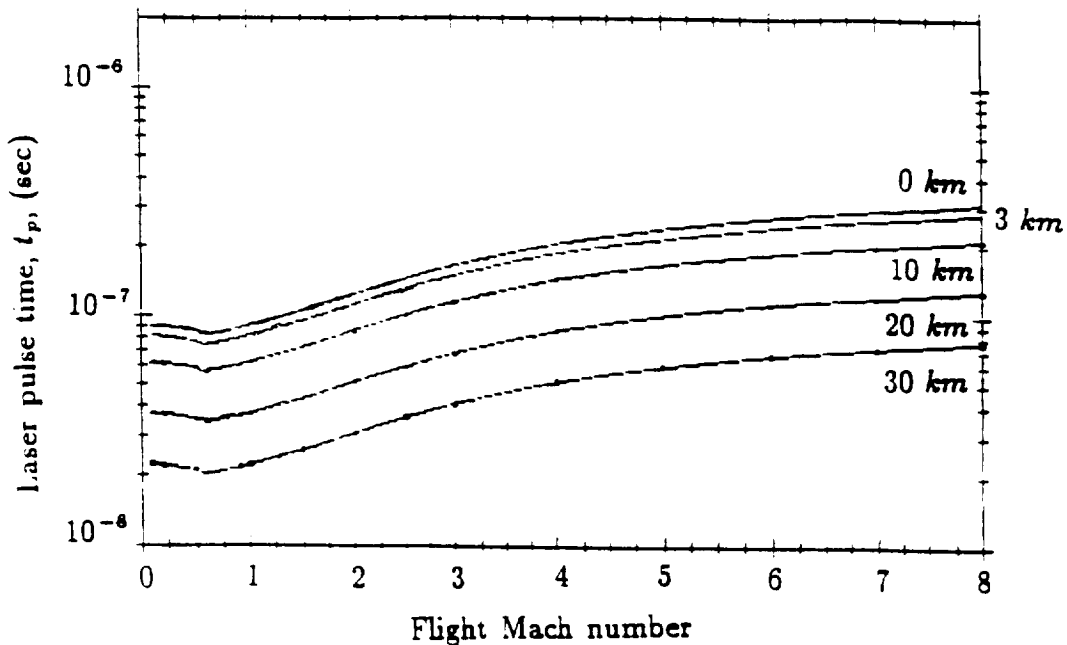


Figure B.17: Laser pulse time vs. Mach number and altitude, with $\tau_{LSD} = 0.25$ cm and $\Phi_{LSD} = 3 \times 10^9$ W/cm² at t_p .

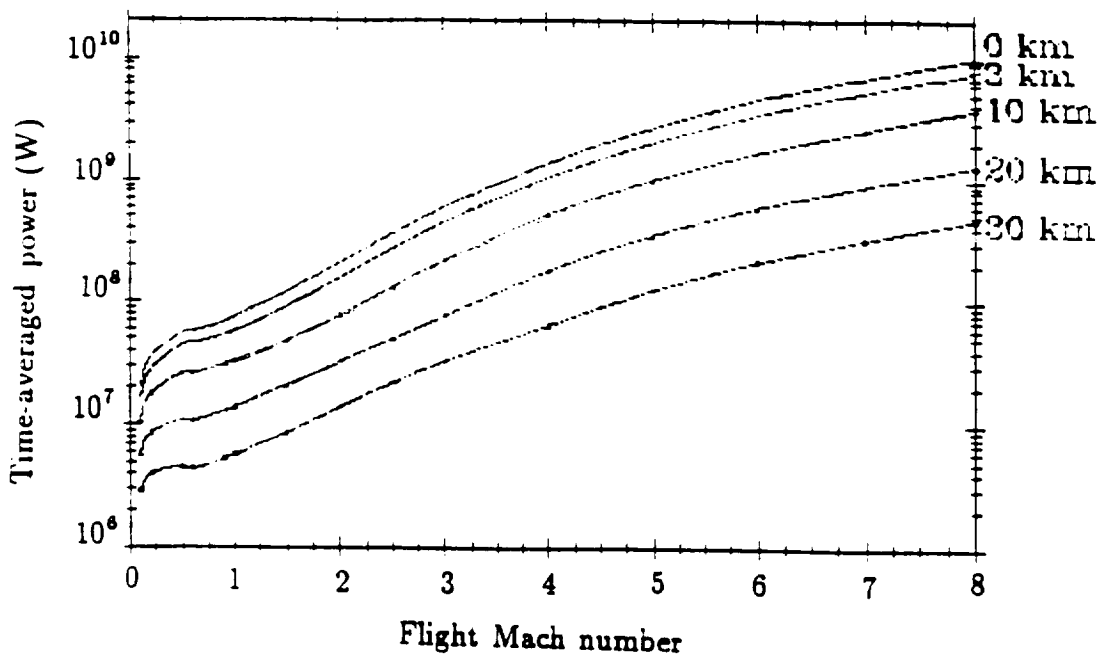


Figure B.18: Time-averaged power vs. Mach number and altitude, with $\tau_{LSD} = 0.25$ cm and $\Phi_{LSD} = 3 \times 10^9$ W/cm² at t_p .

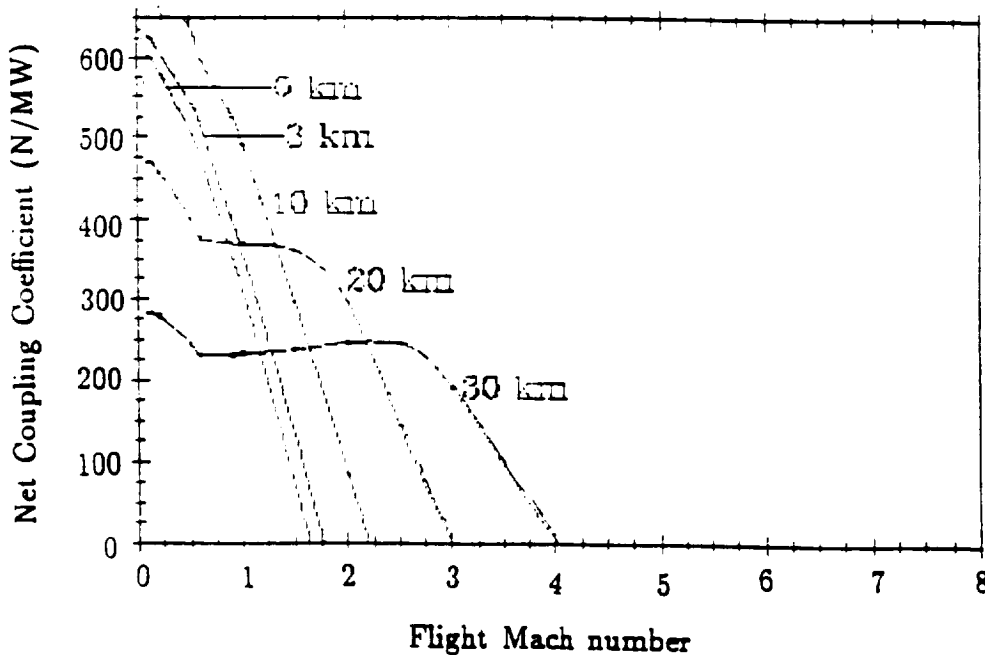


Figure B.19: Net coupling coefficient vs. Mach number and altitude, with $\tau_{LSD} = 0.1$ cm and $\Phi_{LSD} = 10^{10}$ W/cm² at t_p .

ORIGINAL PAGE IS
OF POOR QUALITY

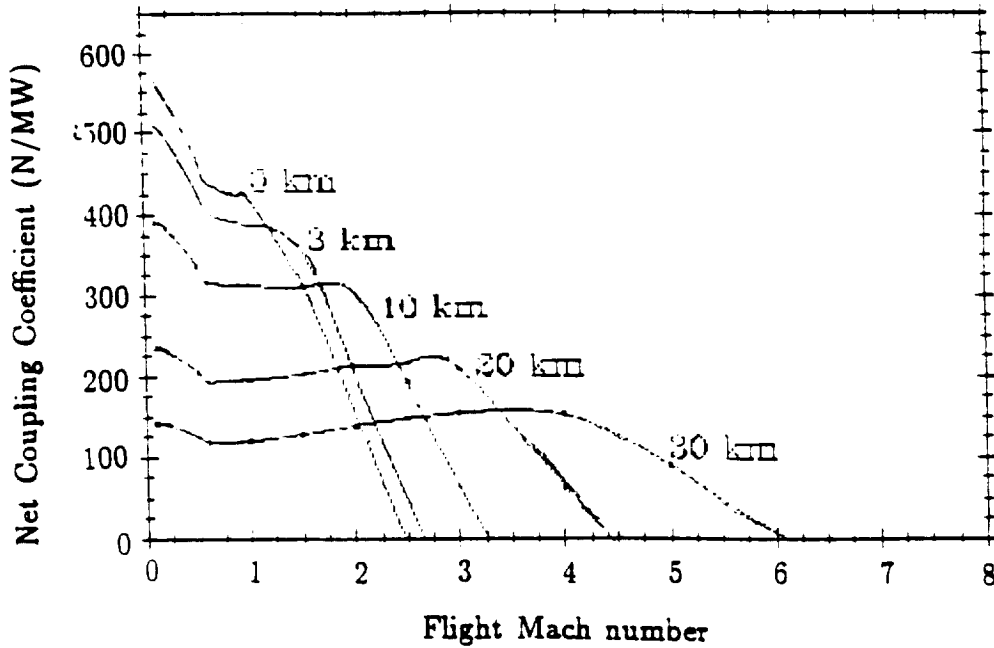


Figure B.20: Net coupling coefficient vs. Mach number and altitude, with $\tau_{LSD} = 0.2$ cm and $\Phi_{LSD} = 10^{10}$ W/cm² at t_p .

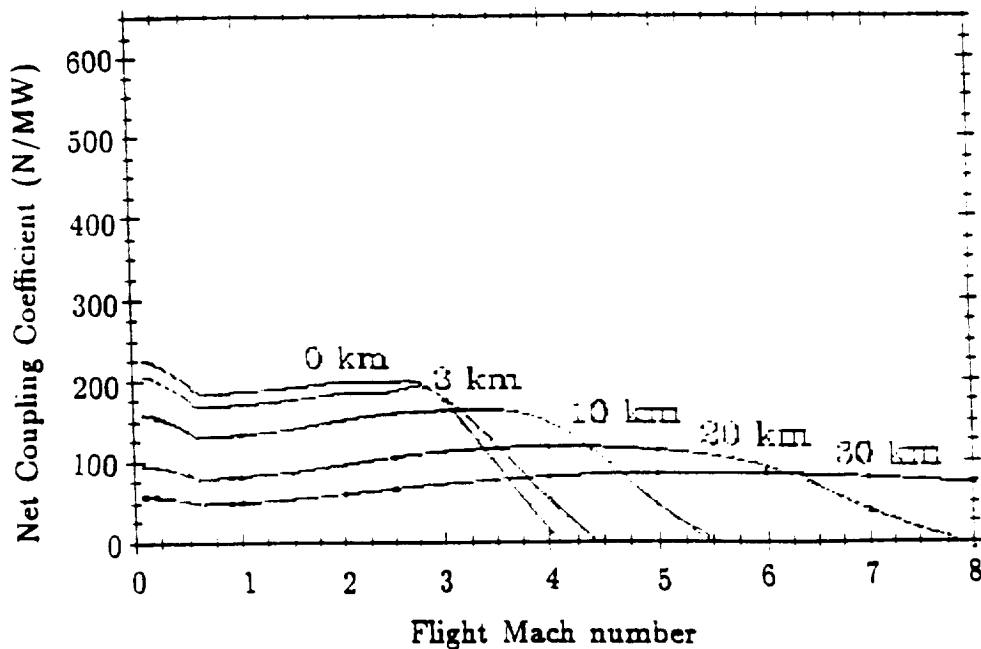


Figure B.21: Net coupling coefficient vs. Mach number and altitude, with $\tau_{LSD} = 0.5$ cm and $\Phi_{LSD} = 10^{10}$ W/cm² at t_p .

ORIGINAL PAGE IS
OF POOR QUALITY

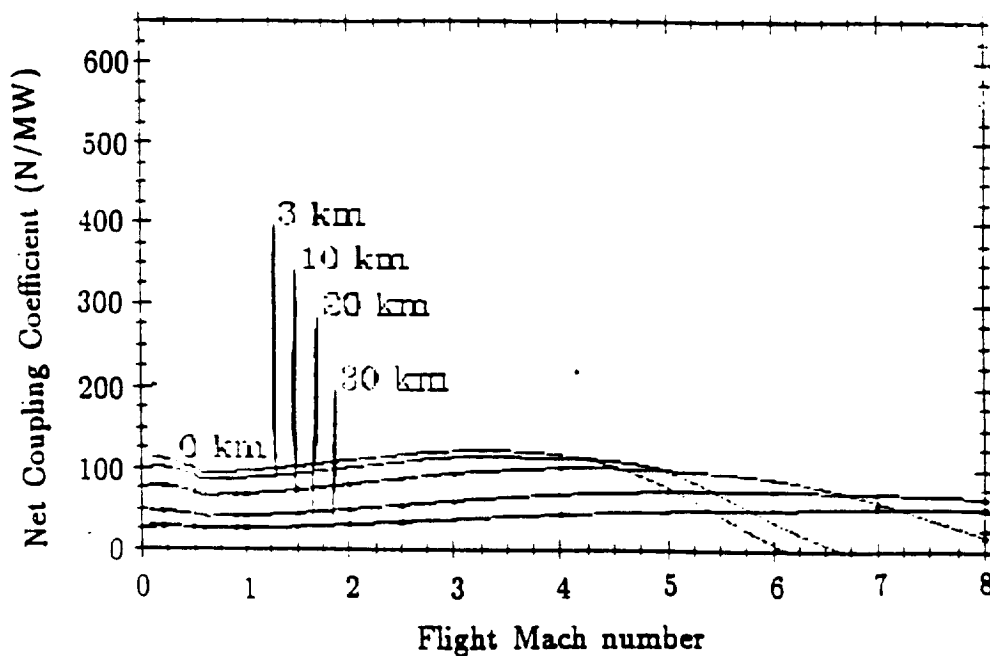


Figure B.22: Net coupling coefficient vs. Mach number and altitude, with $r_{LSD} = 1$ cm and $\Phi_{LSD} = 10^{10}$ W/cm² at t_p .

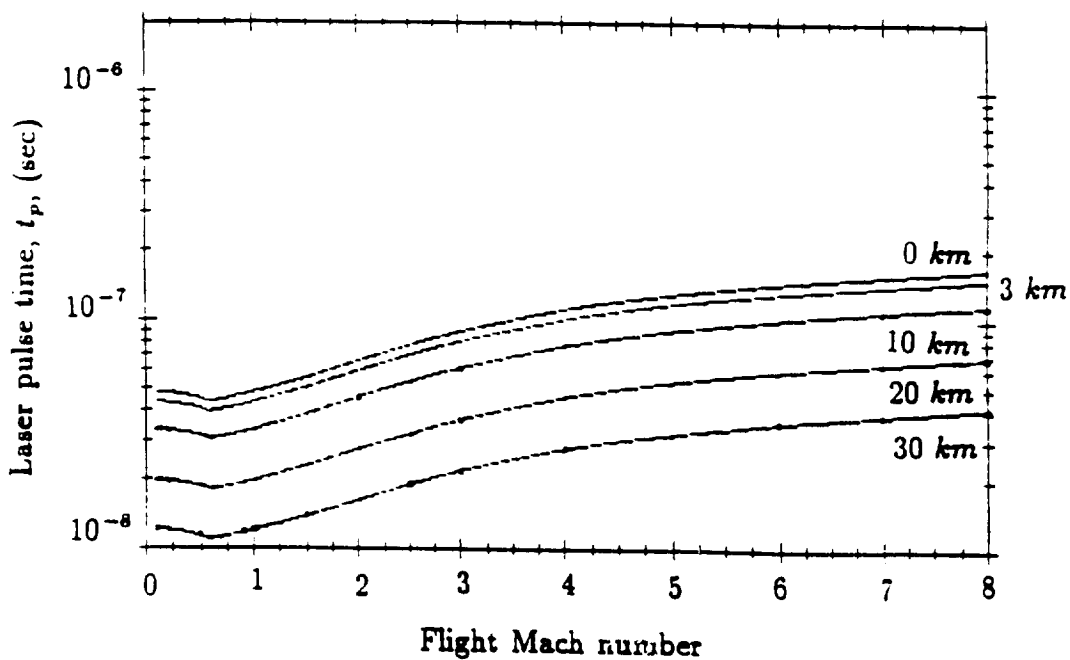


Figure B.23: Laser pulse time vs. Mach number and altitude, with $r_{LSD} = 0.2$ cm and $\Phi_{LSD} = 10^{10}$ W/cm² at t_p .

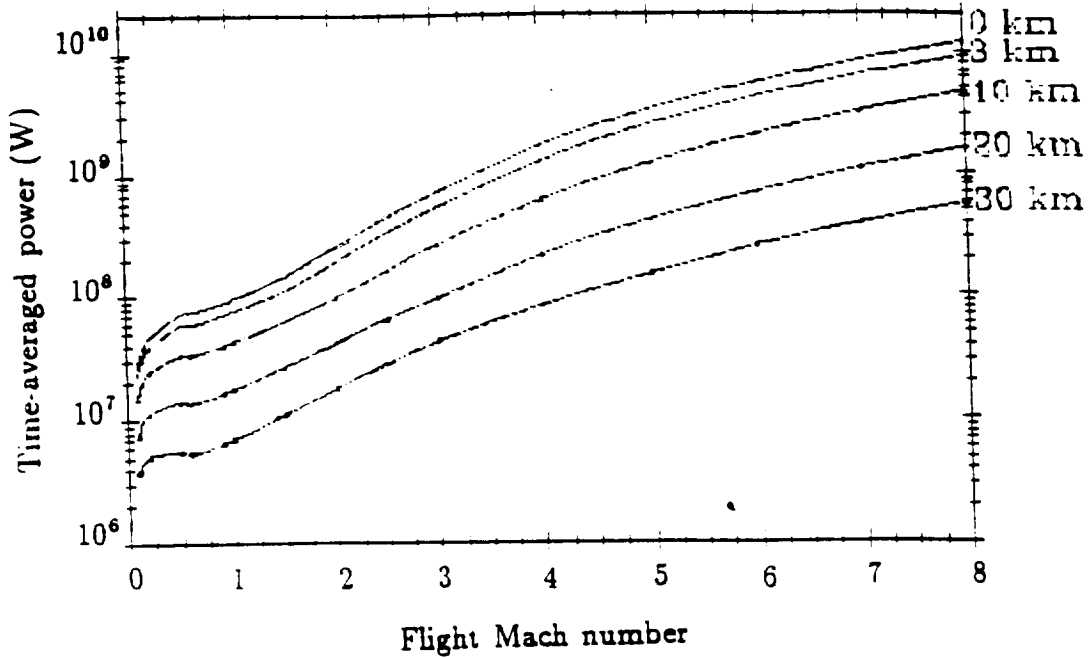


Figure B.24: Time-averaged power vs. Mach number and altitude, with $\tau_{LSD} = 0.2$ cm and $\Phi_{LSD} = 10^{10}$ W/cm² at t_p .

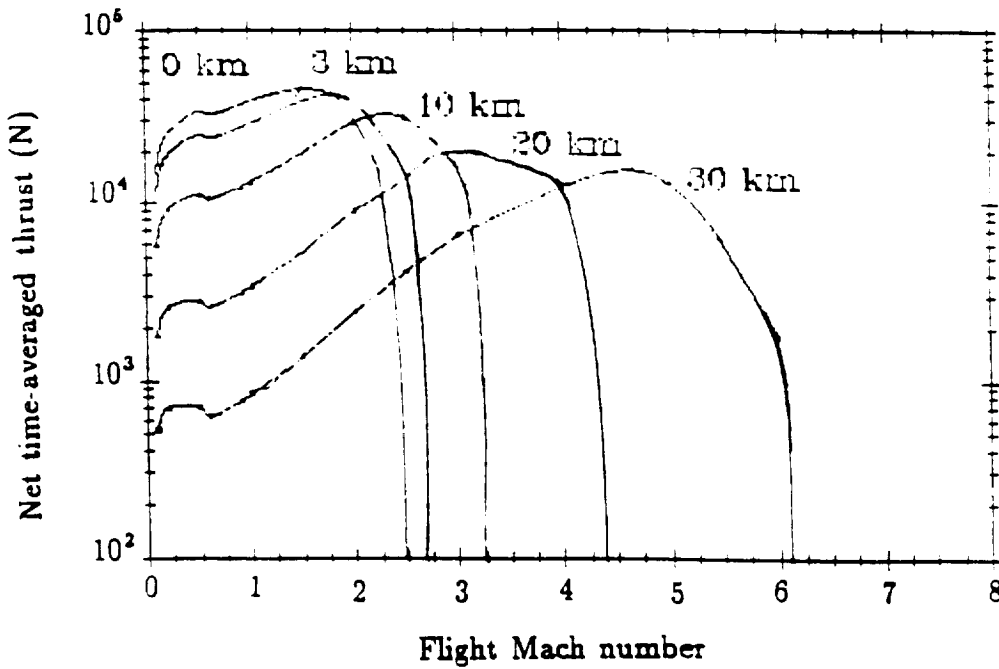


Figure B.25: Net time-averaged thrust vs. Mach number and altitude, with $\tau_{LSD} = 0.2$ cm and $\Phi_{LSD} = 10^{10}$ W/cm² at t_p .

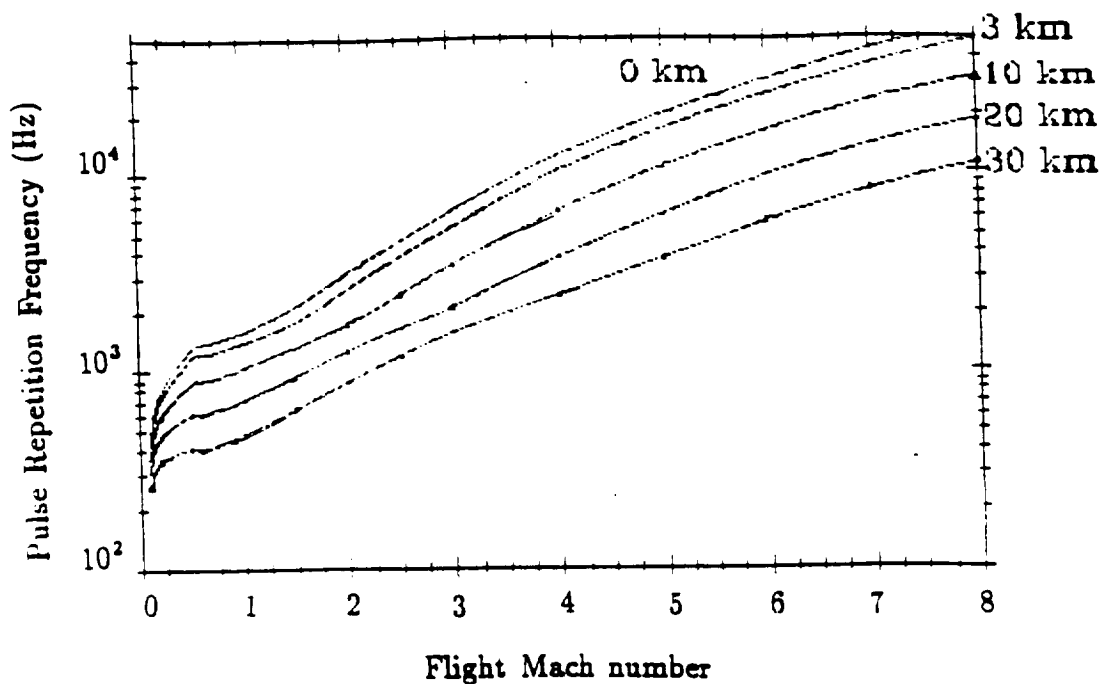


Figure B.26: Pulse Repetition Frequency vs. Mach number and altitude, with $r_{LSD} = 0.2$ cm and $\Phi_{LSD} = 10^{10}$ W/cm² at t_p .

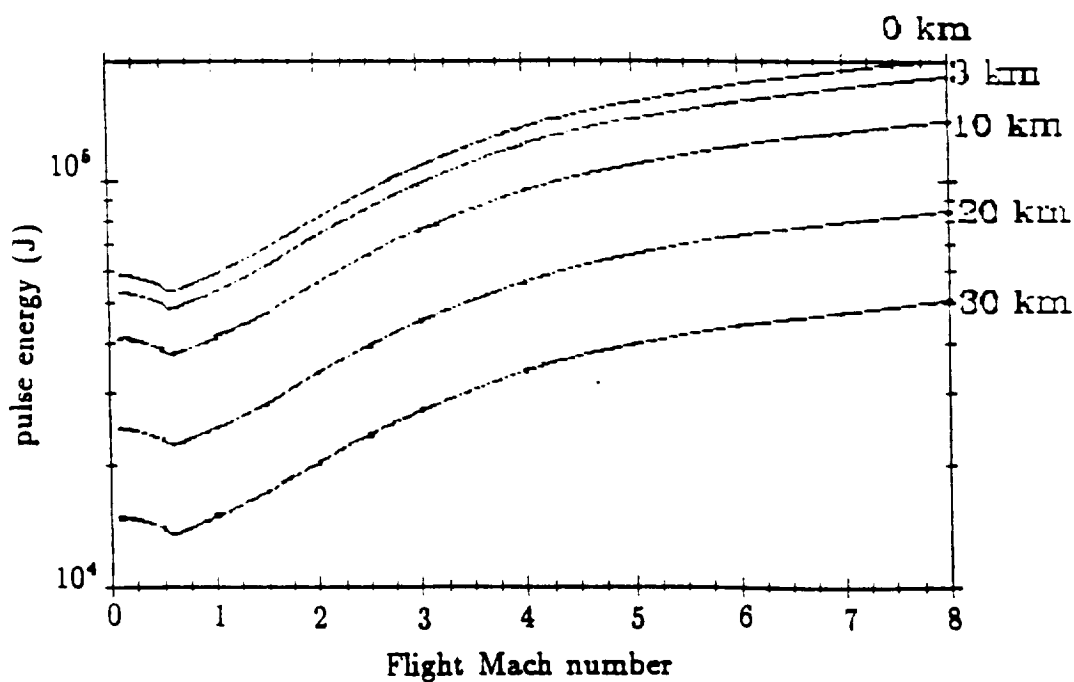


Figure B.27: Pulse energy vs. Mach number and altitude, with $r_{LSD} = 0.2$ cm and $\Phi_{LSD} = 10^{10}$ W/cm² at t_p .

